



# **BROADENING AND SHIFTING OF ATOMIC STRONTIUM AND DIATOMIC BISMUTH SPECTRAL LINES**

DISSERTATION

Jeremy C. Holtgrave, Major, USAF

AFIT/DSP/ENP/03-01

**DEPARTMENT OF THE AIR FORCE  
AIR UNIVERSITY**

## **AIR FORCE INSTITUTE OF TECHNOLOGY**

---

**Wright-Patterson Air Force Base, Ohio**

APPROVED FOR PUBLIC RELEASE; DISTRIBUTION UNLIMITED

The views expressed in this dissertation are those of the author and do not reflect the official policy or position of the United States Air Force, Department of Defense, or the United States Government.

AFIT/DSP/ENP/03-01

BROADENING AND SHIFTING OF ATOMIC STRONTIUM  
AND DIATOMIC BISMUTH SPECTRAL LINES

DISSERTATION

Presented to the Faculty

Department of Engineering Physics

Graduate School of Engineering and Management

Air Force Institute of Technology

Air University

Air Education and Training Command

In Partial Fulfillment of the Requirements for the

Degree of Doctor of Philosophy

Jeremy C. Holtgrave, BS, MS

Major, USAF

May 2003

APPROVED FOR PUBLIC RELEASE; DISTRIBUTION UNLIMITED

BROADENING AND SHIFTING OF ATOMIC STRONTIUM  
AND DIATOMIC BISMUTH SPECTRAL LINES

Jeremy C. Holtgrave, BS, MS  
Major, USAF

Approved:

Date

\_\_\_\_\_  
Paul J. Wolf (Chairman)

\_\_\_\_\_  
Anthony N. Palazotto (Dean's Representative)

\_\_\_\_\_  
Glen P. Perram (Member)

\_\_\_\_\_  
William P. Baker (Member)

\_\_\_\_\_  
David A. Dolson (Member)

Accepted:

\_\_\_\_\_  
Robert A. Calico, Jr.  
Dean, Graduate School of Engineering and Management

\_\_\_\_\_  
Date

## **Acknowledgments**

I am extremely grateful for the assistance of many people who aided directly in this work and to those who helped in other ways. In particular, I thank the chairman of my research committee, Dr Paul Wolf, for his patience and guidance as he saw me through many difficulties. I also thank the members of my research committee: Dr Glen Perram, Dr William Baker, Dr David Dolson, and Dr Anthony Palazotto for their participation and feedback. Among the faculty of the Engineering Physics Department at the Air Force Institute of Technology, I recognize Dr Won Roh, Dr William Bailey, Dr David Weeks, and the department head, Dr Robert Hengehold, who manages to hold it all together. In the lab, I received excellent technical support from Mr Greg Smith and Ms Belinda Johnson, who many times dropped everything to help me. While in residence I was fortunate to have an exceptional collection of classmates. In particular, I thank Maj Mike Dolezal, PhD for his help in understanding the spectroscopy of diatomic bismuth and Lt Col Mark Del Grande, PhD for his friendship. I am especially indebted to my dear friend Maj Robert Pope, PhD. This project would not have been completed without the example he set. Additionally, I thank Maj Amy Magnus, PhD for her love and support and Dr Scott Harris for his friendship. I am also grateful for the assistance of Dr Steve Moosman who helped while I was finishing this work at the Air Force Technical Applications Center. Most of all, I thank my mother who taught me the virtue of hard work and who encouraged me to pursue my dreams.

Jeremy C. Holtgrave

## Table of Contents

	Page
Acknowledgments . . . . .	iv
List of Figures. . . . .	viii
List of Tables . . . . .	xv
Abstract . . . . .	xx
I. Introduction . . . . .	1-1
II. Theory . . . . .	2-1
2.1 Line Broadening and Shifting. . . . .	2-1
2.1.1 Lifetime Broadening . . . . .	2-2
2.1.2 Pressure Broadening . . . . .	2-7
2.1.2.1 Inelastic Collisions and Pressure Broadening . . . . .	2-8
2.1.2.2 Elastic Collisions and Pressure Broadening . . . . .	2-11
2.1.3 Doppler Broadening . . . . .	2-21
2.1.4 The Voigt Profile . . . . .	2-23
2.2 Properties and Spectroscopy of Atomic Strontium and Diatomic Bismuth . . . . .	2-27
2.2.1 Atomic Strontium . . . . .	2-27
2.2.2 Diatomic Bismuth. . . . .	2-34
2.3 Applications of Line Broadening and Shifting . . . . .	2-37
2.3.1 Difference Potentials . . . . .	2-37
2.3.2 Total Quenching Rate Constants . . . . .	2-43

III.	Background . . . . .	3-1
3.1	Line Perturbations and Difference Potentials in Atomic Species. . . . .	3-1
3.1.1	Atomic Calcium . . . . .	3-1
3.1.2	Atomic Strontium . . . . .	3-9
3.1.3	Atomic Barium . . . . .	3-13
3.2	Line Broadening in Diatomic Species . . . . .	3-17
IV.	Broadening and Shifting of Atomic Strontium Spectral Lines . . . . .	4-1
4.1	Measurement of Atomic Strontium Spectral Line Profiles . . . . .	4-1
4.1.1	Absorption Spectroscopy Using a Narrowband Source . . . . .	4-2
4.1.2	Atomic Strontium Experimental Setup . . . . .	4-4
4.1.3	Atomic Strontium Data Acquisition . . . . .	4-11
4.1.4	Atomic Strontium Data Reduction . . . . .	4-16
4.1.5	Atomic Strontium Experimental Results . . . . .	4-25
4.1.6	Systematic Errors in the Atomic Strontium Experiment . . . . .	4-25
4.2	Analysis of Atomic Strontium Line Broadening and Shifting Rates . . . . .	4-28
4.2.1	Atomic Strontium Line Broadening and Shifting Cross Sections . . . . .	4-29
4.2.2	Atomic Strontium and Noble Gas Difference Potentials . . . . .	4-39
4.3	Discussion of the Atomic Strontium Line Broadening and Shifting Experiment . . . . .	4-52
4.3.1	Discussion of Atomic Strontium Line Broadening and Shifting Cross Sections . . . . .	4-52
4.3.2	Discussion of Atomic Strontium and Noble Gas Difference Potentials . . . . .	4-59
4.3.3	Conclusion and Recommendations for Future Research . . . . .	4-62

V.	Broadening of Diatomic Bismuth Spectral Lines . . . . .	5-1
5.1	Measurement of Diatomic Bismuth Spectral Line Profiles . . . . .	5-1
5.1.1	Fluorescence Spectroscopy Using a Narrowband Source . . . . .	5-2
5.1.2	Diatomic Bismuth Experimental Setup . . . . .	5-3
5.1.3	Diatomic Bismuth Data Acquisition . . . . .	5-6
5.1.4	Diatomic Bismuth Data Reduction . . . . .	5-9
5.1.5	Diatomic Bismuth Experimental Results . . . . .	5-14
5.1.6	Systematic Errors in the Diatomic Bismuth Experiment . . . . .	5-17
5.2	Analysis of Diatomic Bismuth Line Broadening Rates . . . . .	5-19
5.2.1	Diatomic Bismuth Line Broadening Cross Sections . . . . .	5-19
5.2.2	Diatomic Bismuth Sum Total Quenching Rate Constants . . . . .	5-28
5.3	Discussion of the Diatomic Bismuth Line Broadening Experiment . . . . .	5-30
5.3.1	Discussion of Diatomic Bismuth Line Broadening Cross Sections. . . . .	5-30
5.3.2	Discussion of Diatomic Bismuth Sum Total Quenching Rate Constants . . . . .	5-35
5.3.3	Conclusion and Recommendations for Future Research . . . . .	5-35
Appendix A.	Theoretical and Measured Bi <sub>2</sub> Rotational Line Positions. . . . .	A-1
Appendix B.	Impact Parameter Integrals . . . . .	B-1
Appendix C.	Line Broadening and Shifting Rates and Cross Sections . . . . .	C-1
Bibliography	. . . . .	BIB-1
Vita	. . . . .	VITA-1



## List of Figures

Figure	Page
2-1. Exponentially decaying sinusoidal oscillator . . . . .	2-3
2-2. Lorentzian lineshape of a transition broadened by lifetime effects . . . . .	2-5
2-3. Transition between the lower and upper energy states of an atom or molecule . . . . .	2-6
2-4. Transition between the lower and upper energy states of an atom or molecule affected by quenching . . . . .	2-9
2-5. Lorentzian lineshape of a transition broadened by both lifetime effects and quenching . . . . .	2-10
2-6. Diagram of the elastic collision process . . . . .	2-12
2-7. The influence of a passing body $b$ on the energy states of body $a$ . . . . .	2-13
2-8. Oscillator angular frequency and electric field magnitude perturbed by elastic collisions as a function of time . . . . .	2-16
2-9. Lorentzian lineshape of a transition broadened and shifted by elastic collisions . . . . .	2-21
2-10. Gaussian lineshape of a transition broadened by the Doppler effect . . . . .	2-23
2-11. Voigt lineshape function of a transition overlaid with Lorentzian and Gaussian lineshape functions . . . . .	2-26
2-12. Lower electronic energy states of atomic strontium . . . . .	2-28
2-13. Hyperfine structure of the $5s5p\ ^3P_1$ and $5s6s\ ^3S_1$ energy states of $^{87}\text{Sr}$ with transitions allowed under the selection rule $\Delta F = 0, \pm 1$ labeled . . . . .	2-32
2-14. Line profile of the atomic strontium $5s^2\ ^1S_0 \rightarrow 5s5p\ ^3P_1$ transition including contributions by the isotopes $^{88}\text{Sr}$ , $^{86}\text{Sr}$ , and the hyperfine levels of $^{87}\text{Sr}$ . . . . .	2-34

2-15.	Line profile of the atomic strontium $5s5p\ ^3P_1 \rightarrow 5s6s\ ^3S_1$ transition including contributions by the isotopes $^{88}\text{Sr}$ , $^{86}\text{Sr}$ , and the hyperfine levels of $^{87}\text{Sr}$ . . . . .	2-35
2-16.	Electronic energy states of diatomic bismuth near the ground state . . . . .	2-36
2-17.	A small portion of the diatomic bismuth spectrum in the $v''=3 \rightarrow v'=1$ vibrational manifold of the $X(0_g^+) \rightarrow A(0_u^+)$ electronic transition . . . . .	2-37
2-18.	$\frac{S(\alpha)}{4B(\alpha)}$ as a function of $\log_{10}(\alpha)$ . . . . .	2-42
3-1.	Lower electronic energy states of atomic calcium . . . . .	3-3
3-2.	Line broadening and shifting cross sections of the atomic calcium $4s4p\ ^3P_{0,1,2} \rightarrow 4s5s\ ^3S_1$ transitions around $16329\text{ cm}^{-1}$ perturbed by helium, neon, and argon as a function of the total angular momentum quantum number $J''$ of the initial state . . . . .	3-6
3-3.	Mid-level electronic energy states of atomic calcium . . . . .	3-7
3-4.	Lower electronic energy states of atomic strontium . . . . .	3-10
3-5.	Lower electronic energy states of atomic barium. . . . .	3-14
3-6.	Line broadening cross sections of the $\text{O}_2$ A band perturbed by helium, neon, argon, and krypton as a function of the branch-independent quantum number $m$ . . . . .	3-19
3-7.	Line broadening cross sections of the NO fundamental band perturbed by helium, neon, argon, and krypton as a function of the branch-independent quantum number $m$ . . . . .	3-20
3-8.	Line broadening cross sections of the CO fundamental band perturbed by helium and argon as a function of the branch-independent quantum number $m$ . . . . .	3-21
4-1.	Schematic diagram of the atomic strontium absorption experimental apparatus . . . . .	4-6
4-2.	Raw data of the atomic strontium $5s5p\ ^3P_0 \rightarrow 5s6s\ ^3S_1$ transition at $14721.275\text{ cm}^{-1}$ perturbed by argon . . . . .	4-17

4-3.	Absorbances of the atomic strontium $5s5p\ ^3P_0 \rightarrow 5s6s\ ^3S_1$ transition at $14721.275\text{ cm}^{-1}$ perturbed by argon before and after Fourier filtering . . .	4-18
4-4.	Comparison of the tube furnace temperatures as determined from the Gaussian linewidths of the reference cell with the temperatures registered by the tube furnace thermocouple . . . . .	4-20
4-5.	Line profiles of the atomic strontium $5s5p\ ^3P_0 \rightarrow 5s6s\ ^3S_1$ transition at $14721.275\text{ cm}^{-1}$ perturbed by argon and fit to Voigt lineshape functions . . .	4-21
4-6.	Unperturbed line profile of the atomic strontium $5s^2\ ^1S_0 \rightarrow 5s5p\ ^3P_1$ transition at $14504.351\text{ cm}^{-1}$ fit to three Voigt lineshape functions . . . . .	4-23
4-7.	Unperturbed line profile of the atomic strontium $5s^2\ ^1S_0 \rightarrow 5s5p\ ^3P_1$ transition at $14504.351\text{ cm}^{-1}$ fit to a single Voigt lineshape function. . . . .	4-23
4-8.	Line profile of the atomic strontium $5s5p\ ^3P_1 \rightarrow 5s6s\ ^3S_1$ transition at $14534.444\text{ cm}^{-1}$ perturbed by 22.1 Torr of helium . . . . .	4-24
4-9.	Lorentzian linewidths (FWHM) and line center shifts of the atomic strontium $5s5p\ ^3P_0 \rightarrow 5s6s\ ^3S_1$ transition at $14721.275\text{ cm}^{-1}$ perturbed by argon as functions of pressure . . . . .	4-25
4-10.	Line broadening and shifting cross sections of the atomic strontium $5s5p\ ^3P_{0,1,2} \rightarrow 5s6s\ ^3S_1$ transitions around $14534\text{ cm}^{-1}$ perturbed by helium, neon, argon, krypton, and xenon as a function of the total angular momentum quantum number $J''$ of the initial state . . . . .	4-33
4-11.	Comparison of the atomic strontium $5s5p\ ^3P_{0,1,2} \rightarrow 5s6s\ ^3S_1$ line broadening cross sections of this work with the atomic calcium $4s4p\ ^3P_{0,1,2} \rightarrow 4s5s\ ^3S_1$ line broadening cross sections reported by O'Neill and Smith [39] for perturbing species helium, neon, and argon . . . . .	4-36
4-12.	Comparison of the atomic strontium $5s5p\ ^3P_{0,1,2} \rightarrow 5s6s\ ^3S_1$ line shifting cross sections of this work with the atomic calcium $4s4p\ ^3P_{0,1,2} \rightarrow 4s5s\ ^3S_1$ line shifting cross sections reported by O'Neill and Smith [39] for perturbing species helium, neon, and argon . . . . .	4-36
4-13.	Ratios of the atomic strontium line shifting rates to line broadening rates compared to the function $\frac{S(\alpha)}{4B(\alpha)}$ for all transitions and noble gases studied in this research . . . . .	4-42

4-14.	Atomic strontium difference potential plots as a function of internuclear separation for all energy states perturbed by all noble gases studied in this research . . . . .	4-44
4-15.	Atomic strontium difference potential plots as a function of internuclear separation for all energy states perturbed by all noble gases studied in this research . . . . .	4-45
4-16.	Comparison of the atomic strontium $5s^2\ ^1S_0$ and $5s5p\ ^3P_1$ difference potentials as a function of internuclear separation of this work with those of the atomic strontium $5s^2\ ^1S_0$ and $5s5p\ ^1P_1$ energy states studied in previous research . . . . .	4-48
4-17.	Comparison of the atomic strontium $5s^2\ ^1S_0$ and $5s5p\ ^3P_1$ difference potentials as a function of internuclear separation of this work with those of the atomic strontium $5s^2\ ^1S_0$ and $5s5p\ ^1P_1$ energy states studied in previous research . . . . .	4-49
4-18.	Comparison of the atomic strontium $5s5p\ ^3P_0$ and $5s6s\ ^3S_1$ difference potentials as a function of internuclear separation of this work with those of the atomic strontium $5s^2\ ^1S_0$ and $5s5p\ ^1P_1$ energy states studied in previous research . . . . .	4-50
4-19.	Comparison of the atomic strontium $5s5p\ ^3P_0$ and $5s6s\ ^3S_1$ difference potentials as a function of internuclear separation of this work with those of the atomic strontium $5s^2\ ^1S_0$ and $5s5p\ ^1P_1$ energy states studied in previous research . . . . .	4-51
4-20.	Line broadening and shifting cross sections of the atomic strontium $5s^2\ ^1S_0 \rightarrow 5s5p\ ^3P_1$ transition at $14504.351\text{ cm}^{-1}$ as a function of the polarizability of the perturbing species helium, neon, argon, krypton, and xenon. . . . .	4-53
4-21.	Line broadening cross sections of the atomic strontium $5s5p\ ^3P_{0,1,2} \rightarrow 5s6s\ ^3S_1$ transitions around $14534\text{ cm}^{-1}$ as a function of the polarizability of the perturbing species helium, neon, argon, krypton, and xenon. . . . .	4-55
4-22.	Line broadening cross sections of the atomic calcium $4s4p\ ^3P_{0,1,2} \rightarrow 4s5s\ ^3S_1$ transitions around $16329\text{ cm}^{-1}$ as a function of the polarizability of the perturbing species helium, neon, and argon . . . . .	4-56

4-23.	Line shifting cross sections of the atomic strontium 5s5p $^3P_{0,1,2} \rightarrow 5s6s \ ^3S_1$ transitions around 14534 cm <sup>-1</sup> as a function of the polarizability of the perturbing species helium, neon, argon, krypton, and xenon . . . . .	4-57
4-24.	Atomic strontium difference potential constant $C_6$ as a function of the polarizability of the perturbing species helium, neon, argon, krypton, and xenon for all energy states studied in this research . . . . .	4-60
4-25.	Atomic strontium difference potential well depths as a function of the polarizability of the perturbing species helium, neon, argon, krypton, and xenon for all energy states studied in this research . . . . .	4-62
4-26.	Difference potential constants $C_6$ and $C_{12}$ of the atomic strontium 5s <sup>2</sup> $^1S_0$ and 5s5p $^3P_1$ energy states perturbed by helium, neon, argon, krypton, and xenon compared to contours of Equation 4-24 . . . . .	4-63
5-1.	Schematic diagram of the diatomic bismuth fluorescence experimental apparatus . . . . .	5-4
5-2.	Raw data of the Bi <sub>2</sub> R(128) and P(115) transitions in the $\nu''=3 \rightarrow \nu'=1$ vibrational manifold of the $X(0_g^+) \rightarrow A(0_u^+)$ electronic transition and I <sub>2</sub> reference spectral lines around 17292.6 cm <sup>-1</sup> perturbed by 102 Torr of neon . . . . .	5-9
5-3.	Bi <sub>2</sub> fluorescence and I <sub>2</sub> absorbance of the Bi <sub>2</sub> R(128) and P(115) transitions in the $\nu''=3 \rightarrow \nu'=1$ vibrational manifold of the $X(0_g^+) \rightarrow A(0_u^+)$ electronic transition around 17292.6 cm <sup>-1</sup> perturbed by 102 Torr of neon . . . . .	5-10
5-4.	Bismuth vapor temperature determination plot . . . . .	5-14
5-5.	Normalized Bi <sub>2</sub> fluorescence of the R(128) and P(115) transitions in the $\nu''=3 \rightarrow \nu'=1$ vibrational manifold of the $X(0_g^+) \rightarrow A(0_u^+)$ electronic transition around 17292.6 cm <sup>-1</sup> perturbed by 102 Torr of neon . . . . .	5-15
5-6.	Lorentzian linewidths (FWHM) of the Bi <sub>2</sub> R(128) and P(115) transitions in the $\nu''=3 \rightarrow \nu'=1$ vibrational manifold of the $X(0_g^+) \rightarrow A(0_u^+)$ electronic transition around 17292.6 cm <sup>-1</sup> as a function of neon pressure superimposed with linear fit. . . . .	5-15

5-7.	Bi <sub>2</sub> line broadening rates of rotational lines in the $v''=3 \rightarrow v'=1$ vibrational manifold of the $X(0_g^+) \rightarrow A(0_u^+)$ electronic transition broadened by helium, neon, argon, and krypton as a function of the branch-independent quantum number $m$ . . . . .	5-16
5-8.	Bi <sub>2</sub> line broadening cross sections of rotational lines in the $v''=3 \rightarrow v'=1$ vibrational manifold of the $X(0_g^+) \rightarrow A(0_u^+)$ electronic transition broadened by helium, neon, argon, and krypton as a function of the branch-independent quantum number $m$ . . . . .	5-22
5-9.	Comparison of line broadening cross sections of O <sub>2</sub> rotational lines perturbed by helium (Pope [41]) with the line broadening cross sections of Bi <sub>2</sub> similarly perturbed from this research . . . . .	5-23
5-10.	Comparison of line broadening cross sections of NO (Pope [41]) and CO (Luo <i>et al.</i> [36]) rotational lines perturbed by helium with the line broadening cross sections of Bi <sub>2</sub> similarly perturbed from this research . . . . .	5-23
5-11.	Comparison of line broadening cross sections of O <sub>2</sub> rotational lines perturbed by neon (Pope [41]) with the line broadening cross sections of Bi <sub>2</sub> similarly perturbed from this research . . . . .	5-24
5-12.	Comparison of line broadening cross sections of NO rotational lines perturbed by neon (Pope [41]) with the line broadening cross sections of Bi <sub>2</sub> similarly perturbed from this research . . . . .	5-25
5-13.	Comparison of line broadening cross sections of Br <sub>2</sub> (Innes <i>et al.</i> [28]) and O <sub>2</sub> (Pope [41]) rotational lines perturbed by argon with the line broadening cross sections of Bi <sub>2</sub> similarly perturbed from this research . . . . .	5-26
5-14.	Comparison of line broadening cross sections of NO (Pope [41]) and CO (Luo <i>et al.</i> [36]) rotational lines perturbed by argon with the line broadening cross sections of Bi <sub>2</sub> similarly perturbed from this research . . . . .	5-26
5-15.	Comparison of line broadening cross sections of O <sub>2</sub> rotational lines perturbed by krypton (Pope [41]) with the line broadening cross sections of Bi <sub>2</sub> similarly perturbed from this research . . . . .	5-27
5-16.	Comparison of line broadening cross sections of NO rotational lines perturbed by krypton (Pope [41]) with the line broadening cross sections of Bi <sub>2</sub> similarly perturbed from this research . . . . .	5-27

- 5-17. Fractions of collisions with enough translational energy for inelastic collisions to raise a molecule one rotational level or more in the upper states of Br<sub>2</sub>, O<sub>2</sub>, NO, and CO as a function of the branch-independent quantum number  $m$  . . . . . 5-33
- 5-18. Fractions of collisions with enough translational energy for inelastic collisions to raise a molecule one rotational level or more in the upper state of Bi<sub>2</sub> as a function of the branch-independent quantum number  $m$  . . . . . 5-34

## List of Tables

Table	Page
2-1. Stable isotopes of strontium and their natural abundances . . . . .	2-27
2-2. Energies of the atomic strontium states connected by the transitions studied in this research [37] . . . . .	2-29
2-3. Atomic strontium emission intensities of transitions studied in this research . . . . .	2-29
2-4. Isotope line center shifts of $^{86}\text{Sr}$ and $^{87}\text{Sr}$ relative to $^{88}\text{Sr}$ . . . . .	2-31
2-5. Magnetic and electric hyperfine coupling constants for the atomic strontium $5s5p\ ^3P_1$ and $5s6s\ ^3S_1$ energy states . . . . .	2-31
2-6. Spectroscopic constants for the $\nu''=3 \rightarrow \nu'=1$ vibrational manifold of the $\text{Bi}_2\ X(0_g^+) \rightarrow A(0_u^+)$ electronic transition as determined by Franklin and Perram [14] . . . . .	2-36
3-1. Line broadening cross sections of atomic calcium transitions perturbed by helium, neon, argon, krypton, and xenon reported by previous researchers . . . . .	3-4
3-2. Line shifting cross sections of atomic calcium transitions perturbed by helium, neon, argon, krypton, and xenon reported by previous researchers . . . . .	3-5
3-3. Difference potential constant $C_6$ for the atomic calcium $4s^2\ ^1S_0$ and $4s4p\ ^1P_1$ energy states perturbed by helium, neon, argon, and krypton reported by previous researchers . . . . .	3-5
3-4. Difference potential constant $C_{12}$ for the atomic calcium $4s^2\ ^1S_0$ and $4s4p\ ^1P_1$ energy states perturbed by helium, neon, argon, and krypton reported by previous researchers . . . . .	3-6
3-5. Line broadening cross sections of atomic strontium transitions perturbed by helium, neon, argon, and xenon reported by previous researchers . . . . .	3-11



3-6.	Line shifting cross sections of atomic strontium transitions perturbed by helium, neon, argon, and xenon reported by previous researchers . . .	3-11
3-7.	Difference potential constant $C_6$ for the atomic strontium $5s^2\ ^1S_0$ and $5s5p\ ^1P_1$ energy states perturbed by helium, neon, argon, krypton, and xenon reported by previous researchers . . .	3-12
3-8.	Difference potential constant $C_{12}$ for the atomic strontium $5s^2\ ^1S_0$ and $5s5p\ ^1P_1$ energy states perturbed by helium, neon, argon, krypton, and xenon reported by previous researchers . . .	3-12
3-9.	Theoretical difference potential constant $C_6$ for the atomic barium $6s^2\ ^1S_0$ and $6s6p\ ^1P_1$ energy states perturbed by helium, neon, argon, and krypton reported by Shabanova [45] . . .	3-15
3-10.	Theoretical difference potential constant $C_{12}$ for the atomic barium $6s^2\ ^1S_0$ and $6s6p\ ^1P_1$ energy states perturbed by helium, neon, argon, and krypton reported by Shabanova [45] . . .	3-15
3-11.	Line broadening cross sections of atomic barium transitions perturbed by helium, neon, and argon reported by previous researchers . . .	3-15
3-12.	Line shifting cross sections of atomic barium transitions perturbed by helium, neon, and argon reported by previous researchers . . .	3-16
4-1.	Absorption cross sections at line center of atomic strontium transitions studied in this research . . .	4-9
4-2.	Diffusion coefficients and diffusion times for typical experimental conditions of this research . . .	4-13
4-3.	Atomic strontium data acquisition matrix . . .	4-15
4-4.	Line broadening and shifting rates for all atomic strontium transitions and noble gases studied in this research . . .	4-26
4-5.	Comparison of the atomic strontium $5s5p\ ^3P_1 \rightarrow 5s6s\ ^3S_1$ line broadening sum total quenching rate constant for helium, neon, and argon of this research with the collisional mixing rate constants of the $5s5p\ ^3P_{0,1,2}$ multiplet published by Kelly <i>et al.</i> [31] . . .	4-30
4-6.	Line broadening and shifting cross sections of the atomic strontium $5s^2\ ^1S_0 \rightarrow 5s5p\ ^3P_1$ transition at $14504.351\text{ cm}^{-1}$ perturbed by helium, neon, argon, krypton, and xenon compared to gas kinetic cross sections . . .	4-32

4-7.	Comparison of the atomic strontium $5s^2\ ^1S_0 \rightarrow 5s5p\ ^3P_1$ line broadening cross sections of this work with analogous transitions of previous research . . . . .	4-34
4-8.	Comparison of the atomic strontium $5s^2\ ^1S_0 \rightarrow 5s5p\ ^3P_1$ line shifting cross sections of this work with analogous transitions of previous research . . . . .	4-35
4-9.	Comparison of the atomic strontium $5s5p\ ^3P_0 \rightarrow 5s6s\ ^3S_1$ line broadening cross sections of this work with atomic calcium, strontium, and barium $^1S_0 \rightarrow ^1P_1$ line broadening cross sections of previous research . . . . .	4-37
4-10.	Comparison of the atomic strontium $5s5p\ ^3P_0 \rightarrow 5s6s\ ^3S_1$ line shifting cross sections of this work with atomic calcium, strontium, and barium $^1S_0 \rightarrow ^1P_1$ line shifting cross sections of previous research . . . . .	4-38
4-11.	Atomic strontium difference potential constants $C_6$ and $C_{12}$ for all energy states perturbed by all noble gases studied in this research . . . .	4-46
4-12.	Comparison of the atomic strontium difference potential constant $C_6$ of the $5s^2\ ^1S_0 \leftrightarrow 5s5p\ ^3P_1$ and $5s5p\ ^3P_0 \leftrightarrow 5s6s\ ^3S_1$ energy states of this work with that of the $^1S_0 \leftrightarrow ^1P_1$ energy states studied in previous research . . . . .	4-47
4-13.	Comparison of the atomic strontium difference potential constant $C_{12}$ of the $5s^2\ ^1S_0 \leftrightarrow 5s5p\ ^3P_1$ and $5s5p\ ^3P_0 \leftrightarrow 5s6s\ ^3S_1$ energy states of this work with that of the $^1S_0 \leftrightarrow ^1P_1$ energy states studied in previous research . . . . .	4-47
4-14.	Polarizability of perturbing species [35] . . . . .	4-53
5-1.	Diatomic bismuth data acquisition matrix . . . . .	5-8
5-2.	P and R branch lines in the $\text{Bi}_2\ v''=3 \rightarrow v'=1$ vibrational manifold of the $X(0_g^+) \rightarrow A(0_u^+)$ electronic transition selected for detailed analysis . . . . .	5-11

5-3.	Comparison of the total quenching rate constants of two diatomic bismuth rotational levels in the $\nu'=1$ vibrational manifold of the $A(0_u^+)$ electronic state reported by Franklin [13] with the sum of the total quenching rate constants derived by Equation 5-12 from the appropriate line broadening rates of this work. . . . .	5-30
5-4.	Upper state rotational constants of Br <sub>2</sub> , O <sub>2</sub> , NO, and CO along with the temperatures at which the line broadening rates of these molecules were measured . . . . .	5-33
A-1.	Theoretical and measured diatomic bismuth rotational line positions in the $\nu''=3 \rightarrow \nu'=1$ vibrational manifold of the $X(0_g^+) \rightarrow A(0_u^+)$ electronic transition . . . . .	A-1
C-1.	Line broadening and shifting rates and cross sections of atomic strontium for all transitions and noble gases studied in this research. . . . .	C-1
C-2.	Line broadening rates and cross sections of diatomic bismuth P branch rotational lines in the $\nu''=3 \rightarrow \nu'=1$ vibrational manifold of the $X(0_g^+) \rightarrow A(0_u^+)$ electronic transition perturbed by helium . . . . .	C-2
C-3.	Line broadening rates and cross sections of diatomic bismuth R branch rotational lines in the $\nu''=3 \rightarrow \nu'=1$ vibrational manifold of the $X(0_g^+) \rightarrow A(0_u^+)$ electronic transition perturbed by helium . . . . .	C-3
C-4.	Line broadening rates and cross sections of diatomic bismuth P branch rotational lines in the $\nu''=3 \rightarrow \nu'=1$ vibrational manifold of the $X(0_g^+) \rightarrow A(0_u^+)$ electronic transition perturbed by neon . . . . .	C-4
C-5.	Line broadening rates and cross sections of diatomic bismuth R branch rotational lines in the $\nu''=3 \rightarrow \nu'=1$ vibrational manifold of the $X(0_g^+) \rightarrow A(0_u^+)$ electronic transition perturbed by neon . . . . .	C-5
C-6.	Line broadening rates and cross sections of diatomic bismuth P branch rotational lines in the $\nu''=3 \rightarrow \nu'=1$ vibrational manifold of the $X(0_g^+) \rightarrow A(0_u^+)$ electronic transition perturbed by argon . . . . .	C-6
C-7.	Line broadening rates and cross sections of diatomic bismuth R branch rotational lines in the $\nu''=3 \rightarrow \nu'=1$ vibrational manifold of the $X(0_g^+) \rightarrow A(0_u^+)$ electronic transition perturbed by argon . . . . .	C-7

- C-8. Line broadening rates and cross sections of diatomic bismuth  
P branch rotational lines in the  $v''=3 \rightarrow v'=1$  vibrational manifold  
of the  $X(0_g^+) \rightarrow A(0_u^+)$  electronic transition perturbed by krypton . . . C-8
- C-9. Line broadening rates and cross sections of diatomic bismuth  
R branch rotational lines in the  $v''=3 \rightarrow v'=1$  vibrational manifold  
of the  $X(0_g^+) \rightarrow A(0_u^+)$  electronic transition perturbed by krypton . . . C-9

**Abstract**

Spectral line broadening and shifting rates of the atomic strontium  $5s^2\ ^1S_0 \rightarrow 5s5p\ ^3P_1$  and  $5s5p\ ^3P_{0,1,2} \rightarrow 5s6s\ ^3S_1$  transitions perturbed by helium, neon, argon, krypton, and xenon were measured using tunable laser absorption spectroscopy. Noble gas pressures ranged from 0 to 1000 Torr. Broadening and shifting rates were converted to cross section and used to determine the Lennard-Jones (6-12) difference potential constants according to the theory of line perturbations by elastic collisions. Broadening cross sections for the  $5s^2\ ^1S_0 \rightarrow 5s5p\ ^3P_1$  transition ranged from  $0.894(0.040) \times 10^{-14}\text{ cm}^2$  for helium to  $3.01(0.20) \times 10^{-14}\text{ cm}^2$  for xenon. Line shifting cross sections ranged from  $0.290(0.015) \times 10^{-14}\text{ cm}^2$  for helium to  $-1.320(0.025) \times 10^{-14}\text{ cm}^2$  for xenon. Line broadening and shifting cross sections and the difference potentials for the  $5s5p\ ^3P_{0,1,2} \rightarrow 5s6s\ ^3S_1$  transitions were observed to be independent of the total angular momentum of the initial state. Line broadening cross sections ranged from  $1.63(0.32) \times 10^{-14}\text{ cm}^2$  for neon to  $7.3(1.6) \times 10^{-14}\text{ cm}^2$  for xenon. Line shifting cross sections ranged from  $0.692(0.042) \times 10^{-14}\text{ cm}^2$  for helium and  $-4.600(0.032) \times 10^{-14}\text{ cm}^2$  for xenon. The van der Waals attractive term in the difference potential was found to correlate with the polarizability of the perturbing species.

Spectral line broadening rates of the diatomic bismuth P(20) through P(195) and R(33) through R(208) rotational transitions in the  $v''=3 \rightarrow v'=1$  vibrational manifold of the  $X(0_g^+) \rightarrow A(0_u^+)$  electronic transition perturbed by helium, neon, argon, and krypton were measured using laser-induced fluorescence spectroscopy. Noble gas pressures

ranged from 0 to 405 Torr. Broadening rates were converted to cross section and to the sum of the total quenching rate constants from the lower and upper states of the transition according to the theory of line perturbations by inelastic collisions. Line broadening cross sections were observed to be independent of the total angular momentum of the initial state and determined to be approximately  $0.6 \times 10^{-14} \text{ cm}^2$ ,  $1.0 \times 10^{-14} \text{ cm}^2$ ,  $2.0 \times 10^{-14} \text{ cm}^2$ , and  $2.3 \times 10^{-14} \text{ cm}^2$  for helium, neon, argon, and krypton respectively. This lack of total angular momentum dependence was explained by the close energy spacing of rotational levels in the diatomic bismuth molecule. The sum of the total quenching rate constants for the P(172) and R(170) transition states perturbed by helium was determined to be  $11.6(2.3) \times 10^{-10} \text{ cm}^3/\text{sec}$  and  $9.8(1.4) \times 10^{-10} \text{ cm}^3/\text{sec}$  respectively and was found to exceed a previous measurement of the total quenching rate constant from the  $J' = 171$  rotational level of the upper state of the transition. Also, the sum of the total quenching rate constants for the R(200) transition states perturbed by helium, neon, and argon was determined to be  $7.9(1.6) \times 10^{-10} \text{ cm}^3/\text{sec}$ ,  $6.35(0.75) \times 10^{-10} \text{ cm}^3/\text{sec}$ , and  $9.2(1.4) \times 10^{-10} \text{ cm}^3/\text{sec}$  respectively. This was also found to exceed previous measurements of the total quenching rate constants from the  $J' = 201$  rotational level of the upper state of the transition.

# BROADENING AND SHIFTING OF ATOMIC STRONTIUM AND DIATOMIC BISMUTH SPECTRAL LINES

## I. Introduction

The objective of this research is to study the effects of noble gases on atomic strontium and diatomic bismuth visible transitions. Specifically, this research seeks to determine if the line broadening and, in the case of atomic strontium, line shifting rates of these transitions in the presence of noble gases depend on the total angular momenta of the energy states involved. It has been known for more than a century that atomic and molecular spectral lines are broadened and shifted by perturbing species. While a considerable body of theoretical work has been accomplished on this topic over the years, only recently have experimental techniques been developed to precisely measure these effects. In particular, the advent of the narrowband tunable dye laser has advanced the state of the art and made high-resolution measurements of spectral line profiles possible. With such data, it is now possible to precisely quantify the broadening and shifting of spectral lines by perturbing species.

The general physical model which accounts for the perturbations of spectral lines is as follows. Atoms and molecules are known to exist in quantized energy states and can transition between states with the absorption or emission of a photon. The presence of perturbing species can alter the energies of these states thereby altering the frequency of

the photon. This kind of influence, which occurs when the perturbing species collides elastically with absorbing or emitting species, leads to a broadening and shifting of the spectral line. It is also possible for perturbing species to collide inelastically and remove population from the lower and upper states of the transition. This kind of influence effectively shortens the lifetimes of the states which increases the uncertainty in the state's energy thereby broadening the transition.

These dual mechanisms for line broadening and shifting, that is, elastic versus inelastic collisions, are central to this work. Any dependences the line broadening and shifting rates exhibit on the total angular momenta of the states involved in the transition must therefore be explained in these terms. When elastic collisions dominate, the interaction potential between the species absorbing or emitting radiation and the perturbing species determines the broadening and shifting rates. Therefore, line broadening and shifting rates are used to characterize the interaction potential between two species. If the line broadening and shifting rates depend on the total angular momenta of the energy states involved, then so must the interaction potential. Similarly, when inelastic collisions dominate, the total quenching rate constants from the lower and upper states of the transition determine the line broadening rate. Therefore, any dependence on total angular momentum exhibited by the line broadening rates indicates an angular momentum dependence of the total quenching rate constants.

This work is presented in two parts. The first is a study of line broadening and shifting of the atomic strontium  $5s^2\ ^1S_0 \rightarrow 5s5p\ ^3P_1$ ,  $5s5p\ ^3P_0 \rightarrow 5s6s\ ^3S_1$ ,  $5s5p\ ^3P_1 \rightarrow 5s6s\ ^3S_1$ , and  $5s5p\ ^3P_2 \rightarrow 5s6s\ ^3S_1$  transitions around  $14500\text{ cm}^{-1}$  by helium, neon, argon, krypton, and xenon. For simplicity, the  $5s5p\ ^3P_0 \rightarrow 5s6s\ ^3S_1$ ,  $5s5p\ ^3P_1 \rightarrow 5s6s\ ^3S_1$ , and



$5s5p\ ^3P_2 \rightarrow 5s6s\ ^3S_1$  transitions are henceforth designated  $5s5p\ ^3P_{0,1,2} \rightarrow 5s6s\ ^3S_1$ . The second is a study of the line broadening of diatomic bismuth rotational lines in the  $v''=3 \rightarrow v'=1$  vibrational manifold of the  $X(0_g^+) \rightarrow A(0_u^+)$  electronic transition around  $17260\text{ cm}^{-1}$ . Specifically, P and R branch lines ranging from P(20) to P(195) and R(33) to R(208) in this manifold are perturbed by helium, neon, argon, and krypton.

A significant amount of new line broadening and shifting data is contained in this document. Of all the transitions and noble gases mentioned in the previous paragraph, only two have been investigated previously. These are the  $5s^2\ ^1S_0 \rightarrow 5s5p\ ^3P_1$  transition perturbed by neon and argon. This work also offers an interesting comparison of line broadening and shifting caused by elastic collisions versus inelastic collisions. The line broadening and shifting in atomic strontium is believed to be due to elastic collisions so the elastic theory of line broadening is applied to this data. In contrast, the line broadening in diatomic bismuth is believed to be due to inelastic collisions so the inelastic theory of line broadening is applied in this case. The two different applications then lead to different physical insights about the interactions between these species and the noble gases.

The motivation for this work has both practical and scientifically interesting aspects. Practical applications are centered around the immediate consequences of line broadening and shifting on atomic and molecular spectra. Because many remote sensing applications rely on knowing these spectra precisely, perturbations by local conditions are important to understand. For example, data from Earth satellites monitoring the spectra of trace molecules in the atmosphere like carbon monoxide and hydroxyl are affected by

other atmospheric constituents. Also, line broadening and shifting has an impact on absorption bands in the atmosphere, which could affect the performance of future Air Force weapon systems like the Airborne Laser and the Spacebased Laser. Additionally, atomic transitions are currently widely used as frequency standards and, in this case, the importance of quantifying frequency perturbations is obvious. And finally, the lineshape functions of some atoms are purposefully altered by perturbing species in order to custom-design absorption filters for the compression of frequency-chirped laser pulses. Understanding line broadening and shifting effects of perturbing species allows this to be accomplished.

From a purely scientific perspective, the study of line broadening and shifting leads to insight about the physics of atomic and molecular collisions. When elastic collisions dominate, line broadening and shifting is used to determine the interaction potentials between two species. This, in turn, is used to validate quantum mechanical calculations. The interaction potential is also important in chemical kinetics where it is the most important paradigm for understanding collisions between species and chemical bonding. When inelastic collisions dominate, the line broadening rate leads to a determination of the sum of the total quenching rate constants from the lower and upper states of a transition. Quenching rate constants are, in turn, an important part of building a physical description of the dynamics of a system in the gaseous phase.

The next chapter presents an overview of the theory necessary to interpret the line broadening and shifting data acquired in this research. Chapter III provides an extensive background review of other research relevant to this investigation. Chapter IV discusses the atomic strontium work beginning with the experimental set up and ending with

conclusions derived from the data analysis. And finally, Chapter V discusses the diatomic bismuth work and is similarly arranged.

## **II. Theory**

This chapter details the theory necessary to analyze and interpret the data that was generated during the experimental portion of this work. To begin, the essential elements of lineshape theory are reviewed with the intent of understanding the causes of line broadening and shifting. The result of this discussion is the development of a mathematical expression for the lineshape function which incorporates these causes. Next, the relevant physical properties and spectroscopic features of atomic strontium and diatomic bismuth are discussed. And finally, two applications for line broadening and shifting analysis are detailed.

### **2.1 Line Broadening and Shifting**

The phenomena known as spectral line broadening and shifting have several causes which are discussed in this section. These include radiative decay (called lifetime or natural broadening), collisions with perturbing species (called collisional or pressure broadening), and the Doppler effect (called Doppler broadening) [7]. In general, spectral lines are perturbed by some or all these effects simultaneously. Therefore, the theory of each mechanism is developed along with a discussion about how they combine with each other. The practical result of this discussion is the derivation of a single lineshape function which accurately models the spectra that are observed here. Since the dependence of the lineshape function on pressure is of primary interest, the relationship between these quantities is highlighted.

**2.1.1 Lifetime Broadening** The goal of this section is to describe lifetime broadening and develop a mathematical expression for the spectral lineshape function of an atomic or molecular transition broadened exclusively by this mechanism. Although lifetime broadening itself is not central to this work, it does contribute to the relevant lineshape function which incorporates the effects of lifetime broadening, pressure broadening, and Doppler broadening. It also serves as a starting point for the theoretical development of pressure broadening by inelastic collisions.

Lifetime broadening, also called natural broadening, results from the fact that atoms or molecules in excited energy states decay to lower states in time. Atoms or molecules radiating electromagnetic energy are modeled classically as charges undergoing simple harmonic motion. The electric fields of such charges are sinusoidal. When an atom or molecule decays from an excited energy state to a lower energy state, it radiates for a period of time and stops after making the transition. Thus the electric field of an ensemble of such bodies is modeled as a sinusoid whose amplitude decays in time as depicted in Figure 2-1. Initially all bodies are in an excited state and are radiating. Over time, each decays according to its probability of decay and the amplitude of the sinusoid drops accordingly [7].

This model applies to absorption as well as emission because an ensemble of bodies will attenuate an oscillating electric field as it absorbs electromagnetic energy. The absorption rate is proportional to the probability of decay as detailed by the Einstein  $A$  and  $B$  coefficient formalism. In this case, the end result is still an exponentially decaying sinusoidal oscillator. Thus lifetime broadening is observed in both absorption and fluorescence. This is important because while this derivation assumes a fluorescence

process, the experimental technique utilized absorption spectroscopy. The following results, however, are valid for both.

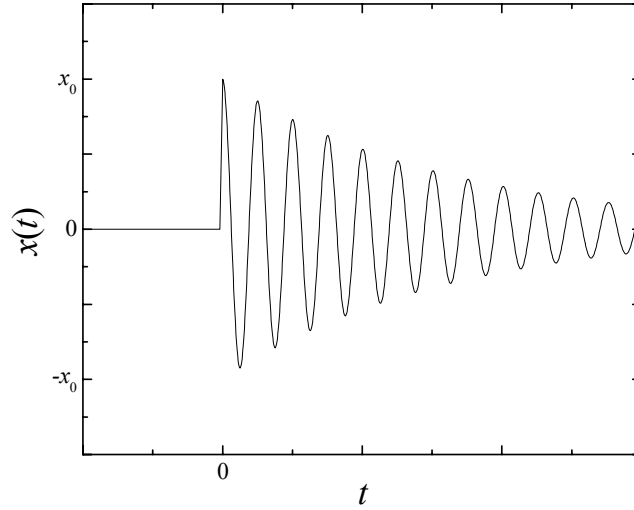


Figure 2-1. Exponentially decaying sinusoidal oscillator. This function describes the electric field of an ensemble of atoms or molecules decaying from an excited energy state.

Mathematically, the lineshape function is defined as the intensity of the radiation absorbed or emitted by a transition per unit frequency as a function of frequency. The intensity per unit frequency is found classically by computing the square of the magnitude of the electric field's Fourier Transform. According to the physical picture described above, the electric field as a function of time,  $x(t)$ , is

$$x(t) = \text{Re} \left\{ x_0 e^{i\omega_0 t - \frac{\gamma}{2} t} \right\} \quad (t > 0) \quad (2-1)$$

where  $x_0$  is the amplitude of oscillation,  $\omega_0$  is the transition angular frequency, and  $\gamma$  is the damping constant. A plot of this function is given in Figure 2-1 and shows the

decaying sinusoidal oscillator. First, intensity per unit frequency is computed and then the relationship between the damping constant and the decay rates of the energy states involved is derived.

The intensity of the transition per unit frequency,  $I_L(\omega)$ , is found by taking the square of the magnitude of the electric field's Fourier Transform. That is,

$$I_L(\omega) = \left| \frac{1}{\sqrt{2\pi}} \int_{-\infty}^{\infty} x(t) e^{-i\omega t} dt \right|^2 \quad (2-2)$$

Substituting Equation 2-1 into 2-2 and performing the integration yields

$$I_L(\omega) = \left| \frac{x_0}{\sqrt{2\pi}} \frac{\frac{\gamma}{2} + i\omega}{\left(\frac{\gamma}{2} + i\omega\right)^2 + \omega_0^2} \right|^2 \quad (2-3)$$

This expression can be rewritten as

$$I_L(\omega) = \left| \frac{x_0}{\sqrt{8\pi}} \left\{ \frac{1}{\frac{\gamma}{2} + i(\omega - \omega_0)} + \frac{1}{\frac{\gamma}{2} + i(\omega + \omega_0)} \right\} \right|^2 \quad (2-4)$$

Computing the square, neglecting the terms with  $(\omega + \omega_0)$  in the denominator [7], and area-normalizing to unity gives

$$I_L(\omega) = \frac{1}{\pi} \frac{\frac{\gamma}{2}}{(\omega - \omega_0)^2 + \left(\frac{\gamma}{2}\right)^2} \quad (2-5)$$

This lineshape function is known as the normalized Lorentzian line profile and is shown in Figure 2-2. It is area-normalized so that  $\int_{-\infty}^{\infty} I_L(\omega) d\omega = 1$  and the full width at half maximum (FWHM),  $\delta\omega_L$ , is

$$\delta\omega_L = \gamma \quad (2-6)$$

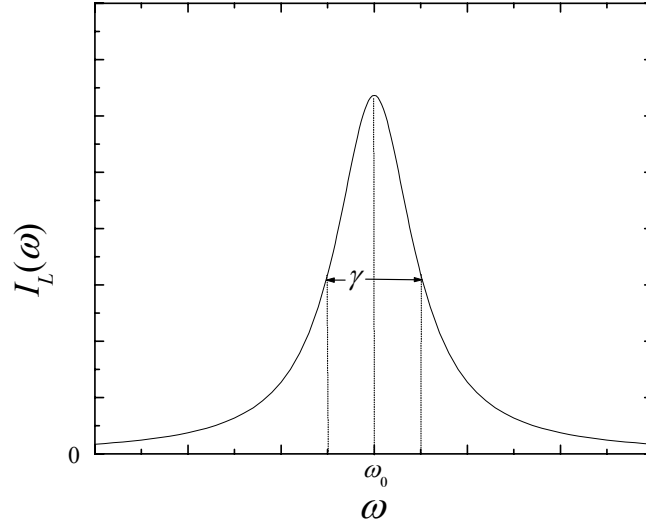


Figure 2-2. Lorentzian lineshape of a transition broadened by lifetime effects. This function is the square of the magnitude of Figure 2-1's Fourier Transform and has a FWHM given by Equation 2-6.

The damping constant  $\gamma$ , which was shown above to be the same as the Lorentzian lineshape function's FWHM, is related to the decay rates of the upper and lower states as follows. The Uncertainty Principle dictates that the lower and upper energy states of a transition are not exactly defined, but uncertain according to the times in which they are observed. Consider Bohr's Equation

$$E_k - E_j = \hbar\omega \quad (2-7)$$

where  $E_j$  and  $E_k$  are the energies of the lower and upper states respectively,  $\hbar$  is Planck's constant  $h$  divided by  $2\pi$ , and  $\omega$  is the angular frequency of the radiation absorbed or emitted. As illustrated in Figure 2-3, if  $E_j$  and  $E_k$  are uncertain, then the resultant angular frequency  $\omega$  is uncertain as well.



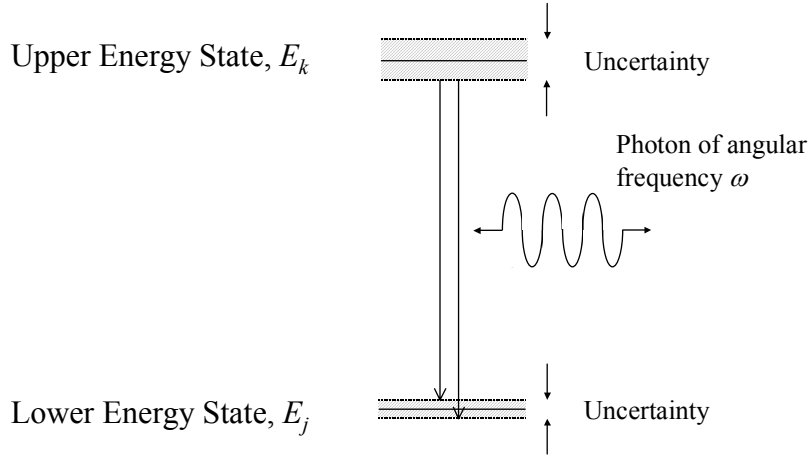


Figure 2-3. Transition between the lower and upper energy states of an atom or molecule. Because of the Uncertainty Principle, the angular frequency of a transition is not an exact quantity. It has an uncertainty that is a function of the uncertainties in the lower and upper state energies.

The FWHM of the Lorentzian lineshape function  $\delta\omega_L$  is regarded as the same as the uncertainty in the transition angular frequency  $\omega$ . Therefore, the mathematical relationship between  $\delta\omega_L$  and the lifetimes of the lower and upper states follows from the Uncertainty Principle. The average times in which the energy states  $j$  and  $k$  can be observed are the lifetimes,  $\tau_j$  and  $\tau_k$ , of these states. This implies that the uncertainties in the energies of these states,  $\Delta E_j$  and  $\Delta E_k$ , are

$$\Delta E_j = \frac{\hbar}{\tau_j} \quad (2-8)$$

and

$$\Delta E_k = \frac{\hbar}{\tau_k} \quad (2-9)$$

Since the angular frequency of radiation emitted during this transition is given by Equation 2-7, the uncertainty in the transition frequency,  $\delta\omega_L$ , is

$$\delta\omega_L = \frac{\Delta E_j + \Delta E_k}{\hbar} = \frac{1}{\tau_j} + \frac{1}{\tau_k} \quad (2-10)$$

The FWHM is equal to the damping constant so that

$$\delta\omega_L = \gamma = \frac{1}{\tau_j} + \frac{1}{\tau_k} \quad (2-11)$$

Therefore, the damping constant is the sum of the inverse lifetimes of the initial and final states [7]. Thus an atomic or molecular transition broadened by lifetime effects has a Lorentzian profile given by Equation 2-5 with a FWHM governed by the lifetimes of the lower and upper states given by Equation 2-11.

**2.1.2 Pressure Broadening** The discussion of lifetime broadening offered in the previous section lays the foundation for further types of spectral line broadening. In this section, pressure broadening, which is the primary topic of this dissertation, is discussed. The objective is to give a physical description of pressure broadening and derive a mathematical representation of the spectral lineshape function resulting from it. In addition, the dependence of the lineshape function on pressure is detailed as well.

Pressure broadening is defined as the perturbation of spectral lines by the pressure under which they are observed. An ensemble of bodies, either atoms or molecules, which are not moving relative to an observer will absorb and emit radiation that is affected only by lifetime broadening. The same bodies in the presence of other bodies are subject to additional broadening and, as will be derived shortly, line shifting. Intuitively, as pressure is raised, the amount of this influence increases. The exact mechanisms by

which the presence of other bodies, often called buffer gases, influence the spectral lineshape is the topic of the remainder of this section. It is broken into two subsections according to the type of interaction, either elastic or inelastic, between the body absorbing or radiating energy and the buffer gas. The goal in each is to derive a lineshape function for that particular mechanism.

### 2.1.2.1 Inelastic Collisions and Pressure Broadening

Inelastic collisions broaden spectral lines by changing the effective lifetimes of the energy states involved in the transition. In the absence of collisions, fluorescent decay is the only means by which an atom or molecule may leave an excited state. The rate of fluorescent decay is determined by the lifetime of the state,  $\tau$ , and is related to the Einstein  $A$  coefficient by Equation 2-12 [7].

$$A = \frac{1}{\tau} \quad (2-12)$$

Another avenue by which atoms or molecules may leave an energy state is by inelastic collisions (see Figure 2-4). The rate at which this occurs is called the quenching rate  $A^q$ . The total rate of decay from a state is then the rate of fluorescent decay plus the quenching rate. If  $A$  is replaced with  $A + A^q$ , the energy state has a new lifetime, an effective lifetime  $\tau^{eff}$ , which is

$$\frac{1}{\tau^{eff}} = A + A^q \quad (2-13)$$

Quenching influences both the lower and upper states of an atom or molecule. Therefore

$$\frac{1}{\tau_j^{eff}} = A_j + A_j^q \quad (2-14)$$

and

$$\frac{1}{\tau_k^{eff}} = A_k + A_k^q \quad (2-15)$$

where the subscripts  $j$  and  $k$  denote the lower and upper states respectively.

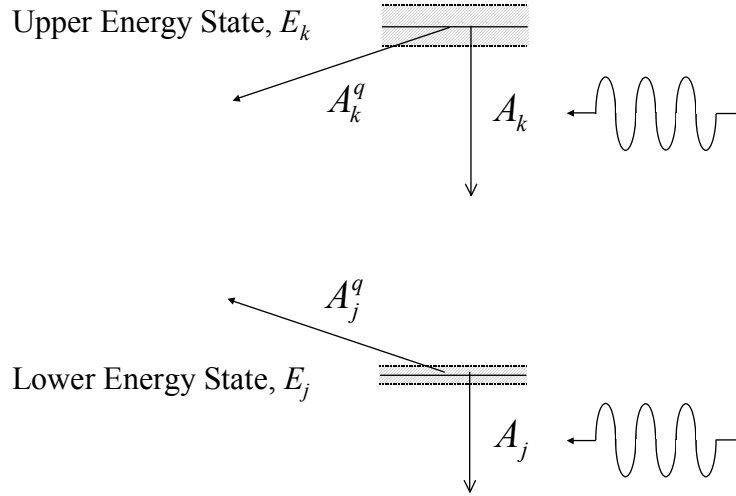


Figure 2-4. Transition between the lower and upper energy states of an atom or molecule affected by quenching. In addition to fluorescent decay, inelastic collisions may remove atoms or molecules from an energy state if other states are energetically accessible. This quenching changes the effective lifetime of the state.

As detailed in the previous section, lifetime broadening results from the lifetimes of energy states. Since quenching collisions effectively change the lifetimes of these states, quenching participates in broadening. The lineshape function is then still a Lorentzian as shown in Figure 2-5, but the FWHM is found by substituting  $\tau_j^{eff}$  and  $\tau_k^{eff}$  for  $\tau_j$  and  $\tau_k$  in Equation 2-11. That is,

$$\delta\omega_L = \frac{1}{\tau_j^{eff}} + \frac{1}{\tau_k^{eff}} = \frac{1}{\tau_j} + \frac{1}{\tau_k} + A_j^q + A_k^q \quad (2-16)$$

Therefore, pressure broadening due to inelastic collisions further broadens spectral lines and the FWHM of the Lorentzian is increased by the total quenching rate of the lower and upper states.

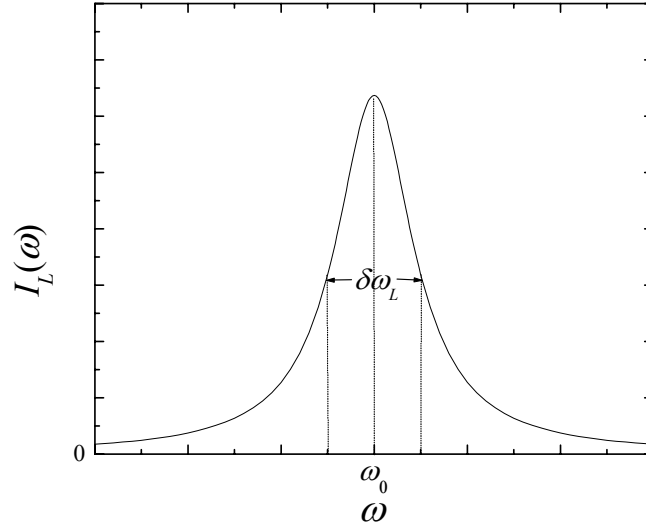


Figure 2-5. Lorentzian lineshape of a transition broadened by both lifetime effects and quenching. This profile has a FWHM given by Equation 2-16.

With the lineshape function for inelastic collisions established, the next step is to derive the dependence of this lineshape on pressure. This is simply a matter of replacing the quenching terms  $A_j^q$  and  $A_k^q$  with terms explicit in pressure. In general,

$$A^q = N \langle v \rangle \sigma^q \quad (2-17)$$

where  $N$  is the density of the perturbing bodies,  $\langle v \rangle$  is the average relative velocity between the bodies absorbing or radiating energy and the perturbing species, and  $\sigma^q$  is the total quenching cross section. Inserting Equation 2-17 into 2-16 and factoring gives

$$\delta\omega_L = \frac{1}{\tau_j} + \frac{1}{\tau_k} + N\langle v \rangle (\sigma_j^q + \sigma_k^q) \quad (2-18)$$

where the subscripts  $j$  and  $k$  refer to the lower and upper energy states respectively. Since pressure is proportional to number density, the FWHM of the Lorentzian lineshape resulting from the combination of pressure broadening and lifetime broadening is linear in the pressure of the perturbing species  $N$ . The rate at which the FWHM changes as a function of pressure is the derivative of Equation 2-18 with respect to  $N$  and is called the broadening rate [7].

**2.1.2.2 Elastic Collisions and Pressure Broadening** Elastic collisions broaden spectral lines by perturbing the phase of the sinusoidal electric field associated with atoms or molecules absorbing or emitting energy. This is different from the mechanisms of lifetime broadening and broadening by inelastic collisions, which perturb the amplitude of the electric field. Although both effects occur simultaneously, perturbations to the amplitude of the electric field are neglected in deriving the influence of elastic collisions on atomic and molecular transitions.

The lineshape function of a transition broadened by elastic collisions is derived according to the following physical description. Consider a body  $a$  to be in the middle of a transition when it experiences an elastic collision with a body  $b$ . In body  $a$ 's frame of reference, body  $b$  has a position  $\vec{r}$ , a relative velocity  $\vec{v}$ , and collides with an impact parameter  $\rho$  as illustrated in Figure 2-6. When body  $b$  is near body  $a$ , the charged particles which make up these bodies interact with each other and shift the energy levels of body  $a$ . Figure 2-7 shows how energy levels  $j$  and  $k$  shift as a function the distance  $r = |\vec{r}|$  between the two bodies. Because angular frequency is a function of the energy

difference between states, this frequency may be altered if the presence of the perturbing body does not shift the upper and lower energy states by the same amount [7].

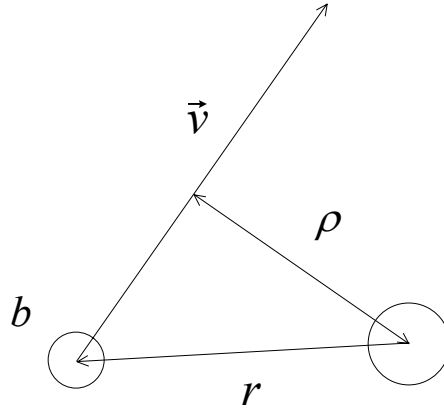


Figure 2-10: Collision of two bodies. Body  $b$  passes by body  $r$  and experiences a change in energy state.

This model can be quantified as follows. A general expression for the electric field as a function of time is

$$x(t) = \text{Re} \left\{ x_0 e^{i \int_0^t \omega(t') dt'} \right\} \quad (t > 0) \quad (2-19)$$

This is the generalized form of Equation 2-1 and is used when the angular frequency of oscillation  $\omega$  is not constant in time. Spectral line perturbations by elastic collisions are then derived by assuming a functional form for  $\omega(t)$ , computing the integral, and taking the square of the magnitude of the electric field's Fourier Transform.

The Lennard-Jones (6-12) potential is a common functional form for the interaction potential. It assumes the interaction potential can be expressed as the sum of

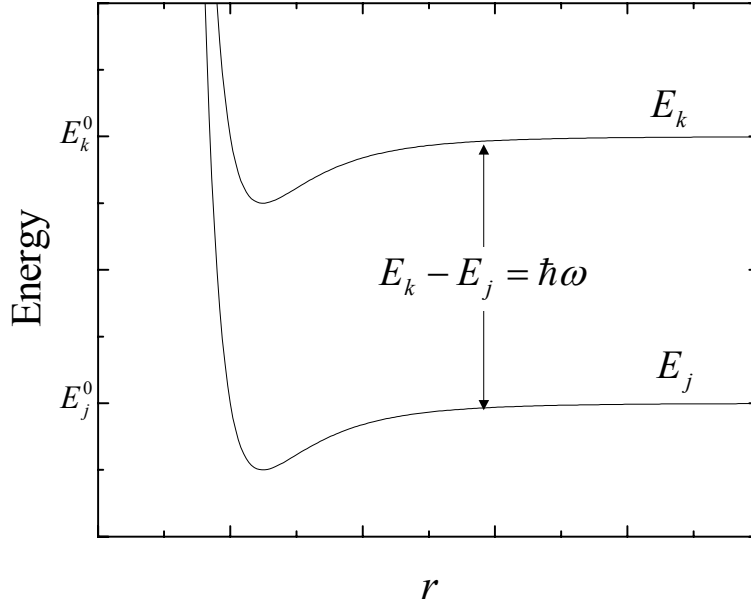


Figure 2-7. The influence of a passing body  $b$  on the energy states of body  $a$ . As body  $b$  passes near body  $a$ , interactions between the two shift  $a$ 's energy levels. Since the transition frequency is a function of the energy difference between the states, frequency is altered accordingly.

three terms: a constant offset, an attractive van der Waals term proportional to  $-r^{-6}$ , and a repulsive term proportional to  $r^{-12}$  [49]. As such, the energies of the lower and upper states are

$$E_j = E_j^0 + \frac{C_{12}^j}{r^{12}} - \frac{C_6^j}{r^6} \quad (2-20)$$

and

$$E_k = E_k^0 + \frac{C_{12}^k}{r^{12}} - \frac{C_6^k}{r^6} \quad (2-21)$$

respectively.  $E_j^0$  and  $E_k^0$  are the constant offsets of the lower and upper energy states respectively. They are the internal energies of the body absorbing or radiating energy



when the perturbing species is far away.  $C_6^j$  and  $C_6^k$  are proportionality constants for the attractive terms of the lower and upper states respectively, and  $C_{12}^j$  and  $C_{12}^k$  are proportionality constants for the repulsive terms of the lower and upper states respectively. Substituting Equations 2-20 and 2-21 into Equation 2-7 and solving for angular frequency gives

$$\omega = \frac{1}{\hbar} \left( E_k^0 - E_j^0 + \frac{(C_{12}^k - C_{12}^j)}{r^{12}} - \frac{(C_6^k - C_6^j)}{r^6} \right) \quad (2-22)$$

In order to make this expression more wieldy, the difference potential,  $V(r)$ , is defined as

$$V(r) = \frac{C_{12}^k}{r^{12}} - \frac{C_6^k}{r^6} - \frac{(C_{12}^k - C_{12}^j)}{r^{12}} - \frac{(C_6^k - C_6^j)}{r^6} \quad (2-23)$$

where  $C_6 = C_6^k - C_6^j$  and  $C_{12} = C_{12}^k - C_{12}^j$ . Substituting Equation 2-23 into 2-22 gives

$$\omega(r) = \frac{1}{\hbar} (E_k^0 - E_j^0 + V(r)) \quad (2-24)$$

At this point,  $\omega$  has been established as a function of  $r$  as expressed by Equation 2-24. In order to solve Equation 2-19, however,  $\omega$  must be converted to a function of time. This is accomplished by applying the Pythagorean Theorem to the quantities defined in Figure 2-6. If the time of closest approach body  $b$  makes to body  $a$  is  $t_0$ , then

$$r = \sqrt{\rho^2 + v^2(t - t_0)^2} \quad (2-25)$$

where  $v = |\vec{v}|$  is the relative speed between bodies  $a$  and  $b$ . Substituting Equation 2-25 into Equation 2-24 gives

$$\omega(t) = \frac{1}{\hbar} \left( E_k^0 - E_j^0 + V \left( \sqrt{\rho^2 + v^2(t - t_0)^2} \right) \right) \quad (2-26)$$

Inserting Equation 2-26 into Equation 2-19 gives

$$x(t) = \text{Re} \left\{ x_0 e^{i \int_0^t \frac{1}{\hbar} \left( E_k^0 - E_j^0 + V \left( \sqrt{\rho^2 + v^2 (t' - t_0)^2} \right) \right) dt'} \right\} \quad (t > 0) \quad (2-27)$$

This is the electric field as a function of time for a body absorbing or emitting radiation while experiencing an elastic collision.

As an example of the effects of phase-perturbing collisions, Equations 2-26 and 2-27 are plotted as functions of time in Figure 2-8 for a body undergoing three elastic collisions consecutively. The result of each collision is to briefly, but radically, perturb the frequency of oscillation. This perturbation, in turn, effectively interrupts the phase of the oscillation by introducing brief periods of oscillation at different frequencies. In this illustration, all three collisions induce positive changes in the oscillation frequency. This is because relatively small impact parameters were chosen causing the first term in Equation 2-23 to be greater than the second at the point of closest approach. It can be

easily shown that an impact parameter greater than  $\left( \frac{C_{12}}{C_6} \right)^{\frac{1}{6}}$  induces a negative

perturbation to the oscillation frequency at the point of closest approach. The magnitude, however, of this perturbation is smaller than in the illustrated case because large impact parameters result in smaller interactions.

Up to now, this approach has provided a clear and intuitive way to proceed. It is abandoned, however, in favor of a similar line of reasoning which makes no assumptions about the interaction potential as was required above. This approach, known as the method of Hindmarsh and Farr [25], begins with Equation 2-19 and derives a lineshape function for transitions perturbed by elastic collisions. As stated previously, the intensity of the transition per unit frequency,  $I_L(\omega)$ , is found by taking the square of the

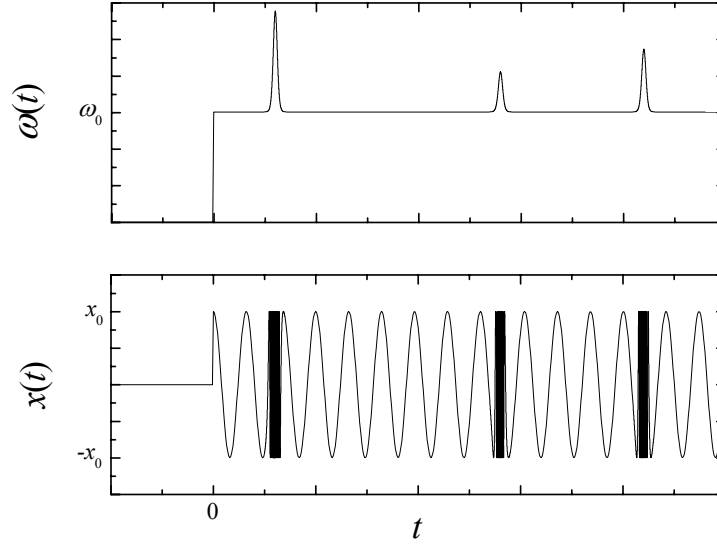


Figure 2-8. Oscillator angular frequency and electric field magnitude perturbed by elastic collisions as a function of time. As shown at the top, the transition frequency  $\omega(t)$  is sharply perturbed by elastic collisions. The effect this has on the electric field  $x(t)$  is shown at the bottom.

magnitude of the electric field's Fourier Transform. The method of Hindmarsh and Farr, which is equivalent, is to first calculate the complex autocorrelation of  $x(t)$  and then take its Fourier Transform [16].

Following this methodology, the autocorrelation of the electric field is

$$\phi(s) = [x^*(t)x(t+s)]_t \quad (2-28)$$

or

$$\phi(s) = \left[ \text{Re} \left\{ x_0 e^{-i \int_0^t \omega(t') dt'} x_0 e^{i \int_0^{t+s} \omega(t') dt'} \right\} \right]_t \quad (2-29)$$

where the brackets indicate an average over time  $t$ . The phase of the electric field is assumed to be the sum of the unperturbed phase and  $\eta(t)$ , which is the departure in phase

of the perturbed oscillation from the unperturbed oscillation caused by a foreign species.

That is,

$$\int_0^t \omega(t') dt' = \omega_0 t + \eta(t) \quad (2-30)$$

and

$$\int_0^{t+s} \omega(t') dt' = \omega_0(t+s) + \eta(t+s) \quad (2-31)$$

Under this assumption, the autocorrelation can be written as

$$\phi(s) = \frac{x_0^2}{2} \left[ \text{Re} \left\{ e^{i2\omega_0 t} e^{i\omega_0 s} e^{i(\eta(t+s) + \eta(t))} \right\} + \text{Re} \left\{ e^{i\omega_0 s} e^{i(\eta(t+s) - \eta(t))} \right\} \right] \quad (2-32)$$

In the optical regime, one oscillation of the electric field occurs in a time much shorter than the collision time of bodies in a gas phase. Thus no significant perturbation of the phase occurs within one oscillation of the field and the first term in Equation 2-32 is zero.

The remaining expression is

$$\phi(s) = \frac{x_0^2}{2} \left[ \text{Re} \left\{ e^{i\omega_0 s} e^{i(\eta(t+s) - \eta(t))} \right\} \right] \quad (2-33)$$

To continue, let

$$\eta(t+s) - \eta(t) = \eta(t,s) \quad (2-34)$$

and apply this to Equation 2-33. This gives

$$\phi(s) = \frac{x_0^2}{2} \left[ \frac{1}{2} \left( e^{i\omega_0 s} e^{i\eta(t,s)} + e^{-i\omega_0 s} e^{-i\eta(t,s)} \right) \right] \quad (2-35)$$

Equation 2-35 may be rewritten as

$$\phi(s) = \frac{x_0^2}{4} \left( e^{i\omega_0 s} \left[ e^{i\eta(t,s)} \right] + e^{-i\omega_0 s} \left[ e^{-i\eta(t,s)} \right] \right) \quad (2-36)$$

or

$$\phi(s) = \psi(s) + \psi^*(s) \quad (2-37)$$

where

$$\psi(s) = \frac{x_0^2}{4} e^{i\omega_0 s} \left[ e^{i\eta(t,s)} \right] \quad (2-38)$$

The Fourier Transform of Equation 2-37 gives the intensity profile and is

$$I_L(\omega) = \int_{-\infty}^{\infty} \psi(s) e^{-i\omega s} ds + \int_{-\infty}^{\infty} \psi^*(s) e^{-i\omega s} ds \quad (2-39)$$

The next step is to evaluate the time average in Equation 2-38 before applying it to Equation 2-39 and performing the integration. Consider a change in the quantity

$\psi(s) e^{-i\omega_0 s}$  corresponding to a change in  $s$  called  $\Delta s$ . Then

$$\Delta \left\{ \psi(s) e^{-i\omega_0 s} \right\} = \frac{x_0^2}{4} \Delta \left[ e^{i\eta(t,s)} \right] \quad (2-40)$$

Writing out the delta on the right side of the equation explicitly gives

$$\Delta \left\{ \psi(s) e^{-i\omega_0 s} \right\} = \frac{x_0^2}{4} \left[ e^{i\eta(t,s+\Delta s)} - e^{i\eta(t,s)} \right] \quad (2-41)$$

This equation can be written more simply by defining  $\Delta\eta = \eta(t, s + \Delta s) - \eta(t, s)$ . This gives

$$\Delta \left\{ \psi(s) e^{-i\omega_0 s} \right\} = \frac{x_0^2}{4} \left[ e^{i\eta(t,s)} (e^{i\Delta\eta} + 1) \right] \quad (2-42)$$

Because  $\Delta\eta$  occurs in a manner which is statistically independent of  $\eta$ , the time average may be distributed over the two factors of Equation 2-42. This leads to

$$\Delta \left\{ \psi(s) e^{-i\omega_0 s} \right\} = \frac{x_0^2}{4} \left[ e^{i\eta(t,s)} \right] \left[ e^{i\Delta\eta} - 1 \right] \quad (2-43)$$

Substituting Equation 2-38 into the above equation gives

$$\Delta \left\{ \psi(s) e^{-i\omega_0 s} \right\} = \psi(s) e^{-i\omega_0 s} \left[ e^{i\Delta\eta} - 1 \right] \quad (2-44)$$

The second factor in Equation 2-44 is evaluated by applying the impact approximation as follows. The factor  $\left[ e^{i\Delta\eta} - 1 \right]$  is the time average of the function  $e^{i\Delta\eta} - 1$  in the time interval  $\Delta s$ . The impact approximation assumes that  $\Delta\eta$  is the result

of all collisions which occur in the same time interval. Assuming all species follow rectilinear trajectories, the number of collisions with impact parameters between  $\rho$  and  $d\rho$  which occur in the time interval  $\Delta s$  is

$$2\pi N \langle v \rangle |\Delta s| \rho d\rho \quad (2-45)$$

Knowing this, it is possible to replace the time average of the function  $e^{i\Delta\eta} - 1$  with the sum over all impact parameters of the function  $2\pi N \langle v \rangle |\Delta s| \{e^{i\eta(\rho)} - 1\} \rho d\rho$ , where  $\eta(\rho)$  is the phase perturbation of a collision with impact parameter  $\rho$ . Thus

$$[e^{i\Delta\eta} - 1] = 2\pi N \langle v \rangle |\Delta s| \int_0^\infty \{e^{i\eta(\rho)} - 1\} \rho d\rho \quad (2-46)$$

With the second factor in Equation 2-44 written in more manageable terms, it is possible to derive an expression for  $\psi(s)$  before inserting it into Equation 2-39. Inserting Equation 2-46 into Equation 2-44 and rearranging gives

$$\frac{\Delta \{\psi(s) e^{-i\omega_0 s}\}}{\psi(s) e^{-i\omega_0 s}} = 2\pi N \langle v \rangle |\Delta s| \int_0^\infty \{e^{i\eta(\rho)} - 1\} \rho d\rho \quad (2-47)$$

Since the average over a large number of collisions is involved, this can be treated as a differential equation whose solution is

$$\psi(s) = C e^{(i\omega_0 - N \langle v \rangle (\sigma_r - i\sigma_i)) |s|} \quad (2-48)$$

where  $C$  is the integration constant and

$$\sigma_r = 2\pi \int_0^\infty (1 - \cos \eta(\rho)) \rho d\rho \quad (2-49)$$

and

$$\sigma_i = 2\pi \int_0^\infty \sin \eta(\rho) \rho d\rho \quad (2-50)$$

To conclude the derivation, Equation 2-48 is inserted into Equation 2-39 and the integration performed. This gives

$$I_L(\omega) = 2N\langle v \rangle \sigma_r \left\{ \frac{1}{\left( \omega + \left( \omega_0 + N\langle v \rangle \sigma_i \right) \right)^2 + \left( N\langle v \rangle \sigma_r \right)^2} + \frac{1}{\left( \omega - \left( \omega_0 + N\langle v \rangle \sigma_i \right) \right)^2 + \left( N\langle v \rangle \sigma_r \right)^2} \right\} \quad (2-51)$$

The first term is neglected because in the optical regime,  $\omega + \omega_0$  is a very large number.

After area-normalizing the remaining term to unity ( $\int_{-\infty}^{\infty} I_L(\omega) d\omega = 1$ ), this leaves

$$I_L(\omega) = \frac{1}{\pi} \frac{N\langle v \rangle \sigma_r}{\left( \omega - \left( \omega_0 + N\langle v \rangle \sigma_i \right) \right)^2 + \left( N\langle v \rangle \sigma_r \right)^2} \quad (2-52)$$

This is again a Lorentzian lineshape function. It has a broadening term which governs the FWHM and is given by

$$\delta\omega_L = 2N\langle v \rangle \sigma_r \quad (2-53)$$

The line center is shifted by the amount  $\Delta\omega$  and is given by

$$\Delta\omega = N\langle v \rangle \sigma_i \quad (2-54)$$

In the above derivation, the effect of lifetime broadening is ignored. According to Demtröder [7], this effect is additive so that the Lorentzian linewidth is further augmented by Equation 2-11. That is,

$$\delta\omega_L = \frac{1}{\tau_j} + \frac{1}{\tau_k} + 2N\langle v \rangle \sigma_r \quad (2-55)$$

Altering Equation 2-52 so its FWHM is defined by Equation 2-55 gives

$$I_L(\omega) = \frac{1}{\pi} \frac{\frac{1}{2} \left( \frac{1}{\tau_j} + \frac{1}{\tau_k} \right) + N \langle v \rangle \sigma_r}{\left( \omega - \left( \omega_0 + N \langle v \rangle \sigma_i \right) \right)^2 + \left( \frac{1}{2} \left( \frac{1}{\tau_j} + \frac{1}{\tau_k} \right) + N \langle v \rangle \sigma_r \right)^2} \quad (2-56)$$

This lineshape function, which is illustrated in Figure 2-9, is again Lorentzian. It has a FWHM given by Equation 2-55 and a line center shift given by Equation 2-54. Also, since pressure is directly proportional to number density, both the FWHM and the line center shift are linear in pressure. The rates at which the FWHM and the line center change as a function of pressure are the derivatives of Equations 2-55 and 2-54 with respect to  $N$  and are called the broadening and shifting rates respectively.

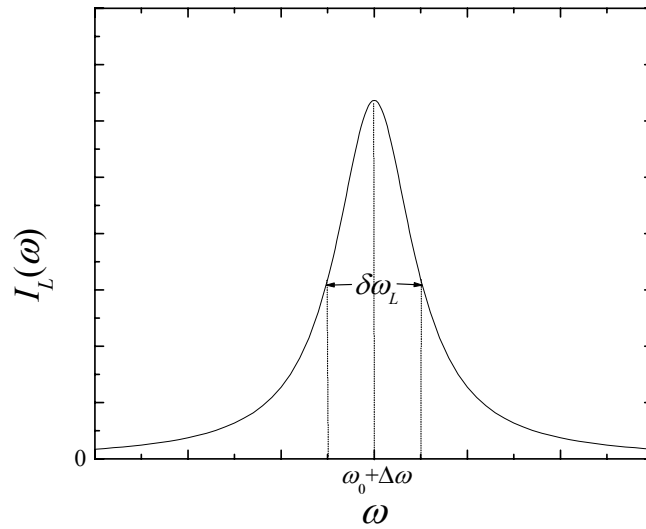


Figure 2-9. Lorentzian lineshape of a transition broadened and shifted by elastic collisions. Its FWHM is given by Equation 2-55 and its line center shift is given by Equation 2-54.

**2.1.3 Doppler Broadening** This type of line broadening results from the fact that atoms and molecules in the gas phase are in constant thermal motion. Because of this, the frequency of the radiation absorbed or emitted by the atom or molecule is Doppler shifted when observed in the laboratory frame of reference. A body that



happens to be moving towards an observer because of thermal motion will absorb or emit light of higher frequency because of its Doppler shift to the blue in the absorber's frame of reference. Similarly, a body that happens to be moving away will absorb or emit light of lower frequency because of its Doppler shift to the red in the absorber's frame of reference.

The lineshape function caused by Doppler broadening is Gaussian in nature and is given by Equation 2-57. The derivation of this expression is grounded in statistical mechanics and for an account, the reader is referred to Demtröder [7].

$$I_G(\omega) = \sqrt{\frac{m}{2\pi k_B T}} \frac{c}{\omega_0} e^{-\left( \frac{c(\omega - \omega_0)}{\omega_0 \sqrt{\frac{2k_B T}{m}}} \right)^2} \quad (2-57)$$

$I_G(\omega)$  is the intensity of radiation absorbed or emitted per unit frequency as a function of angular frequency  $\omega$ ,  $k_B$  is Boltzmann's constant,  $T$  is absolute temperature,  $c$  is the speed of light, and  $m$  is the mass of the species. This function is known as the normalized Gaussian line profile and is shown in Figure 2-10. It is area-normalized to unity and the FWHM is proportional to the square root of the temperature as given by

$$\delta\omega_G = \left( \frac{\omega_0}{c} \right) \sqrt{\frac{8 \ln(2) k_B T}{m}} \quad (2-58)$$

All spectra of atoms and molecules in the gas phase exhibit this kind of broadening in addition to the other types already discussed. Exactly how these types of broadening combine is the subject of the next section. The key point here is that Doppler broadening is an experimental effect which must be accounted for in the data analysis.

Knowing that the FWHM of the Gaussian lineshape is proportional to the square root of the temperature allows this to be accomplished.

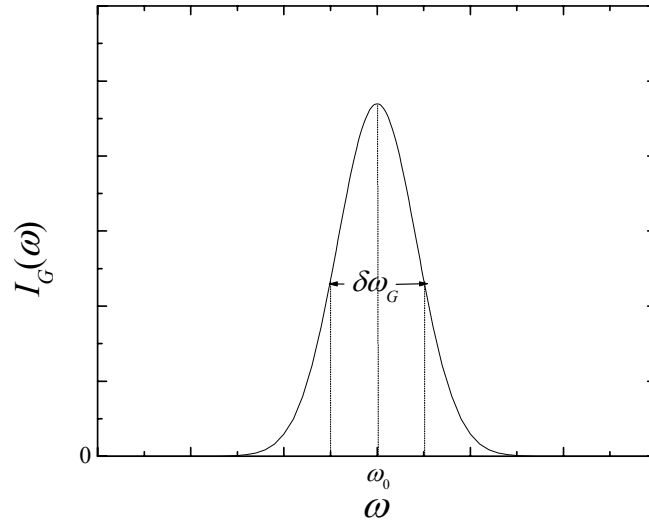


Figure 2-10. Gaussian lineshape of a transition broadened by the Doppler effect. This type of broadening is due to the Doppler shift associated with the thermal motion of bodies absorbing or emitting radiation. Its FWHM is given by Equation 2-58.

**2.1.4 The Voigt Profile** In this final section, the effects of lifetime broadening, pressure broadening, and Doppler broadening are combined into a single lineshape function which accurately models the line profiles observed in this research. This is done by recognizing the fact that Doppler broadening is caused by ensembles of bodies moving in different directions relative to the observer. The Gaussian line profile which results is the summation of radiation absorbed or emitted by these ensembles. Since each of these ensembles exhibits its own combined lifetime and pressure broadening/shifting effects as manifested in the Lorentzian lineshape function, the combined lineshape function is the summation of all the Lorentzian lineshape functions of all ensembles.

That is, the combined lineshape function is the convolution of the Lorentzian and Gaussian lineshape functions or [30]

$$I_V(\omega) = \int_{-\infty}^{\infty} I_L(\omega - y) I_G(y) dy \quad (2-59)$$

To derive a combined lineshape function, expressions for the Lorentzian and Gaussian lineshape functions are substituted into Equation 2-59. As derived previously, the Lorentzian lineshape function is

$$I_L(\omega) = \frac{1}{2\pi} \frac{\delta\omega_L}{(\omega - (\omega_0 + \Delta\omega))^2 + \left(\frac{\delta\omega_L}{2}\right)^2} \quad (2-60)$$

Depending on the type of pressure broadening that applies, The FWHM  $\delta\omega_L$  is given by either Equation 2-18 or Equation 2-55 and the line center shift is either zero or given by Equation 2-54. The Gaussian lineshape function is

$$I_G(y) = \sqrt{\frac{4\ln(2)}{\pi}} \frac{1}{\delta\omega_G} e^{-\left(\frac{2\sqrt{\ln(2)}y}{\delta\omega_G}\right)^2} \quad (2-61)$$

where  $y = \omega - \omega_0$  and  $\delta\omega_G$  is given by Equation 2-58. Substituting these into Equation 2-59 gives

$$I_V(\omega) = \frac{2\ln(2)}{\sqrt{\pi^3}} \frac{\delta\omega_L}{(\delta\omega_G)^2} \int_{-\infty}^{\infty} \frac{e^{-y^2}}{\left(2\sqrt{\ln(2)} \frac{\omega - (\omega_0 + \Delta\omega)}{\delta\omega_G} - y\right)^2 + \ln(2) \left(\frac{\delta\omega_L}{\delta\omega_G}\right)^2} dy \quad (2-62)$$

This is known as the Voigt lineshape function [30]. It has four parameters: line center ( $\omega_0$ ), line center shift ( $\Delta\omega$ ), Lorentzian linewidth ( $\delta\omega_L$ ), and Gaussian linewidth ( $\delta\omega_G$ ). It is also area-normalized to unity.

While there is no way to analytically accomplish the improper integral in Equation 2-62, this result may be manipulated to make it more amenable to computation.

Consider the following simplified version of Equation 2-62

$$I_V(A) = C \int_{-\infty}^{\infty} \frac{e^{-y^2}}{(A-y)^2 + B^2} dy \quad (2-63)$$

where

$$A = 2\sqrt{\ln(2)} \frac{\omega - (\omega_0 + \Delta\omega)}{\delta\omega_G} \quad (2-64)$$

$$B = \sqrt{\ln(2)} \frac{\delta\omega_L}{\delta\omega_G} \quad (2-65)$$

and

$$C = \frac{2\ln(2)}{\sqrt{\pi^3}} \frac{\delta\omega_L}{(\delta\omega_G)^2} \quad (2-66)$$

The integrand may be rewritten as

$$I_V(A) = C \int_{-\infty}^{\infty} \left\{ \frac{e^{-y^2}}{y - (A + iB)} + \frac{e^{-y^2}}{y - (A - iB)} \right\} dy \quad (2-67)$$

and each term integrated separately so that

$$I_V(A) = \frac{C}{2B} \left\{ e^{-(A+iB)^2} \pi(1 - \text{Erf}(B - iA)) + e^{-(A-iB)^2} \pi(1 - \text{Erf}(B + iA)) \right\} \quad (2-68)$$

Simplifying and rewriting in its original terms gives

$$\begin{aligned} I_V(\omega) = & \sqrt{\frac{\ln(2)}{\pi}} \frac{1}{\delta\omega_G} 2^{\left( \frac{\delta\omega_L^2}{\delta\omega_G^2} - 4 \frac{(\omega - \omega_0)^2}{\delta\omega_G^2} \right)} \left\{ 2 \cos\left( 4 \ln(2) (\omega - \omega_0) \frac{\delta\omega_L}{\delta\omega_G^2} \right) \right. \\ & - e^{-i 4 \ln(2) (\omega - \omega_0) \frac{\delta\omega_L}{\delta\omega_G^2}} \text{Erf}\left( \sqrt{\ln(2)} \frac{\delta\omega_L}{\delta\omega_G} - i 2 \sqrt{\ln(2)} \frac{\omega - \omega_0}{\delta\omega_G} \right) \\ & \left. - e^{i 4 \ln(2) (\omega - \omega_0) \frac{\delta\omega_L}{\delta\omega_G^2}} \text{Erf}\left( \sqrt{\ln(2)} \frac{\delta\omega_L}{\delta\omega_G} + i 2 \sqrt{\ln(2)} \frac{\omega - \omega_0}{\delta\omega_G} \right) \right\} \end{aligned} \quad (2-69)$$

The improper integral has been traded for the complex error function which itself contains an improper integral that is evaluated by numerical methods.

Figure 2-11 shows a plot of the Voigt lineshape function superimposed with Lorentzian and Gaussian lineshape functions of equal linewidth. The Voigt has the same wide central region as the Gaussian lineshape, but with broader wings like the Lorentzian. It includes the effects of lifetime broadening, pressure broadening, and Doppler broadening. The core is characteristic of Doppler broadening while the broad wings are characteristic of pressure broadening.

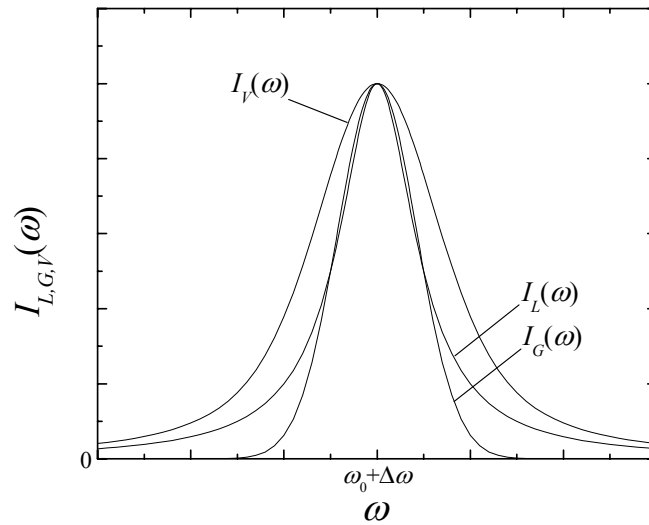


Figure 2-11. Voigt lineshape function of a transition overlaid with Lorentzian and Gaussian lineshape functions. In this illustration,  $\delta\omega_L = \delta\omega_G$  so the Lorentzian and Gaussian lineshape functions cross at the angular frequencies of half intensity for each. The Voigt lineshape is a convolution of the Lorentzian and Gaussian lineshape function and therefore has features of both.

## 2.2 Properties and Spectroscopy of Atomic Strontium and Diatomic Bismuth

The two species studied in this research are atomic strontium and diatomic bismuth. This section details the relevant physical properties of these bodies and discusses the spectroscopy of each. Atomic strontium is described first followed by diatomic bismuth.

**2.2.1 Atomic Strontium** The properties of atomic strontium are as follows. It is an alkaline earth metal found in the second column of the periodic table of elements below calcium. It has atomic number 38 and an atomic weight of 87.62 amu [54]. There are four stable strontium isotopes with abundances given in Table 2-1 [56]. Of these isotopes,  $^{87}\text{Sr}$  is the only one which possesses a nuclear spin ( $I = \frac{1}{2}$ ) [53]. This causes a hyperfine splitting in some energy states of  $^{87}\text{Sr}$  which will be discussed shortly. Also, the ground state electronic configuration of atomic strontium is  $[\text{Kr}]5s^2$  [23].

Table 2-1. Stable isotopes of strontium and their natural abundances

Isotope	Abundance (%)
$^{88}\text{Sr}$	82.58
$^{86}\text{Sr}$	9.86
$^{87}\text{Sr}$	7.00
$^{84}\text{Sr}$	0.56

The energy levels of atomic strontium have been known for some time and a diagram of the states nearest the ground state is given in Figure 2-12 [38]. The two valence shell electrons give rise to singlet and triplet terms. The atomic strontium transitions studied in this research are also indicated in Figure 2-12 and the energies of

the states connected by these transitions are given in Table 2-2 [38]. The three triplet-to-triplet absorption transitions  $5s5p\ ^3P_{0,1,2} \rightarrow 5s6s\ ^3S_1$  around  $14534\text{ cm}^{-1}$  (688 nm) are chosen in order to investigate the dependence of line broadening on the total angular momentum quantum number  $J''$  of the initial state. The ground state-to-triplet state intercombination transition  $5s^2\ ^1S_0 \rightarrow 5s5p\ ^3P_1$  at  $14504.351\text{ cm}^{-1}$  (689.4 nm), which lies near the other three, is studied to validate the experimental apparatus and analysis techniques and to expand upon previous work accomplished on this transition.

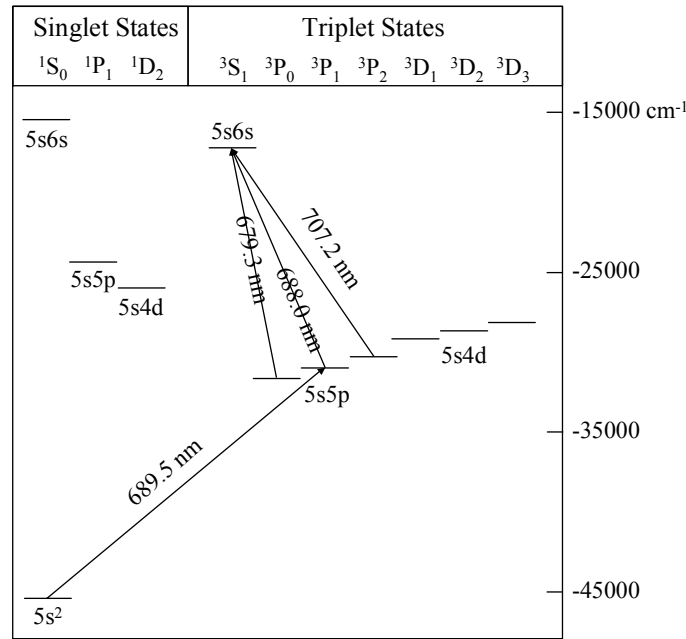


Figure 2-12. Lower electronic energy states of atomic strontium. The transitions of interest are noted.

The emission intensities of the transitions studied in this research have been investigated previously. The  $5s^2\ ^1S_0 \leftarrow 5s5p\ ^3P_1$  intercombination transition emission intensity is reported by Havey *et al.* [22] and the three  $5s5p\ ^3P_{0,1,2} \leftarrow 5s6s\ ^3S_1$  transition

emission intensities are reported by García and Campos [15]. All four emission intensities are listed in Table 2-3. The forbidden intercombination transition is relatively weak and the triplet-to-triplet transition intensities scale according to the degeneracies of the states involved. Since there are  $2J + 1$  degenerate states for each term, the emission intensities of the  $5s5p\ ^3P_{0,1,2} \leftarrow 5s6s\ ^3S_1$  transitions are weighted by  $\frac{2J'+1}{2J''+1}$  [23]. With this, the relative emission intensities are computed for each transition and reported in Table 2-3. They agree well with the experimental results of García and Campos.

Table 2-2. Energies of the atomic strontium states connected by the transitions studied in this research [37]

Energy State	Energy (cm <sup>-1</sup> )
$5s6s\ ^3S_1$	-16886.805
$5s5p\ ^3P_2$	-31027.037
$5s5p\ ^3P_1$	-31421.249
$5s5p\ ^3P_0$	-31608.080
$5s^2\ ^1S_0$	-45925.600

Table 2-3. Atomic strontium emission intensities of transitions studied in this research

Transition	Emission Intensity (10 <sup>6</sup> sec <sup>-1</sup> )	Relative Intensity (unitless)	Reference
$5s^2\ ^1S_0 \leftarrow 5s5p\ ^3P_1$	0.048(0.002)	-	[22]
$5s5p\ ^3P_0 \leftarrow 5s6s\ ^3S_1$	8.9(0.8)	$\frac{1}{9}$	[15]
$5s5p\ ^3P_1 \leftarrow 5s6s\ ^3S_1$	27.1(2.0)	$\frac{3}{9}$	
$5s5p\ ^3P_2 \leftarrow 5s6s\ ^3S_1$	41.5(4.0)	$\frac{5}{9}$	



The spectra of atomic strontium have been reported to exhibit features due to isotope shifts and hyperfine structure [2]. It is important to understand these features because of their possible influence on the line profiles measured in this research. That is, what appears in the laboratory to be a single, broad transition may, in fact, be several less broad transitions spaced closely together. Without properly accounting for this, the evaluation of the linewidth may be overstated. In the remainder of this section, the isotope shifts and hyperfine structure of atomic strontium are reviewed leading to the generation of two theoretical line profiles which account for these effects.

Barsanti *et al.* have investigated the isotope shifts and hyperfine structure of a number of atomic strontium transitions and energy states [2]. Relevant to this work is their reported shifts of the  $5s^2\ ^1S_0 \rightarrow 5s5p\ ^3P_1$  and  $5s5p\ ^3P_1 \rightarrow 5s6s\ ^3S_1$  transitions for  $^{86}\text{Sr}$  and  $^{87}\text{Sr}$  and the hyperfine structure of the  $5s5p\ ^3P_1$  and  $5s6s\ ^3S_1$  energy states of  $^{87}\text{Sr}$ . Table 2-4 gives the spectral line center shifts of the less-abundant isotopes  $^{86}\text{Sr}$  and  $^{87}\text{Sr}$  relative to  $^{88}\text{Sr}$  for the  $5s^2\ ^1S_0 \rightarrow 5s5p\ ^3P_1$  and  $5s5p\ ^3P_1 \rightarrow 5s6s\ ^3S_1$  transitions. The positive shifts indicate a displacement to lower energy. Also, Table 2-5 gives the magnetic and electric hyperfine coupling constants  $A$  and  $B$  for the  $5s5p\ ^3P_1$  and  $5s6s\ ^3S_1$  energy states of  $^{87}\text{Sr}$ . The displacement  $\Delta E_m$  of an energy state due to magnetic hyperfine coupling between the nuclear spin quantum number  $I$  and the total angular momentum quantum number  $J$  is given by

$$\Delta E_m = \frac{A}{2} \{ (F(F+1) - I(I+1) - J(J+1)) \} \quad (2-70)$$

where the new total angular momentum quantum number  $F$  takes on the range of values  $I+J, I+J-1, \dots, |I-J|$  [50]. The displacement  $\Delta E_e$  of an energy state due to

electric hyperfine coupling between the nuclear charge distribution and the electron cloud charge distribution is given by

$$\Delta E_e = B \left\{ \frac{\left( \frac{3C}{4} \right) (C+1) - I(I+1)J(J+1)}{2I(2I-1)J(2J-1)} \right\} \quad (2-71)$$

where [50]

$$C = F(F+1) - I(I+1) - J(J+1) \quad (2-72)$$

Table 2-4. Isotope line center shifts of  $^{86}\text{Sr}$  and  $^{87}\text{Sr}$  relative to  $^{88}\text{Sr}$ . A positive shift represents a displacement to lower energy. These values are reported by Barsanti *et al.* [2].

Transition	$^{86}\text{Sr}$ ( $\text{cm}^{-1}$ )	$^{87}\text{Sr}$ ( $\text{cm}^{-1}$ )
$5s^2\ ^1\text{S}_0 \rightarrow 5s5p\ ^3\text{P}_1$	0.00534(0.00017)	0.00217(0.00033)
$5s5p\ ^3\text{P}_1 \rightarrow 5s6s\ ^3\text{S}_1$	0.06585(0.00067)	0.01748(0.00067)

Table 2-5. Magnetic and electric hyperfine coupling constants for the atomic strontium  $5s5p\ ^3\text{P}_1$  and  $5s6s\ ^3\text{S}_1$  energy states. These values are reported by Barsanti *et al.* [2].

Energy State	$A$ ( $\text{cm}^{-1}$ )	$B$ ( $\text{cm}^{-1}$ )
$5s5p\ ^3\text{P}_1$	-0.008739(0.000067)	-0.00123(0.00030)
$5s6s\ ^3\text{S}_1$	-0.018113(0.000067)	-

Figure 2-13 shows energy levels of the  $^{87}\text{Sr}$   $5s^2\ ^1\text{S}_0$ ,  $5s5p\ ^3\text{P}_1$ , and  $5s6s\ ^3\text{S}_1$  states including their hyperfine structure. The selection rule for transitions between hyperfine levels is  $\Delta F = 0, \pm 1$  [23] and the allowed transitions are labeled. Therefore, including the isotope shifts, there are five distinct atomic strontium  $5s^2\ ^1\text{S}_0 \rightarrow 5s5p\ ^3\text{P}_1$  transitions. These include two due to  $^{88}\text{Sr}$  and  $^{86}\text{Sr}$  and three due to the hyperfine structure of the  $^{87}\text{Sr}$   $5s5p\ ^3\text{P}_1$  energy levels. Barsanti *et al.* report no isotope shift data on  $^{84}\text{Sr}$  because of its

low abundance [2]. Therefore, it is henceforth neglected. Also, there are nine distinct atomic strontium  $5s5p\ ^3P_1 \rightarrow 5s6s\ ^3S_1$  transitions. These include two due to  $^{88}\text{Sr}$  and  $^{86}\text{Sr}$  and seven due to the hyperfine splittings of the  $^{87}\text{Sr}$   $5s5p\ ^3P_1$  and  $5s6s\ ^3S_1$  energy states.

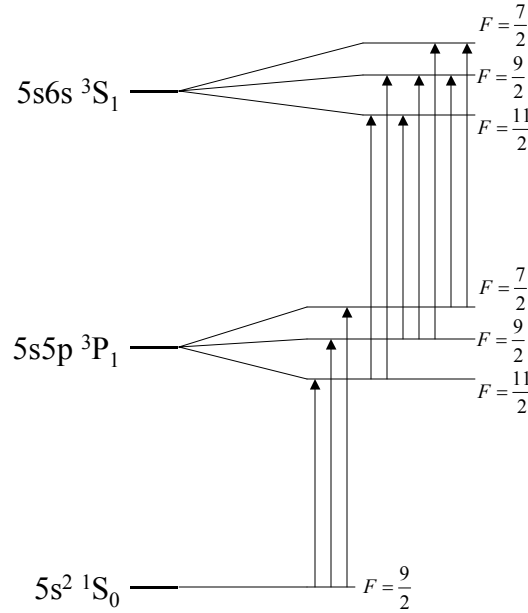


Figure 2-13. Hyperfine structure of the  $5s5p\ ^3P_1$  and  $5s6s\ ^3S_1$  energy states of  $^{87}\text{Sr}$  with transitions allowed under the selection rule  $\Delta F = 0, \pm 1$  labeled. Three transitions are allowed in the  $5s^2\ ^1S_0 \rightarrow 5s5p\ ^3P_1$  manifold and seven in the  $5s5p\ ^3P_1 \rightarrow 5s6s\ ^3S_1$  manifold.

With the information given above, it is possible to generate theoretical line profiles for the atomic strontium  $5s^2\ ^1S_0 \rightarrow 5s5p\ ^3P_1$  and  $5s5p\ ^3P_1 \rightarrow 5s6s\ ^3S_1$  transitions. For unbroadened transitions, the Gaussian lineshape function given by Equation 2-57 adequately models the line profile. The line centers are given by the isotope shifts in Table 2-4 and the hyperfine transition energies of  $^{87}\text{Sr}$  are computed using the energy

state perturbations prescribed by Equations 2-70, 2-71, and 2-72 with the constants in Table 2-5. The Gaussian linewidth is given by the temperature as indicated in Equation 2-58. And finally, the signal strengths of the three isotopes are determined by their natural abundances as given in Table 2-1. Since the  $^{87}\text{Sr}$  isotope spectral line is split by hyperfine structure, the signal strengths of these components are dictated by the degeneracies of the states involved. Similar to the relative emission intensities of the  $5s5p\ ^3P_{0,1,2} \leftarrow 5s6s\ ^3S_1$  transitions described previously, the signal strengths are weighted by  $\frac{2F'+1}{2F''+1}$  [23].

Figure 2-14 shows a theoretical line profile of the atomic strontium  $5s^2\ ^1S_0 \rightarrow 5s5p\ ^3P_1$  transition with the isotope shift and hyperfine structure described in the previous paragraph. The Gaussian linewidth corresponds to a temperature of 728 K. This value was chosen because, as will be reported in Chapter IV, it was the temperature at which the transition was observed in this research. The transition due to  $^{86}\text{Sr}$  is only slightly offset from the main line and introduces no discernable asymmetry to the total line profile. However, the hyperfine structure of the  $^{87}\text{Sr}$  transition introduces a slight asymmetry to the wings of the total line profile.

Similarly, Figure 2-15 shows a theoretical line profile of the atomic strontium  $5s5p\ ^3P_1 \rightarrow 5s6s\ ^3S_1$  transition with the isotope shift and hyperfine structure described above. The Gaussian linewidth corresponds to a temperature of 1473 K. Again, this value was chosen because, as will be reported in Chapter IV, it was the temperature at which the transition was observed in this research. In this case, the transition due to  $^{86}\text{Sr}$  exhibits a large offset from the main line and introduces a major asymmetry to the total

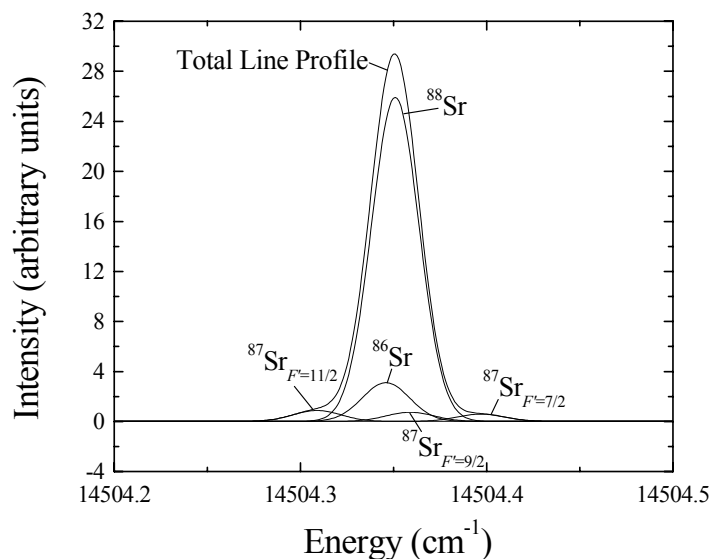


Figure 2-14. Line profile of the atomic strontium  $5s^2\ ^1S_0 \rightarrow 5s5p\ ^3P_1$  transition including contributions by the isotopes  $^{88}\text{Sr}$ ,  $^{86}\text{Sr}$ , and the hyperfine levels of  $^{87}\text{Sr}$ . The hyperfine levels produce a slight asymmetry in the wings of the total line profile.

line profile. The intensity of the hyperfine structure of the  $^{87}\text{Sr}$  transitions is small because it is spread over seven lines and, as such, introduces no discernable asymmetry to the wings of the line profile.

In conclusion, it is clear that the isotope shifts and hyperfine structure of atomic strontium are important to the observations of this experiment. Armed with the insight gained above, however, it is possible to account for these effects in the data analysis.

**2.2.2 Diatomic Bismuth** The properties of atomic bismuth are as follows. It is the heaviest element in the 15th column of the periodic table of elements. It has atomic number 83, atomic weight 208.98037 amu [54], and only one stable isotope:  $^{209}\text{Bi}$  [33]. Its ground state electronic configuration is  $[\text{Xe}]4f^{14}5d^{10}6s^2p^3$  meaning it has five valence shell electrons [23]. Two of these are in a closed sub-orbital and the remaining three are in a half-filled sub-orbital.

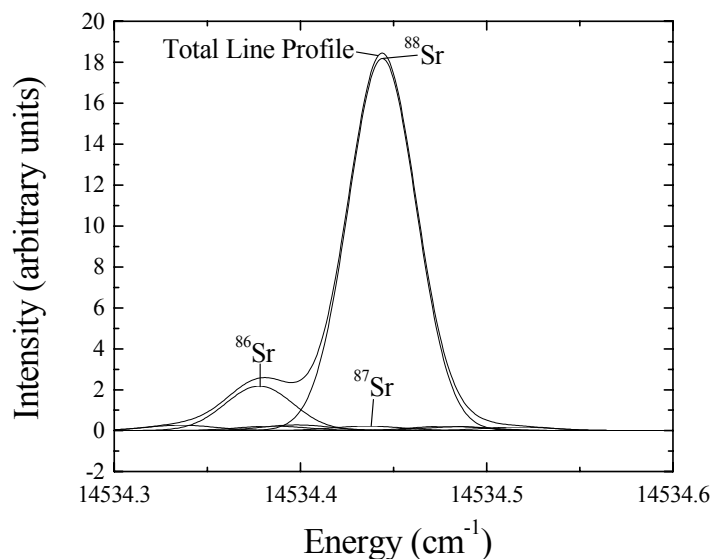


Figure 2-15. Line profile of the atomic strontium  $5s5p\ ^3P_1 \rightarrow 5s6s\ ^3S_1$  transition including contributions by the isotopes  $^{88}\text{Sr}$ ,  $^{86}\text{Sr}$ , and the hyperfine levels of  $^{87}\text{Sr}$ . The isotope shift of  $^{86}\text{Sr}$  produces a large asymmetry in the total line profile.

Bismuth forms a stable, heavy molecule for which Hund's case (c) coupling applies. Figure 2-16 shows the electronic energy states of  $\text{Bi}_2$  near the ground state [9]. The ground state term is  $X(0_g^+)$  and the excited state term studied here is  $A(0_u^+)$  [13]. According to theory, the rovibrational energy levels,  $E(v, J)$ , as a function of the vibrational quantum number  $v$  and the total angular momentum quantum number  $J$  are given by [24]

$$E(v, J) = T(v) + B(v)J(J+1) - D(v)J^2(J+1)^2 \quad (2-73)$$

$T(v)$  is the combined electronic and vibrational energy while  $B(v)$  and  $D(v)$  are constants associate with rotational energy. In this research, the  $v''=3 \rightarrow v'=1$  vibrational manifold is studied and the spectroscopic constants for this manifold, as determined by Franklin, are given in Table 2-6 [14].

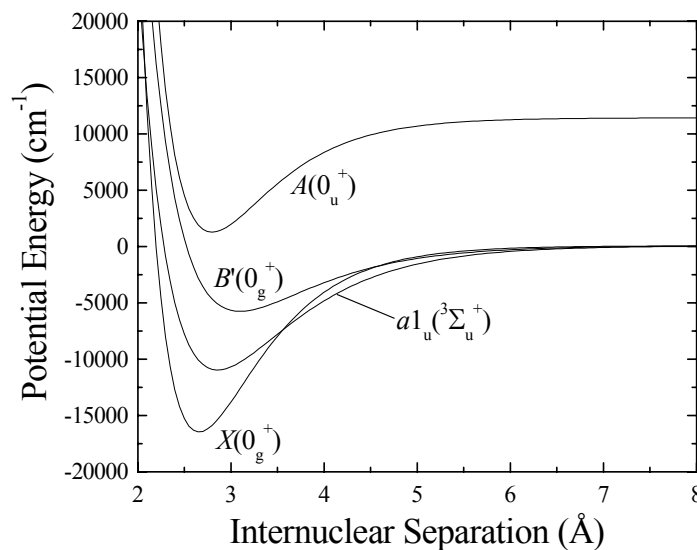


Figure 2-16. Electronic energy states of diatomic bismuth near the ground state

Table 2-6. Spectroscopic constants for the  $\nu''=3 \rightarrow \nu'=1$  vibrational manifold of the  $\text{Bi}_2$   $X(0_g^+) \rightarrow A(0_u^+)$  electronic transition as determined by Franklin and Perram [14]

	$\nu''=3$ ( $\text{cm}^{-1}$ )	$\nu'=1$ ( $\text{cm}^{-1}$ )
$T(\nu)$	600.991	17938.565
$B(\nu)$	0.022622	0.019592
$D(\nu)$	$1.635 \times 10^{-9}$	$1.761 \times 10^{-9}$

Figure 2-17 shows a small portion of the  $\text{Bi}_2$  spectrum in the  $\nu''=3 \rightarrow \nu'=1$  vibrational manifold. Rotational lines appear in P and R branch pairs 13 levels apart. Appendix A lists the P and R branch rotational line centers in this vibrational manifold as determined by the spectroscopic constants of Table 2-6 [14] as well as the line centers measured by Franklin [13]. These numbers generally agree to within approximately several hundredths of a wavenumber. Therefore, it is possible to assign the spectrum unambiguously using Equation 2-73 and these constants.

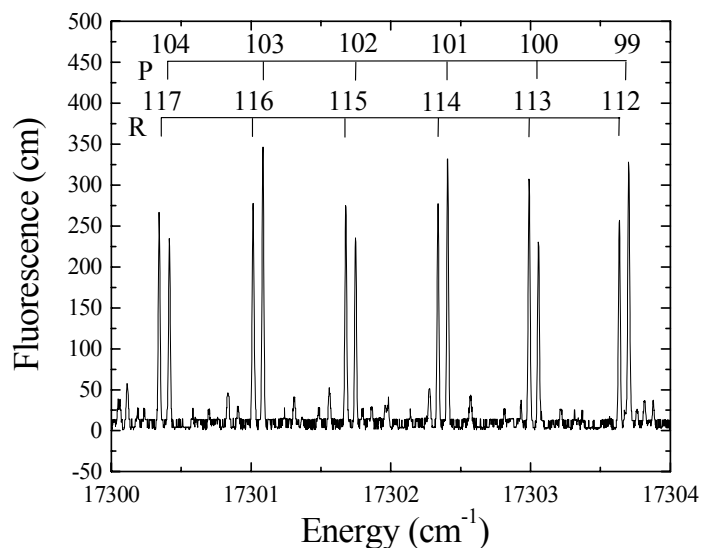


Figure 2-17. A small portion of the diatomic bismuth spectrum in the  $\nu''=3 \rightarrow \nu'=1$  vibrational manifold of the  $X(0_g^+) \rightarrow A(0_u^+)$  electronic transition. Rotational lines appear in P and R branch pairs 13 levels apart.

## 2.3 Applications of Line Broadening and Shifting

This section describes how line broadening and shifting rates induced by elastic collisions may be used to determine the difference potential between states. It also discusses how the line broadening rate induced by inelastic collisions is related to the total quenching rate constants of the lower and upper states of a transition.

**2.3.1 Difference Potentials** The difference potential was introduced briefly in Section 2.1.2.2, Elastic Collisions and Pressure Broadening. It is defined as the energy difference between two states ignoring the unperturbed energy gap between them. Referring to Figure 2-7, the difference potential,  $V(r)$ , is defined mathematically here as

$$V(r) = E_k - E_j - (E_k^0 - E_j^0) \quad (2-74)$$



If the lower and upper state energies  $E_j$  and  $E_k$  vary exactly the same way as a foreign body perturbs a body absorbing or radiating energy, then the energy gap between the states remains constant and the difference potential is exactly zero. If they do not, then the difference potential exists as defined by Equation 2-74. This section begins where Section 2.1.2.2 ends and presents a method for determining the difference potential from the broadening and shifting rates of spectral lines perturbed by elastic collisions.

The difference potential is derived from  $\eta(\rho)$ , which, as stated previously, is the departure in phase of the perturbed electric field oscillation from the unperturbed oscillation caused by an elastic collision of impact parameter  $\rho$  [25]. To begin, the results of Section 2.1.2.2 are transcribed below. The FWHM of a transition broadened by elastic collisions is

$$\delta\omega_L = \frac{1}{\tau_j} + \frac{1}{\tau_k} + 2N\langle v \rangle \sigma_r \quad (2-75)$$

and the line center shift is

$$\Delta\omega = N\langle v \rangle \sigma_i \quad (2-76)$$

where

$$\sigma_r = 2\pi \int_0^\infty (1 - \cos \eta(\rho)) \rho d\rho \quad (2-77)$$

and

$$\sigma_i = 2\pi \int_0^\infty \sin \eta(\rho) \rho d\rho \quad (2-78)$$

The line broadening and shifting rates which follow from Equations 2-75 and 2-76 are

$$\frac{\Delta(\delta\omega_L)}{\Delta N} = 2\langle v \rangle \sigma_r \quad (2-79)$$

and

$$\frac{\Delta(\Delta\omega)}{\Delta N} = \langle v \rangle \sigma_i \quad (2-80)$$

The approach is to derive an expression for  $\eta(\rho)$  which involves the difference potential, insert it into the above equations, and solve for the difference potential.

Recall from Equation 2-24 that the angular frequency of a transition is a function of the separation  $r$  between the absorbing or radiating body and perturbing body.  $r$  itself is a function of time so that Equation 2-24 may be more explicitly written as

$$\omega(t) = \frac{1}{\hbar} (E_k^0 - E_j^0 + V(r(t))) \quad (2-81)$$

Using this expression for the angular frequency, the phase of the oscillation is then

$$\int \omega(t') dt' = \int \frac{1}{\hbar} (E_k^0 - E_j^0 + V(r(t'))) dt' \quad (2-82)$$

or

$$\int \omega(t') dt' = \omega_0 t + \frac{1}{\hbar} \int V(r(t')) dt' \quad (2-83)$$

Comparing this equation with Equation 2-30 yields the following expression for  $\eta(t)$

$$\eta(t) = \frac{1}{\hbar} \int V(r(t')) dt' \quad (2-84)$$

To aid in the evaluation of this integral, a change of variables is accomplished. The integral in time is exchanged for an integral over distance according to the relationship between time and impact parameter  $\rho$  prescribed by Equation 2-25. That is,

$$\eta(\rho) = \frac{2}{\hbar \langle v \rangle} \int_{\rho}^{\infty} \frac{V(r) r dr}{\sqrt{r^2 - \rho^2}} \quad (2-85)$$

To evaluate the integral in Equation 2-85, a functional form for the difference potential  $V(r)$  must be applied. Again, the Lennard-Jones (6-12) potential expressed in Equation 2-23 is chosen. That is,

$$V(r) = \frac{C_{12}}{r^{12}} - \frac{C_6}{r^6} \quad (2-86)$$

Inserting Equation 2-86 into 2-85 and evaluating the integral gives

$$\eta(x) = \frac{\alpha}{x^{11}} - \frac{1}{x^5} \quad (2-87)$$

where

$$\alpha = \frac{63\pi}{256} \left( \frac{8}{3\pi} \right)^{\frac{11}{5}} \langle v \rangle^{\frac{6}{5}} \frac{C_{12} \hbar^{\frac{6}{5}}}{C_6^{\frac{11}{5}}} \quad (2-88)$$

and

$$x = \rho \left( \frac{3\pi}{8} \frac{C_6}{\hbar \langle v \rangle} \right)^{-\frac{1}{5}} \quad (2-89)$$

The next step is to insert the expression for  $\eta(x)$  into the cross section integrals of Equations 2-77 and 2-78 and press to a conclusion. Performing this operation gives

$$\sigma_r = 8\pi \left( \frac{3\pi}{8} \frac{C_6}{\hbar \langle v \rangle} \right)^{\frac{2}{5}} B(\alpha) \quad (2-90)$$

and

$$\sigma_i = 2\pi \left( \frac{3\pi}{8} \frac{C_6}{\hbar \langle v \rangle} \right)^{\frac{2}{5}} S(\alpha) \quad (2-91)$$

where

$$B(\alpha) = \int_0^\infty \sin^2 \left( \frac{1}{2} \left( \frac{\alpha}{x^{11}} - \frac{1}{x^5} \right) \right) x dx \quad (2-92)$$

and

$$S(\alpha) = \int_0^\infty \sin \left( \frac{\alpha}{x^{11}} - \frac{1}{x^5} \right) x dx \quad (2-93)$$

These integrals are solved analytically by *Mathematica*; the results of which are quite long and presented in Appendix B.

Inserting Equations 2-90 and 2-91 into Equations 2-79 and 2-80 gives

$$\frac{\Delta(\delta\omega_L)}{\Delta N} = 16\pi \langle v \rangle \left( \frac{3\pi}{8} \frac{C_6}{\hbar \langle v \rangle} \right)^{\frac{2}{5}} B(\alpha) \quad (2-94)$$

and

$$\frac{\Delta(\Delta\omega)}{\Delta N} = 2\pi \langle v \rangle \left( \frac{3\pi}{8} \frac{C_6}{\hbar \langle v \rangle} \right)^{\frac{2}{5}} S(\alpha) \quad (2-95)$$

This is a system of two equations and two unknowns where the unknowns are the difference potential constants  $C_6$  and  $C_{12}$ . The constant  $C_6$  is stated explicitly while  $C_6$  and  $C_{12}$  are incorporated in the constant  $\alpha$ .

While there is no way to invert these equations and express  $C_6$  and  $C_{12}$  analytically, there is a way to obtain a numerical result. Taking the ratio of the line shifting rate to the line broadening rate gives

$$\frac{\frac{\Delta(\Delta\omega)}{\Delta N}}{\frac{\Delta(\delta\omega_L)}{\Delta N}} = \frac{S(\alpha)}{4B(\alpha)} \quad (2-96)$$

Equation 2-96, plotted in Figure 2-18, is an implicit equation for  $\alpha$  which can be solved by numerical methods. With  $\alpha$  known,  $C_6$  is calculated by either Equation 2-94 or 2-95. And finally,  $C_{12}$  is determined by Equation 2-88.

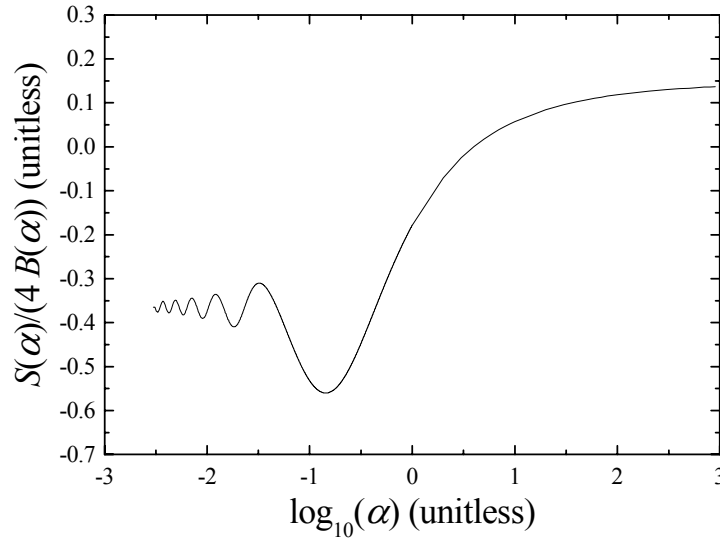


Figure 2-18.  $\frac{S(\alpha)}{4B(\alpha)}$  as a function of  $\log_{10}(\alpha)$

A special case arises in the limit as  $\alpha$  goes to infinity, which is evaluated numerically to be approximately 0.146813. If the measured ratio of the line shifting rate to line broadening rate falls above this value, the Lennard-Jones (6-12) potential is not an accurate description of the difference potential. In this case, it is assumed to be completely repulsive so that

$$V(r) = \frac{C_{12}}{r^{12}} \quad (2-97)$$

Inserting this into Equation 2-85 and integrating yields

$$\eta(\rho) = \frac{C_{12}}{\langle v \rangle \hbar} \frac{63\pi}{256\rho^{11}} \quad (2-98)$$

Applying this result to Equations 2-77 and 2-78 gives

$$\sigma_r = \pi^{\frac{12}{11}} \left( \frac{C_{12}}{\langle v \rangle \hbar} \right)^{\frac{2}{11}} \left( \frac{\Gamma(\frac{11}{2})}{\Gamma(6)} \right)^{\frac{2}{11}} \Gamma(\frac{9}{11}) \cos(\frac{\pi}{11}) \quad (2-99)$$

and

$$\sigma_i = \pi^{\frac{12}{11}} \left( \frac{C_{12}}{\langle v \rangle \hbar} \right)^{\frac{2}{11}} \left( \frac{\Gamma(\frac{11}{2})}{\Gamma(6)} \right)^{\frac{2}{11}} \Gamma(\frac{9}{11}) \sin(\frac{\pi}{11}) \quad (2-100)$$

And finally, relating these cross sections to the line broadening and shifting rates of Equations 2-79 and 2-80 gives

$$\frac{\Delta(\delta\omega_L)}{\Delta N} = 2\pi^{\frac{12}{11}} \left( \frac{\langle v \rangle^{\frac{9}{2}} C_{12}}{\hbar} \right)^{\frac{2}{11}} \left( \frac{\Gamma(\frac{11}{2})}{\Gamma(6)} \right)^{\frac{2}{11}} \Gamma(\frac{9}{11}) \cos(\frac{\pi}{11}) \quad (2-101)$$

and

$$\frac{\Delta(\Delta\omega)}{\Delta N} = \pi^{\frac{12}{11}} \left( \frac{\langle v \rangle^{\frac{9}{2}} C_{12}}{\hbar} \right)^{\frac{2}{11}} \left( \frac{\Gamma(\frac{11}{2})}{\Gamma(6)} \right)^{\frac{2}{11}} \Gamma(\frac{9}{11}) \sin(\frac{\pi}{11}) \quad (2-102)$$

In this case, the difference potential constant  $C_{12}$  is over-constrained by the two equations above [25].

**2.3.2 Total Quenching Rate Constants** The goal of this section is to show that the line broadening rate caused by inelastic collisions is the sum of the total quenching rate constants of the lower and upper states of a transition. Total quenching rate here, and throughout this dissertation, refers to total rotational energy transfer out of a state. It is the total removal rate from a rotational state and can involve transfers to other rotational

states in the same vibrational manifold or to other vibrational manifolds in either the same or other electronic states.

To begin, Equation 2-18, which is the result of Section 2.1.2.1, Inelastic Collisions and Pressure Broadening, is transcribed below.

$$\delta\omega_L = \frac{1}{\tau_j} + \frac{1}{\tau_k} + N\langle v \rangle (\sigma_j^q + \sigma_k^q) \quad (2-103)$$

The line broadening rate is the derivative of the FWHM with respect to number density.

$$\frac{\Delta(\delta\omega_L)}{\Delta N} = \langle v \rangle (\sigma_j^q + \sigma_k^q) \quad (2-104)$$

Since the conversion from cross section to rate constant  $k$  is

$$\sigma = \frac{k}{\langle v \rangle} \quad (2-105)$$

the line broadening rate is [32]

$$\frac{\Delta(\delta\omega_L)}{\Delta N} = (k_j^q + k_k^q) \quad (2-106)$$

That is, when inelastic collisions dominate, the line broadening rate is the same as the sum of the total quenching rate constant from the lower state,  $k_j^q$ , and the total quenching rate constant from the upper state  $k_k^q$ . Equation 2-106 is simplified by defining the sum total quenching rate constant  $k^q$  as follows

$$k^q = k_j^q + k_k^q \quad (2-107)$$

This gives

$$\frac{\Delta(\delta\omega_L)}{\Delta N} = k^q \quad (2-108)$$

Stated again in these terms, when inelastic collisions dominate, the line broadening rate is the same as the sum total quenching rate constant.



### **III. Background**

The purpose of this chapter is to explore all previous relevant work in the line broadening and shifting of atoms and molecules. In addition to summarizing previous such research in atomic strontium, atomic calcium and barium are reviewed as well because of their structural similarity to strontium. In the case of diatomic bismuth, the literature was scanned for line broadening work in any diatomic species with an emphasis on heavy diatomics. In addition to providing previous results for comparison, this chapter also serves to place the current work in the context of other research. It is divided into two sections. The first contains a discussion of relevant research in atomic calcium, strontium, and barium. The second reviews line broadening in a variety of diatomic species.

#### **3.1 Line Perturbations and Difference Potentials in Atomic Species**

This section reviews all previous line broadening and shifting research in atomic calcium, strontium, and barium. It also includes research on difference potentials of these atoms; regardless of whether they are derived from experimental data or computed from first principles. Line broadening and shifting rates reported by previous researchers are converted to cross section and summarized here along with difference potential constants.

**3.1.1 Atomic Calcium** Atomic calcium has been studied extensively for a number of reasons. For one, it is a relatively simple atom compared to strontium and barium making it amenable to quantum mechanical calculation [18]. Also, the

broadening and shifting of calcium transitions by atomic hydrogen are observed in stellar spectra indicating the surface gravity of stars [39, 48]. Similarly, local conditions of atomic calcium in plasmas may be determined from such measurements [27, 5]. And finally, the  $4s^2\ ^1S_0 \rightarrow 4s4p\ ^3P_1$  intercombination transition at  $15210.067\text{ cm}^{-1}$  (657.5 nm) has been proposed as an optical frequency standard [43] and for compression of frequency-chirped laser pulses [6].

The first modern study of line broadening and shifting of atomic calcium was undertaken by Ch'en and Lonseth in 1971. They investigated broadening and shifting in the strong  $4s^2\ ^1S_0 \rightarrow 4s4p\ ^1P_1$  transition (see Figure 3-1) at  $23652.324\text{ cm}^{-1}$  (422.8 nm) using the absorption of a broadband optical source and a grating spectrograph. These researchers report line broadening and shifting rates of this transition perturbed by helium and argon. These rates are converted to cross section by Equations 2-79 and 2-80 and reproduced in Tables 3-1 and 3-2. Ch'en and Lonseth also performed difference potential calculations and report the constants  $C_6$  and  $C_{12}$ . These constants are displayed in Tables 3-3 and 3-4 [5].

A year later, Smith reported line broadening and shifting rates of the same transition with the same experimental technique, but extended the set of perturbing species to include neon, krypton, and xenon. Smith's line broadening and shifting rates are converted to cross section by Equations 2-79 and 2-80 and summarized in Tables 3-1 and 3-2 [46]. In 1974, Shabanova computed theoretical difference potential constants  $C_6$  and  $C_{12}$  for the energy states connected by this transition perturbed by helium, neon, argon, and krypton. His results are reproduced in Tables 3-3 and 3-4 [45].

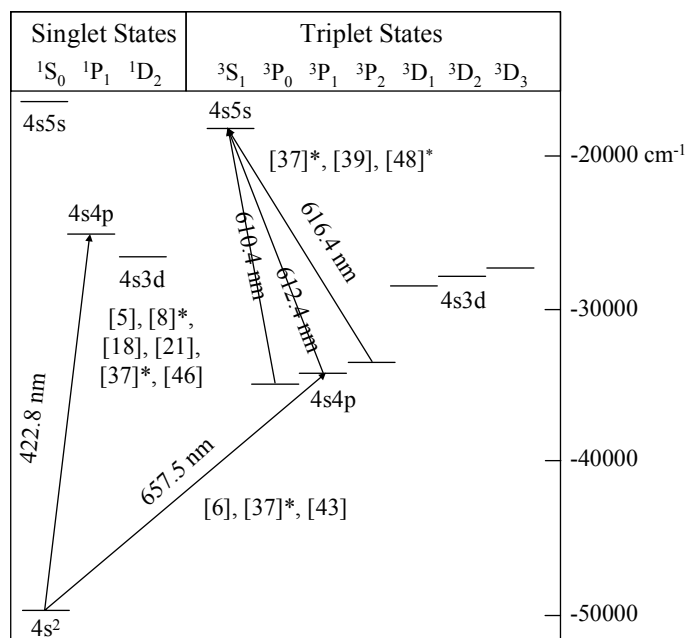


Figure 3-1. Lower electronic energy states of atomic calcium. Transitions studied previously are referenced. The asterisk indicates theoretical work.

In 1977, Malvern published theoretical calculations of the broadening and shifting of the  $4s^2 \ ^1S \rightarrow 4s4p \ ^1P$ ,  $4s^2 \ ^1S \rightarrow 4s4p \ ^3P$ , and  $4s4p \ ^3P \rightarrow 4s5s \ ^3S$  ( $\sim 16329 \text{ cm}^{-1}$  or 613 nm) transitions perturbed by helium and neon. He ignored the fine structure of the atom and, in the case of the  $4s4p \ ^3P \rightarrow 4s5s \ ^3S$  transitions, justified this by claiming that the broadening rate is due mostly to the upper state. Since the upper state is the same in this multiplet, the broadening rates should be the same and the fine structure can be ignored. The line broadening and shifting rates calculated by this researcher are converted to cross section by Equations 2-79 and 2-80 and summarized in Tables 3-1 and 3-2. Also, the line broadening and shifting cross sections for the  $4s4p \ ^3P \rightarrow 4s5s \ ^3S$  multiplet are plotted in Figure 3-2 for comparison with other experimental work on this transition [37].

Table 3-1. Line broadening cross sections of atomic calcium transitions perturbed by helium, neon, argon, krypton, and xenon reported by previous researchers. All cross sections except those reported by Crane *et al.* [6] and Devdariani *et al.* [8] are determined from the published line broadening rates using Equation 2-79. The asterisk indicates theoretical work.

	He	Ne	Ar	Kr	Xe
	Broadening Cross Section ( $10^{-14} \text{ cm}^2$ )	Broadening Cross Section ( $10^{-14} \text{ cm}^2$ )	Broadening Cross Section ( $10^{-14} \text{ cm}^2$ )	Broadening Cross Section ( $10^{-14} \text{ cm}^2$ )	Broadening Cross Section ( $10^{-14} \text{ cm}^2$ )
$4s^2\ ^1S_0 \rightarrow 4s4p\ ^1P_1$ (23652.324 $\text{cm}^{-1}$ )					
[5]	1.0	-	2.5	-	-
[46]	1.14(0.03)	1.2(0.05)	3.95(0.43)	3.60(0.30)	4.29(0.40)
[37]*	1.14	1.1	-	-	-
[18]	1.96(0.29)	-	-	-	-
[8]*	0.92	1.53	-	-	-
[21]	1.03(0.01)	1.20(0.04)	2.74(0.05)	3.32(0.07)	4.12(0.07)
$4s^2\ ^1S_0 \rightarrow 4s4p\ ^3P_1$ (15210.067 $\text{cm}^{-1}$ )					
[37]*	0.551	0.937	-	-	-
[43]	1.00(0.05)	1.45(0.11)	3.12(0.16)	-	-
[6]	-	0.77(0.06)	1.27(0.21)	-	-
$4s4p\ ^3P \rightarrow 4s5s\ ^3S$ ( $\sim 16329 \text{ cm}^{-1}$ )					
[37]*	2.27	1.89	-	-	-

The first experimental study of the  $4s4p\ ^3P_{0,1,2} \rightarrow 4s5s\ ^3S_1$  multiplet was conducted by O'Neill and Smith in 1980. They used broadband absorption and a monochromator to study the broadening and shifting of these transitions by helium, neon, and argon. This work is directly relevant to the current research because it involves the analogous transitions which were studied in strontium. Their results are converted to cross section according to Equations 2-79 and 2-80 and plotted in Figure 3-2. There appears to be no consistent trend of cross section as a function of the total angular momentum quantum number of the initial state  $J''$  in either the broadening or shifting cross section. Also, it is interesting to note that the line broadening cross section is

smallest for neon and not for helium, the lightest of the perturbing species, as one might expect. And finally, the shifting cross section for helium is positive indicating a shift of the line center towards the blue and negative for neon and argon [39].

Table 3-2. Line shifting cross sections of atomic calcium transitions perturbed by helium, neon, argon, krypton, and xenon reported by previous researchers. All cross sections except those reported by Devdariani *et al.* [8] are determined from the published line shifting rates using Equation 2-80. The asterisk indicates theoretical work.

	He	Ne	Ar	Kr	Xe
	Shifting Cross Section ( $10^{-14} \text{ cm}^2$ )	Shifting Cross Section ( $10^{-14} \text{ cm}^2$ )	Shifting Cross Section ( $10^{-14} \text{ cm}^2$ )	Shifting Cross Section ( $10^{-14} \text{ cm}^2$ )	Shifting Cross Section ( $10^{-14} \text{ cm}^2$ )
$4s^2 \ ^1S_0 \rightarrow 4s4p \ ^1P_1$ ( $23652.324 \text{ cm}^{-1}$ )					
[5]	-0.060	-	-1.7	-	-
[46]	-0.073(0.004)	-0.640(0.003)	-1.93(0.01)	-2.08(0.02)	-2.53(0.02)
[37]*	0.13	-0.12	-	-	-
[18]	-1.39(0.21)	-	-	-	-
[8]*	-0.08	-0.74	-	-	-
$4s^2 \ ^1S_0 \rightarrow 4s4p \ ^3P_1$ ( $15210.067 \text{ cm}^{-1}$ )					
[37]*	0.24	0.52	-	-	-
$4s4p \ ^3P \rightarrow 4s5s \ ^3S$ ( $\sim 16329 \text{ cm}^{-1}$ )					
[37]*	0.73	0.23	-	-	-

Table 3-3. Difference potential constant  $C_6$  for the atomic calcium  $4s^2 \ ^1S_0$  and  $4s4p \ ^1P_1$  energy states perturbed by helium, neon, argon, and krypton reported by previous researchers. The asterisk indicates theoretical work.

	He	Ne	Ar	Kr
	$C_6$ ( $10^{-58} \text{ erg cm}^6$ )	$C_6$ ( $10^{-58} \text{ erg cm}^6$ )	$C_6$ ( $10^{-58} \text{ erg cm}^6$ )	$C_6$ ( $10^{-58} \text{ erg cm}^6$ )
[5]	0.92	-	9.2	-
[45]*	0.26	0.50	1.9	3.3

Table 3-4. Difference potential constant  $C_{12}$  for the atomic calcium  $4s^2\ ^1S_0$  and  $4s4p\ ^1P_1$  energy states perturbed by helium, neon, argon, and krypton reported by previous researchers. The asterisk indicates theoretical work.

	He	Ne	Ar	Kr
	$C_{12}$ ( $10^{-101}$ erg cm $^{12}$ )	$C_{12}$ ( $10^{-101}$ erg cm $^{12}$ )	$C_{12}$ ( $10^{-101}$ erg cm $^{12}$ )	$C_{12}$ ( $10^{-101}$ erg cm $^{12}$ )
[5]	109	-	76	-
[45]*	0.080	0.062	0.52	1.9

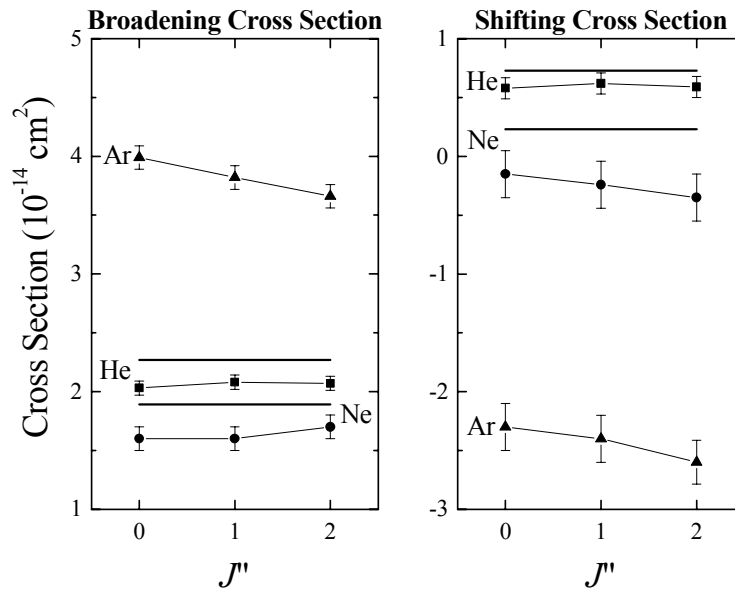


Figure 3-2. Line broadening and shifting cross sections of the atomic calcium  $4s4p\ ^3P_{0,1,2} \rightarrow 4s5s\ ^3S_1$  transitions around  $16329\text{ cm}^{-1}$  perturbed by helium, neon, and argon as a function of the total angular momentum quantum number  $J''$  of the initial state. These cross sections are computed from the line broadening and shifting values published by O'Neill and Smith [39] and Malvern [37] using Equations 2-79 and 2-80. Malvern's theoretical results, being independent of  $J''$ , are plotted as horizontal lines.

In 1981, Smith and Raggett conducted an extensive experimental survey of atomic calcium line broadening in mid-level transitions. They used broadband absorption and a spectrograph to resolve the lines, and the transitions were broadened by helium.

Figure 3-3 shows which transitions were studied. Line broadening cross sections from

the  $4s3d\ ^3D \rightarrow 3d4p\ ^3F$  multiplets showed no dependence on the total angular momentum quantum number  $J$  of either the initial or final states. Neither did the line broadening cross sections from the  $4s3d\ ^3D \rightarrow 3d4p\ ^3D$  multiplets [47]. This provides further experimental evidence that line broadening in atoms is not dependent on total angular momentum.

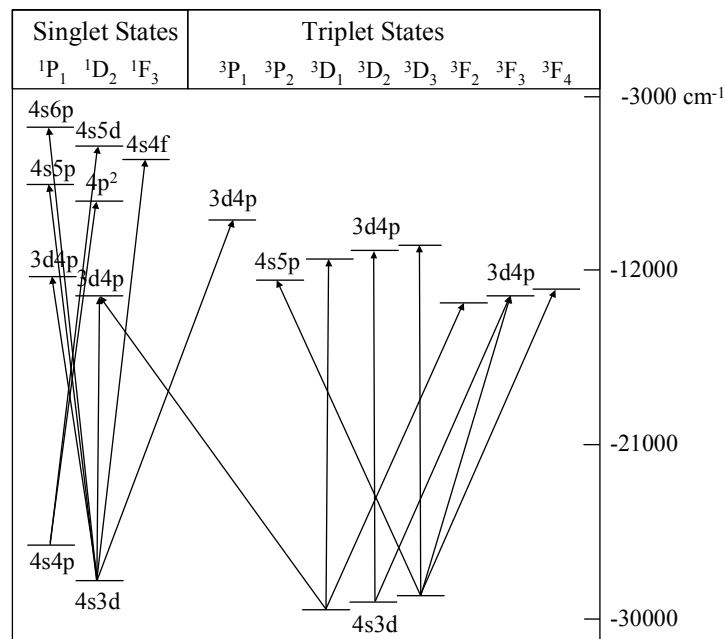


Figure 3-3. Mid-level electronic energy states of atomic calcium. Transitions studied by Smith and Raggett [47] are noted.

Giles and Lewis revisited the  $4s^2\ ^1S_0 \rightarrow 4s4p\ ^1P_1$  transition in 1982 and studied the broadening and shifting of this line and other higher level transitions by argon. Again, the absorption profiles of these transitions were measured against a broadband source using a monochromater. Their line broadening and shifting rates are converted to

cross section by Equations 2-79 and 2-80 and included in Tables 3-1 and 3-2 [18]. In 1985, Devdariani *et al.* published theoretical line broadening and shifting cross sections for this transition perturbed by helium and neon. Their results are directly reproduced in Tables 3-1 and 3-2 [8].

Next, Harris *et al.* studied the broadening of this transition perturbed by helium, neon, argon, krypton, and xenon in 1986 using laser spectroscopy. Their work is significant because it is the first reported atomic calcium line broadening experiment using the laser-induced fluorescence of a transition. This technique is superior to broadband absorption because the line broadening introduced by monochromators is eliminated. Their line broadening rates are converted to cross section by Equation 2-79 and displayed in Table 3-1 [21].

Spielfiedel *et al.* published theoretical calculations in 1991 of the broadening of the atomic calcium  $4s4p\ ^3P_{0,1,2} \rightarrow 4s5s\ ^3S_1$  transitions perturbed by hydrogen. This work is noteworthy because it indicates a line broadening dependence on the total angular momentum quantum number of the initial state  $J''$ . This trend, however, is not linear in  $J''$ . Since this work only reports perturbations by a non-noble gas, the line broadening rates are not converted to cross section and included here for comparison [48].

And finally, Röhe-Hansen and Helbig studied the  $4s^2\ ^1S_0 \rightarrow 4s4p\ ^3P_1$  transition broadened by helium, neon, and argon in 1992 using Doppler-free laser spectroscopy [43]. Crane *et al.* also studied this transition perturbed by neon and argon in 1994 using a new, indirect technique of determining the Lorentzian linewidth [6]. Since this transition is analogous to the strontium  $5s^2\ ^1S_0 \rightarrow 5s5p\ ^3P_1$  transition studied in this research, the results of both groups are presented in Table 3-1. The line broadening rates of Röhe-



Hansen and Helbig are converted to cross section by Equation 2-79 while the cross sections published by Crane *et al.* are reproduced directly.

In summary, all previous experimental atomic calcium line broadening and shifting work involving transitions within a multiplet have indicated there is no dependence of the line broadening rate on the total angular momentum quantum number  $J$  of either the initial or final states. Furthermore, the theoretical work involving calcium transitions within a multiplet does not definitively predict such a dependence. Line broadening and shifting rates have been measured for the calcium  $4s^2\ ^1S_0 \rightarrow 4s4p\ ^3P_1$  and  $4s4p\ ^3P_{0,1,2} \rightarrow 4s5s\ ^3S_1$  transitions which are analogous to the strontium transitions studied in this research. The calcium line broadening data in the  $4s4p\ ^3P_{0,1,2} \rightarrow 4s5s\ ^3S_1$  transitions indicate neon, not helium, produces the least amount of line broadening. Also, helium induces a positive line shift (to the blue) in this transition while neon and argon induce a negative shift.

**3.1.2 Atomic Strontium** The line perturbations and difference potentials of this atom are less researched than those of atomic calcium. Nevertheless, these aspects of atomic strontium are studied for many of the same reasons. In reviewing the literature, it appears the primary reason for studying line perturbations in atomic strontium is to validate interaction potentials calculated by theoretical physicists [19]. Also, many researchers who performed these experiments on atomic calcium also performed them on atomic strontium for comparison.

Farr and Hindmarsh performed the first study of the line broadening and shifting of an atomic strontium transition in recent times. In 1971, they investigated the strong  $5s^2\ ^1S_0 \rightarrow 5s5p\ ^1P_1$  transition (see Figure 3-4) at  $21698.482\text{ cm}^{-1}$  (460.9 nm) perturbed by

helium and argon using the absorption of a broadband optical source and a spectrograph. In addition to publishing line broadening and shifting rates for this transition, they use them to determine the difference potential between the lower and upper states. Their line broadening and shifting rates are converted to cross section by Equations 2-79 and 2-80 and presented in Tables 3-5 and 3-6. The difference potential constants  $C_6$  and  $C_{12}$  are presented in Tables 3-7 and 3-8 [12].

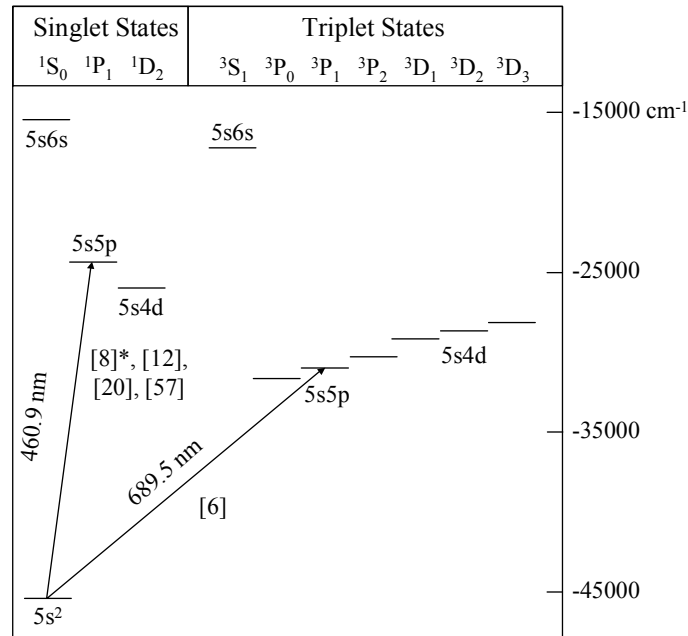


Figure 3-4. Lower electronic energy states of atomic strontium. Transitions studied previously are referenced. The asterisk indicates theoretical work.

In 1974, Shabanova computed theoretical strontium difference potential constants  $C_6$  and  $C_{12}$  for the energy states connected by the  $5s^2 \ ^1S_0 \rightarrow 5s5p \ ^1P_1$  transition perturbed by helium, neon, argon, and krypton. His results are reproduced in Tables 3-7 and 3-8 [45]. Wang and Ch'en repeated the experiment of Farr and Hindmarsh on this transition

Table 3-5. Line broadening cross sections of atomic strontium transitions perturbed by helium, neon, argon, and xenon reported by previous researchers. The cross sections of Farr and Hindmarsh [12] and Wang and Ch'en [57] are determined from their published line broadening rates using Equation 2-79. The asterisk indicates theoretical work.

	He	Ne	Ar	Xe
	Broadening Cross Section ( $10^{-14} \text{ cm}^2$ )	Broadening Cross Section ( $10^{-14} \text{ cm}^2$ )	Broadening Cross Section ( $10^{-14} \text{ cm}^2$ )	Broadening Cross Section ( $10^{-14} \text{ cm}^2$ )
$5s^2 \ ^1S_0 \rightarrow 5s5p \ ^1P_1 \ (21698.482 \text{ cm}^{-1})$				
[12]	0.627(0.014)	-	1.69(0.04)	-
[57]	0.96	-	3.0	5.4
[20]	1.17(0.10)	1.35(0.15)	-	-
[8]*	0.98	1.65	-	-
$5s^2 \ ^1S_0 \rightarrow 5s5p \ ^3P_1 \ (14504.351 \text{ cm}^{-1})$				
[6]	-	0.98(0.12)	1.52(0.18)	-

Table 3-6. Line shifting cross sections of atomic strontium transitions perturbed by helium, neon, argon, and xenon reported by previous researchers. The cross sections of Farr and Hindmarsh [12] and Wang and Ch'en [57] are determined from their published line shifting rates using Equation 2-80. The asterisk indicates theoretical work.

	He	Ne	Ar	Xe
	Shifting Cross Section ( $10^{-14} \text{ cm}^2$ )	Shifting Cross Section ( $10^{-14} \text{ cm}^2$ )	Shifting Cross Section ( $10^{-14} \text{ cm}^2$ )	Shifting Cross Section ( $10^{-14} \text{ cm}^2$ )
$5s^2 \ ^1S_0 \rightarrow 5s5p \ ^1P_1 \ (21698.482 \text{ cm}^{-1})$				
[12]	0.00(0.03)	-	-2.0(0.1)	-
[57]	0.1	-	-2.5	-1.3
[8]*	-0.18	-0.73	-	-

in 1979, except they recorded absorption profiles at extremely high pressures and extended the set of perturbing species to include xenon. Their line broadening and shifting rates are converted to cross section by Equations 2-79 and 2-80 and presented in Tables 3-5 and 3-6. They also perform difference potential calculations with their line broadening and shifting rates. These results are presented in Tables 3-7 and 3-8 [57].

Table 3-7. Difference potential constant  $C_6$  for the atomic strontium  $5s^2\ ^1S_0$  and  $5s5p\ ^1P_1$  energy states perturbed by helium, neon, argon, krypton, and xenon reported by previous researchers. The asterisk indicates theoretical work.

	He	Ne	Ar	Kr	Xe
	$C_6$ ( $10^{-58}$ erg cm <sup>6</sup> )	$C_6$ ( $10^{-58}$ erg cm <sup>6</sup> )	$C_6$ ( $10^{-58}$ erg cm <sup>6</sup> )	$C_6$ ( $10^{-58}$ erg cm <sup>6</sup> )	$C_6$ ( $10^{-58}$ erg cm <sup>6</sup> )
[12]	1.06(0.15)	-	4.3(0.4)	-	-
[45]*	0.26	0.52	2.2	3.2	-
[57]	0.541	-	10.2	-	44.4
[20]	-	-	3.4(1.0)	13(4)	18(5)

Table 3-8. Difference potential constant  $C_{12}$  for the atomic strontium  $5s^2\ ^1S_0$  and  $5s5p\ ^1P_1$  energy states perturbed by helium, neon, argon, krypton, and xenon reported by previous researchers. The asterisk indicates theoretical work.

	He	Ne	Ar	Kr	Xe
	$C_{12}$ ( $10^{-101}$ erg cm <sup>12</sup> )	$C_{12}$ ( $10^{-101}$ erg cm <sup>12</sup> )	$C_{12}$ ( $10^{-101}$ erg cm <sup>12</sup> )	$C_{12}$ ( $10^{-101}$ erg cm <sup>12</sup> )	$C_{12}$ ( $10^{-101}$ erg cm <sup>12</sup> )
[12]	2.5(0.8)	-	1.3(0.3)	-	-
[45]*	0.099	0.081	0.75	2.7	-
[57]	0.426	-	86	988	-
[20]	-	-	0.71(0.50)	5.4(3.0)	8.1(4.0)

Harima *et al.* studied the atomic strontium  $5s^2\ ^1S_0 \rightarrow 5s5p\ ^1P_1$  transition perturbed by helium, neon, argon, krypton, and xenon in 1983. They measured the absorption coefficients of this transition in the far wings and applied the Unified Franck-Condon method of Szudy and Baylis [51] to determine difference potentials directly from the lineshape. This method is fundamentally different from the approach of Hindmarsh and Farr [25] which utilizes both line broadening and shifting rates. Harima *et al.* report line broadening cross sections for this transition perturbed by helium and neon and difference potential constants of the lower and upper states of this transition for argon, krypton, and

xenon. The former results are summarized in Table 3-5 and the latter in Tables 3-7 and 3-8 [20].

In 1985, Devdariani *et al.* published theoretical line broadening and shifting cross sections for this transition perturbed by helium and neon. Their results are directly reproduced in Tables 3-5 and 3-6 [8]. And finally, Crane *et al.* studied the atomic strontium  $5s^2\ ^1S_0 \rightarrow 5s5p\ ^3P_1$  intercombination transition at  $14504.351\text{ cm}^{-1}$  (689.5 nm) perturbed by neon and argon in 1994 using a new, indirect technique of determining the Lorentzian linewidth. The line broadening cross sections of this transition are remeasured in the current research and the results of Crane *et al.* are transcribed in Table 3-5 [6].

In summary, perturbations to the atomic strontium  $5s^2\ ^1S_0 \rightarrow 5s5p\ ^1P_1$  transition have been fairly well researched. While difference potential constants exist for the lower and upper states perturbed by helium, neon, argon, krypton, and xenon, there is no data in the literature on the line broadening and shifting rates of this transition perturbed by krypton. There has been only one previous study of the  $5s^2\ ^1S_0 \rightarrow 5s5p\ ^3P_1$  intercombination transition and in this case, only the line broadening was examined and no difference potential work was performed. No previous line perturbation or difference potential work has been accomplished on the  $5s5p\ ^3P_{0,1,2} \rightarrow 5s6s\ ^3S_1$  transitions around  $14534\text{ cm}^{-1}$  (688 nm). The current research explores this multiplet in an effort to address this shortcoming.

**3.1.3 Atomic Barium** Of the three atoms reviewed in this chapter, barium has the least amount of previous line perturbation or difference potential work accomplished on it. Like calcium and strontium, studies of atomic barium transitions are motivated by

interest in the long range forces between atoms. Recent experiments and theoretical work on this element have served to quantify the nature of these interactions. Also, barium has the potential for use as a narrow-band blocking filter for laser radars [34].

Shabanova's theoretical work in 1974 included a calculation of the difference potential constants  $C_6$  and  $C_{12}$  for the  $6s^2\ ^1S_0$  and  $6s6p\ ^1P_1$  energy states of atomic barium (see Figure 3-5) perturbed by helium, neon, argon, and krypton. His results are presented in Tables 3-9 and 3-10 [45]. This work is followed in 1985 by the work of Devdariani *et al.* who published theoretical line broadening and shifting cross sections for the atomic barium  $6s^2\ ^1S_0 \rightarrow 6s6p\ ^1P_1$  transition at  $18060.264\text{ cm}^{-1}$  (553.7 nm) perturbed by helium and neon. Their results are directly reproduced in Tables 3-11 and 3-12 [8].

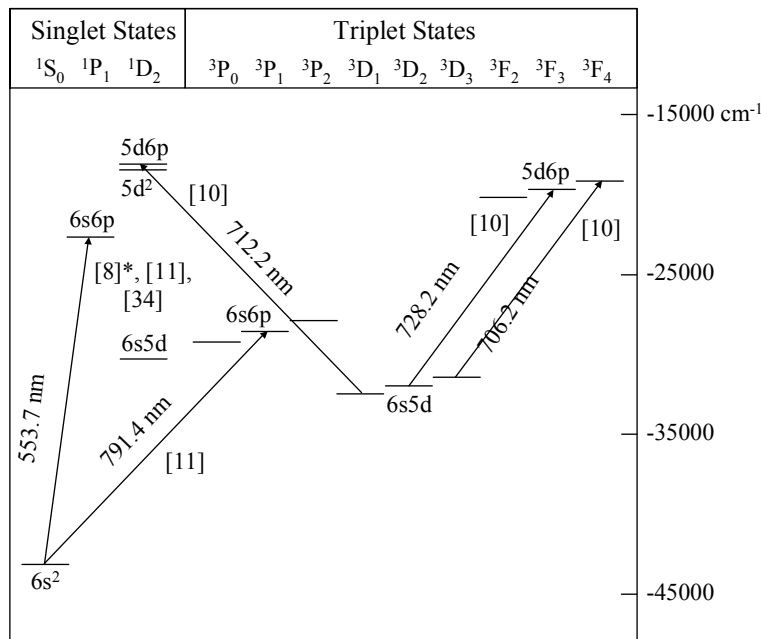


Figure 3-5. Lower electronic energy states of atomic barium. Transitions studied previously are referenced. The asterisk indicates theoretical work.

Table 3-9. Theoretical difference potential constant  $C_6$  for the atomic barium  $6s^2\ ^1S_0$  and  $6s6p\ ^1P_1$  energy states perturbed by helium, neon, argon, and krypton reported by Shabanova [45].

He	Ne	Ar	Kr
$C_6$ ( $10^{-58}$ erg cm <sup>6</sup> )	$C_6$ ( $10^{-58}$ erg cm <sup>6</sup> )	$C_6$ ( $10^{-58}$ erg cm <sup>6</sup> )	$C_6$ ( $10^{-58}$ erg cm <sup>6</sup> )
0.20	0.40	1.7	2.8

Table 3-10. Theoretical difference potential constant  $C_{12}$  for the atomic barium  $6s^2\ ^1S_0$  and  $6s6p\ ^1P_1$  energy states perturbed by helium, neon, argon, and krypton reported by Shabanova [45].

He	Ne	Ar	Kr
$C_{12}$ ( $10^{-101}$ erg cm <sup>12</sup> )	$C_{12}$ ( $10^{-101}$ erg cm <sup>12</sup> )	$C_{12}$ ( $10^{-101}$ erg cm <sup>12</sup> )	$C_{12}$ ( $10^{-101}$ erg cm <sup>12</sup> )
0.11	0.043	0.42	1.6

Table 3-11. Line broadening cross sections of atomic barium transitions perturbed by helium, neon, and argon reported by previous researchers. All cross sections except those of Devdariani [8] are determined from their published line broadening rates using Equation 2-79. The asterisk indicates theoretical work.

	He	Ne	Ar
	Broadening Cross Section ( $10^{-14}$ cm <sup>2</sup> )	Broadening Cross Section ( $10^{-14}$ cm <sup>2</sup> )	Broadening Cross Section ( $10^{-14}$ cm <sup>2</sup> )
$6s^2\ ^1S_0 \rightarrow 6s6p\ ^1P_1$ ( $18060.264\text{ cm}^{-1}$ )			
[8]*	0.99	1.66	-
[34]	2.4(0.2)	-	7.0(0.7)
[11]	0.93(0.29)	-	2.4(0.6)
$6s5d\ ^3D_1 \rightarrow 5d6p\ ^1D_2$ ( $14040.431\text{ cm}^{-1}$ )			
[10]	0.889(0.074)	-	2.14(0.16)
$6s5d\ ^3D_2 \rightarrow 5d6p\ ^3F_3$ ( $13731.920\text{ cm}^{-1}$ )			
[10]	0.873(0.076)	-	2.20(0.18)
$6s5d\ ^3D_3 \rightarrow 5d6p\ ^3F_4$ ( $14160.526\text{ cm}^{-1}$ )			
[10]	0.882(0.081)	-	2.37(0.19)
$6s^2\ ^1S_0 \rightarrow 6s6p\ ^3P_1$ ( $12636.616\text{ cm}^{-1}$ )			
[11]	1.03(0.09)	-	1.53(0.14)

Table 3-12. Line shifting cross sections of atomic barium transitions perturbed by helium, neon, and argon reported by previous researchers. All cross sections except those of Devdariani [8] are determined from their published line shifting rates using Equation 2-80. The asterisk indicates theoretical work.

	He	Ne	Ar
	Shifting Cross Section ( $10^{-14} \text{ cm}^2$ )	Shifting Cross Section ( $10^{-14} \text{ cm}^2$ )	Shifting Cross Section ( $10^{-14} \text{ cm}^2$ )
$6s^2 \text{ } ^1\text{S}_0 \rightarrow 6s6p \text{ } ^1\text{P}_1$ (18060.264 $\text{cm}^{-1}$ )			
[8]*	-0.15	-0.57	-
$6s5d \text{ } ^3\text{D}_1 \rightarrow 5d6p \text{ } ^1\text{D}_2$ (14040.431 $\text{cm}^{-1}$ )			
[10]	0.44(0.07)	-	-1.92(0.19)
$6s5d \text{ } ^3\text{D}_2 \rightarrow 5d6p \text{ } ^3\text{F}_3$ (13731.920 $\text{cm}^{-1}$ )			
[10]	0.34(0.07)	-	-2.01(0.18)
$6s5d \text{ } ^3\text{D}_3 \rightarrow 5d6p \text{ } ^3\text{F}_4$ (14160.526 $\text{cm}^{-1}$ )			
[10]	0.34(0.07)	-	-1.74(0.19)
$6s^2 \text{ } ^1\text{S}_0 \rightarrow 6s6p \text{ } ^3\text{P}_1$ (12636.616 $\text{cm}^{-1}$ )			
[11]	0.17(0.08)	-	-0.98(0.21)

The first modern experimental paper on line perturbations in atomic barium was published by Kuchta *et al.* in 1990. They performed a Doppler-free laser spectroscopy experiment on barium and report the line broadening rates of the  $6s^2 \text{ } ^1\text{S}_0 \rightarrow 6s6p \text{ } ^1\text{P}_1$  transition perturbed by helium and argon. Their results are converted to cross section by Equation 2-79 and displayed in Table 3-11 [34]. Ehlacher and Huennekens followed this work in 1992 by performing laser absorption experiments on the  $6s5d \text{ } ^3\text{D}_1 \rightarrow 5d6p \text{ } ^1\text{D}_2$  at 14040.431  $\text{cm}^{-1}$  (712.2 nm),  $6s5d \text{ } ^3\text{D}_2 \rightarrow 5d6p \text{ } ^3\text{F}_3$  at 13731.920  $\text{cm}^{-1}$  (728.2 nm), and  $6s5d \text{ } ^3\text{D}_3 \rightarrow 5d6p \text{ } ^3\text{F}_4$  at 14160.526  $\text{cm}^{-1}$  (706.2 nm) transitions of atomic barium perturbed by helium and argon. They report both line broadening and shifting rates for these transitions and their results are converted to cross section by Equations 2-79 and 2-80 and presented in Tables 3-11 and 3-12 [10]. And finally, in 1993 Ehlacher and



Huennekens performed a similar experiment on the  $6s^2\ ^1S_0 \rightarrow 6s6p\ ^1P_1$  and  $6s^2\ ^1S_0 \rightarrow 6s6p\ ^3P_1$  at  $12636.616\text{ cm}^{-1}$  (791.4 nm) transitions perturbed by helium and argon. These results are converted to cross section by Equations 2-79 and 2-80 and presented in Tables 3-11 and 3-12 [11].

In summary, there has been relatively little experimental or theoretical work on line perturbations or difference potentials of atomic barium. In particular, the  $6s6p\ ^3P_{0,1,2} \rightarrow 6s7s\ ^3S_1$  multiplet, which is analogous to the strontium transitions studied in this research, has not been studied. As such, no conclusions can be drawn from atomic barium about the dependence of line perturbations on the total angular momentum quantum number  $J$  of either the initial or final state of a transition. The only barium work which is directly comparable to this research is the line broadening and shifting work of Ehrlacher and Huennekens on the intercombination transition  $6s^2\ ^1S_0 \rightarrow 6s6p\ ^3P_1$ . This corresponds directly to the atomic strontium  $5s^2\ ^1S_0 \rightarrow 5s5p\ ^3P_1$  transition which is also examined in this research.

### 3.2 Line Broadening in Diatomic Species

Line broadening in diatomic species has been studied for two primary reasons. The first is its important role in remote sensing applications; especially in diagnosing the conditions of the atmosphere from space. In this case, trace atmospheric molecules, like carbon monoxide and hydroxyl, are examples of the species of interest [42, 40]. The second reason is basic science. As discussed in the previous chapter, line broadening is caused, in part, by inelastic collisions. Investigations into the line broadening rates of molecules perturbed by buffer gases give insight into the kinetics of these systems.

After reviewing the literature, it is clear that a considerable amount of research has been accomplished on the broadening of infrared spectral lines in light diatomic molecules. While little research has been accomplished on heavier species, none has been performed on the broadening of diatomic bismuth lines. In the remainder of this chapter, four previous diatomic line broadening studies are summarized. These include line broadening in Br<sub>2</sub>, O<sub>2</sub>, NO, and CO. In particular, the dependence of the line broadening cross section on rotational level is highlighted.

In 1976, Innes *et al.* studied the broadening of diatomic bromine lines by argon. These researchers performed an absorption experiment using a broadband light source and recorded P and R branch lines ranging from  $J'' = 20$  to  $J'' = 80$  in the  $v'' = 1 \rightarrow v' = 19$  vibrational manifold of the Br<sub>2</sub>  $X^1\Sigma_g^+ \rightarrow B^3\Pi_{O_u^+}$  electronic transition. This work is significant because, like the current study, it involves a large number of heavy diatomic rotational levels perturbed by a noble gas. They report no dependence of the line broadening rate on branch or on total angular momentum quantum number  $J''$  of the initial state. Their line broadening rate is converted to total cross section by Equation 2-104 and has a value of  $3.00(0.41) \times 10^{-14} \text{ cm}^2$  [28].

Another work of interest is the study of line broadening in the O<sub>2</sub> A band and NO fundamental band performed by Pope in 1998. In this work, absorption spectroscopy using a broadband infrared source and a Fourier transform spectrometer was used to measure the pressure broadening rates of nearly all the observable spectral lines in the respective bands broadened by helium, neon, argon, and krypton. His results for O<sub>2</sub> and NO are converted to total cross section by Equation 2-104 and plotted in Figures 3-6 and

3-7 respectively. They are displayed as functions of the branch-independent quantum number  $m$ ; which is  $-J''$  for the P branch and  $J''+1$  for the R branch [1]. Although  $O_2$  and NO are relatively light molecules compared to  $Bi_2$ , this work is relevant because of its comprehensiveness and because it showcases the trend of decreasing line broadening cross section with increasing total angular momentum quantum number  $J''$  of the initial state in both branches for all perturbing species [41].

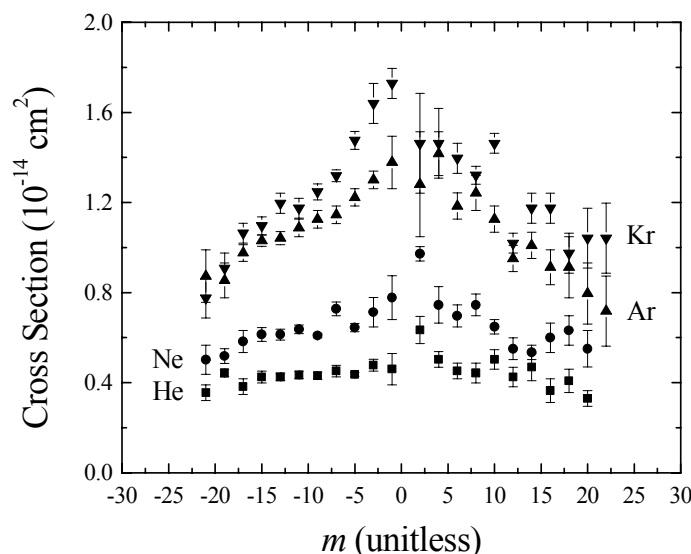


Figure 3-6. Line broadening cross sections of the  $O_2$  A band perturbed by helium, neon, argon, and krypton as a function of the branch-independent quantum number  $m$ . These cross sections are determined from the data reported by Pope [41] using Equation 2-104.

The last work chosen for summary is a study of the carbon monoxide fundamental band by Luo *et al.* in 2001. These researchers performed a laser absorption experiment on the P and R branch lines of this band perturbed by helium and argon. Their results are converted to total cross section by Equation 2-104 and plotted in Figure 3-8 as functions

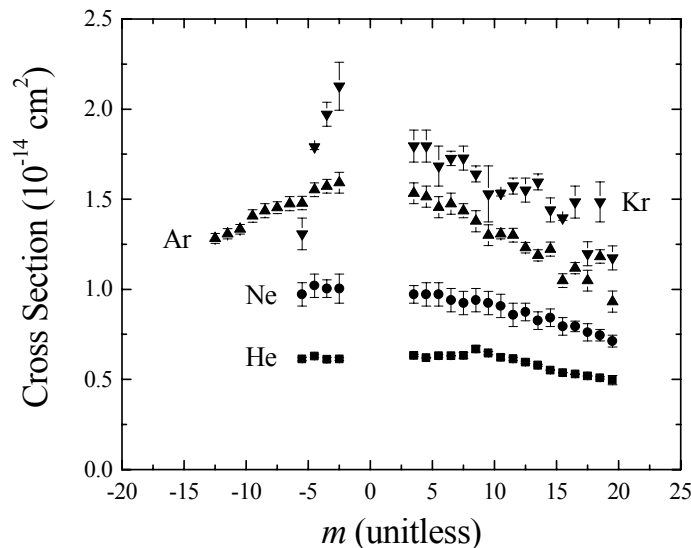


Figure 3-7. Line broadening cross sections of the NO fundamental band perturbed by helium, neon, argon, and krypton as a function of the branch-independent quantum number  $m$ . These cross sections are determined from the data reported by Pope [41] using Equation 2-104.

of the branch-independent quantum number  $m$ . As with Pope's data, this research exhibits the trend of increasing broadening cross section with decreasing total angular momentum quantum number  $J''$  of the initial state in both branches and for both perturbing species. This dependence, however, is much less pronounced in helium than in argon [36].

In summary, the line broadening cross section of light molecules perturbed by noble gases appears to depend on the total angular momentum quantum number  $J''$  of the initial state. Specifically, this cross section appears to rise with decreasing  $J''$ . There is currently no theoretical explanation for this behavior found in the literature. While this trend appears in light molecules, it disappears in at least one heavy diatomic:  $\text{Br}_2$ . The

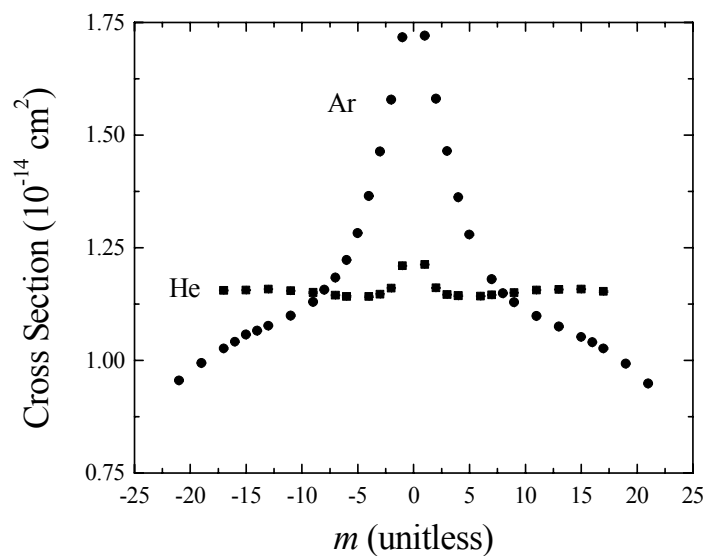


Figure 3-8. Line broadening cross sections of the CO fundamental band perturbed by helium and argon as a function of the branch-independent quantum number  $m$ . These cross sections are determined from the data reported by Luo *et al.* [36] using Equation 2-104.

current research investigates line broadening in another heavy diatomic molecule,  $\text{Bi}_2$ , to discover if this lack of trend is characteristic of heavy species.

## IV. Broadening and Shifting of Atomic Strontium Spectral Lines

Broadening and shifting of the atomic strontium  $5s^2\ ^1S_0 \rightarrow 5s5p\ ^3P_1$  and  $5s5p\ ^3P_{0,1,2} \rightarrow 5s6s\ ^3S_1$  transitions by noble gases were investigated using absorption spectroscopy. This chapter discusses the details of this experiment and what was learned from it. It is split into three sections. The first covers the design of the experiment, data acquisition and reduction details, results, and sources of error. The second provides an analysis of the data and includes a comparison with previous research. And finally, the last section draws conclusions from the analysis and makes recommendations for future research.

### 4.1 Measurement of Atomic Strontium Spectral Line Profiles

Lineshape profiles of the atomic strontium  $5s^2\ ^1S_0 \rightarrow 5s5p\ ^3P_1$  and  $5s5p\ ^3P_{0,1,2} \rightarrow 5s6s\ ^3S_1$  transitions perturbed by the nobles gases helium, neon, argon, krypton, and xenon were observed using the absorption of a narrowband tunable laser. The laser, being monochromatic compared to the frequency range of the transition, offered a direct means of observing the absorption profile. The first part of this section compares standard absorption spectroscopy with another similar technique and derives the equation necessary for reducing the data generated during this experiment. The second describes the experimental apparatus. The next three subsections discuss data acquisition and reduction details and results, and the final subsection discusses possible sources of systematic error.

#### 4.1.1 Absorption Spectroscopy Using a Narrowband Source

Absorption spectroscopy using a narrowband source is perhaps the most direct and intuitive way of observing the lineshape function of a transition. By this technique, a monochromatic tunable source is directed through a medium and the intensity observed upon exit. As the frequency of the source is tuned across a transition, the absorption in the medium is given by the Lambert-Beer Law [7].

$$I(x) = I_0(x)e^{-\alpha(x)} \quad (4-1)$$

$I_0(x)$  is the intensity of the light incident upon the medium at wavenumber  $x$ ,  $I(x)$  is the intensity of light exiting the medium, and  $\alpha(x)$  is the absorbance. The absorbance depends on many things, the most intuitive of which is the path length the light travels through the medium.

Although direct absorption spectroscopy using a narrowband source may be the most obvious way to observe a line profile, it is not the only technique available. In recent years, polarization spectroscopy has gained popularity as a means of observing spectral lines free of Doppler broadening. This technique uses a circularly polarized laser pump beam to selectively saturate a transition thereby making the medium birefringent to a linearly polarized probe beam. The degree of birefringence is directly proportional to the saturation of the medium making this technique a type of saturation spectroscopy. Furthermore, the pump and probe beams are counter-propagating, which allows for absorption only by velocity-specific ensembles of bodies. That is, because of the Doppler effect, only absorbing bodies with velocity vectors transverse to the pump and probe beams yield a signal. Therefore, the line profile is Doppler free [7].

While polarization spectroscopy may be an ideal experimental technique for some investigations and has the added appeal of being Doppler free, it was not suitable for this research because of the properties of the atomic strontium energy states involved. In polarization spectroscopy, the pump beam, with a circular polarization of  $\sigma^+$  or  $\sigma^-$ , induces transitions according to the selection rule  $\Delta J_m = \pm 1$ , where  $J_m$  is the projection of the total angular momentum quantum number  $J$  onto an arbitrary axis and takes on the values  $-J, -J+1, \dots, +J$ . The initial state is therefore depleted of bodies with particular values of  $J_m$  causing the linearly polarized probe beam, which is equal parts left and right-hand circular polarized, to be preferentially absorbed of light with the opposite circular polarization. This birefringence causes a rotation in the plane of the linearly polarized probe beam, which can be detected if the beam is observed through a linear polarizer [7]. However, this technique only works for  $J \geq 1$  because there must be more than one initial state to absorb the circularly polarized light causing the medium to become birefringent. When  $J = 0$ , the only state available to absorb light is the  $J_m = 0$  state, which is saturated by the pump beam leaving the probe beam with nothing to observe. In this research, two of the four transitions observed, the  $5s^2\ ^1S_0 \rightarrow 5s5p\ ^3P_1$  and the  $5s5p\ ^3P_0 \rightarrow 5s6s\ ^3S_1$  transitions, have  $J = 0$ . Therefore, polarization spectroscopy was not a viable option.

When studying spectral line profiles by standard absorption spectroscopy, the absorbance's dependence on wavenumber is the feature of interest. Absorbance can be written as the product of three terms.

$$\alpha(x) = N_j \ell \sigma_{abs}(x) \quad (4-2)$$



where  $N_j$  is the density of bodies through which the light travels in the lower quantum state  $j$ ,  $\ell$  is path length, and  $\sigma_{abs}(x)$  is the absorption cross section. The absorption cross section can be expanded as

$$\sigma_{abs}(x) = \left( \frac{1}{8\pi} \right) A_{kj} \left( \frac{g_k}{g_j} \right) \left( \frac{1}{x_0^2} \right) \left( \frac{1}{c} \right) f(x) \quad (4-3)$$

where  $A_{kj}$  is the Einstein  $A$  coefficient of the transition,  $g_j$  and  $g_k$  are the degeneracies of the lower and upper states respectively,  $x_0$  is the center wavenumber of the transition, and  $f(x)$  is the lineshape function. The lineshape function as expressed above is given per unit frequency and therefore has units of length when wavenumbers are used.

Solving for the lineshape function  $f(x)$ , Equations 4-3, 4-2, and 4-1 are combined to give

$$f(x) = \left( \frac{8\pi}{N_j \ell} \right) \left( \frac{c x_0^2}{A_{kj}} \right) \left( \frac{g_j}{g_k} \right) \ln \left( \frac{I_0(x)}{I(x)} \right) \quad (4-4)$$

Thus the lineshape function is a series of constants times the natural log of the ratio of the incident light intensity to the transmitted light intensity [7]. This is the fundamental equation used to process the raw data from this experiment.

**4.1.2 Atomic Strontium Experimental Setup** The experimental apparatus was designed to create a strontium vapor, mix it with a buffer gas, and record the transition profiles of interest as they were perturbed by the buffer gas. Strontium is a solid at room temperature so vapor was created in a tube furnace. The  $5s^2 \ ^1S_0 \rightarrow 5s5p \ ^3P_1$  transition at  $14504.351 \text{ cm}^{-1}$  (689.4 nm) was observed at a furnace temperature of 455 C. The  $5s5p \ ^3P_{0,1,2} \rightarrow 5s6s \ ^3S_1$  transitions at  $14721.275 \text{ cm}^{-1}$  (679.3 nm),  $14534.444 \text{ cm}^{-1}$  (688.0 nm),

and  $14140.232\text{ cm}^{-1}$  (707.2 nm) respectively were observed at a furnace temperature of 1200 C. The remainder of this section details the experimental apparatus and discusses the signal-to-noise ratios of the atomic strontium transitions observed with it.

A schematic diagram of the experimental apparatus is given in Figure 4-1. A Coherent 899-21 ring laser was configured in dye mode and pumped with a Spectra Physics model 2080 argon ion laser lasing at 488 and 514.5 nm simultaneously. The ring laser used Exciton dye LDS 698 (Pyradine 1), which lases between  $12821$  and  $14925\text{ cm}^{-1}$  (780 and 670 nm), along with a combination of Pyradine 2 and DCM Special optics. The argon ion laser power output was approximately 7 W and the ring laser output was between 100 and 200 mW. This quantity varied depending on the alignment of the optics, the condition of the dye, and the wavelength to which the laser was tuned. As will be discussed later, this power level was reduced considerably for application in this experiment. The ring laser was integrated with a wavemeter for frequency control and the system was operated by computer, which was also used to record experimental data. The ring laser center frequency was controlled to within  $0.0017\text{ cm}^{-1}$  (50 MHz) and the linewidth was nominally less than  $0.000033\text{ cm}^{-1}$  (1.0 MHz).

To create an atomic strontium vapor, several grams of strontium granules (Aldrich, 99%) were placed inside quartz tubes that were heated by a Lindberg model 55342-4 hinged tube furnace. The quartz tubes were 1.83 m long and 3.8 cm in diameter. They were specially manufactured for this work (Quartz Scientific) and lined with tantalum foil (ESPI, 3 mils, 99%) to prevent strontium from reacting with quartz. They were also manufactured with openings at each end for connection to a gas handling system. The heated length of the tube furnace was 0.76 m which allowed 0.54 m of

quartz tube to protrude from each end. The experiment was designed this way for two reasons. First, the tube had to be connected to a gas handling system and it was not possible to do this inside the furnace. Second, the windows at the ends of the tube needed to be away from the strontium vapor so as not to be degraded by it. Consequently, the strontium vapor created in the center of the tube diffused to the cool ends and plated out on the cell walls.

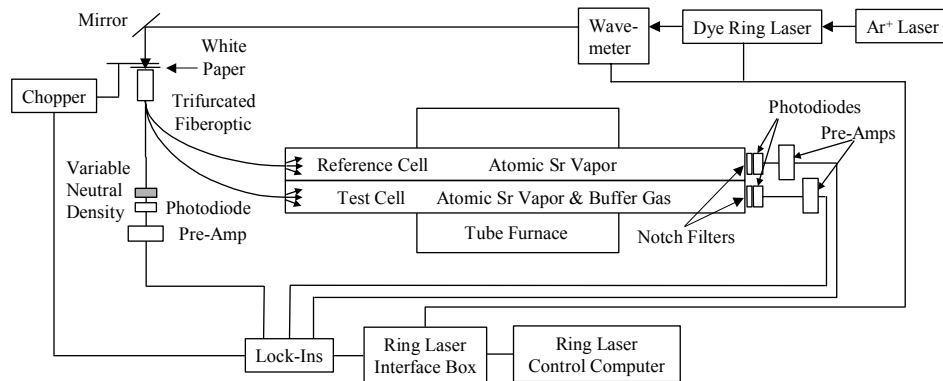


Figure 4-1. Schematic diagram of the atomic strontium absorption experimental apparatus

Two tubes were employed side by side in the furnace during each data run. One was kept at constant pressure while the pressure in the other was varied to bring about the line broadening and shifting effects. This provided a constant frequency reference by which to observe line shifting. The tube furnace temperature could be varied between ambient temperature and 1200 C and held constant.

In order to avoid interference effects, diffuse light rather than the coherent collimated light exiting the dye laser was used. Towards this end, the ring laser beam

was directed onto a piece of white paper. A trifurcated fiber optic cable was placed on the reverse side of the paper and the light split into three roughly equal parts. One part was used, in conjunction with a variable neutral density filter to avoid detector saturation, to monitor the laser intensity as a function of wavenumber. The second part was used on the quartz tube held at constant pressure; hereafter called the reference cell. And the third part was used on the quartz tube with varying pressure; hereafter called the test cell.

All three signals were monitored by identical Hamamatsu type S2281 silicon photodiodes. The two photodiodes used to monitor the reference and test cells were covered with notch filters (Corion P70-700-F) which passed light between 13596 and 15449  $\text{cm}^{-1}$  (735.5 and 647.3 nm). This was to reduce signal generated by the heat of the tube furnace. The dye laser source beam was chopped by a Stanford Research Systems model SR540 chopper operating at 330 Hz immediately before it was incident on the white paper. The detector signals were sent to three independent battery operated pre-amps and then to three Stanford Research Systems model SR850 lock-in amplifiers set to the chopping frequency. The signal outputs from the lock-ins were sent to the laser control computer where they were digitized and stored as the laser was scanned.

Both the test cell and the reference cell were evacuated by a Varian SD-300 roughing pump. This achieved a pressure on the order of  $10^{-3}$  Torr before the data acquisition process was begun. Pressure in the reference cell was monitored by an MKS Baratron capacitance manometer that was sensitive to 100 Torr. Pressure in the test cell was monitored by an MKS Baratron capacitance manometer that was sensitive to just over 1000 Torr. Signals from both devices were conditioned by type 270 MKS Baratron signal conditioners. The signal conditioners were zeroed after the system was baked out

and allowed to pump down for several hours. Because the strontium was observed to plate out on the cool interior cell walls outside the furnace, pressure registered by the manometers was buffer gas pressure only.

As mentioned previously, the atomic strontium  $5s^2\ ^1S_0 \rightarrow 5s5p\ ^3P_1$  transition was observed at a furnace temperature of 455 C. At this temperature, the signal-to-noise ratio of the line profile ranged from approximately 20:1 to 3:2 during the course of the experiment. The  $5s5p\ ^3P_{0,1,2} \rightarrow 5s6s\ ^3S_1$  transitions were observed at a furnace temperature of 1200 C. At this temperature, the signal-to-noise ratios of the line profiles ranged from approximately 70:1 to 5:1 during the course of the experiment. This difference in signal-to-noise ratios is explained as follows.

The absorption signals observed in this experiment are the products of three competing factors: absorption cross section, vapor pressure of atomic strontium in the absorption cell, and fraction of strontium atoms in the initial state of the transition. The absorption cross section can be calculated from Equation 4-3. For an unbroadened transition, the line profile is assumed to be Gaussian and the lineshape function  $f(x)$  takes the form of Equation 2-57. With the furnace temperatures given above, all quantities are known and the absorption cross section at line center can be computed. These numbers are presented in Table 4-1. The atomic strontium  $5s5p\ ^3P_{0,1,2} \rightarrow 5s6s\ ^3S_1$  transition absorption cross sections are two to three orders of magnitude larger than those of the  $5s^2\ ^1S_0 \rightarrow 5s5p\ ^3P_1$  transition.

The next factor to be considered is the vapor pressure of atomic strontium created in the absorption cells by heating solid strontium. For the  $5s^2\ ^1S_0 \rightarrow 5s5p\ ^3P_1$  transition,

Table 4-1. Absorption cross sections at line center of the atomic strontium transitions studied in this research. These cross sections are computed from Equation 4-3 assuming a Gaussian line profile with the appropriate temperature and using the transition emission intensities listed in Table 2-3.

Transition	Cross Section ( $10^{-14} \text{ cm}^2$ )
$5s^2 \ ^1S_0 \rightarrow 5s5p \ ^3P_1$	2.850
$5s5p \ ^3P_0 \rightarrow 5s6s \ ^3S_1$	356.3
$5s5p \ ^3P_1 \rightarrow 5s6s \ ^3S_1$	1127
$5s5p \ ^3P_2 \rightarrow 5s6s \ ^3S_1$	1875

strontium granules were heated to 455 C, which is well below the strontium melting point of 777 C. For a system in equilibrium, the vapor pressure of atomic strontium at this temperature is on the order of  $10^{-4}$  Torr. For the  $5s5p \ ^3P_{0,1,2} \rightarrow 5s6s \ ^3S_1$  transitions, strontium granules were heated to 1200 C, which exceeds the strontium melting point and approaches its boiling point of 1382 C. In this case, the atomic strontium vapor pressure is reported to be on the order of  $10^2$  Torr for a system in equilibrium [35]. The experimental apparatus for this research, as described above, was an open system in which a strontium vapor was continuously created and lost. As such, there was a non-uniform vapor density across the heated cell length which never reached equilibrium. In this situation, the true atomic strontium vapor pressures are thought to have been lower than predicted above. However, the relative pressures should have been at least approximately correct. Therefore, the atomic strontium vapor pressure for the  $5s5p \ ^3P_{0,1,2} \rightarrow 5s6s \ ^3S_1$  transitions observed at 1200 C is estimated to have been six orders of magnitude larger than the atomic strontium vapor pressure for the  $5s^2 \ ^1S_0 \rightarrow 5s5p \ ^3P_1$  transition observed at 455 C.

And finally, the third factor governing the absorption signal is the fraction of strontium atoms in the initial state of the transition. According to the Boltzmann distribution, the fraction of atoms in an excited state  $j$  compared to the ground state is

$$\frac{N_j}{N_0} = \frac{2J_j + 1}{2J_0 + 1} e^{\frac{-\Delta E}{k_B T}} \quad (4-5)$$

where  $N_0$  and  $N_j$  are the number densities of atoms in the ground and excited states respectively,  $J_0$  and  $J_j$  are the total angular momentum quantum numbers of the ground and excited states respectively, and  $\Delta E$  is the energy difference of the excited state above the ground state [52]. Inserting the appropriate quantities for the  $5s5p \ ^3P_{0,1,2}$  energy states into Equation 4-5 ( $\Delta E$  is computed from the values presented in Table 2-2) gives numbers on the order of  $10^{-6}$  compared to the ground  $5s^2 \ ^1S_0$  state. Therefore, the  $5s5p \ ^3P_{0,1,2}$  energy levels were only sparsely populated compared to the ground state.

The results presented above are combined as follows to predict the difference in absorption signals between the atomic strontium  $5s5p \ ^3P_{0,1,2} \rightarrow 5s6s \ ^3S_1$  transitions and the  $5s^2 \ ^1S_0 \rightarrow 5s5p \ ^3P_1$  transition. According to Table 4-1, the absorption cross sections of the  $5s5p \ ^3P_{0,1,2} \rightarrow 5s6s \ ^3S_1$  transitions are two to three orders of magnitude larger than the  $5s^2 \ ^1S_0 \rightarrow 5s5p \ ^3P_1$  transition. The vapor pressure is estimated to have been six orders of magnitude larger for the  $5s5p \ ^3P_{0,1,2} \rightarrow 5s6s \ ^3S_1$  transitions than for the  $5s^2 \ ^1S_0 \rightarrow 5s5p \ ^3P_1$  transition because of the higher oven temperature. And finally, the Boltzmann factor reduces the number of atoms available for the  $5s5p \ ^3P_{0,1,2} \rightarrow 5s6s \ ^3S_1$  transitions by six orders of magnitude. Taken together, the absorption of the  $5s5p \ ^3P_{0,1,2} \rightarrow 5s6s \ ^3S_1$  transitions is predicted to be two to three orders of magnitude larger than the absorption

of the  $5s^2\ ^1S_0 \rightarrow 5s5p\ ^3P_1$  transition. While this difference in signal is much larger than what was actually observed, it does support the observation that the signal-to-noise ratios of the  $5s5p\ ^3P_{0,1,2} \rightarrow 5s6s\ ^3S_1$  transitions were larger than the signal-to-noise ratios of the  $5s^2\ ^1S_0 \rightarrow 5s5p\ ^3P_1$  transition.

**4.1.3 Atomic Strontium Data Acquisition** The data acquisition phase of this experiment involved preparing a strontium vapor with the test cell under noble gas pressure and recording a transition profile. The ring laser was set to scan one wavenumber (30 GHz) across the atomic strontium transitions of interest with the line profile roughly centered in the scan. This scan length was a compromise between the need to scan as far out into the line wings as possible and the dissipative nature of the experiment. Once the tube furnace was elevated to a temperature which generated a high absorption signal without making the medium opaque (between 80 and 90% absorption), data acquisition proceeded until the absorption signal had declined to approximately 10 to 20%. The signal was generally considered unusable when the signal-to-noise ratio dropped below one. This loss of signal over time was caused by the fact that the test and reference cells were longer than the tube furnace allowing the strontium to diffuse to the cool ends and plate out on the cell walls. At this point the apparatus was cooled, cleaned, and reloaded with strontium.

Each experimental run took between 30 and 45 minutes before strontium was depleted. This time is understood in terms of the diffusion coefficient of the atomic strontium/buffer gas mixture and its impact on the diffusion time for atomic strontium to travel the half-length of the absorption cell. According to Steinfeld *et al.* [49], the diffusion time,  $t$ , for a body to travel a distance  $d$  in a cylinder is given by



$$t = \frac{3d^2}{4D} \quad (4-6)$$

The diffusion coefficient  $D$  is known to be

$$D = \frac{3\langle v \rangle}{32N\sigma^2} \quad (4-7)$$

where  $\langle v \rangle$  is the average relative velocity between the diffusing body and the buffer gas,  $N$  is the total number density of the diffusing body/buffer gas combination, and  $\sigma$  is the collision diameter of the diffusing body/buffer gas pair. Furthermore, The average relative velocity is

$$\langle v \rangle = \sqrt{\frac{8k_B T}{\pi\mu}} \quad (4-8)$$

where  $\mu$  is the reduced mass of the diffusing body/buffer gas pair. Therefore, given the temperature and density of the system and the masses and radii of the diffusing body/buffer gas pair, the diffusion coefficient and diffusion time can be calculated.

The diffusion coefficients and diffusion times for typical sets of experimental conditions are computed from Equations 4-7, 4-6, and 4-8 and reported in Table 4-2. This computation is performed for two cases. The first case is for the atomic strontium  $5s^2\ ^1S_0 \rightarrow 5s5p\ ^3P_1$  transition perturbed by a typical neon pressure when the oven temperature was 455 C. The second case is for the atomic strontium  $5s5p\ ^3P_1 \rightarrow 5s6s\ ^3S_1$  transition perturbed by a typical krypton pressure when the oven temperature was 1200 C. The distance  $d$  is assumed to be half the heated length of the absorption cells, which was 38 cm. The number density of atomic strontium is computed from the vapor pressure of strontium given as a function of temperature in the *CRC Handbook of*

*Chemistry and Physics* [35]. Collision diameters are computed from the atomic strontium radius given by Brown *et al.* ( $r_{Sr} = 2.15 \text{ \AA}$ ) [4] and the noble gas radii given by Hirschfelder *et al.* ( $r_{Ne} = 1.412 \text{ \AA}$ ,  $r_{Kr} = 1.81 \text{ \AA}$ ) [26].

Table 4-2. Diffusion coefficients and diffusion times for typical experimental conditions of this research. The diffusion time is the time required for atomic strontium in the vapor phase to travel 38 cm, which was half the length of the absorption cells.

Atomic Strontium Vapor Pressure [35] (Torr)	Buffer Gas Pressure (Torr)	Diffusion Coefficient (cm <sup>2</sup> /sec)	Diffusion Time (minutes)
$5s^2\ ^1S_0 \rightarrow 5s5p\ ^3P_1$ Perturbed by Neon (455 C)			
$8.30 \times 10^{-4}$	0	$4.47 \times 10^5$	$4.04 \times 10^{-5}$
	199.9	2.70	6.68
$5s5p\ ^3P_1 \rightarrow 5s6s\ ^3S_1$ Perturbed by Krypton (1200 C)			
200	29.0	3.38	5.34
	152.0	2.20	8.21

According to Table 4-2, the diffusion coefficient is very large and the diffusion time short when no buffer gas is present. This situation, however, changes dramatically with the addition of even a modest amount of buffer gas. For the  $5s5p\ ^3P_1 \rightarrow 5s6s\ ^3S_1$  transition, 29.0 Torr of krypton reduces the diffusion coefficient and raises the diffusion time to over five minutes. Further addition of buffer gas continues to reduce the diffusion coefficient and raise the diffusion time. Therefore, as the experiment began, atomic strontium quickly diffused to the cool ends of the absorption cell where it was lost. However, with a fresh supply of strontium in the absorption cell, the absorption signal remained high. As the experiment progressed, the strontium supply was depleted, yet the decreasing diffusion coefficient, caused by the addition of buffer gas, allowed the signal to remain measurable. The data acquisition phase of this experiment was, therefore, a

balance between a decreasing supply of strontium in the absorption cell and an increasing buffer gas pressure. Taken together, these effects allowed for data acquisition over a 30 to 45 minute time frame.

The ring laser control computer was set to collect a data point from each of the three lock-in amplifiers every  $0.00083\text{ cm}^{-1}$  (25 MHz). This led to the acquisition of 1200 data points across the transition. A one-wavenumber scan was completed in one minute which resulted in a scan rate of  $0.017\text{ cm}^{-1}$  (0.50 GHz) per second. This combination of data interval and scan rate meant that a data point was taken every 50 ms. To accommodate this interval, the lock-in time constants were set to 10 ms.

During the  $5s^2\ ^1S_0 \rightarrow 5s5p\ ^3P_1$  data acquisition, the reference cell was left at zero Torr. However, for the  $5s5p\ ^3P_{0,1,2} \rightarrow 5s6s\ ^3S_1$  data acquisition, the reference cell was back-filled with about 30 Torr of buffer gas to prolong the absorption signal. Although this shifted the transition line center, pressure was not changed during the experiment and this line center remained a fixed reference. The test cell was filled to various pressures of noble gases and a test cell and reference cell data set were collected simultaneously.

Table 4-3 details the data acquisition matrix of the entire strontium experiment. The first column indicates the noble gas used to perturb the transition. The second column gives the temperature at which the tube furnace was set for that noble gas. The third column gives the pressure to which the reference cell was backfilled and held. The subsequent columns give the discrete pressures to which the test cell was filled for that data point.

The number of data points taken ranged between four and eight depending on the signal intensity and how long it lasted. The range of pressures varied widely depending

Table 4-3. Atomic strontium data acquisition matrix. This table gives the noble gas pressures and oven (tube furnace) temperatures at which the atomic strontium transitions were observed in the test and reference cells.

	Oven Temp (C)	Ref Cell (Torr)	Test Cell (Torr)							
$5s^2\ ^1S_0 \rightarrow 5s5p\ ^3P_1$ (14504.351 cm <sup>-1</sup> )										
He	455	0	0	249.8	499.6	748.7	1003.3	-	-	-
Ne	455	0	0	100.3	199.9	299.9	400.2	-	-	-
Ar	475	0	0	200.4	401.9	600.4	800.4	-	-	-
Kr	455	0	0	75.0	150.3	224.9	300.3	-	-	-
Xe	455	0	0	75.1	150.1	225.1	300.1	-	-	-
$5s5p\ ^3P_0 \rightarrow 5s6s\ ^3S_1$ (14721.275 cm <sup>-1</sup> )										
He	1200	20.3	19.5	74.4	100.5	139.2	181.7	219.9	-	-
Ne	1200	30.5	30.1	60.1	90.2	119.9	150.1	199.8	249.8	300.1
Ar	1200	20.9	20.3	40.1	66.5	80.0	100.5	119.9	140.0	180.0
Kr	1200	33.4	30.2	59.7	86.7	121.1	147.5	179.9	-	-
Xe	1200	29.9	29.9	59.8	89.8	120.1	150.2	180.0	209.8	239.8
$5s5p\ ^3P_1 \rightarrow 5s6s\ ^3S_1$ (14534.444 cm <sup>-1</sup> )										
He	1200	23.6	22.1	61.1	103.3	140.8	178.2	-	-	-
Ne	1200	35.6	32.5	63.9	93.0	122.4	151.9	179.7	-	-
Ar	1200	30.5	23.1	68.8	124.9	160.6	-	-	-	-
Kr	1200	29.5	29.0	64.8	109.6	152.0	201.7	260.7	-	-
Xe	1200	33.9	28.7	64.7	83.3	104.2	-	-	-	-
$5s5p\ ^3P_2 \rightarrow 5s6s\ ^3S_1$ (14140.232 cm <sup>-1</sup> )										
He	1200	20.5	20.5	52.1	100.0	150.1	200.7	-	-	-
Ne	1200	39.9	29.0	70.9	101.7	160.8	214.3	252.6	304.9	454.4
Ar	1200	32.3	27.9	64.6	103.4	150.0	210.5	253.3	-	-
Kr	1200	34.5	33.8	71.2	93.2	120.2	150.6	180.3	213.0	243.6
Xe	1200	38.7	37.3	61.0	101.4	153.2	203.7	250.9	303.4	353.1

on how much the signal strength was suppressed with the addition of noble gas. For the  $5s^2\ ^1S_0 \rightarrow 5s5p\ ^3P_1$  transition, over 1000 Torr of helium was added yet the signal strength remained high enough to record a viable profile. In contrast, for the  $5s5p\ ^3P_1 \rightarrow 5s6s\ ^3S_1$  transition, only about 100 Torr of xenon was added before the signal became unusable.

An example of raw experimental data is given in Figure 4-2. It shows the reference cell signal, test cell signal, and laser power for the atomic strontium  $5s5p\ ^3P_0 \rightarrow 5s6s\ ^3S_1$  transition at  $14721.275\text{ cm}^{-1}$  perturbed by argon. The reference cell was kept at 20.9 Torr and the test cell was at 140.0 Torr. The signal strength from the three detectors was read into the computer in discreet increments ranging from 0 to 4095. The absorption dips are visible, but obscured somewhat by the discontinuity at about  $14721.41\text{ cm}^{-1}$ . This discontinuity was caused by the fact that the ring laser scans in  $0.33\text{ cm}^{-1}$  ( $10\text{ GHz}$ ) increments and concatenates subsequent scans to cover the desired range. The power output of the ring laser was often variable across the  $0.33\text{ cm}^{-1}$  scan length and from scan to scan causing a distortion in the absorption signal. This distortion, however, is normalized out by Equation 4-4.

**4.1.4 Atomic Strontium Data Reduction** All data taken as described in the previous section was reduced according to Equation 4-4. That is, the test and reference cell absorbances were computed to be the natural logarithm of the ratio of the laser power to the cell signal strength. The data in Figure 4-2 is reduced in this manner and presented in Figure 4-3. These lineshape functions were then smoothed out using a Fourier filter. It was found that the application of the Fourier filter reduced the noise in the absorbance without removing or altering fundamental information extracted from these curves.

The reference cell line profiles were fit to the Voigt lineshape function given by Equation 2-69 using the nonlinear least squares fitting algorithm offered in a program called PeakFit v4.0 (Jandel) [29]. Each fit provided the following parameters: signal strength, line center, Gaussian linewidth, and Lorentzian linewidth along with statistical estimates of their uncertainties. Also, each parameter was allowed to float during the fit.

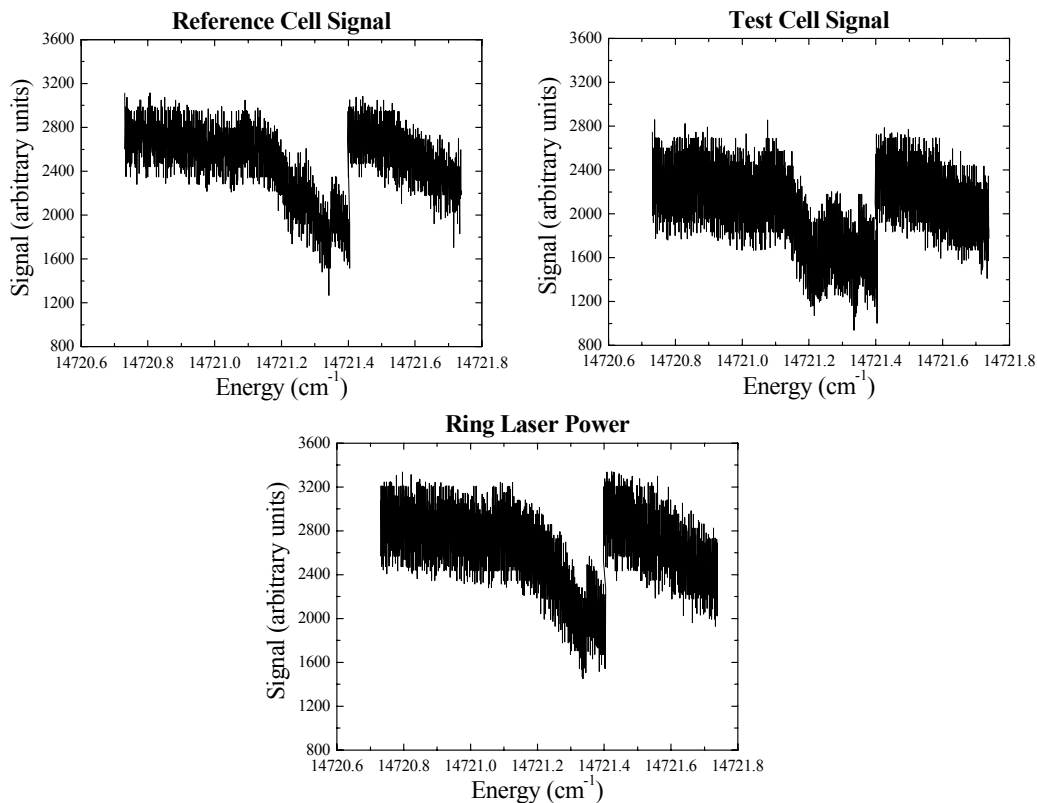


Figure 4-2. Raw data of the atomic strontium  $5s5p\ ^3P_0 \rightarrow 5s6s\ ^3S_1$  transition at  $14721.275\text{ cm}^{-1}$  perturbed by argon. The reference cell was backfilled with 20.9 Torr of argon to stabilize the signal while the test cell contained 140.0 Torr of argon.

Three of these four parameters were used for specific purposes. The line center was used as a fixed reference point by which to gauge the line center shift in the test cell. The Gaussian linewidth in the reference cell was used to determine temperature. The purpose of this was to fix the Gaussian linewidth when the test cell data was fit. And finally, since the pressure in the reference cell was fixed, the standard deviation in the Lorentzian linewidths measured in the reference cell was used to establish the relative uncertainty in the Lorentzian linewidth of the reference cell [3]. This relative uncertainty was then applied to the Lorentzian linewidths measured in the test cell.

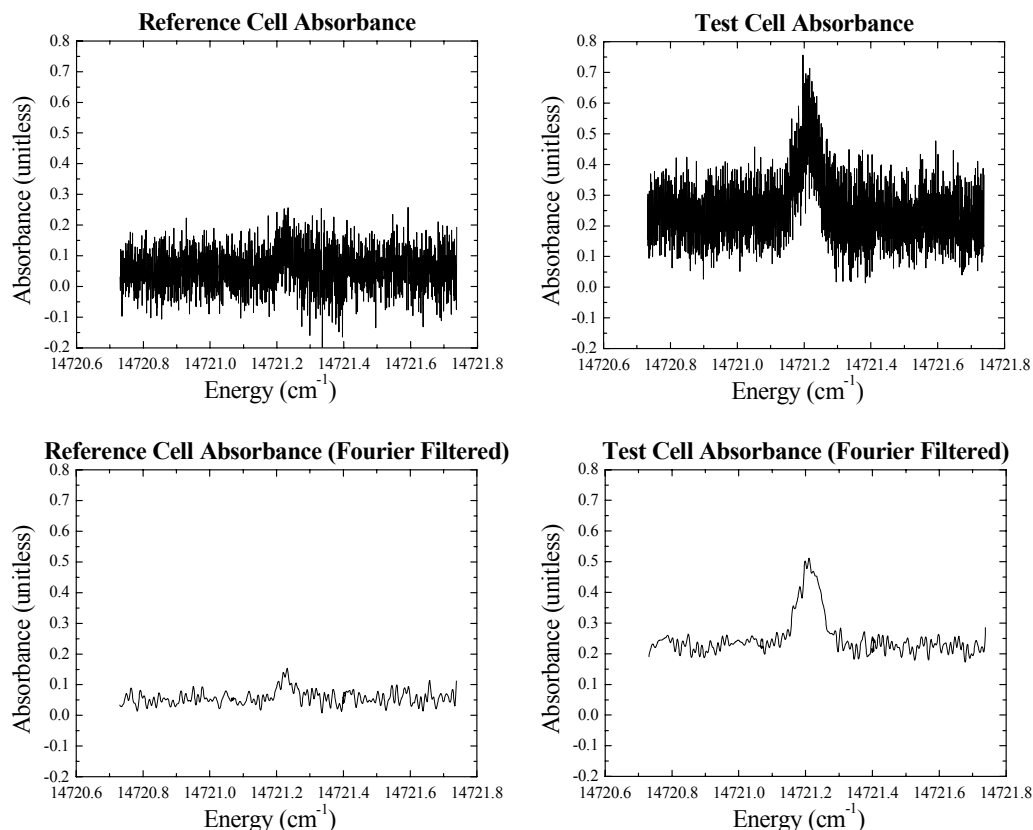


Figure 4-3. Absorbances of the atomic strontium  $5s5p\ ^3P_0 \rightarrow 5s6s\ ^3S_1$  transition at  $14721.275\text{ cm}^{-1}$  perturbed by argon before and after Fourier filtering. The filtering algorithm reduced the noise in the data without removing fundamental information about the lineshape.

In order to use the temperatures determined from the Gaussian linewidths in the reference cell and apply them to the fits in the test cell, the temperatures were assumed to be the same in both. This assumption was verified by first fitting both the reference and test cell atomic strontium line profiles to Voigt lineshape functions allowing all parameters to float. The temperatures determined from the Gaussian linewidths using Equation 2-58 were then compared between the two. The atomic strontium  $5s^2\ ^1S_0 \rightarrow 5s5p\ ^3P_1$  transition perturbed by argon represents a typical case. All five spectral line

profiles from both the reference and test cells were fit to Voigt lineshape functions allowing all parameters to float. In the reference cell, the temperature was determined to be 616(72) K, while in the test cell it was determined to be 690(256) K. In both cases, the uncertainty in the temperature was determined from the standard deviation of the Gaussian linewidths [3]. These two values lie within the uncertainty estimates of each other. In another typical case, the atomic strontium  $5s5p\ ^3P_0 \rightarrow 5s6s\ ^3S_1$  transition perturbed by krypton gave a reference cell temperature of 1008(97) K and a test cell temperature of 1062(74) K with the uncertainty determined as before. Again, these two values lie within the uncertainty estimates of each other. Therefore, the assumption that the reference and test cell temperatures are the same was verified.

The temperature inside the reference and test cells was determined by Equation 2-58 from the average Gaussian linewidth of all peaks fit from the reference cell during a single run of the experiment. Figure 4-4 shows a comparison of the temperature derived this way with the thermocouple readings of the tube furnace. The abscissa is simply run number and has no physical significance. The temperatures from the ground state to triplet state experiment are the five data points at the left when the tube furnace temperature was much lower. The remaining 15 data points at the right are temperatures from the triplet-to-triplet state runs when the tube furnace was set to its maximum temperature. As before, the uncertainty in the temperature was determined from the standard deviation of the Gaussian widths while the thermocouple readings were assumed to be exact. In most cases the thermocouple temperature was within the experimental uncertainty of the temperature determined from the Gaussian linewidths of the reference cell peaks. This gave further confidence that the temperature derived from the average



Gaussian linewidths in the reference cell furnished a reasonable Gaussian linewidth to be used in analyzing the test cell data.

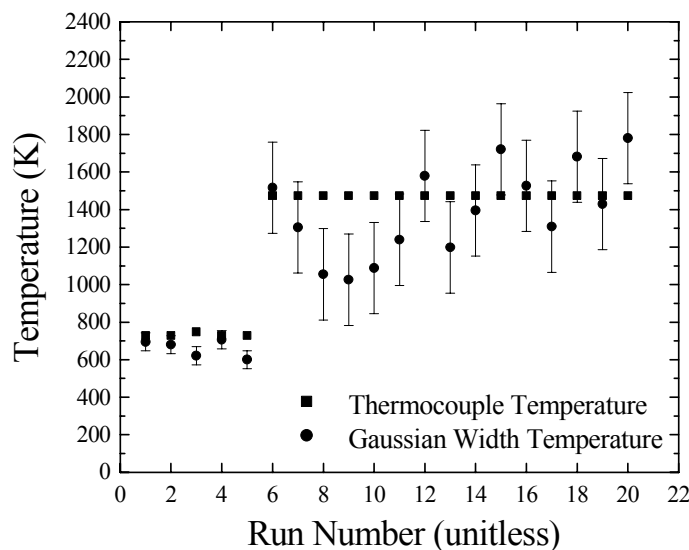


Figure 4-4. Comparison of the tube furnace temperatures as determined from the Gaussian linewidths of the reference cell with the temperatures registered by the tube furnace thermocouple. The thermocouple temperatures fall within the Gaussian width temperature uncertainty most of the time.

Test cell line profiles were fit to the Voigt lineshape function and all parameters except the Gaussian linewidth were allowed to float freely. The Gaussian linewidths were fixed to the temperatures derived from the reference cell data as described above. This meant that a different linewidth, each corresponding to the temperatures shown in Figure 4-4, was computed for each noble gas. Continuing with the example featured in Figures 4-2 and 4-3, Figure 4-5 shows the reference and test cell line profiles fit in this manner with the residuals of the fit displayed beneath each. The residuals appear random which gives confidence that the Voigt lineshape function is a good model of the observed

line profile. Although the reference cell signal was weak in this example, it provided a sufficient reference from which to measure the test cell line center shift.

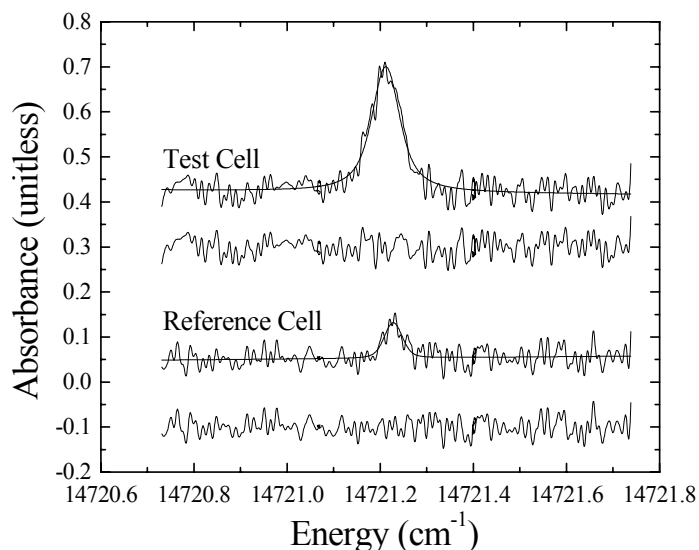


Figure 4-5. Line profiles of the atomic strontium  $5s5p\ ^3P_0 \rightarrow 5s6s\ ^3S_1$  transition at  $14721.275\text{ cm}^{-1}$  perturbed by argon and fit to Voigt lineshape functions. Residuals of the fit are displayed beneath each profile. The test cell data and residuals are displaced upward and the reference cell residuals downward for clarity.

The unbroadened atomic strontium  $5s^2\ ^1S_0 \rightarrow 5s5p\ ^3P_1$  transition exhibited features due to the hyperfine structure of  $^{87}\text{Sr}$  as predicted in Chapter II. That is, the asymmetry in the line wings of this transition depicted in Figure 2-14 was noticeable in the experimental data with no perturbing species present. However, these features merged into a single line profile with the addition of buffer gas to the absorption cell.

To determine if this asymmetry had a significant impact on the Lorentzian linewidth and line center, the unperturbed line profiles were fit to three Voigts to account for the hyperfine structure of  $^{87}\text{Sr}$ . All parameters were allowed to float with the

restriction that the three Gaussian linewidths be equal and the three Lorentzian linewidths be equal. The results of this fit overlaid with the experimental data are presented in Figure 4-6 and give a Lorentzian linewidth of  $0.00552(0.00043) \text{ cm}^{-1}$  and line center of  $14504.35130(0.00005) \text{ cm}^{-1}$ . Next, the same profile was fit to a single Voigt lineshape function again allowing all parameters to float. The results of this fit overlaid with the experimental data are presented in Figure 4-7 and give a Lorentzian linewidth of  $0.00568(0.00042) \text{ cm}^{-1}$  and a line center of  $14504.35140(0.00004) \text{ cm}^{-1}$ . The uncertainties associated with these values are the statistical uncertainties of the nonlinear fit. Therefore, the two results are not statistically different from each other. Thus the asymmetry in the line profile of the atomic strontium  $5s^2 \text{ } ^1\text{S}_0 \rightarrow 5s5p \text{ } ^3\text{P}_1$  transition due to hyperfine structure had no significant impact on the Lorentzian linewidth or line center. It was therefore possible to fit all atomic strontium  $5s^2 \text{ } ^1\text{S}_0 \rightarrow 5s5p \text{ } ^3\text{P}_1$  transition profiles to a single Voigt yielding an accurate Lorentzian linewidth and line center.

According to the theoretical line profile presented in Figure 2-15, the atomic strontium  $5s5p \text{ } ^3\text{P}_1 \rightarrow 5s6s \text{ } ^3\text{S}_1$  transition should exhibit a significant asymmetry in the left wing due to the isotope shift of  $^{86}\text{Sr}$ . However, Figure 4-8, which shows the experimental data for this transition perturbed by 22.1 Torr of helium, fails to corroborate this feature. That is, the isotope shift of  $^{86}\text{Sr}$  reported by Barsanti *et al.* [2] was not observed in this research. Therefore, a single Voigt profile was used to fit the line profiles of this transition.

All line profiles were analyzed by fitting a single Voigt lineshape function to the absorbance profiles. As an example, Figure 4-9 shows a plot of the Lorentzian linewidth and line center shift as a function of test cell pressure for the  $5s5p \text{ } ^3\text{P}_0 \rightarrow 5s6s \text{ } ^3\text{S}_1$

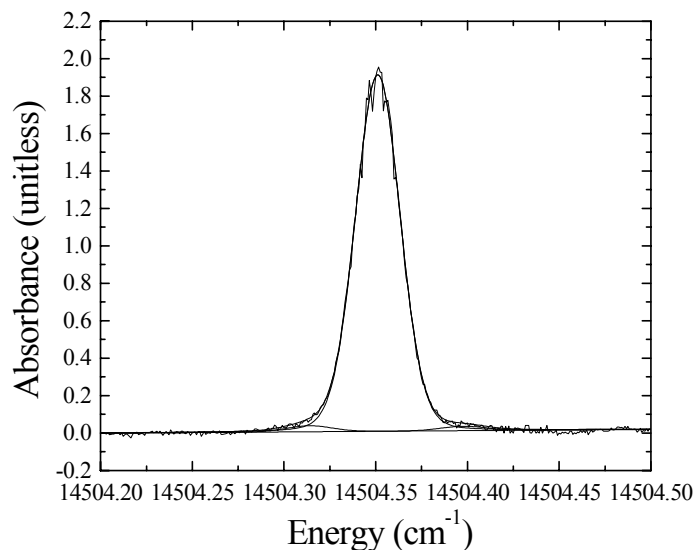


Figure 4-6. Unperturbed line profile of the atomic strontium  $5s^2\ ^1S_0 \rightarrow 5s5p\ ^3P_1$  transition at  $14504.351\text{ cm}^{-1}$  fit to three Voigt lineshape functions. This was to account for the asymmetry in the wings due to hyperfine structure. The Gaussian linewidths were set to be equal as were the Lorentzian linewidths.

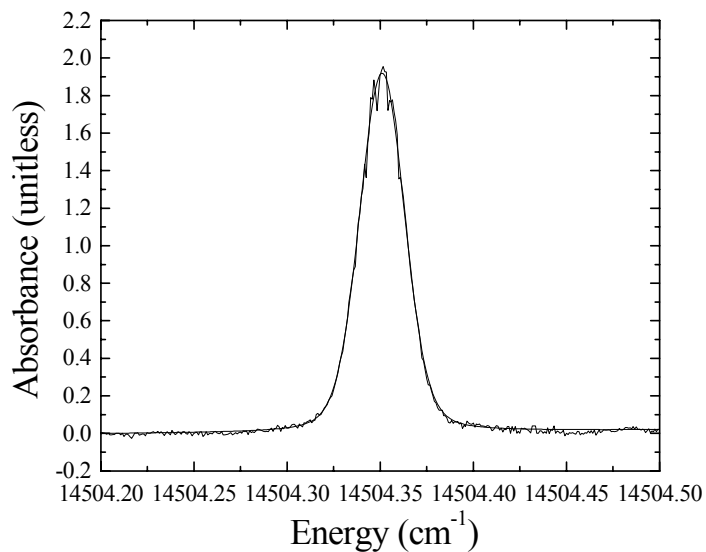


Figure 4-7. Unperturbed line profile of the atomic strontium  $5s^2\ ^1S_0 \rightarrow 5s5p\ ^3P_1$  transition at  $14504.351\text{ cm}^{-1}$  fit to a single Voigt lineshape function. The Lorentzian linewidth determined from this fit are not significantly different than the Lorentzian linewidths of Figure 4-6.

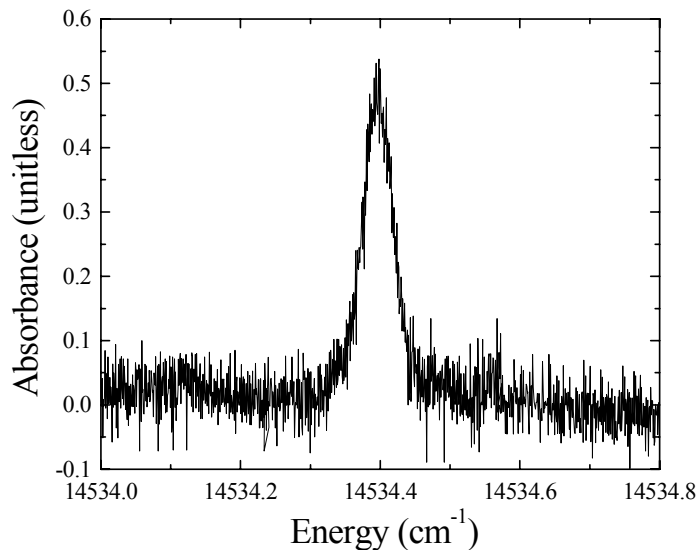


Figure 4-8. Line profile of the atomic strontium  $5s5p\ ^3P_1 \rightarrow 5s6s\ ^3S_1$  transition at  $14534.444\text{ cm}^{-1}$  perturbed by 22.1 Torr of helium. The large asymmetry in the left wing due to  $^{86}\text{Sr}$  reported by Barsanti *et al.* [2] is not observed in this research.

transition perturbed by argon. As stated previously, the uncertainty in the Lorentzian linewidth was assumed to be the standard deviation of the Lorentzian linewidths observed in the reference cell. The uncertainty in the line center shift is the square root of the sum of the squares of the statistical uncertainties in the fits giving the reference cell line center and the test cell line center. It is clear that both the Lorentzian linewidth and the line center shift are linear in pressure as predicted by theory and a least-squares fit to a straight line is included in the figure. This linear fit gives the line broadening rate and line shifting rate, which was the objective of the experiment. The line center shift is defined as the test cell line center minus the reference cell line center. Thus a positive shifting rate indicates the line center is shifting to higher energy (blue) with increasing pressure and a negative shifting rate indicates the line center is shifting to lower energy (red).

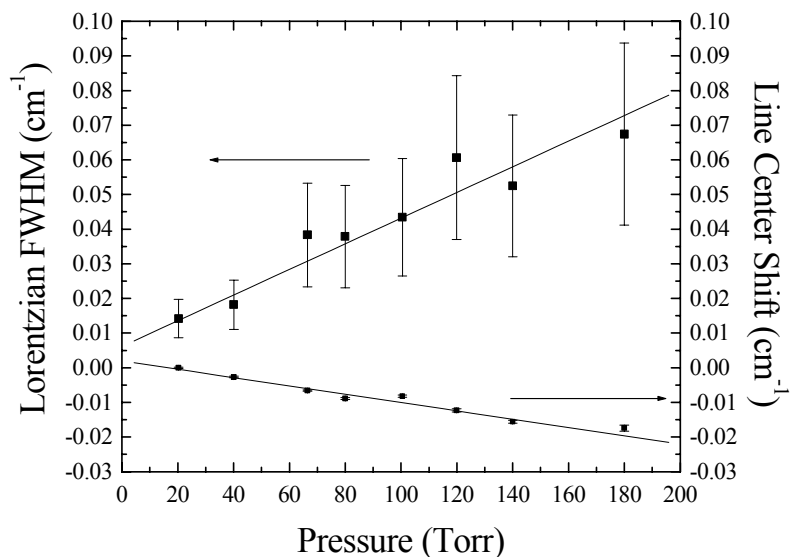


Figure 4-9. Lorentzian linewidths (FWHM) and line center shifts of the atomic strontium  $5s5p\ ^3P_0 \rightarrow 5s6s\ ^3S_1$  transition at  $14721.275\text{ cm}^{-1}$  perturbed by argon as functions of pressure. Linear fits are superimposed.

**4.1.5 Atomic Strontium Experimental Results** Line broadening and shifting rates of the atomic strontium  $5s^2\ ^1S_0 \rightarrow 5s5p\ ^3P_1$  and  $5s5p\ ^3P_{0,1,2} \rightarrow ^3S_1$  transitions perturbed by helium, neon, argon, krypton, and xenon were measured as described in the previous two sections. The results are summarized in Table 4-4. These results are also duplicated in Appendix C, which gives a comprehensive account of all data reported in this dissertation. The uncertainties in these measurements are the uncertainties in the slope parameter of the least-squares fit to a straight line.

**4.1.6 Systematic Errors in the Atomic Strontium Experiment** Up to this point, the only discussion of uncertainty has been in regards to the random errors associated with measuring physical quantities. Indeed, the uncertainty in the test cell Lorentzian linewidths of all transitions measured in the atomic strontium experiment was derived from the standard deviation of the Lorentzian linewidths observed in the

Table 4-4. Line broadening and shifting rates for all atomic strontium transitions and noble gases studied in this research

	Broadening Rate ( $10^{-4} \text{ cm}^{-1}/\text{Torr}$ )	Shifting Rate ( $10^{-5} \text{ cm}^{-1}/\text{Torr}$ )
$5s^2\ ^1S_0 \rightarrow 5s5p\ ^3P_1$ ( $14504.351 \text{ cm}^{-1}$ )		
He	2.53(0.11)	4.09(0.21)
Ne	1.733(0.085)	-2.12(0.14)
Ar	1.636(0.024)	-4.84(0.13)
Kr	2.06(0.10)	-5.09(0.16)
Xe	2.29(0.15)	-5.035(0.097)
$5s5p\ ^3P_0 \rightarrow 5s6s\ ^3S_1$ ( $14721.275 \text{ cm}^{-1}$ )		
He	3.94(0.50)	6.41(0.65)
Ne	1.56(0.30)	-2.49(0.23)
Ar	3.70(0.36)	-12.0(1.0)
Kr	3.48(0.46)	-10.39(0.39)
Xe	3.65(0.11)	-12.334(0.085)
$5s5p\ ^3P_1 \rightarrow 5s6s\ ^3S_1$ ( $14534.444 \text{ cm}^{-1}$ )		
He	4.86(0.28)	5.63(0.54)
Ne	1.63(0.23)	-1.45(0.29)
Ar	3.44(0.50)	-11.135(0.082)
Kr	3.17(0.32)	-9.69(0.64)
Xe	3.90(0.88)	-9.7(1.4)
$5s5p\ ^3P_2 \rightarrow 5s6s\ ^3S_1$ ( $14140.232 \text{ cm}^{-1}$ )		
He	3.64(0.48)	6.88(0.41)
Ne	1.57(0.12)	-1.51(0.10)
Ar	3.13(0.23)	-13.17(0.45)
Kr	3.46(0.23)	-9.33(0.32)
Xe	3.70(0.15)	-12.12(0.38)

reference cell. Since conditions in the reference cell did not change, any deviation in the Lorentzian linewidth was due to random error. This section, however, explores the impact of systematic error on the results presented above.

It is argued that three possible sources of systematic error to the line broadening and shifting rates presented in Table 4-4 did not significantly contribute to the uncertainties reported there. This is mainly because line broadening and shifting rates are ratios of changes in quantities and even if the quantities themselves are inaccurate,

changes should not be. The three possible sources of systematic error considered here include errors in the Gaussian linewidth (or temperature), pressure, and energy calibration. Each is considered separately.

As stated above, the Gaussian linewidths of the Voigt line profiles fit to the test cell data were locked during the fitting process to the average value of the Gaussian linewidths measured in the reference cell. The impact of an inaccurate determination of this linewidth on the Lorentzian linewidth was determined through a sensitivity analysis. That is, for a given set of data, the Gaussian linewidth was varied and the data refit to determine its impact on the Lorentzian linewidth. It was found that although changes in the Gaussian linewidth had an impact on the Lorentzian linewidth (raising the Gaussian linewidth lowered the Lorentzian linewidth and vice versa), there was no significant change to the overall line broadening or shifting rate. In quantitative terms, changing the Gaussian linewidth by 6% had less than a 0.5% impact on the line broadening rate. This is well within the experimental uncertainty previously established for line broadening rate measurements in this research. Also, changing the Gaussian linewidth by 6% had no impact on the line shifting rate. Therefore, systematic errors in the Gaussian linewidth did not contribute significantly to the uncertainty in the atomic strontium line broadening and shifting rates.

The next possible source of systematic error in the line broadening and shifting rates is the measurement of buffer gas pressure. As stated above, buffer gas pressures were measured outside the test and reference cells. Because atomic strontium was observed to have plated out on the interior walls of the absorption cells immediately outside the tube furnace, the capacitance manometers only registered buffer gas pressure.



Any systematic error in this pressure reading would have no impact on the line broadening and shifting rates because these rates only depend on the change in and not the absolute magnitude of the pressure. Therefore, systematic errors in pressure did not contribute to the uncertainty in the atomic strontium line broadening and shifting rates.

The last possible source of systematic error was the energy calibration of the line profiles. The ring laser and its associated control computer were first calibrated to known frequency standards ensuring the atomic strontium transitions were unambiguously identified. Further refinement in the calibration was unnecessary because both the Lorentzian linewidth and the line center shift are changes in energy and not absolute values. Therefore, even if the measured line center did not exactly agree with the currently accepted values for those transitions, the linewidths and shifts were still accurately measured as long as the ring laser changed energy linearly over the transition profile. That is, the absolute values of the energies reported by the ring laser control computer were much less important than linearity of the scan. Since the ring laser was designed to precisely scan ranges of hundreds of wavenumbers, it was believed to be linear over the one wavenumber scan length of this experiment. Therefore, systematic errors in energy calibration did not contribute significantly to the uncertainty in the atomic strontium line broadening and shifting rates.

## **4.2 Analysis of Atomic Strontium Line Broadening and Shifting Rates**

The atomic strontium line broadening and shifting rate measurements described in the previous section are analyzed in this section. It is divided into two parts. The first part converts the line broadening and shifting rates to cross section and compares these

results with those of previous researchers. The second part uses the line broadening and shifting rates to derive the difference potential between the energy states connected by each transition perturbed by the noble gas. These results are then compared to those of previous work.

**4.2.1 Atomic Strontium Line Broadening and Shifting Cross Sections** In this section, the conversion from line broadening and shifting rate to cross section is derived and applied to the data in Table 4-4. These cross sections are then compared to results published by previous authors. First, however, the proper conversion must be determined. According to the theory of Chapter II, there are two ways to convert broadening rate to cross section depending on the type of interaction which occurs between the species of interest and the perturbing species. If elastic collisions dominate, Equation 2-79 is used. If inelastic collisions dominate, Equation 2-104 is used. This distinction is important because these equations differ by a factor of two.

In order to determine which type of collision dominates the interaction of atomic strontium with noble gases, it is first assumed to be inelastic collisions and several line broadening rates in Table 4-4 are converted to sum total quenching rate constants by Equation 2-108. These numbers are then compared to collisional mixing rate constants by helium, neon, and argon in the atomic strontium  $5s5p\ ^3P_{0,1,2}$  multiplet published in 1988 by Kelly *et al.* [31]. The conversion of line broadening rate  $\frac{\Delta(\delta x_L)}{\Delta P}$  to sum total quenching rate constant  $k^q$  is

$$k^q = 2\pi k_B T_C \frac{\Delta(\delta x_L)}{\Delta P} \quad (4-9)$$

This will be formally derived in Chapter V and is given here without proof.

Equation 4-9 is applied to the helium, neon, and argon line broadening rates of the  $5s5p\ ^3P_1 \rightarrow 5s6s\ ^3S_1$  transition given in Table 4-4 and compared to the mixing rate constants of Kelly *et al.* [31] in Table 4-5. The mixing rate constants are very small compared to the line broadening rates indicating that inelastic collisions do not significantly contribute to line broadening. Therefore, elastic collisions must dominate line broadening in atomic strontium and Equation 2-79 is used to convert line broadening rate to cross section. Similarly, Equation 2-80 is used to convert line shifting rate to cross section.

Table 4-5. Comparison of the atomic strontium  $5s5p\ ^3P_1 \rightarrow 5s6s\ ^3S_1$  line broadening sum total quenching rate constant for helium, neon, and argon of this research with the collisional mixing rate constants of the  $5s5p\ ^3P_{0,1,2}$  multiplet published by Kelly *et al.* [31]. The mixing rate constants are very small compared to the sum total quenching rate constants justifying the neglect of inelastic collisions.

	Line Broadening Sum Total Quenching Rate Constant ( $10^{-10}\text{ cm}^3/\text{s}$ )	Mixing Rate Constant $J''=1 \rightarrow J'=0$ ( $10^{-10}\text{ cm}^3/\text{s}$ )	Mixing Rate Constant $J''=1 \rightarrow J'=2$ ( $10^{-10}\text{ cm}^3/\text{s}$ )
He	140(8)	0.042(0.001)	0.056(0.001)
Ne	46.8(6.6)	0.000056(0.000005)	0.000252(0.000010)
Ar	99(14)	0.000038(0.000007)	0.000123(0.000006)

With the proper conversion to cross section established, Equations 2-79 and 2-80 are rewritten in terms of pressure, temperature, and wavenumber. This conversion requires three steps. The first is to write the average relative velocity between the species of interest and the perturbing species in terms of temperature. The second is to convert number density to pressure. And the third is to convert angular frequency to wavenumber.

To start, the relationships between line broadening and shifting rate and cross section given by Equations 2-79 and 2-80 respectively are reproduced below.

$$\frac{\Delta(\delta\omega_L)}{\Delta N} = 2\langle v \rangle \sigma_r \quad (4-10)$$

$$\frac{\Delta(\Delta\omega)}{\Delta N} = \langle v \rangle \sigma_i \quad (4-11)$$

The average relative velocity between the species of interest and the perturbing species is given by Equation 4-8. Number density  $N$  can be related to pressure  $P$  assuming the Ideal Gas Law holds true. Thus

$$\Delta N = \frac{\Delta P}{k_B T} \quad (4-12)$$

And finally, changes in angular frequency are related to changes in wavenumber as follows:

$$\Delta(\delta\omega_L) = 2\pi c \Delta(\delta x_L) \quad (4-13)$$

$$\Delta(\Delta\omega) = 2\pi c \Delta(\Delta x) \quad (4-14)$$

Inserting Equations 4-8, 4-12, 4-13, and 4-14 into Equations 4-10 and 4-11 and solving for cross section gives

$$\sigma_r = \sqrt{\frac{\pi^3 \mu k_B T c^2}{8}} \frac{\Delta(\delta x_L)}{\Delta P} \quad (4-15)$$

and

$$\sigma_i = 2\sqrt{\frac{\pi^3 \mu k_B T c^2}{8}} \frac{\Delta(\Delta x)}{\Delta P} \quad (4-16)$$

Equation 4-15 converts the Lorentzian line broadening rate  $\frac{\Delta(\delta\omega_L)}{\Delta P}$  into a cross section  $\sigma_r$ , and Equation 4-16 converts the line shifting rate  $\frac{\Delta(\Delta\omega)}{\Delta P}$  into a cross section  $\sigma_i$ . The

subscripts  $r$  and  $i$  refer to the real and imaginary parts of the cross section introduced during the development of the Lorentzian lineshape function from elastic collisions.

The line broadening and shifting rates of the atomic strontium  $5s^2\ ^1S_0 \rightarrow 5s5p\ ^3P_1$  transition perturbed by helium, neon, argon, krypton, and xenon are converted to cross section by Equations 4-15 and 4-16 and presented in Table 4-6. Also, gas kinetic cross sections are computed from the atomic radius of strontium given in the previous section and the atomic radii of the noble gases given by Hirschfelder *et al.* [26]. Both the noble gas atomic radii and gas kinetic cross sections are also displayed in Table 4-6. The gas kinetic cross sections are found to be an order of magnitude smaller than the line broadening and shifting cross sections. This is expected because the gas kinetic cross sections represent a hard-shell type of collision. The line broadening and shifting cross sections, however, result from the elastic collision associated with the noble gas atom passing near the strontium atom, but not necessarily as close as in the hard-shell case.

Table 4-6. Line broadening and shifting cross sections of the atomic strontium  $5s^2\ ^1S_0 \rightarrow 5s5p\ ^3P_1$  transition at  $14504.351\text{ cm}^{-1}$  perturbed by helium, neon, argon, krypton, and xenon compared to gas kinetic cross sections. The broadening and shifting cross sections are computed from the line broadening and shifting rates presented in Table 4-4 using Equations 4-15 and 4-16. Gas kinetic cross sections are computed from the strontium atomic radius given by Brown *et al.* [4] and the atomic radii of noble gases given by Hirschfelder *et al.* [26].

	Broadening Cross Section ( $10^{-14}\text{ cm}^2$ )	Shifting Cross Section ( $10^{-14}\text{ cm}^2$ )	Atomic Radius [26] (Å)	Gas Kinetic Cross Section ( $10^{-15}\text{ cm}^2$ )
He	0.894(0.040)	0.290(0.015)	1.288	3.71
Ne	1.269(0.062)	-0.310(0.021)	1.412	3.99
Ar	1.571(0.023)	-0.929(0.026)	1.721	4.71
Kr	2.43(0.12)	-1.206(0.037)	1.81	4.91
Xe	3.01(0.20)	-1.320(0.025)	2.028	5.48

Similarly, the line broadening and line shifting rates of the atomic strontium  $5s5p\ ^3P_{0,1,2} \rightarrow 5s6s\ ^3S_1$  transitions perturbed by the same collection of noble gases are converted to cross section by Equations 4-15 and 4-16 and presented in Figure 4-10. This figure plots the cross sections as a function of the total angular momentum quantum number  $J''$  of the initial state. Additionally, all line broadening and shifting cross sections reported here are listed in table form in Appendix C.

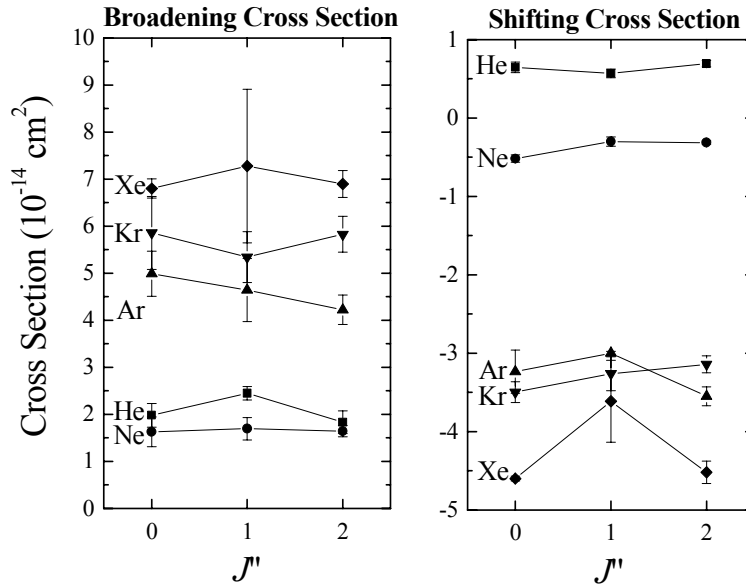


Figure 4-10. Line broadening and shifting cross sections of the atomic strontium  $5s5p\ ^3P_{0,1,2} \rightarrow 5s6s\ ^3S_1$  transitions around  $14534\text{ cm}^{-1}$  perturbed by helium, neon, argon, krypton, and xenon as a function of the total angular momentum quantum number  $J''$  of the initial state. These cross sections are computed from the line broadening and shifting rates presented in Table 4-4 using Equations 4-15 and 4-16.

Next, prior relevant research outlined in Chapter III is compared to the results given above to gain confidence in this analysis. The atomic strontium  $5s^2\ ^1S_0 \rightarrow 5s5p\ ^3P_1$  cross sections are discussed first followed by the  $5s5p\ ^3P_{0,1,2} \rightarrow 5s6s\ ^3S_1$  cross sections.

According to Chapter III, only one researcher has previously studied broadening of the atomic strontium  $5s^2\ ^1S_0 \rightarrow 5s5p\ ^3P_1$  transition by noble gases. Several authors have investigated line broadening in the analogous atomic calcium  $4s^2\ ^1S_0 \rightarrow 4s4p\ ^3P_1$  transition, and one has studied the atomic barium  $6s^2\ ^1S_0 \rightarrow 6s6p\ ^3P_1$  transition. The results of this research are presented with this earlier work in Table 4-7 for comparison. Although no one has previously published line shifting results for the atomic strontium  $5s^2\ ^1S_0 \rightarrow 5s5p\ ^3P_1$  transition, some research has been accomplished on the analogous transitions of calcium and barium. Again, the results of this research are given with this earlier work in Table 4-8 for comparison. The closeness of the current results to previous work confirms the credibility of this research, at least for this transition.

Table 4-7. Comparison of the atomic strontium  $5s^2\ ^1S_0 \rightarrow 5s5p\ ^3P_1$  line broadening cross sections of this work with analogous transitions of previous research. The asterisk indicates theoretical work. The current research is shaded in gray.

		He	Ne	Ar	Kr	Xe
		Broadening Cross Section ( $10^{-14}\text{ cm}^2$ )	Broadening Cross Section ( $10^{-14}\text{ cm}^2$ )	Broadening Cross Section ( $10^{-14}\text{ cm}^2$ )	Broadening Cross Section ( $10^{-14}\text{ cm}^2$ )	Broadening Cross Section ( $10^{-14}\text{ cm}^2$ )
1	[37]*	0.551	0.937	-	-	-
	[43]	1.00(0.05)	1.45(0.11)	3.12(0.16)	-	-
	[6]	-	0.77(0.06)	1.27(0.21)	-	-
2	[6]	-	0.98(0.12)	1.52(0.18)	-	-
		0.894(0.040)	1.269(0.062)	1.571(0.023)	2.43(0.12)	3.01(0.20)
3	[11]	1.03(0.09)	-	1.53(0.14)	-	-
<sup>1</sup> Ca $4s^2\ ^1S_0 \rightarrow 4s4p\ ^3P_1$ ( $15210.067\text{ cm}^{-1}$ )						
<sup>2</sup> Sr $5s^2\ ^1S_0 \rightarrow 5s5p\ ^3P_1$ ( $14504.351\text{ cm}^{-1}$ )						
<sup>3</sup> Ba $6s^2\ ^1S_0 \rightarrow 6s6p\ ^3P_1$ ( $12636.616\text{ cm}^{-1}$ )						

Table 4-8. Comparison of the atomic strontium  $5s^2\ ^1S_0 \rightarrow 5s5p\ ^3P_1$  line shifting cross sections of this work with analogous transitions of previous research. The asterisk indicates theoretical work. The current research is shaded in gray.

		He	Ne	Ar	Kr	Xe
		Shifting Cross Section ( $10^{-14}\text{ cm}^2$ )	Shifting Cross Section ( $10^{-14}\text{ cm}^2$ )	Shifting Cross Section ( $10^{-14}\text{ cm}^2$ )	Shifting Cross Section ( $10^{-14}\text{ cm}^2$ )	Shifting Cross Section ( $10^{-14}\text{ cm}^2$ )
1	[37]*	0.24	0.52	-	-	-
2		0.290(0.015)	-0.310(0.021)	-0.929(0.026)	-1.206(0.037)	-1.320(0.025)
3	[11]	0.17(0.08)	-	-0.98(0.21)	-	-
<sup>1</sup> Ca $4s^2\ ^1S_0 \rightarrow 4s4p\ ^3P_1$ ( $15210.067\text{ cm}^{-1}$ )						
<sup>2</sup> Sr $5s^2\ ^1S_0 \rightarrow 5s5p\ ^3P_1$ ( $14504.351\text{ cm}^{-1}$ )						
<sup>3</sup> Ba $6s^2\ ^1S_0 \rightarrow 6s6p\ ^3P_1$ ( $12636.616\text{ cm}^{-1}$ )						

Although no previous work has been accomplished on the broadening or shifting of the atomic strontium  $5s5p\ ^3P_{0,1,2} \rightarrow 5s6s\ ^3S_1$  transitions, the analogous transition has been examined in atomic calcium. The line broadening and shifting results of this research are compared to the experimental line broadening and shifting work performed on atomic calcium by O'Neill and Smith [39] in Figures 4-11 and 4-12 respectively. The line broadening and shifting cross sections appear to agree fairly well for helium and neon, but not as well for argon. Even so, this agreement is surprisingly good considering calcium and strontium are different species.

Although the  $^1S_0 \rightarrow ^1P_1$  transition was not studied as part of this research, it is useful to compare the previous research on this transition in calcium, strontium, and barium to the current results. Table 4-9 compares the atomic strontium  $5s5p\ ^3P_0 \rightarrow 5s6s\ ^3S_1$  line broadening cross sections of this research with the atomic calcium, strontium, and barium  $^1S_0 \rightarrow ^1P_1$  line broadening cross sections reviewed in the previous chapter. This atomic transition is chosen because it has the same change in total angular



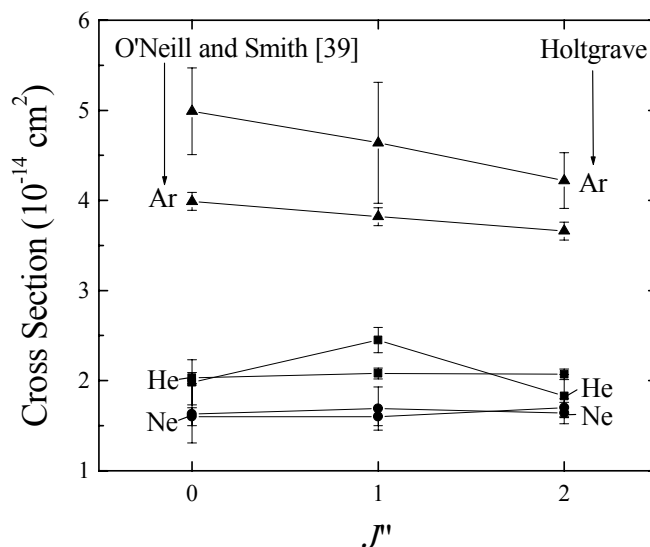


Figure 4-11. Comparison of the atomic strontium  $5s5p \ ^3P_{0,1,2} \rightarrow 5s6s \ ^3S_1$  line broadening cross sections of this work with the atomic calcium  $4s4p \ ^3P_{0,1,2} \rightarrow 4s5s \ ^3S_1$  line broadening cross sections reported by O'Neill and Smith [39] for perturbing species helium, neon, and argon. Cross sections are plotted as a function of the total angular momentum quantum number  $J''$  of the initial state.

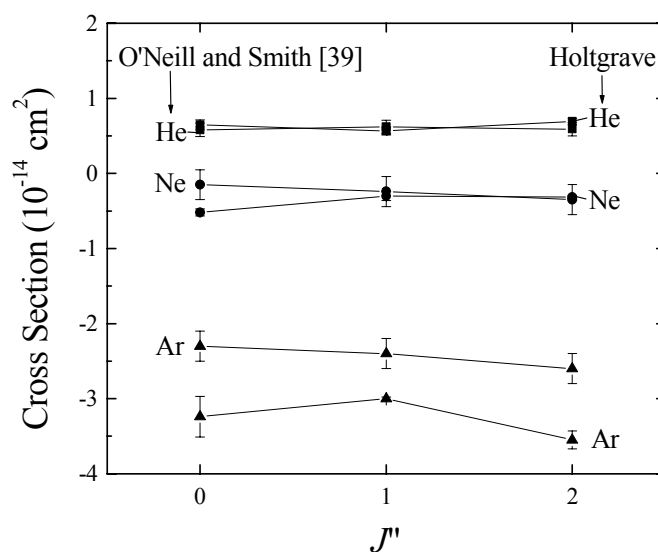


Figure 4-12. Comparison of the atomic strontium  $5s5p \ ^3P_{0,1,2} \rightarrow 5s6s \ ^3S_1$  line shifting cross sections of this work with the atomic calcium  $4s4p \ ^3P_{0,1,2} \rightarrow 4s5s \ ^3S_1$  line shifting cross sections reported by O'Neill and Smith [39] for perturbing species helium, neon, and argon. Cross sections are plotted as a function of the total angular momentum quantum number  $J''$  of the initial state.

momentum as the  $^1S_0 \rightarrow ^1P_1$  transitions. Likewise, Table 4-10 compares the atomic strontium  $5s5p\ ^3P_0 \rightarrow 5s6s\ ^3S_1$  line shifting cross sections of this research with those of the atomic calcium, strontium, and barium  $^1S_0 \rightarrow ^1P_1$  line shifting cross sections reviewed previously.

Table 4-9. Comparison of the atomic strontium  $5s5p\ ^3P_0 \rightarrow 5s6s\ ^3S_1$  line broadening cross sections of this work with atomic calcium, strontium, and barium  $^1S_0 \rightarrow ^1P_1$  line broadening cross sections of previous research. The asterisk indicates theoretical work. The current research is shaded in gray.

		He	Ne	Ar	Kr	Xe
		Broadening Cross Section ( $10^{-14}\text{ cm}^2$ )	Broadening Cross Section ( $10^{-14}\text{ cm}^2$ )	Broadening Cross Section ( $10^{-14}\text{ cm}^2$ )	Broadening Cross Section ( $10^{-14}\text{ cm}^2$ )	Broadening Cross Section ( $10^{-14}\text{ cm}^2$ )
1	[5]	1.0	-	2.5	-	-
	[46]	1.14(0.03)	1.2(0.05)	3.95(0.43)	3.60(0.30)	4.29(0.40)
	[37]*	1.14	1.1	-	-	-
	[18]	1.96(0.29)	-	-	-	-
	[8]*	0.92	1.53	-	-	-
	[21]	1.03(0.01)	1.20(0.04)	2.74(0.05)	3.32(0.07)	4.12(0.07)
2	[12]	0.627(0.014)	-	1.69(0.04)	-	-
	[57]	0.96	-	3.0	-	5.4
	[20]	1.17(0.10)	1.35(0.15)	-	-	-
	[8]*	0.98	1.65	-	-	-
3	[8]*	0.99	1.66	-	-	-
	[34]	2.4(0.2)	-	7.0(0.7)	-	-
	[11]	0.93(0.29)	-	2.4(0.6)	-	-
4		1.98(0.25)	1.63(0.32)	4.99(0.48)	5.86(0.78)	6.80(0.20)
<sup>1</sup> Ca $4s^2\ ^1S_0 \rightarrow 4s4p\ ^1P_1$ (23652.324 $\text{cm}^{-1}$ )						
<sup>2</sup> Sr $5s^2\ ^1S_0 \rightarrow 5s5p\ ^1P_1$ (21698.482 $\text{cm}^{-1}$ )						
<sup>3</sup> Ba $6s^2\ ^1S_0 \rightarrow 6s6p\ ^1P_1$ (18060.264 $\text{cm}^{-1}$ )						
<sup>4</sup> Sr $5s5p\ ^3P_0 \rightarrow 5s6s\ ^3S_1$ (14721.275 $\text{cm}^{-1}$ )						

The line broadening cross sections of this research are slightly larger than those reported previously, but this is understandable considering the fact that the transitions

Table 4-10. Comparison of the atomic strontium  $5s5p\ ^3P_0 \rightarrow 5s6s\ ^3S_1$  line shifting cross sections of this work with atomic calcium, strontium, and barium  $^1S_0 \rightarrow ^1P_1$  line shifting cross sections of previous research. The asterisk indicates theoretical work. The current research is shaded in gray.

		He	Ne	Ar	Kr	Xe
		Shifting Cross Section ( $10^{-14}\text{ cm}^2$ )	Shifting Cross Section ( $10^{-14}\text{ cm}^2$ )	Shifting Cross Section ( $10^{-14}\text{ cm}^2$ )	Shifting Cross Section ( $10^{-14}\text{ cm}^2$ )	Shifting Cross Section ( $10^{-14}\text{ cm}^2$ )
1	[5]	-0.060	-	-1.7	-	-
	[46]	-0.073(0.004)	-0.640(0.003)	-1.93(0.01)	-2.08(0.02)	-2.53(0.02)
	[37]*	0.13	-0.12	-	-	-
	[18]	-1.39(0.21)	-	-	-	-
	[8]*	-0.08	-0.74	-	-	-
2	[12]	0.00(0.03)	-	-2.0(0.1)	-	-
	[57]	0.1	-	-2.5	-	-1.3
	[8]*	-0.18	-0.73	-	-	-
3	[8]*	-0.15	-0.57	-	-	-
4		0.646(0.066)	-0.520(0.047)	-3.24(0.27)	-3.50(0.13)	-4.600(0.032)
<sup>1</sup> Ca $4s^2\ ^1S_0 \rightarrow 4s4p\ ^1P_1$ (23652.324 $\text{cm}^{-1}$ )						
<sup>2</sup> Sr $5s^2\ ^1S_0 \rightarrow 5s5p\ ^1P_1$ (21698.482 $\text{cm}^{-1}$ )						
<sup>3</sup> Ba $6s^2\ ^1S_0 \rightarrow 6s6p\ ^1P_1$ (18060.264 $\text{cm}^{-1}$ )						
<sup>4</sup> Sr $5s5p\ ^3P_0 \rightarrow 5s6s\ ^3S_1$ (14721.275 $\text{cm}^{-1}$ )						

investigated in this research begin and end in excited states. The work to which this is being compared examined a transition which begins in the ground state and ends in an excited state. Since the average distance to the nucleus is greater for the optically active electrons of excited states, it makes sense that this research should report larger cross sections.

For the line shifting cross sections, the trend identified above is less clear for helium and neon, but definite for argon, krypton, and xenon. In fact, in helium, the line shift is so slight that there is no agreement among researchers whether it is positive or

negative. Even the theoretical work disagrees on this point. It is also interesting to note that the neon line shift is approximately the same between these two transitions.

In summary, it is clear that the line broadening and shifting cross sections of the atomic strontium  $5s^2\ ^1S_0 \rightarrow 5s5p\ ^3P_1$  and  $5s5p\ ^3P_{0,1,2} \rightarrow 5s6s\ ^3S_1$  transitions perturbed by helium, neon, argon, krypton, and xenon reported in this research are similar to earlier work.

**4.2.2 Atomic Strontium and Noble Gas Difference Potentials** In this section, the algorithm for determining atomic strontium and noble gas difference potentials from line broadening and shifting rates is described and applied to the data in Table 4-4. The difference potentials are then compared to results published by previous authors. The Lennard-Jones (6-12) potential is assumed to accurately model the interaction between atomic strontium and noble gases. Thus the difference potential is reported as the constants  $C_6$  and  $C_{12}$ .

Unfortunately, there is no way to analytically determine the  $C_6$  and  $C_{12}$  difference potential constants directly from line broadening and shifting rates. Instead, the following numerical approach is used. According to Equation 2-96, the ratio of the line shifting rate  $\frac{\Delta(\Delta\omega)}{\Delta N}$  to the line broadening rate  $\frac{\Delta(\delta\omega_L)}{\Delta N}$  is

$$\frac{\frac{\Delta(\Delta\omega)}{\Delta N}}{\frac{\Delta(\delta\omega_L)}{\Delta N}} = \frac{S(\alpha)}{4B(\alpha)} \quad (4-17)$$

where  $S(\alpha)$  and  $B(\alpha)$  are given by Equations 2-93 and 2-92 respectively. These functions have analytical representations which are given in Appendix B and, knowing these,  $\alpha$  can be determined numerically. With this, the difference potential constant  $C_6$

can be found through either Equation 2-94 or 2-95. Rewriting these equations in terms of wavenumber and pressure, replacing the average relative velocity  $\langle v \rangle$  with Equation 4-8, and solving for  $C_6$  gives

$$C_6 = \left( \frac{1}{\pi^{\frac{1}{4}}} \right) \left( \frac{1}{2^{\frac{17}{4}}} \right) \left( \frac{1}{3} \right) \left( \hbar \mu^{\frac{3}{4}} \right) (k_B T)^{\frac{7}{4}} \left( \frac{c}{B(\alpha)} \frac{\Delta(\delta x_L)}{\Delta P} \right)^{\frac{5}{2}} \quad (4-18)$$

and

$$C_6 = \left( \frac{1}{\pi^{\frac{1}{4}}} \right) \left( \frac{2^{\frac{3}{4}}}{3} \right) \left( \hbar \mu^{\frac{3}{4}} \right) (k_B T)^{\frac{7}{4}} \left( \frac{c}{S(\alpha)} \frac{\Delta(\Delta x)}{\Delta P} \right)^{\frac{5}{2}} \quad (4-19)$$

$C_{12}$  is then found by substituting these expressions for  $C_6$  into Equation 2-88 giving

$$C_{12} = \pi^{\frac{5}{4}} \left( \frac{1}{2^{\frac{39}{4}}} \right) \left( \frac{1}{63} \right) \left( \alpha \hbar \mu^{\frac{9}{4}} \right) (k_B T)^{\frac{13}{4}} \left( \frac{c}{B(\alpha)} \frac{\Delta(\delta x_L)}{\Delta P} \right)^{\frac{11}{2}} \quad (4-20)$$

and

$$C_{12} = \pi^{\frac{5}{4}} \left( \frac{2^{\frac{5}{4}}}{63} \right) \left( \alpha \hbar \mu^{\frac{9}{4}} \right) (k_B T)^{\frac{13}{4}} \left( \frac{c}{S(\alpha)} \frac{\Delta(\Delta x)}{\Delta P} \right)^{\frac{11}{2}} \quad (4-21)$$

Thus the difference potential constants  $C_6$  and  $C_{12}$  can be found two ways using experimental measurements of the line broadening rate, the line shifting rate, and the temperature.

As mentioned in Chapter II, a special case arises when the ratio of the line shifting rate to the line broadening rate is greater than approximately 0.146813. In this case, the difference potential is completely repulsive and  $C_6 = 0$ .  $C_{12}$  is determined analytically by solving Equations 2-101 and 2-102 giving

$$C_{12} = \left( \frac{\pi^{\frac{7}{4}}}{2^{\frac{27}{4}}} \right) \left( \frac{\Gamma(6)}{\Gamma(\frac{11}{2})\Gamma(\frac{11}{2})\cos^{\frac{11}{2}}(\frac{\pi}{11})} \right) \left( \hbar\mu^{\frac{9}{4}} \right) (k_B T)^{\frac{13}{4}} \left( c \frac{\Delta(\delta x_L)}{\Delta P} \right)^{\frac{11}{2}} \quad (4-22)$$

and

$$C_{12} = \left( \frac{\pi^{\frac{7}{4}}}{2^{\frac{5}{4}}} \right) \left( \frac{\Gamma(6)}{\Gamma(\frac{11}{2})\Gamma(\frac{11}{2})\sin^{\frac{11}{2}}(\frac{\pi}{11})} \right) \left( \hbar\mu^{\frac{9}{4}} \right) (k_B T)^{\frac{13}{4}} \left( c \frac{\Delta(\Delta x)}{\Delta P} \right)^{\frac{11}{2}} \quad (4-23)$$

Again, the difference potential constant  $C_{12}$  can be found two ways using experimental measurements of either the line broadening rate or the line shifting rate and the temperature.

The methodology described above is applied to the atomic strontium line broadening and shifting rates of Table 4-4. Figure 4-13 gives a graphical comparison of the line shifting to broadening rate ratios to the function  $\frac{S(\alpha)}{4B(\alpha)}$ . From this comparison, the corresponding values of  $\alpha$  for which the curves cross is computed. In several cases, the helium ratio is found to be greater than approximately 0.146813 and above the range of this function. It is treated according to the special case described earlier. In several other instances, the ratio of the line shifting to broadening rates crosses the curve more than once leading to multiple values of  $\alpha$ . These cases are sequentially numbered.

With the values for  $\alpha$  determined, it is possible to proceed with the determination of the difference potential constants  $C_6$  and  $C_{12}$ . As mentioned previously, Equations 4-18 through 4-21 give two possible routes for determining  $C_6$  and  $C_{12}$ . Both routes, however, lead to the same result. The uncertainty in  $C_6$  and  $C_{12}$  is determined from the uncertainty in  $\alpha$ . For the special case where the ratio of the line shifting to broadening rate is outside the range of the function  $\frac{S(\alpha)}{4B(\alpha)}$ ,  $C_{12}$  is determined from Equations 4-22 and

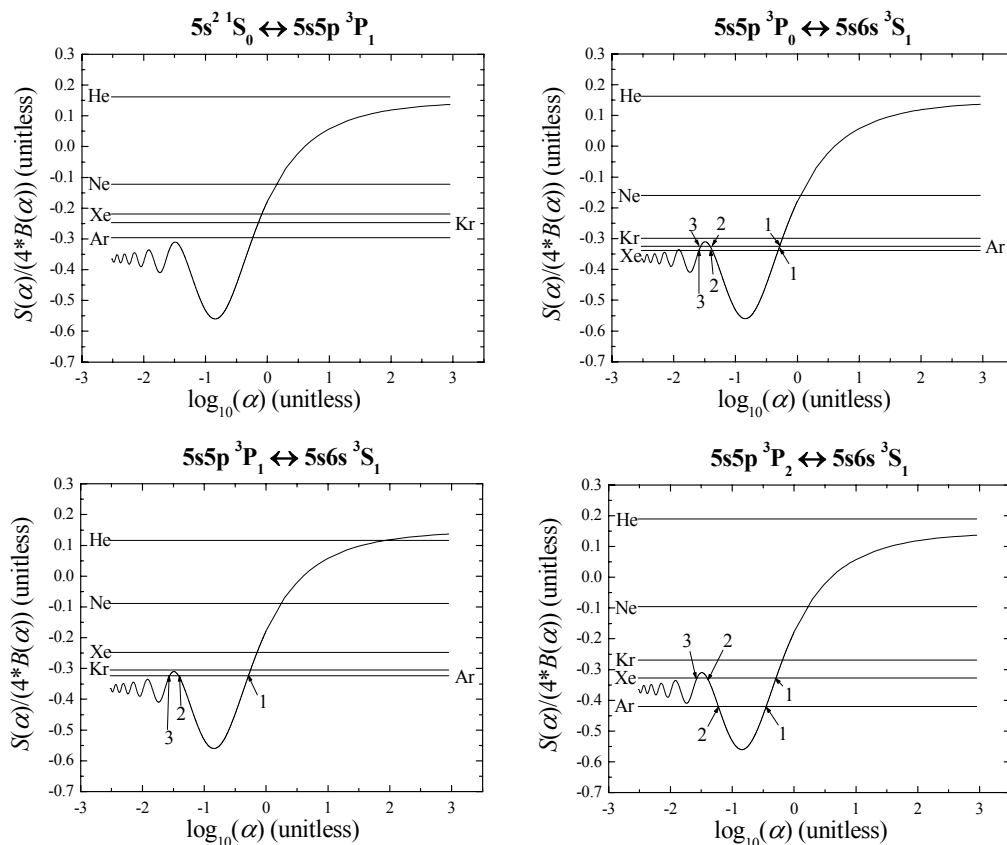


Figure 4-13. Ratios of the atomic strontium line shifting rates to line broadening rates compared to the function  $\frac{S(\alpha)}{4B(\alpha)}$  for all transitions and noble gases studied in this research.

In the cases where the ratio crosses the function more than once, each crossing is sequentially numbered for future reference.

4-23. In this case, the two equations do not lead to the same result because two independent pieces of information are used to determine the same quantity. The two results and their uncertainties are combined in a weighted average to give the final result. The temperatures registered by the tube furnace (see Table 4-3) are used for  $T$  in all cases.

Figure 4-14 uses the difference potential constants  $C_6$  and  $C_{12}$  as determined above to plot the difference potential as a function of internuclear separation. For

perturbing species where more than one solution exists for  $\alpha$ , multiple difference potentials are computed and plotted. These difference potentials are labeled with superscripts corresponding to the curve crossings identified in Figure 4-13. One would expect the difference potential barrier to occur at larger and larger internuclear separations as the mass of the perturbing species increases. This is indeed the case for the  $5s^2\ ^1S_0 \leftrightarrow 5s5p\ ^3P_1$  difference potential depicted in the upper left corner of Figure 4-14. For the  $5s5p\ ^3P_{0,1,2} \leftrightarrow 5s6s\ ^3S_1$  difference potentials, however, this trend can only be followed if the curve crossings with superscript “1” are used. The other solutions, therefore, are disregarded as giving unrealistic difference potentials. Figure 4-15 plots the difference potentials which remain and Table 4-11 lists these difference potential constants and their uncertainties.

Next, prior relevant research outlined in Chapter III is compared to the results in Table 4-11 in order to gain confidence in the analysis presented here. As shown in Chapter III, there has been no previous difference potential work on either the  $^1S_0$  and  $^3P_1$  or  $^3P_{0,1,2}$  and  $^3S_1$  energy states in either calcium, strontium, or barium. All previous such work has been on the  $^1S_0$  and  $^1P_1$  states. Nevertheless, a comparison is made between these difference potential constants and those of the atomic strontium  $5s^2\ ^1S_0$  and  $5s5p\ ^3P_1$  and  $5s5p\ ^3P_0$  and  $5s6s\ ^3S_1$  states derived from this research. As before, these energy states are chosen because they have the same difference in total angular momentum as the  $^1S_0$  and  $^1P_1$  energy states. The difference potential constant  $C_6$  is compared to previous work in Table 4-12 while  $C_{12}$  is compared in Table 4-13.



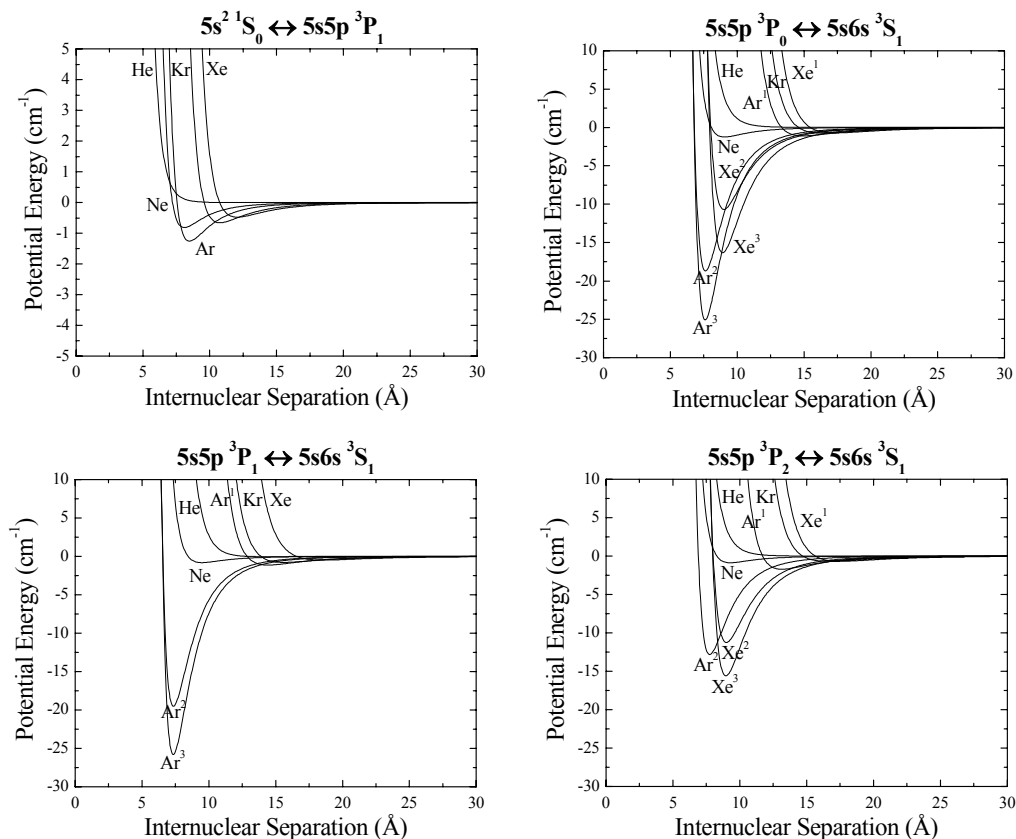


Figure 4-14. Atomic strontium difference potential plots as a function of internuclear separation for all energy states perturbed by all noble gases studied in this research. Cases for which multiple difference potentials exist are numbered by superscripts corresponding to the curve crossings identified in Figure 4-13.

The values for the attractive term  $C_6$  reported in Table 4-12 do not agree particularly well with each other and range two orders of magnitude. Similarly, the values for the repulsive term  $C_{12}$  reported in Table 4-13 also do not agree with each other and range six orders of magnitude. There could be several reasons for this. Perhaps unidentified systematic errors in the experiments of the various researchers are leading to erroneous results. Perhaps the lineshape data is good, but the methods for extracting the Lorentzian linewidth from it are poor. Certainly this is plausible in the broadband

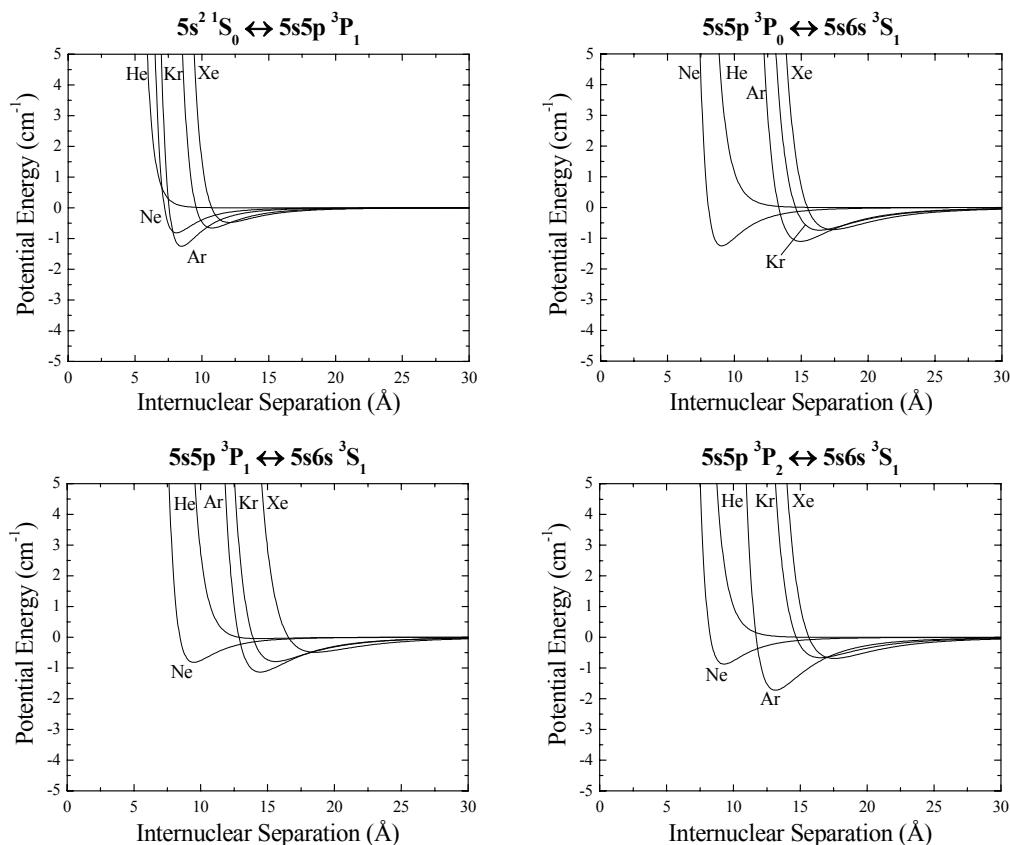


Figure 4-15. Atomic strontium difference potential plots as a function of internuclear separation for all energy states perturbed by all noble gases studied in this research. The Lennard-Jones (6-12) potential is assumed to be an accurate model of the interaction.

absorption experiments where the true absorption profile must be separated from the instrument lineshape function. And finally, it could be the Lennard-Jones (6-12) potential is not an accurate model for the interaction between atomic calcium, strontium, and barium with noble gases. In any event, the point here is to place the current research into the context of previous research and the difference potential constants reported here appear to be within the range of other work. Thus the difference potential results of this research are deemed credible.

Table 4-11. Atomic strontium difference potential constants  $C_6$  and  $C_{12}$  for all energy states perturbed by all noble gases studied in this research

	$C_6$ ( $10^{-58}$ erg cm <sup>6</sup> )	$C_{12}$ ( $10^{-101}$ erg cm <sup>12</sup> )
$5s^2\ ^1S_0 \leftrightarrow 5s5p\ ^3P_1$		
He	0	0.186(0.036)
Ne	0.912(0.032)	1.285(0.018)
Ar	1.860(0.027)	3.473(0.024)
Kr	4.04(0.12)	31.276(0.065)
Xe	5.80(0.20)	89.26(0.48)
$5s5p\ ^3P_0 \leftrightarrow 5s6s\ ^3S_1$		
He	0	23(11)
Ne	2.73(0.28)	7.50(0.29)
Ar	48.9(2.9)	2730(160)
Kr	56.3(3.8)	5410(220)
Xe	77.99(0.99)	10670(160)
$5s5p\ ^3P_1 \leftrightarrow 5s6s\ ^3S_1$		
He	1.58(0.60)	69.8(4.5)
Ne	2.36(0.21)	8.52(0.34)
Ar	40.8(2.8)	1840(120)
Kr	45.2(2.6)	3250(130)
Xe	80(11)	16480(530)
$5s5p\ ^3P_2 \leftrightarrow 5s6s\ ^3S_1$		
He	0	20.1(7.6)
Ne	2.231(0.085)	7.19(0.12)
Ar	35.11(0.70)	900(110)
Kr	52.9(1.9)	5341(49)
Xe	79.8(1.8)	11700(260)

While comparing the values of the difference potential constants  $C_6$  and  $C_{12}$  directly with other work is useful, it is also valuable to study the appearance of the difference potentials graphically. Figures 4-16 and 4-17 show side by side comparisons of the difference potentials of the atomic strontium  $5s^2\ ^1S_0$  and  $5s5p\ ^3P_1$  energy states studied here with those of the atomic strontium  $5s^2\ ^1S_0$  and  $5s5p\ ^1P_1$  studied elsewhere. The left hand column is the same in all four cases as the upper left hand plot of Figure

Table 4-12. Comparison of the atomic strontium difference potential constant  $C_6$  of the  $5s^2\ ^1S_0 \leftrightarrow 5s5p\ ^3P_1$  and  $5s5p\ ^3P_0 \leftrightarrow 5s6s\ ^3S_1$  energy states of this work with that of the  $^1S_0 \leftrightarrow ^1P_1$  energy states studied in previous research. The asterisk indicates theoretical work. The current research is shaded in gray.

		He	Ne	Ar	Kr	Xe
		$C_6$ ( $10^{-58}$ erg cm <sup>6</sup> )	$C_6$ ( $10^{-58}$ erg cm <sup>6</sup> )	$C_6$ ( $10^{-58}$ erg cm <sup>6</sup> )	$C_6$ ( $10^{-58}$ erg cm <sup>6</sup> )	$C_6$ ( $10^{-58}$ erg cm <sup>6</sup> )
1	[5]	0.92	-	9.2	-	-
	[45]*	0.26	0.50	1.9	3.3	-
2	[12]	1.06(0.15)	-	4.3(0.4)	-	-
	[45]*	0.26	0.52	2.2	3.2	-
	[57]	0.541	-	10.2	-	44.4
	[20]	-	-	3.4(1.0)	13(4)	18(5)
3	[45]*	0.20	0.40	1.7	2.8	-
4		0	0.912(0.032)	1.860(0.027)	4.04(0.12)	5.80(0.20)
5		0	2.73(0.28)	48.9(2.9)	56.3(3.8)	77.99(0.99)
<sup>1</sup> Ca $4s^2\ ^1S_0 \leftrightarrow 4s4p\ ^1P_1$						
<sup>2</sup> Sr $5s^2\ ^1S_0 \leftrightarrow 5s5p\ ^1P_1$						
<sup>3</sup> Ba $6s^2\ ^1S_0 \leftrightarrow 6s6p\ ^1P_1$						
<sup>4</sup> Sr $5s^2\ ^1S_0 \leftrightarrow 5s5p\ ^3P_1$						
<sup>5</sup> Sr $5s5p\ ^3P_0 \leftrightarrow 5s6s\ ^3S_1$						

Table 4-13. Comparison of the atomic strontium difference potential constant  $C_{12}$  of the  $5s^2\ ^1S_0 \leftrightarrow 5s5p\ ^3P_1$  and  $5s5p\ ^3P_0 \leftrightarrow 5s6s\ ^3S_1$  energy states of this work with that of the  $^1S_0 \leftrightarrow ^1P_1$  energy states studied in previous research. The asterisk indicates theoretical work. The current research is shaded in gray.

		He	Ne	Ar	Kr	Xe
		$C_{12}$ ( $10^{-101}$ erg cm <sup>12</sup> )	$C_{12}$ ( $10^{-101}$ erg cm <sup>12</sup> )	$C_{12}$ ( $10^{-101}$ erg cm <sup>12</sup> )	$C_{12}$ ( $10^{-101}$ erg cm <sup>12</sup> )	$C_{12}$ ( $10^{-101}$ erg cm <sup>12</sup> )
1	[5]	109	-	76	-	-
	[45]*	0.080	0.062	0.52	1.9	-
2	[12]	2.5(0.8)	-	1.3(0.3)	-	-
	[45]*	0.099	0.081	0.75	2.7	-
	[57]	0.426	-	86	988	-
	[20]	-	-	0.71(0.50)	5.4(3.0)	8.1(4.0)
3	[45]*	0.11	0.043	0.42	1.6	-
4		0.186(0.036)	1.285(0.018)	3.473(0.024)	31.276(0.065)	89.26(0.48)
5		23(11)	7.50(0.29)	2730(160)	5410(220)	10670(160)
<sup>1</sup> Ca $4s^2\ ^1S_0 \leftrightarrow 4s4p\ ^1P_1$						
<sup>2</sup> Sr $5s^2\ ^1S_0 \leftrightarrow 5s5p\ ^1P_1$						
<sup>3</sup> Ba $6s^2\ ^1S_0 \leftrightarrow 6s6p\ ^1P_1$						
<sup>4</sup> Sr $5s^2\ ^1S_0 \leftrightarrow 5s5p\ ^3P_1$						
<sup>5</sup> Sr $5s5p\ ^3P_0 \leftrightarrow 5s6s\ ^3S_1$						

4-15. The axes, however, are varied to allow a direct comparison to the results of other researchers given in the right hand column. The same applies to Figures 4-18 and 4-19, except that in this case it is the atomic strontium  $5s5p\ ^3P_0$  and  $5s6s\ ^3S_1$  difference potentials of this work in the left hand column. Again, the plot in the left hand column is the same in all four cases and is the same as the plot in the upper right hand corner of Figure 4-15. Also again, the axes are varied to allow direct comparisons to the plots of other authors in the right hand column.

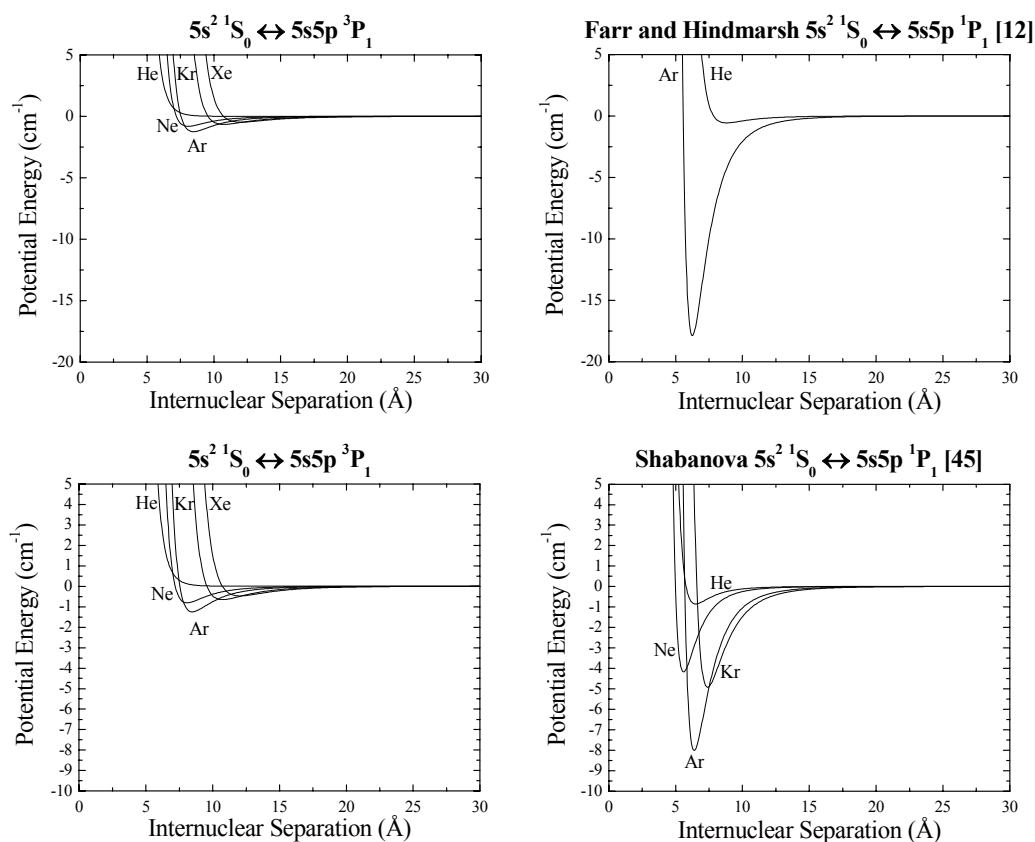


Figure 4-16. Comparison of the atomic strontium  $5s^2\ ^1S_0$  and  $5s5p\ ^3P_1$  difference potentials as a function of internuclear separation of this work with those of the atomic strontium  $5s^2\ ^1S_0$  and  $5s5p\ ^1P_1$  energy states studied in previous research. This includes the work of Farr and Hindmarsh [12] and Shabanova [45].

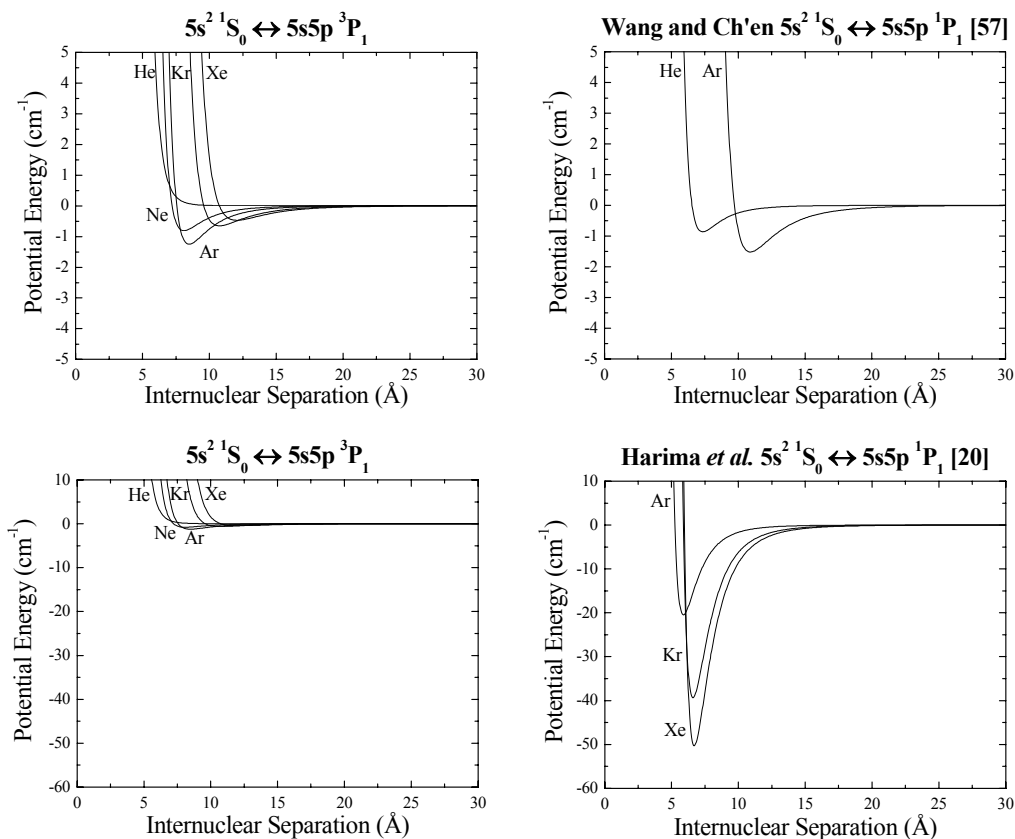


Figure 4-17. Comparison of the atomic strontium  $5s^2 \ ^1S_0$  and  $5s5p \ ^3P_1$  difference potentials as a function of internuclear separation of this work with those of the atomic strontium  $5s^2 \ ^1S_0$  and  $5s5p \ ^3P_1$  energy states studied in previous research. This includes the work of Wang and Ch'en [57] and Harima *et al.* [20].

Some observations regarding Figures 4-16 through 4-19 are in order at this point.

The depths of the difference potential wells given by the work of Harima *et al.* [20] are far deeper than those of any other researcher. Perhaps this is because they used the Unified Franck-Condon method to determine the difference potential while the others used the method of Hindmarsh and Farr [25]. The results of Wang and Ch'en [57] appear to coincide with this work as do the helium results of Farr and Hindmarsh [12]. Their argon well depth and location of the repulsive barrier, however, do not agree with this

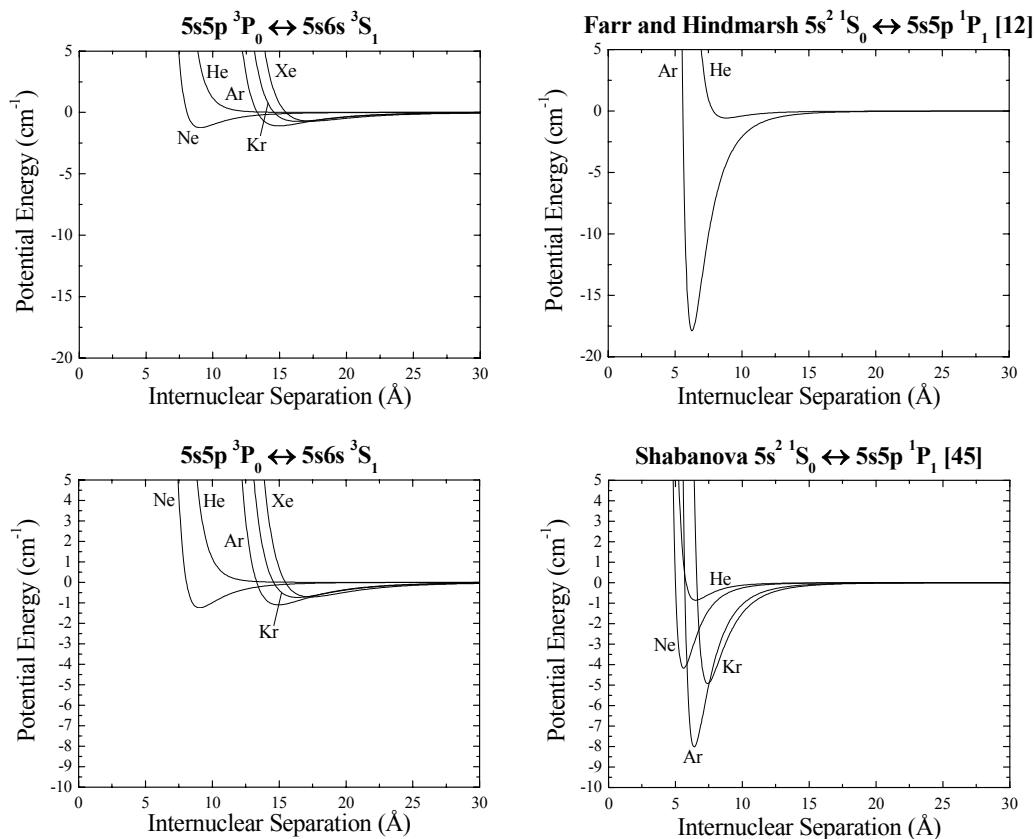


Figure 4-18. Comparison of the atomic strontium  $5s5p\ ^3P_0 \leftrightarrow 5s6s\ ^3S_1$  difference potentials as a function of internuclear separation of this work with those of the atomic strontium  $5s^2\ ^1S_0 \leftrightarrow 5s5p\ ^1P_1$  energy states studied in previous research. This includes the work of Farr and Hindmarsh [12] and Shabanova [45].

work. And finally, the theoretical results of Shabanova [45] trend the same as the  $5s5p\ ^3P_{0,1,2} \leftrightarrow 5s6s\ ^3S_1$  results of this research. On the whole, the appearances of the difference potentials of this work do not appear to lie significantly outside the range of difference potentials published by other researchers.

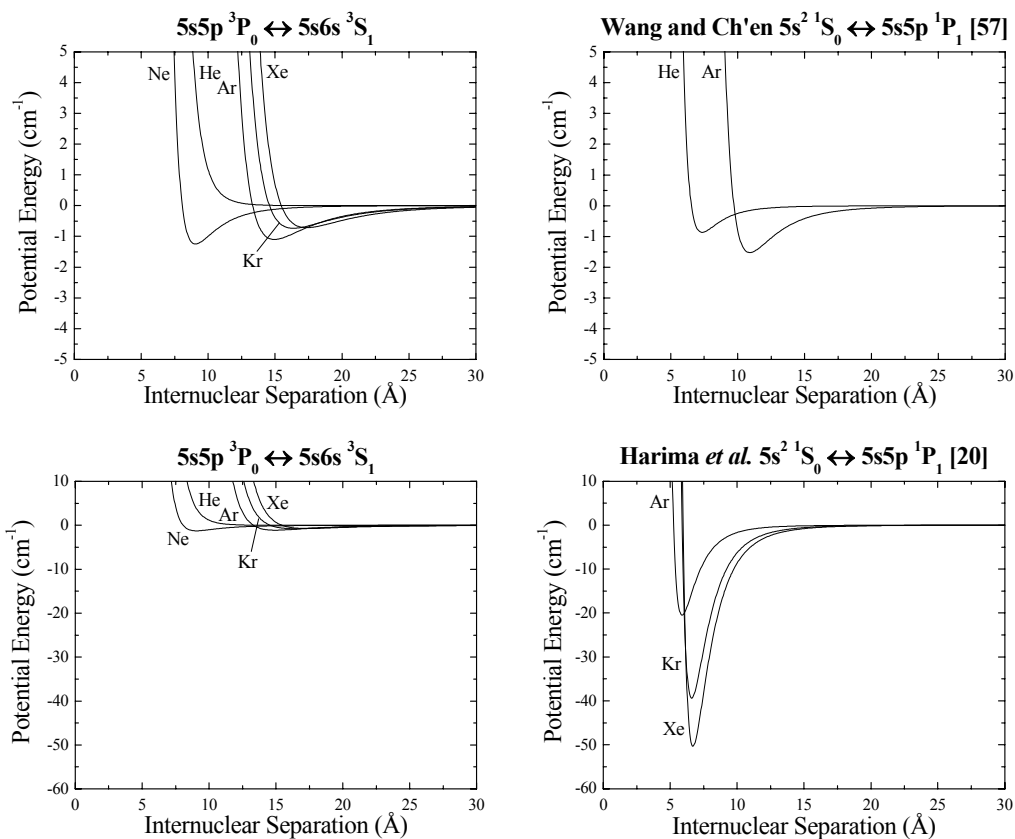


Figure 4-19. Comparison of the atomic strontium  $5s5p\ ^3P_0$  and  $5s6s\ ^3S_1$  difference potentials as a function of internuclear separation of this work with those of the atomic strontium  $5s^2\ ^1S_0$  and  $5s5p\ ^1P_1$  energy states studied in previous research. This includes the work of Wang and Ch'en [57] and Harima *et al.* [20].



### 4.3 Discussion of the Atomic Strontium Line Broadening and Shifting Experiment

In this final section, some observations are made and conclusions drawn from the atomic strontium line broadening and shifting rate analysis presented in the previous section. It is split into three subsections; one concerning the atomic strontium line broadening and shifting cross sections presented in Section 4.2.1, another concerning the atomic strontium difference potentials presented in Section 4.2.2, and a summary and recommendations for future research.

#### 4.3.1 Discussion of Atomic Strontium Line Broadening and Shifting Cross

**Sections** The atomic strontium line broadening and line shifting cross sections of the  $5s^2\ ^1S_0 \rightarrow 5s5p\ ^3P_1$  transition presented in Table 4-6 are discussed first. These cross sections are plotted as functions of the polarizability of the perturbing species in Figure 4-20. Noble gas polarizabilities are taken from the *CRC Handbook of Chemistry and Physics* [35] and listed in Table 4-14. The line broadening cross sections clearly increase with the polarizability of the perturbing species while the line shifting cross sections become more negative. This trend is understandable in terms of the perturbing species' ability to influence a body absorbing or emitting radiation. Atoms with larger polarizabilities exert a stronger dispersion force on other atoms thereby yielding larger cross sections.

Perhaps the most interesting feature of Figure 4-20 is the fact that helium shifts spectral lines to the blue and the other noble gases shift them to the red. This blue shift caused by helium leads to a positive shifting cross section which, according to the theory of Hindmarsh and Farr [25], is a necessary, but not sufficient, condition for an entirely repulsive potential. In order for the entirely repulsive potential case to apply, the ratio of the line shifting to line broadening rates must be greater than approximately 0.146813. In

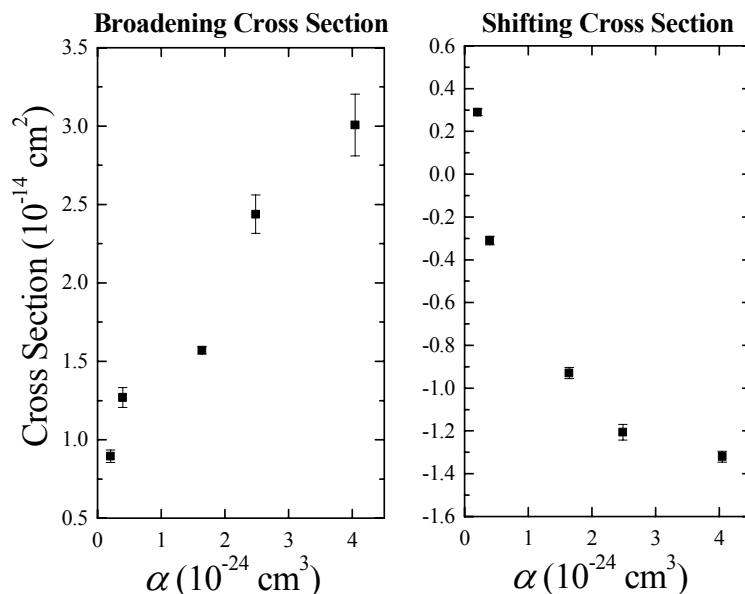


Figure 4-20. Line broadening and shifting cross sections of the atomic strontium  $5s^2 \ ^1S_0 \rightarrow 5s5p \ ^3P_1$  transition at  $14504.351 \text{ cm}^{-1}$  as a function of the polarizability of the perturbing species helium, neon, argon, krypton, and xenon. The data points are taken from Table 4-6.

Table 4-14. Polarizability of perturbing species [35]

Perturbing Species	Polarizability ( $\text{\AA}^3$ )
He	0.2049569
Ne	0.3956
Ar	1.6411
Kr	2.4844
Xe	4.044

order for this to be true, the line shift must, at the very least, be positive. The conclusion, therefore, is that an attractive interaction between atomic strontium in both the  $5s^2 \ ^1S_0$  and  $5s5p \ ^3P_1$  states and helium may be nonexistent. The only way to confirm this is to compute the ratios of the line shifting to line broadening rates and compare the results to

0.146813. This is performed in the difference potential analysis and will be discussed in the next section.

Moving on to the atomic strontium line broadening cross sections of the  $5s5p\ ^3P_{0,1,2} \rightarrow 5s6s\ ^3S_1$  transitions presented in Figure 4-10, the same general trends observed of the atomic strontium  $5s^2\ ^1S_0 \rightarrow 5s5p\ ^3P_1$  transition in the previous paragraph apply with one glaring exception. The line broadening cross sections do not appear to increase uniformly with the polarizability of the perturbing species. This trend is shown explicitly in Figure 4-21, which plots the atomic strontium line broadening cross sections of the  $5s5p\ ^3P_{0,1,2} \rightarrow 5s6s\ ^3S_1$  transitions as a function of the polarizability of the perturbing species. The cross sections fall going from helium to neon and then rise again through argon, krypton, and xenon. This counterintuitive trend is observed across all three transitions. For comparison, the atomic calcium line broadening cross sections of the  $4s4p\ ^3P_{0,1,2} \rightarrow 4s5s\ ^3S_1$  transitions measured by O'Neill and Smith [39] are presented as a function of the polarizability of the perturbing species in Figure 4-22. Interestingly, this trend is observed in the atomic calcium line broadening cross sections as well.

The non-uniform trends depicted in Figures 4-21 and 4-22 have no immediate or obvious explanation. One consideration is the fact that helium shifts the atomic strontium spectral lines observed here to the blue while the other noble gases shift them to the red. Although this is true for the atomic strontium  $5s5p\ ^3P_{0,1,2} \rightarrow 5s6s\ ^3S_1$  transitions, it is also true for the  $5s^2\ ^1S_0 \rightarrow 5s5p\ ^3P_1$  transition where the cross sections trend intuitively. The conclusion, therefore, is that line broadening cross sections are not directly correlated with the polarizability of the perturbing species. The relationship between the two is

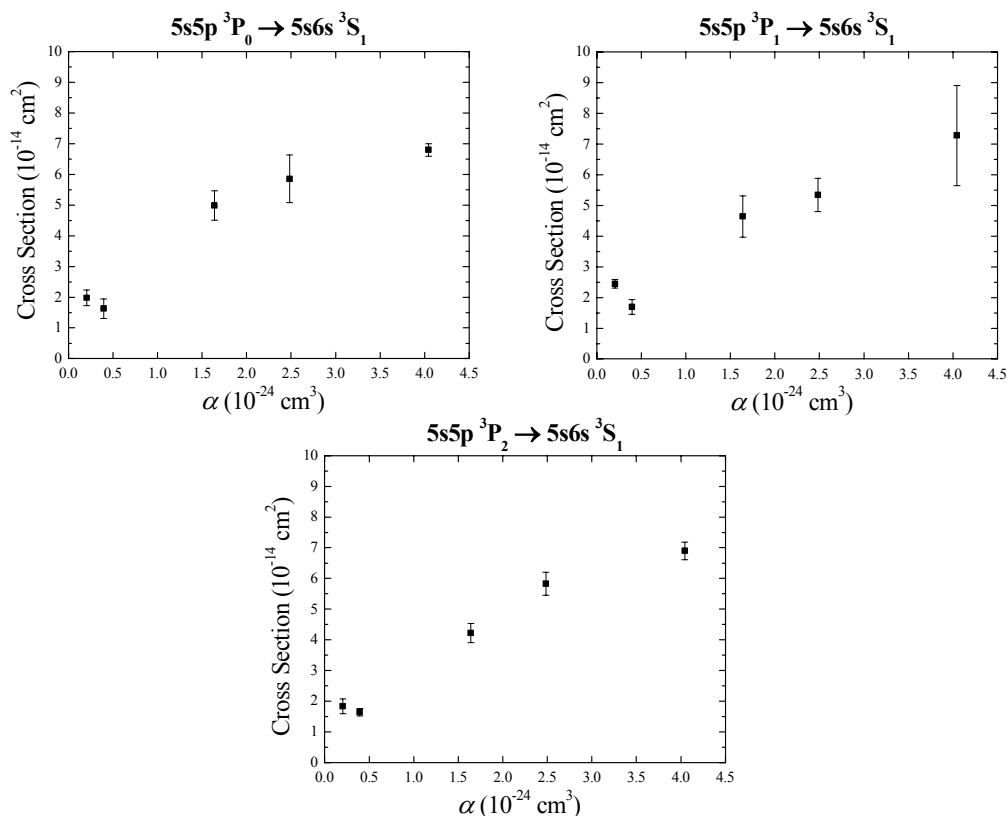


Figure 4-21. Line broadening cross sections of the atomic strontium  $5s5p \ ^3P_{0,1,2} \rightarrow 5s6s \ ^3S_1$  transitions around  $14534 \text{ cm}^{-1}$  as a function of the polarizability of the perturbing species helium, neon, argon, krypton, and xenon. It is the same data presented in Figure 4-10.

complex and any theory which aspires to predict line broadening cross sections directly from the polarizability of the perturbing species must account for this.

The atomic strontium line shifting cross sections of the  $5s5p \ ^3P_{0,1,2} \rightarrow 5s6s \ ^3S_1$  transitions presented in Figure 4-10 appear to exhibit the same trend as the line shifting cross sections of the  $5s^2 \ ^1S_0 \rightarrow 5s5p \ ^3P_1$  transition discussed above. Figure 4-23 reveals this explicitly by plotting these cross sections as a function of the polarizability of the perturbing species. This trend is further confirmed by the line shifting cross sections of the analogous atomic calcium transition reported by O'Neill and Smith [39]. The

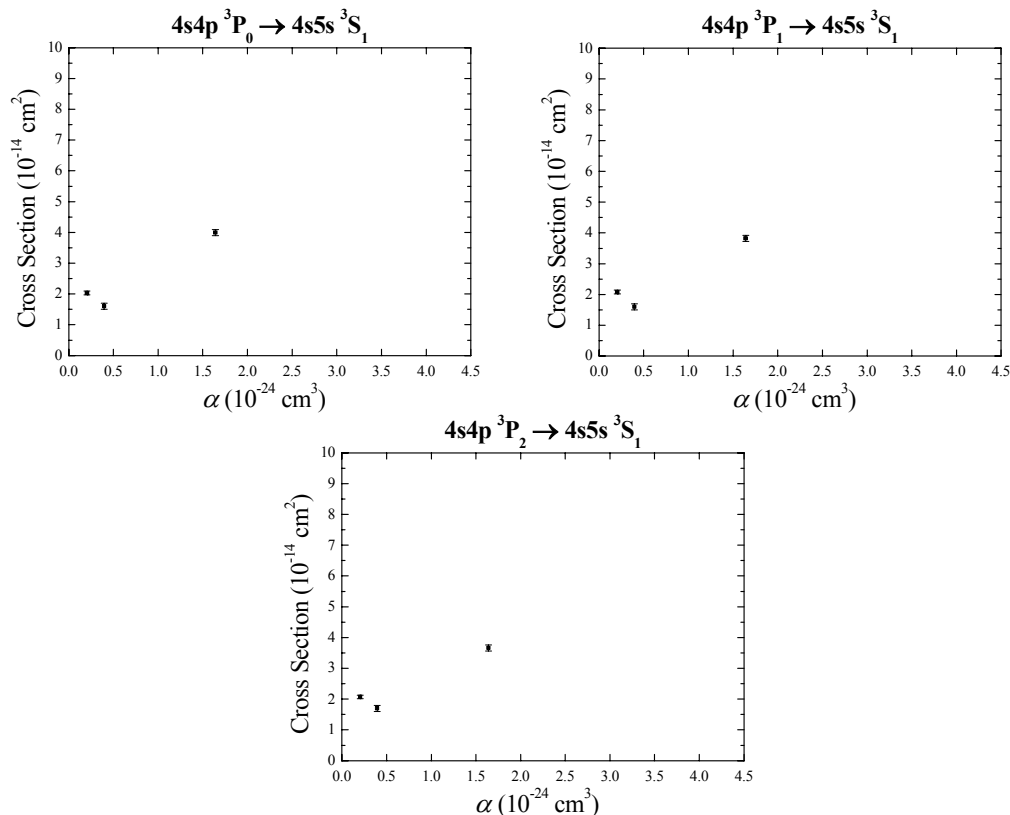


Figure 4-22. Line broadening cross sections of the atomic calcium  $4s4p \ ^3P_{0,1,2} \rightarrow 4s5s \ ^3S_1$  transitions around  $16329 \text{ cm}^{-1}$  as a function of the polarizability of the perturbing species helium, neon, and argon. These cross sections are derived from line broadening data reported by O'Neill and Smith [39] and are the same as those presented Figure 3-2.

observation that the helium line shifting cross section is positive in all three cases leads to the same conclusion which was discussed above for the helium line shifting cross section of the atomic strontium  $5s^2 \ ^1S_0 \rightarrow 5s5p \ ^3P_1$  transition. That is, the difference potential may be entirely repulsive. Again, the only way to confirm this is to compute the ratio of the line shifting to line broadening rates and compare the results to 0.146813. This is performed in the difference potential analysis and will be discussed shortly.

A significant conclusion from an examination of the atomic strontium line broadening cross sections of the  $5s5p \ ^3P_{0,1,2} \rightarrow 5s6s \ ^3S_1$  transitions shown in Figure 4-10

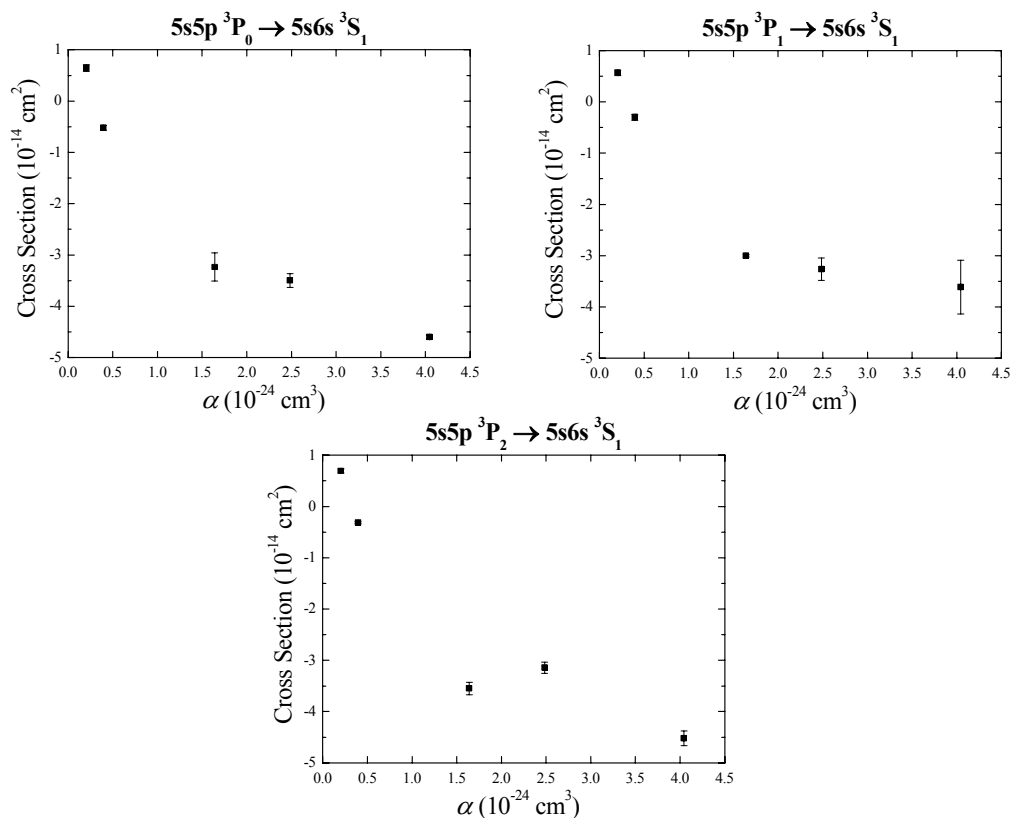


Figure 4-23. Line shifting cross sections of the atomic strontium  $5s5p \ ^3P_{0,1,2} \rightarrow 5s6s \ ^3S_1$  transitions around  $14534 \text{ cm}^{-1}$  as a function of the polarizability of the perturbing species helium, neon, argon, krypton, and xenon. It is the same data as presented in Figure 4-10.

is that there do not appear to be any trends of cross section as a function of the total angular momentum of the initial state. The cross sections appear to remain constant within the uncertainty of the experiment, which is approximately 10%. This lack of a trend is interesting because it is different from what has been observed in molecular line broadening. As noted in Chapter III, several researchers have observed that the line broadening cross section in molecules appears to decrease with increasing magnitude of the branch-independent quantum number  $m$ . In particular, the work of Pope on the  $\text{O}_2$  line broadening cross sections of the A band and NO fundamental band perturbed by

helium, neon, argon, krypton, and xenon displayed in Figures 3-6 and 3-7 exhibit this trend [41]. Also, the work of Luo *et al.* on the line broadening cross sections of the CO fundamental band perturbed by helium and neon displayed in Figure 3-8 exhibit this trend as well [36].

The observation that the atomic strontium line broadening cross sections do not appear to be dependent on the total angular momentum quantum number  $J''$  of the initial state as it does in molecules could be for several reasons. For one, previous researchers claim that the line broadening cross section is dominated by the upper state [37, 39]. If it is the same in all transitions, then no total angular momentum dependence is expected. Also, the causes of line broadening are different between atoms and molecules. Elastic collisions are believed to be the cause of line broadening in atoms while inelastic collisions are generally thought to be the cause of line broadening in molecules. When elastic collisions dominate, the line broadening cross section is the result of the difference potential while when inelastic collisions dominate, the total quenching rates of the upper and lower states determine the line broadening cross section.

Pursuing the case of broadening by elastic collisions, it was shown in Chapter II that the line broadening and shifting cross sections are determined by the difference potential, although not in an entirely direct way. The line broadening cross section is given by Equation 2-90 which is a function of Equation 2-92. Similarly, the line shifting cross section is given by Equation 2-91 which is a function of Equation 2-93. All these equations, however, are functions of the difference potential constants  $C_6$  and  $C_{12}$ . Therefore, if there is a lack of a trend in the line broadening and shifting cross sections across the three transitions, then this indicates a lack of a trend in the difference potentials

across the three transitions as well. Or, more simply, the difference potential does not appear to depend on the total angular momentum of the initial state.

#### **4.3.2 Discussion of Atomic Strontium and Noble Gas Difference Potentials**

The first issue addressed here is whether or not the strontium-helium difference potentials are entirely repulsive. As shown in Figure 4-13, the ratios of the line shifting to line broadening rates exceed approximately 0.146813 in three of the four transitions studied. Therefore the difference potential is entirely repulsive in those cases. In the fourth case, the atomic strontium  $5s5p\ ^3P_1 \rightarrow 5s6s\ ^3S_1$  transition, the ratio does not exceed this quantity and therefore is not entirely repulsive. This is an example of the case where the positive line broadening cross section alone is not a sufficient condition for the difference potential to be entirely positive.

The difference potential constant  $C_6$ , also known as the attractive van der Waals term, is known from theory to depend linearly on the polarizability of the perturbing species [45]. It also depends on the ionization energy, energy levels, and oscillator strengths of the perturbing species, which perturbs this linear dependence. Nevertheless, it is useful to examine the van der Waals term as a function of the polarizability of the perturbing species to see if any interesting trends emerge. This is accomplished in Figure 4-24 for all energy states studied in this research. The trend is approximately linear in all cases as expected from theory.

An interesting trend observed in Figure 4-15 for all difference potentials reported in this research is that the well depths do not appear to deepen with increasing polarizability of the perturbing species as might be expected. This can be shown explicitly by calculating the difference potential well depths directly from the Lennard-



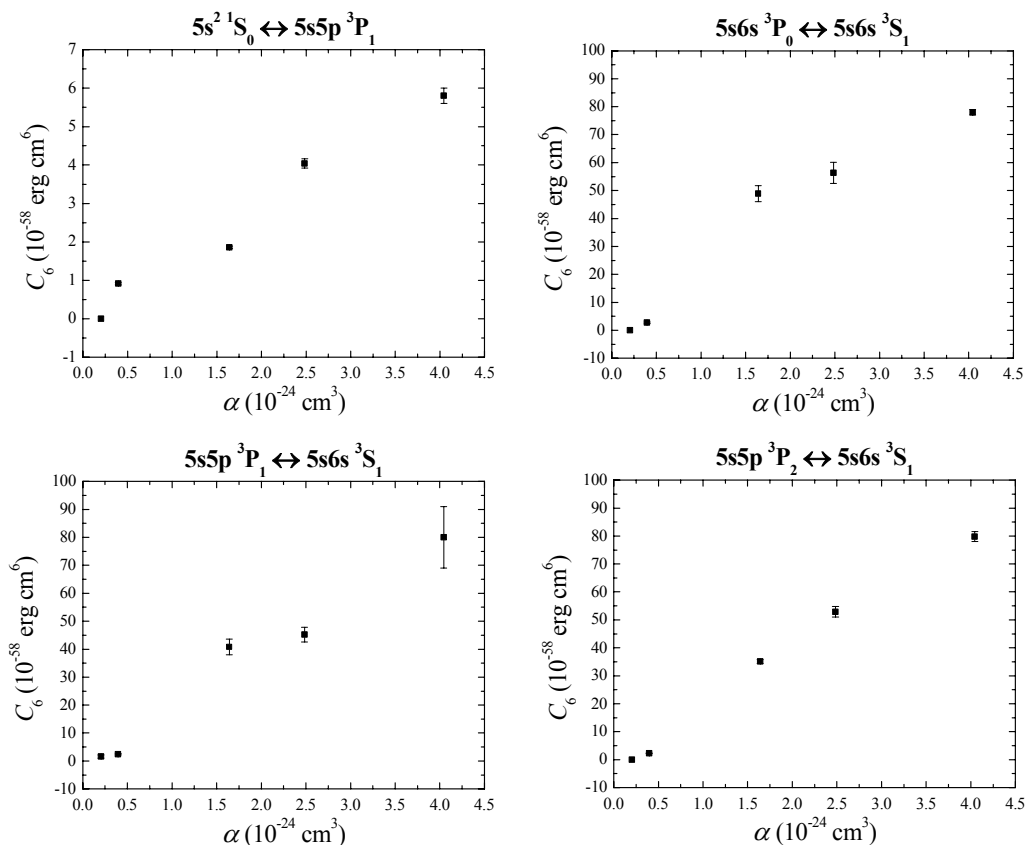


Figure 4-24. Atomic strontium difference potential constant  $C_6$  as a function of the polarizability of the perturbing species helium, neon, argon, krypton, and xenon for all energy states studied in this research. The difference potential constant is approximately linear in all cases.

Jones (6-12) difference potential constants  $C_6$  and  $C_{12}$  using the following equation

$$V(r_{\min}) = \frac{-C_6^2}{4C_{12}} \quad (4-24)$$

where  $V(r_{\min})$  is the value of the difference potential at the deepest part of the well. This calculation is performed on all the atomic strontium difference potential constants reported in Table 4-11 and the well depths are plotted in Figure 4-25 as a function of the polarizability of the perturbing species. In all cases except for the atomic strontium 5s5p

$^3P_0$  and  $5s6s\ ^3S_1$  energy states, the difference potential well depth appears to deepen from helium to argon, where it is deepest, and then to shallow out again through krypton and xenon. Between the  $5s5p\ ^3P_0$  and  $5s6s\ ^3S_1$  energy states, the well depth is deepest for neon and shallows out again through argon, krypton, and xenon. Similar behavior is observed in the theoretical work of Shabanova as can be seen in the lower right hand corners of Figures 4-16 and 4-18 [45]. This behavior is also observed in the difference potentials of other atoms. Rotondaro and Perram report the same trend in the difference potentials of atomic rubidium  $5^2S_{1/2}$  and  $5^2P_{1/2}$  and  $5^2S_{1/2}$  and  $5^2P_{3/2}$  energy states perturbed by helium, neon, argon, krypton, and xenon [44].

The trend observed in the previous paragraph is explained as follows. According to Equation 4-24, the difference potential well depths depend on the interplay between the difference potential constants  $C_6$  and  $C_{12}$ . That is, they depend on the balance between the attractive term  $C_6$  and the repulsive term  $C_{12}$ . If  $C_6$  and  $C_{12}$  are thought of as coordinates in a space, the difference potential constants may be plotted in a two dimensions and compared to contours of Equation 4-24. This is accomplished in Figure 4-26 for the difference potential constants of the  $5s^2\ ^1S_0$  and  $5s5p\ ^3P_1$  energy states given in Table 4-11. Each contour represents a well depth and only the first three contours, corresponding to well depths of  $-0.025$ ,  $-0.050$ , and  $-0.075\text{ cm}^{-1}$ , are labeled for clarity. The data points are plotted as open circles. As can be seen from this figure, the well depths for helium and xenon lie fairly near the “top” of the terrain while the argon data point lies deeper. Thus the well depths deepen from helium to argon and shallow out again from argon to xenon.

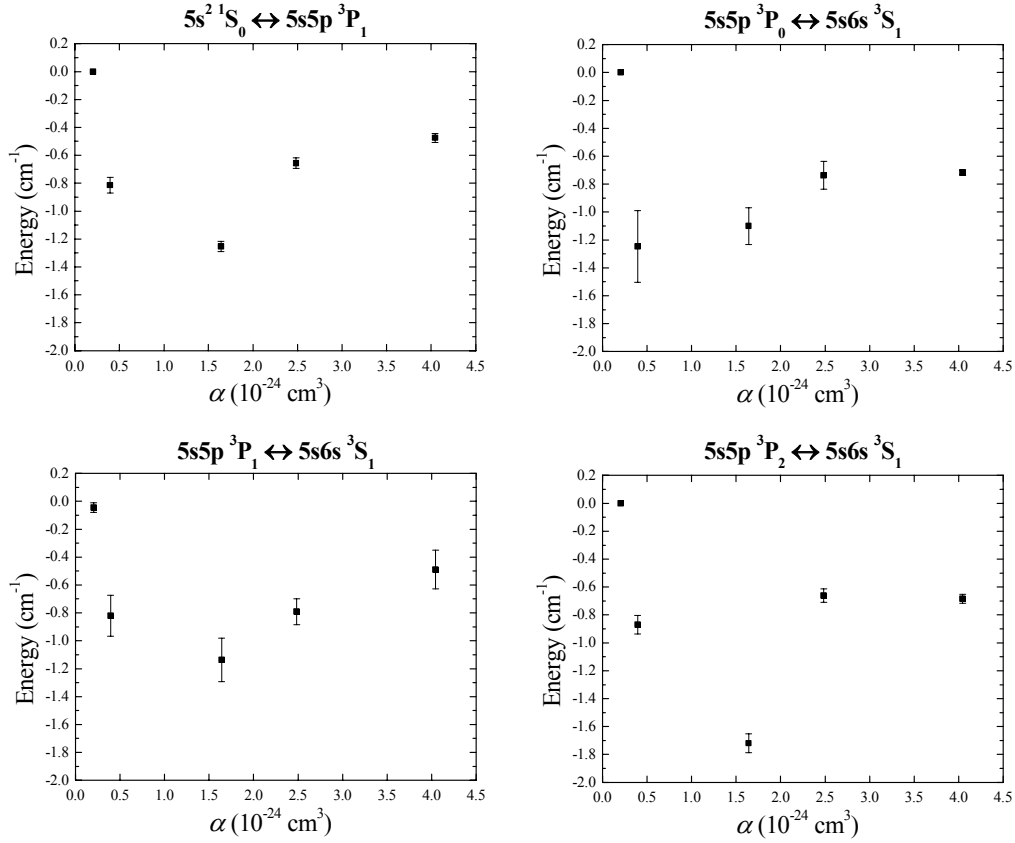


Figure 4-25. Atomic strontium difference potential well depths as a function of the polarizability of the perturbing species helium, neon, argon, krypton, and xenon for all energy states studied in this research

**4.3.3 Conclusion and Recommendations for Future Research** In summary, it appears that the line broadening and shifting cross section trends of the atomic strontium  $5s^2 \ ^1S_0 \rightarrow 5s5p \ ^3P_1$  transition with perturbing species' polarizability are consistent with physical intuition. That is, the line broadening cross sections increase uniformly with the polarizability of the perturbing species while the line shifting cross sections decrease uniformly. This trend, however, is not exhibited for the atomic strontium  $5s5p \ ^3P_{0,1,2} \rightarrow 5s6s \ ^3S_1$  transitions. In this case, the line broadening cross sections of all three transitions are smallest when perturbed by neon. This trend, while unexplained, is also reported by

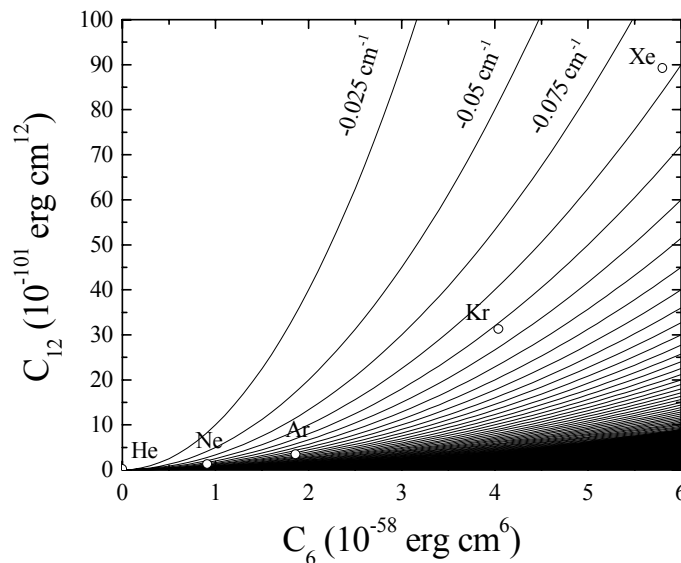


Figure 4-26. Difference potential constants  $C_6$  and  $C_{12}$  of the atomic strontium  $5s^2\ ^1S_0$  and  $5s5p\ ^3P_1$  energy states perturbed by helium, neon, argon, krypton, and xenon compared to contours of Equation 4-24. The helium and xenon data points lie on shallow parts of this terrain while argon lies deeper leading to the trends observed in Figure 4-25.

previous research on the analogous transitions of atomic calcium perturbed by the same species. The atomic strontium line shifting cross sections of these transitions, however, do uniformly decrease as expected.

To within 10%, the atomic strontium line broadening and shifting cross sections of the  $5s5p\ ^3P_{0,1,2} \rightarrow 5s6s\ ^3S_1$  transitions do not appear to exhibit any trends with the total angular momentum of the initial state. This lack of trend is different from what is observed in molecules. Previous researchers, however, claim that the upper state dominates the interaction and if the upper state is the same for all three transitions, no trend is expected [37, 39]. Also, atomic line broadening is thought to be dominated by elastic collisions while molecular line broadening by inelastic collisions. Since difference potentials are the origin of line broadening and shifting when elastic collisions

dominate, this apparent lack of trend in the line broadening and shifting cross sections indicates a lack of trend in the difference potentials.

The atomic strontium and noble gas difference potentials show that the helium difference potential is, in three of four cases, entirely repulsive. Also, the difference potential constant  $C_6$  trends appropriately with the polarizability of the perturbing species. And finally, the depth of the difference potential well for all energy states studied here is deepest for argon, yet relatively shallow for helium and xenon. This trend is also observed in previous research and explained in terms of the interplay between the difference potential constants  $C_6$  and  $C_{12}$ .

For future research, it should be noted that the line broadening and shifting measurements of atomic strontium performed in this dissertation have never been accomplished before. As is often the case with new work, the results come with large estimates of uncertainty. This is clearly seen by examining the atomic strontium line broadening and shifting cross sections presented in Figure 4-10. Future work in this area should then address this deficiency and produce less uncertain results. Several specific ideas to accomplish this are proposed.

The atomic strontium experiment of this research used absorption spectroscopy to measure spectral line profiles. Absorption spectroscopy, however, produces high signal-to-noise ratios because the reduction of a large signal is measured. The signal-to-noise issues of this research are clearly seen in Figure 4-2 where the “constant” laser source was quite noisy leading to the noisy line profiles of Figure 4-3. These noisy line profiles then led to Lorentzian linewidths with relatively large estimates of uncertainty.

With this in mind, the entire experiment should be reaccomplished using fluorescence spectroscopy instead. Fluorescence spectroscopy has the advantage of measuring signals on no background leading to much higher signal-to-noise ratios. If absorption spectroscopy is used again, however, it is recommended that a heat pipe apparatus be employed so the line profile may be measured and remeasured many times to reduce the signal-to-noise ratio.

Another interesting idea is to follow up on the observation of this work that the atomic strontium line broadening cross sections appear to be independent of the total angular momentum quantum number  $J''$  of the initial state. To investigate this, an atom with a large number of fine structure states corresponding to a wide range of  $J''$  values should be chosen for study. It would then be possible to measure the line broadening rates out of these states to see if any trends with  $J''$  emerge.

## V. Broadening of Diatomic Bismuth Spectral Lines

Broadening of rotational lines in the  $\nu''=3 \rightarrow \nu'=1$  vibrational manifold of the  $X(0_g^+) \rightarrow A(0_u^+)$  electronic transition of diatomic bismuth by noble gases was investigated using fluorescence spectroscopy. This chapter discusses the details of this experiment and what was learned from it. It is split into three sections. The first covers the design of the experiment, data acquisition and reduction details, results, and sources of error. The second provides an analysis of the data and includes a comparison with previous research. And finally, the last section draws conclusions from the analysis and makes recommendations for future research.

### 5.1 Measurement of Diatomic Bismuth Spectral Line Profiles

Lineshape profiles of diatomic bismuth rotational transitions in the  $\nu''=3 \rightarrow \nu'=1$  vibrational manifold of the  $X(0_g^+) \rightarrow A(0_u^+)$  electronic transition perturbed by the noble gases helium, neon, argon, and krypton were observed using the fluorescence induced by a narrowband tunable laser. The laser, being monochromatic compared to the frequency range of the transition, offered a direct means of observing the line profiles of each transition. The subsection to follow derives the equation necessary for reducing the data generated during this experiment. After that, the experimental apparatus is detailed. The next three subsections discuss data acquisition and reduction details and results, and the final subsection discusses possible sources of systematic error.

**5.1.1 Fluorescence Spectroscopy Using a Narrowband Source** Fluorescence spectroscopy using a narrowband source is perhaps the most efficient and noise-free way of observing the line profile of a transition. By this technique, a monochromatic tunable source is directed through a medium and the total laser-induced fluorescence intensity is observed from the side. This method is particularly effective because it involves observing a signal against a dark background. This often leads to a higher signal-to-noise ratio than absorption spectroscopy where the change in a large signal is measured.

As mentioned above, the line profile is observed indirectly as the total laser-induced fluorescence emitted by a medium when a monochromatic light source is scanned across a transition. The fluorescence intensity is governed by the rate at which an excited state is populated, which is, in turned, governed by the absorption rate. Mathematically, the absorption rate is expressed as

$$V \frac{dN_j}{dt} = N_j \ell \sigma_{abs}(x) I_0(x) \quad (5-1)$$

where  $V$  is the volume of medium illuminated by light of intensity  $I_0(x)$  at wavenumber  $x$ ,  $N_j$  is the number density of absorbing bodies in the lower quantum state  $j$ ,  $\ell$  is path length, and  $\sigma_{abs}(x)$  is the absorption cross section.

In the steady state, the absorption rate is the same as the radiative fluorescence rate  $I_{fl}(x)$  so that

$$I_{fl}(x) = N_j \ell \sigma_{abs}(x) I_0(x) \quad (5-2)$$

Substituting Equation 4-3 for the absorption cross section and solving for the lineshape functions gives



$$f(x) = \left( \frac{8\pi}{N_j \ell} \right) \left( \frac{cx_0^2}{A_{kj}} \right) \left( \frac{g_j}{g_k} \right) \left( \frac{I_f(x)}{I_0(x)} \right) \quad (5-3)$$

Similar to Equation 4-4, the lineshape function here is a series of constants times the ratio of the fluorescence intensity to incident light intensity [55]. This ratio is also called the normalized fluorescence intensity as it eliminates variations in the data due to source fluctuations. Equation 5-3 is the fundamental equation used to process raw data from the diatomic bismuth fluorescence experiment.

**5.1.2 Diatomic Bismuth Experimental Setup** The experimental apparatus was designed to create a bismuth vapor, mix it with a buffer gas, and record the transition profiles of interest as they were perturbed by a buffer gas. Bismuth is a solid at room temperature so vapor was created by heating a crucible of bismuth pellets in a six-way cross. P and R branch rotational line profiles were measured from  $J''=0$  to approximately  $J''=212$ . Rather than measure rotational lines individually, continuous spectra spanning an energy range of approximately  $130 \text{ cm}^{-1}$  from  $17208$  to  $17338 \text{ cm}^{-1}$  were measured.

A schematic diagram of the experimental apparatus is given in Figure 5-1. A Coherent 899-21 ring laser configured in dye mode and pumped by a Spectra Physics model 2080 argon ion laser lasing in the green at  $514.5 \text{ nm}$  was used to generate diatomic bismuth fluorescence in a six-way cross. The ring laser was operated with Exciton dye Rhodamine 590 Chloride which lases between  $16393$  and  $17544 \text{ cm}^{-1}$  ( $610$  and  $570 \text{ nm}$ ). The argon ion laser power output was about  $7 \text{ W}$  and the ring laser output ranged between  $300$  and  $400 \text{ mW}$ . This quantity varied depending on the alignment of the optics, the condition of the dye, and the wavelength to which the laser was tuned. The

ring laser was integrated with a wavemeter for frequency control and the system was operated by computer, which was also used to record experimental data. The ring laser center frequency was controlled to within  $0.0017\text{ cm}^{-1}$  (50 MHz) and its linewidth was nominally less than  $0.000033\text{ cm}^{-1}$  (1.0 MHz).

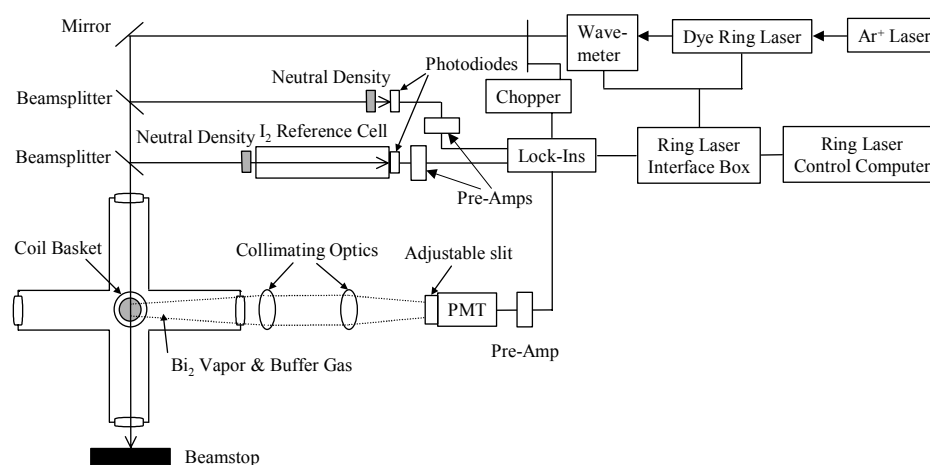


Figure 5-1. Schematic diagram of the diatomic bismuth fluorescence experimental apparatus

A  $\text{Bi}_2$  vapor was created in a six-way cross by heating bismuth pellets (Fluka, 99.998%) in a tungsten wire coil basket. The six-way cross provided vacuum containment for the introduction and control of buffer gases and was designed with windows through which laser light was introduced and side fluorescence observed. The coil basket was mounted on feed-through electrodes which were connected to a Lakeshore model 647 electromagnet constant-current power supply. The temperature of the bismuth pellets was controlled by adjusting the current through the tungsten wire coil basket from the constant-current power supply. Since this was the only part of the

apparatus which was heated, bismuth vapor diffused to the relatively cool walls of the six-way cross and plated out.

The dye laser beam was chopped by a Stanford Research Systems model SR540 chopper operating at 330 Hz and subsequently split in two places. The first split directed a beam onto a Hamamatsu type S2281 silicon photodiode shielded by a neutral density filter ( $N.D. = 3.3$ ) to monitor laser power. The second split directed a beam through a neutral density filter ( $N.D. = 3.0$ ), a cell containing an  $I_2$  vapor, and onto another Hamamatsu silicon photodiode. The absorption lines of  $I_2$  in this beam were used as frequency references. The neutral density filters kept the beams from saturating the detectors. Both photodiodes were powered by independent battery powered pre-amplifiers whose outputs were fed into separate Stanford Research Systems model SR850 lock-in amplifiers sensitive to the beam chopping frequency. The remaining beam was directed through the six-way cross directly above the heated bismuth and used to probe the transitions of interest.

Laser-induced fluorescence was monitored with an RCA C31034 photomultiplier tube which was chilled for optimal performance. It was powered by a Stanford Research Systems model PS325 high voltage power supply operated at 1200 V. The fluorescence was focused onto an adjustable slit using a pair of collimating optics (focal lengths 250 and 150 mm respectively). The slit was mated with a fiberoptic cable which was fed into the photomultiplier tube. The slit was also mounted on a three-degree of freedom translatable assembly which allowed it to be moved to maximize signal strength. The output of the photomultiplier was fed into a Stanford Research Systems model SR850 lock-in amplifier sensitive to the frequency at which the beam was chopped. The outputs

from all three lock-in amplifiers were fed into the computer controlling the laser so that signals as a function of frequency were recorded.

The six-way cross was connected to a gas handling system which allowed the chamber to be evacuated by a Varian SD-300 roughing pump. This achieved a pressure on the order of  $10^{-3}$  Torr before data was acquired. Pressure in the six-way cross was monitored through a tube leading to the edge of the six-way cross by an MKS Baratron capacitance manometer sensitive up to 1000 Torr. The signal from this device was conditioned by a type 270 MKS Baratron signal conditioner. The pressure reading was zeroed after the system was allowed to pump down for several hours. Because the diatomic bismuth was observed to have plated out on the interior walls of the six-way cross, the manometer only registered buffer gas pressure.

**5.1.3 Diatomic Bismuth Data Acquisition** The data acquisition phase of this experiment involved preparing a bismuth vapor under noble gas pressure and recording a spectrum. It was, however, not practical to scan the laser across the  $130\text{ cm}^{-1}$  range of interest in one session. While the laser operated reliably over wavelength ranges on the order of tens of wavenumbers, it required adjustments beyond that. Also, the amount of bismuth loaded in the cell was depleted after a limited period of time. For these reasons, the  $130\text{ cm}^{-1}$  region of interest was arbitrarily divided into an  $11\text{ cm}^{-1}$  region, six  $18\text{ cm}^{-1}$  regions, and a  $15\text{ cm}^{-1}$  region. These scans overlapped by  $0.33\text{ cm}^{-1}$  (10 GHz) to verify the computer controlling the laser was setting it to accurate starting and stopping points. Also, the  $130\text{ cm}^{-1}$  region of interest was scanned twice and the starting point shifted by  $0.167\text{ cm}^{-1}$  (5 GHz). This had the effect of placing the  $0.33\text{ cm}^{-1}$  breaks described in Section 4.1.3 exactly out of phase with the first scan. This was done to minimize the

impact the  $0.33\text{ cm}^{-1}$  breaks would have on the data analysis. If a break occurred at the height of a peak of interest then the second scan was used knowing the break would be  $0.167\text{ cm}^{-1}$  away.

As was mentioned in the previous section, the laser beam passed directly over the wire coil which heated the bismuth. In fact, the coil, which glowed white-hot when current was applied to it, was placed low in the six-way cross to keep it out of the field of view of the collimating optics and viewing slit so as not to flood the photomultiplier tube. This arrangement, however, produced a weak fluorescence signal. To increase it, buffer gas was allowed to flow from a port at the base of the six-way cross up to the vacuum port at the top of the cross. This had the effect of drawing the bismuth vapor plume up and raising the signal to a sufficient level.

The ring laser control computer was set to collect data from each of the three lock-in amplifiers every  $0.00167\text{ cm}^{-1}$  (50 MHz) and was scanned at a rate of  $0.033\text{ cm}^{-1}$  (1 GHz) per second. This was half the data density acquired in the atomic strontium experiment and the scan rate was twice as fast. The increase in scan speed was needed in order to collect a reasonable amount of data before the bismuth was depleted. The decrease in data density was acceptable because the signal-to-noise ratio remained relatively high at approximately 36:1 through the course of the data acquisition. Because of this, fewer data points were needed to accurately gauge the true signal strength. This combination of data interval and scan rate meant that a data point was taken every 50 ms. To accommodate this interval, the lock-in time constants were set to 10 ms.

Table 5-1 details the data acquisition matrix of the entire diatomic bismuth experiment. The goal was to obtain data points at equal pressure intervals. As in the

atomic strontium experiment, however, the signal strength diminished more rapidly with pressure as the atomic weight of the buffer gas increased. This is reflected in the maximum pressure applied for each noble gas. While the weakest usable signal was observed at approximately 400 Torr for helium and neon, this was true at only 305 Torr for argon and 100 Torr for krypton. In most cases only four data points were needed to accurately determine the spectral line broadening rate. This was because the signal-to-noise ratio in this experiment was consistently relatively high compared to the atomic strontium experiment. For krypton, only two data points were taken before lab supplies were depleted.

Table 5-1. Diatomic bismuth data acquisition matrix. This table gives the pressures at which the diatomic bismuth rotational line profiles were measured for each noble gas.

	Pressure (Torr)	Pressure (Torr)	Pressure (Torr)	Pressure (Torr)
He	103	205	305	405
Ne	102	202	303	404
Ar	102	202	250	305
Kr	50	100	-	-

An example of the raw data is given in Figure 5-2. It shows a small portion of the diatomic bismuth fluorescence signal, absorption signal in the iodine cell, and laser power as it was scanned incrementally across  $130\text{ cm}^{-1}$ . This particular example features the R(128) and P(115) rotational lines around  $17292.6\text{ cm}^{-1}$  perturbed by 102 Torr of neon. As before, there is a discontinuity every  $0.33\text{ cm}^{-1}$  (10 GHz). This was explained in Section 4.1.3. Also as before, the signals from the three detectors were read into the computer in discrete increments ranging from 0 to 4095. The absorption dips in iodine

were identified with an iodine atlas [17] and used as a frequency reference in order to assign the diatomic bismuth spectrum unambiguously. This was necessary because of interloping rotational lines from other vibrational manifolds that are clearly visible in Figure 5-2.

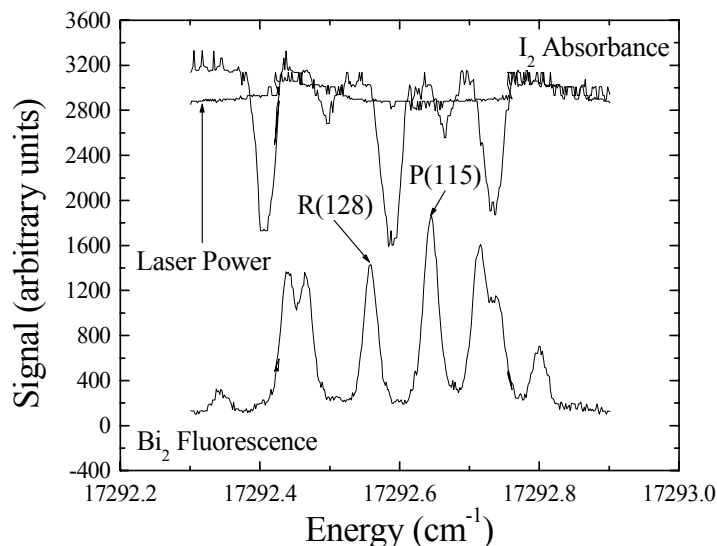


Figure 5-2. Raw data of the  $\text{Bi}_2$  R(128) and P(115) transitions in the  $v''=3 \rightarrow v'=1$  vibrational manifold of the  $X(0_g^+) \rightarrow A(0_u^+)$  electronic transition and  $\text{I}_2$  reference spectral lines around  $17292.6 \text{ cm}^{-1}$  perturbed by 102 Torr of neon

**5.1.4 Diatomic Bismuth Data Reduction** Raw diatomic bismuth fluorescence data was normalized to the laser signal intensity to give the lineshape profiles according to Equation 5-3. The iodine lineshape profiles were determined by taking the natural logarithm of the laser signal divided by the iodine absorption signal as given in Equation 4-4. The raw data presented in Figure 5-2 was reduced in this manner and is presented in

Figure 5-3. Because the signal-to-noise ratio remained relatively high through the course of the fluorescence experiment, Fourier filtering was not used on the final lineshape data.

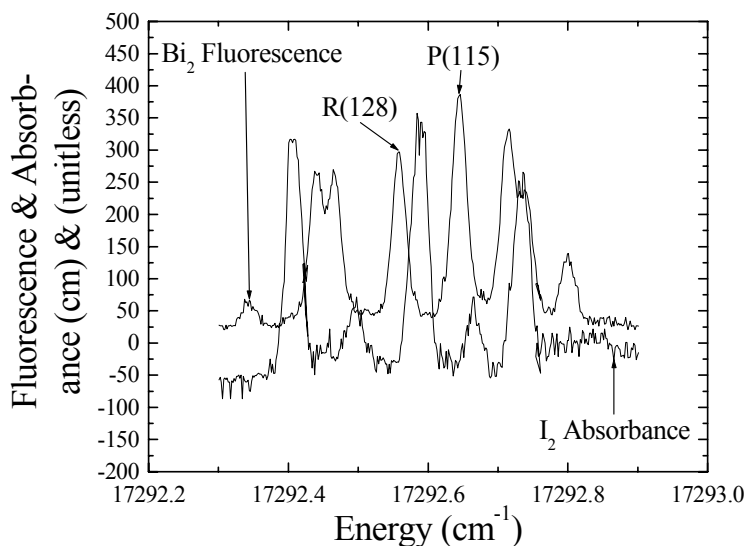


Figure 5-3.  $\text{Bi}_2$  fluorescence and  $\text{I}_2$  absorbance of the  $\text{Bi}_2$  R(128) and P(115) transitions in the  $\nu''=3 \rightarrow \nu'=1$  vibrational manifold of the  $X(0_g^+) \rightarrow A(0_u^+)$  electronic transition around  $17292.6 \text{ cm}^{-1}$  perturbed by 102 Torr of neon

Although 212 P and R branch rotational lines in the  $\nu''=3 \rightarrow \nu'=1$  vibrational manifold were observed in the  $130 \text{ cm}^{-1}$  range of data taken, only approximately every fifth P and R branch pair was analyzed. Table 5-2 gives a list of which lines were selected for detailed analysis. While most of the peaks analyzed occurred in pairs, an interloping peak occasionally disrupted one of the peaks and another nearby line was analyzed instead. The unidentified  $\text{Bi}_2$  lines in Figure 5-3 are from the  $\nu''=4 \rightarrow \nu'=2$  vibrational manifold within the same electronic transition. During the line fitting process they were included as extra peaks to be fit, but their fit parameters were discarded.



Table 5-2. P and R branch lines in the  $\text{Bi}_2$   $v''=3 \rightarrow v'=1$  vibrational manifold of the  $X(0_g^+) \rightarrow A(0_u^+)$  electronic transition selected for detailed analysis

P( $J''$ )	R( $J''$ )
20	33
50	63
55	68
60	73
65	78
70	83
75	88
80	93
85	98
90	103
95	108
100	113
105	118
110	123
115	128
120	133
125	140
127	143
131	148
135	154
140	158
141	164
145	169
150	170
155	173
160	178
165	183
171	185
172	188
175	194
180	199
186	200
187	203
190	208
195	-

Temperature determination was a major issue in this experiment as there was no thermocouple inside the six-way cross nor was there a reference cell whose data could be monitored for such information. The only possible experimental parameter which might have indicated bismuth temperature was the amount of current to heat the tungsten coil. This parameter, however, was thought to correspond poorly to bismuth temperature because the plume rose into a buffer gas at room temperature and was assumed to thermalize rapidly.

The temperature in the bismuth vapor was determined from the signal strengths of all observed transitions across the spectrum. Evaluating Equation 5-2 at line center  $x_0$  gives

$$I_f(x_0) = N_j \ell \sigma_{abs}(x_0) I_0(x_0) \quad (5-4)$$

According to the Boltzmann distribution

$$N_j = N \frac{(2J_j + 1)}{Z} e^{\frac{-E_j}{k_B T}} \quad (5-5)$$

where  $N$  is the density of diatomic bismuth,  $J_j$  is the rotational level of the lower state,  $E_j$  is the energy of the lower state, and  $Z$  is the partition function [52]. The energy of the lower state is known from the spectroscopy of diatomic bismuth and is given by Equation 2-73. To a very good approximation, this equation can be written as

$$E(3, J_j) \cong T(3) + B(3) J_j (J_j + 1) \quad (5-6)$$

The spectroscopic constants  $T(3)$  and  $B(3)$  are listed in Table 2-6. Inserting Equation 5-6 into Equation 5-5, Equation 5-5 into Equation 5-4, and rearranging gives

$$\ln\left(\frac{I_{fl}(x_0)}{I_0(x_0)(2J_j+1)}\right) = \frac{-B(3)}{k_B T} J_j(J_j+1) + \sigma_{abs}(x_0) \frac{N\ell}{Z} e^{\frac{-T(3)}{k_B T}} \quad (5-7)$$

Thus the natural logarithm of the ratio of the normalized peak fluorescence signal to the quantity twice the total angular momentum quantum number of the ground state plus one is linear in  $J_j(J_j+1)$ . The slope of this line is  $\frac{-B(3)}{k_B T}$ . All constants in this equation are

known except for temperature, which is then solved for if the slope is known.

Figure 5-4 gives an example of this method to determine temperature. The data set illustrated is from the diatomic bismuth spectrum perturbed by 102 Torr of neon. In this particular example, the slope of the line leads to a temperature of 303 K. This is approximately room temperature and verifies the assumption that the bismuth vapor thermalized rapidly as it rose into the viewing region. This method of temperature determination was applied to six data sets in which the signal strengths exhibited the linear trend and the bismuth temperature was found to be  $343 \pm 39$  K. This number was converted to a Gaussian FWHM of  $0.0112 \text{ cm}^{-1}$  and used as a fixed constant in the data fitting process. It was assumed to apply to all peaks at all pressures.

Normalized fluorescence profiles of the rotational lines were fit to the Voigt lineshape function and all parameters except the Gaussian linewidth were allowed to float. The Gaussian linewidth was held constant to the value reported in the previous paragraph. Continuing with the example featured in Figure 5-3, Figure 5-5 shows the two rotational lines fit in this manner. Given below the fit are the residuals. In all cases the residuals appear to be random giving confidence that the Voigt lineshape function accurately models the transition profiles. As stated previously, the lines interloping from

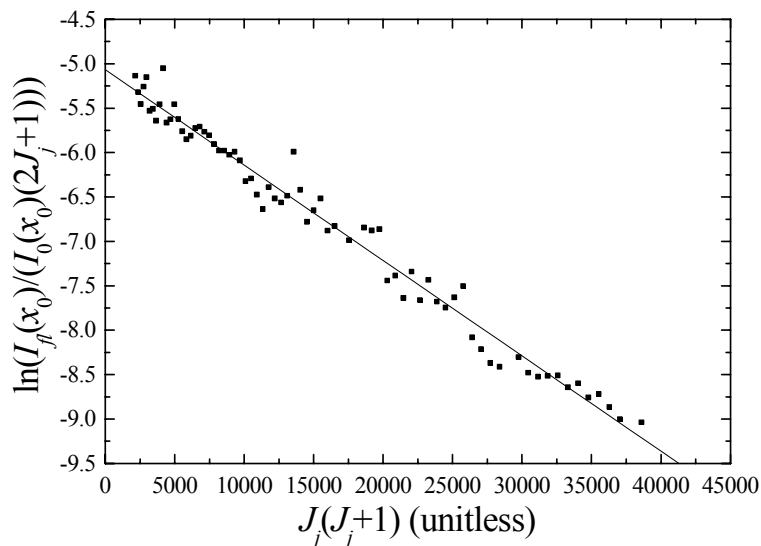


Figure 5-4. Bismuth vapor temperature determination plot. The signal strength data was taken from the diatomic bismuth spectrum perturbed by 102 Torr of neon.

the  $\nu''=4 \rightarrow \nu'=2$  vibrational manifold were also fit to Voigt profiles, but their fit parameters were discarded.

The Lorentzian linewidths were then plotted as a function of pressure and the data points fit to a line yielding the line broadening rate. For the R(128) and P(115) lines broadened by neon, these plots and the linear fit are given in Figure 5-6. The statistical uncertainty of the Lorentzian linewidth parameter of the Voigt fit was used as an estimate of the uncertainty in the linewidth. The uncertainty in the slope parameter of the least-squares fit to a line was used as an estimate of the uncertainty in the line broadening rate.

**5.1.5 Diatomic Bismuth Experimental Results** The line broadening rates of the  $\text{Bi}_2$  P and R branch lines from  $J''=20$  through  $J''=208$  are plotted in Figure 5-7 for perturbing gases helium, neon, argon, and krypton. The branch-independent quantum number  $m$  given by  $m = -J''$  in the P branch and  $m = J''+1$  in the R branch is used in this

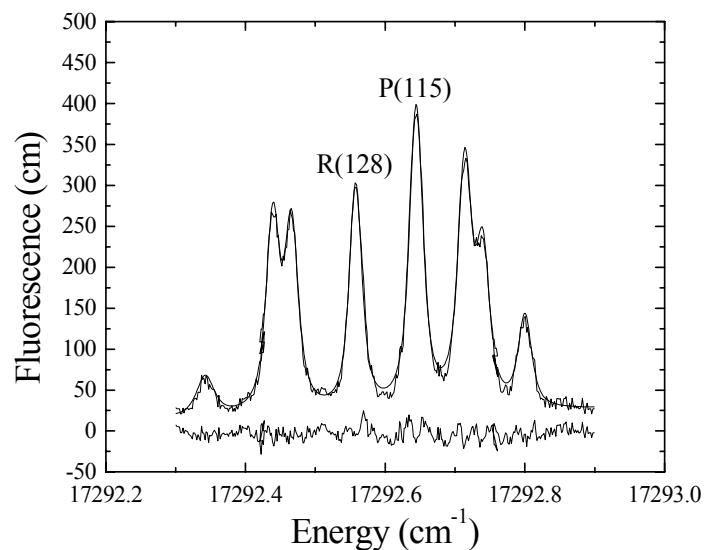


Figure 5-5. Normalized  $\text{Bi}_2$  fluorescence of the R(128) and P(115) transitions in the  $\nu''=3 \rightarrow \nu'=1$  vibrational manifold of the  $X(0_g^+) \rightarrow A(0_u^+)$  electronic transition around  $17292.6 \text{ cm}^{-1}$  perturbed by 102 Torr of neon. A Voigt profile fit to these lines is superimposed on the data and the residuals given below.

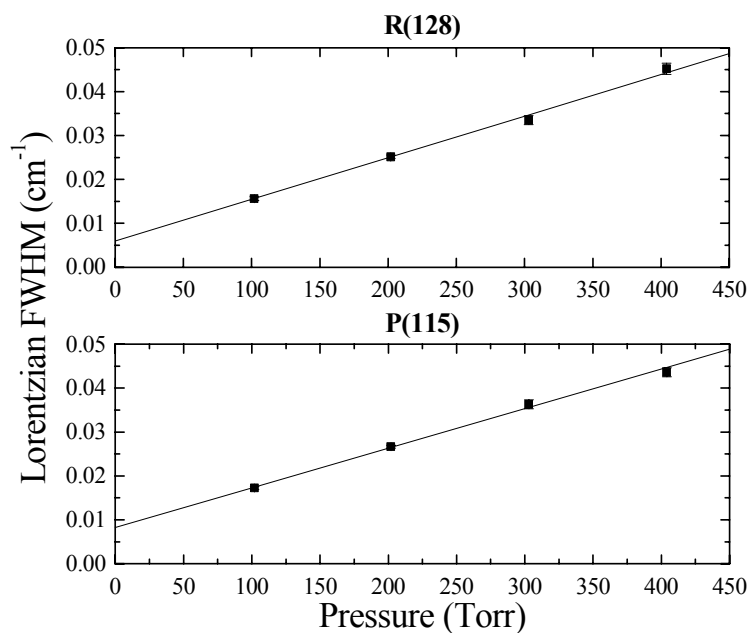


Figure 5-6. Lorentzian linewidths (FWHM) of the  $\text{Bi}_2$  R(128) and P(115) transitions in the  $\nu''=3 \rightarrow \nu'=1$  vibrational manifold of the  $X(0_g^+) \rightarrow A(0_u^+)$  electronic transition around  $17292.6 \text{ cm}^{-1}$  as a function of neon pressure superimposed with linear fits

plot [1]. Only one pair of lines below  $J''=50$  was analyzed because P and R branch lines were so close together below this level that they were indistinguishable when broadened and were not suitable for analysis. The krypton line broadening rates have no estimate of uncertainty because only two pressure data points were taken in that case yielding an unambiguous linear fit. A list of the line broadening rates and their uncertainties is given in Appendix C.

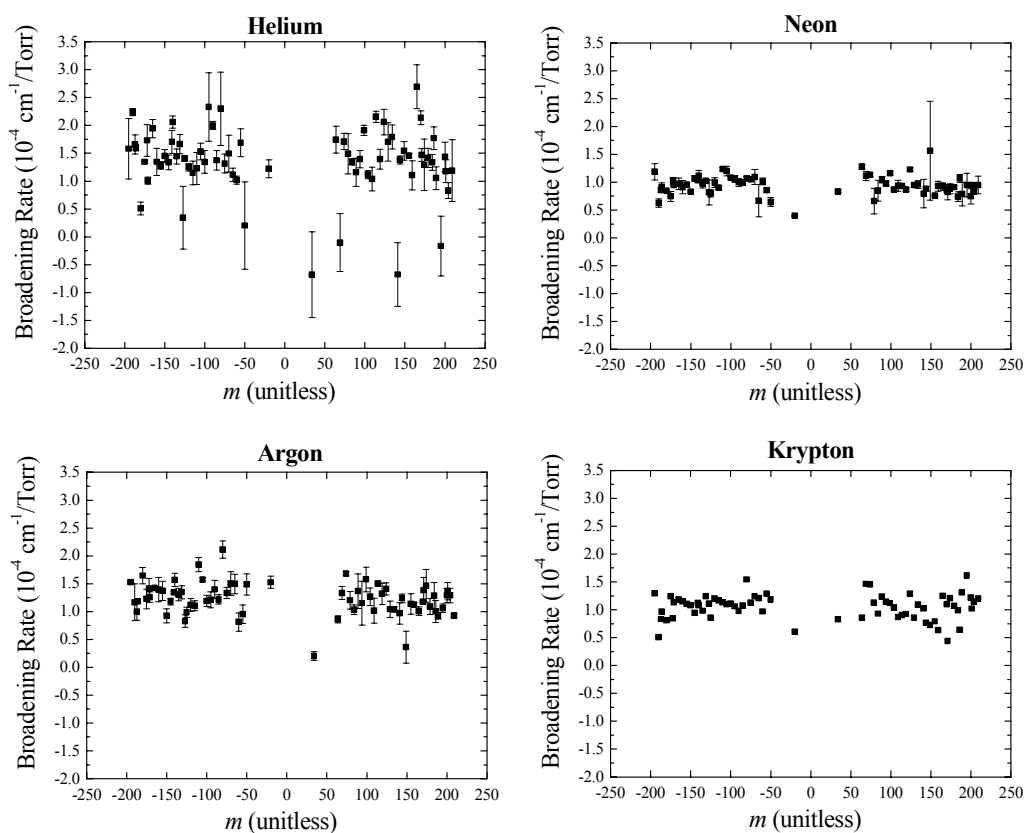


Figure 5-7.  $\text{Bi}_2$  line broadening rates of rotational lines in the  $\nu''=3 \rightarrow \nu'=1$  vibrational manifold of the  $X(0_g^+) \rightarrow A(0_u^+)$  electronic transition broadened by helium, neon, argon, and krypton as a function of the branch-independent quantum number  $m$

**5.1.6 Systematic Errors in the Diatomic Bismuth Experiment** Up to this point, the only discussion of uncertainty has been in regards to the statistical uncertainty associated with the Lorentzian linewidth of the nonlinear Voigt fit and the uncertainty of the slope parameter in the linear fit of the Lorentzian linewidths as a function of pressure. Neither of these uncertainties account for possible sources of systematic error. This is addressed in the current section.

As in the previous chapter, it is argued that three possible sources of systematic error to the line broadening rates presented in Figure 5-7 did not significantly contribute to the uncertainties reported there. This, again, is mainly because line broadening rates are ratios of changes in quantities and even if the quantities themselves are inaccurate, changes are not necessarily so. The three possible sources of systematic error considered here include errors in the Gaussian linewidth (or temperature), pressure, and energy calibration. Each is considered separately.

As stated above, the Gaussian linewidths of the Voigt line profiles fit to the fluorescence data were locked during the fitting process to  $0.0112 \text{ cm}^{-1}$ . The impact of an inaccurate determination of this linewidth on the Lorentzian linewidth was determined through a sensitivity analysis. That is, for a given set of data, the Gaussian linewidth was varied and the data refit to determine its impact on the Lorentzian linewidth. It was found that although changes in the Gaussian linewidth had an impact on the Lorentzian linewidth (raising the Gaussian linewidth lowered the Lorentzian linewidth and vice versa), there was no significant change to the overall line broadening or shifting rate. In quantitative terms, changing the Gaussian linewidth by 6% had less than a 0.5% impact on the line broadening rate. This is within the experimental uncertainty previously

established for line broadening rate measurements in this research. Therefore, systematic errors in the Gaussian linewidth did not contribute significantly to the uncertainty in the diatomic bismuth line broadening rates.

The next possible source of systematic error in the line broadening rates is the measurement of buffer gas pressure. As stated above, buffer gas pressures were measured in a tube leading to the edge of the six-way cross. Because diatomic bismuth was observed to have plated out on the interior walls of the six-way cross, the capacitance manometer only registered buffer gas pressure. Any systematic error in this pressure reading would have no impact on the line broadening and shifting rates because these rates only depend on the change in and not the absolute magnitude of the pressure. Therefore, systematic errors in pressure did not contribute to the uncertainty in the diatomic bismuth broadening rates.

The last possible source of systematic error was the energy calibration of the line profiles. This possibility, however, is immediately dismissed because of the accuracy of the calibration as displayed in Appendix A. Using the I<sub>2</sub> absorption lines and the iodine atlas [17], the ring laser and its associated control computer were calibrated to give all transition lines to within several hundredths of a wavenumber of the known values reported by Franklin [13]. This accuracy was achieved across the entire 130 cm<sup>-1</sup> range of the experiment. Therefore, the accuracy across a one-tenth wavenumber region of an individual rotational line was very good.



## 5.2 Analysis of Diatomic Bismuth Line Broadening Rates

The diatomic bismuth line broadening rate measurements described in the previous section are analyzed in this section. It is divided into two parts. The first part converts the line broadening rates to cross section and compares these results to previous researchers. The second part converts the line broadening rates of a few particular transitions studied here to sum total quenching rate constants and compares these to total quenching rate constants measured by a previous researcher.

**5.2.1 Diatomic Bismuth Line Broadening Cross Sections** In this section, the conversion from line broadening rate to cross section is derived and applied to the data in Figure 5-7. These cross sections are then compared to results published by previous authors. First, however, the proper conversion must be determined. According to the theory of Chapter II, there are two ways to convert broadening rate to cross section depending on the type of interaction which occurs between the species of interest and the perturbing species. If elastic collisions dominate, Equation 2-79 is used. If inelastic collisions dominate, Equation 2-104 is used. This distinction is important because these equations differ by a factor of two.

In order to determine which type of collision dominates the interaction of diatomic bismuth with noble gases, the energy spacing between a rotational energy level and the next higher level in the lower state of the transition is compared to the average kinetic energy of collision. This will indicate whether rotational energy transfer to higher states is possible. If so, then inelastic collisions are assumed to dominate since rotational energy transfer to lower states is always possible regardless of the energy spacing of the states.

Rotational energy spacing is given to a sufficient accuracy by Equation 5-6. This implies that the energy difference between a state  $j$  and the next higher state  $j+1$

$\Delta E(3, J_{j,j+1})$  is

$$\Delta E(3, J_{j,j+1}) = 2B(3)(J_j + 1) \quad (5-8)$$

The average kinetic energy of a collision between two species in the gas phase, here called  $KE_{avg}$ , is given by [52]

$$KE_{avg} = \frac{3}{2} k_B T \quad (5-9)$$

Applying the appropriate constants to Equations 5-8 and evaluating it for the range of rotational levels investigated in this research ( $20 \leq J_j \leq 208$ ) gives  $0.950 \text{ cm}^{-1} \leq$

$\Delta E(3, J_{j+1,j}) \leq 9.46 \text{ cm}^{-1}$ . The average kinetic energy of collision according to Equation 5-9, however, is  $358 \text{ cm}^{-1}$ . The average kinetic energy of collision greatly exceeds the energy spacing between an energy level and the next higher level thereby easily allowing collisional energy transfer to higher rotational energy states. Therefore, inelastic collisions are assumed to dominate and Equation 2-104 is used to convert line broadening rate to cross section.

With the proper conversion to cross section established, Equation 2-104 is rewritten in terms of pressure, temperature, and wavenumber. This conversion is outlined in Section 4.2.1 and, when applied to Equation 2-104, gives

$$\sigma^q = \sqrt{\frac{\pi^3 \mu k_B T c^2}{2}} \frac{\Delta(\delta x_L)}{\Delta P} \quad (5-10)$$

where  $\sigma^q$  is the sum of the total quenching cross sections from the lower and upper states  $\sigma_j^q$  and  $\sigma_k^q$  respectively. That is,

$$\sigma^q = \sigma_j^q + \sigma_k^q \quad (5-11)$$

Equation 5-10 converts the Lorentzian line broadening rate  $\frac{\Delta(\delta x_L)}{\Delta P}$  into a cross section  $\sigma^q$ .

The diatomic bismuth line broadening rates of P and R branch lines in the  $v''=3 \rightarrow v'=1$  vibrational manifold of the  $X(0_g^+) \rightarrow A(0_u^+)$  electronic transition shown in Figure 5-7 are converted to cross section by Equation 5-10. The results of this are presented in Figure 5-8. Also, a list of the line broadening cross sections is given in Appendix C.

Next, prior relevant research outlined in Chapter III is compared to the results displayed above in order to gain confidence in the analysis presented here. For each noble gas, two figures are presented. The first plots the results of this work with previous work on the homonuclear molecules  $O_2$  and  $Br_2$ . The second figure plots the results of this work with previous work on the heteronuclear molecules  $NO$  and  $CO$ . The comparison is performed in this fashion to avoid cluttered plots.

Beginning with helium, Figure 5-9 shows the line broadening cross sections of  $Bi_2$  perturbed by helium along with the  $O_2$  results of Pope [41]. The two results are on the same order of magnitude, however, the uncertainties of the  $Bi_2$  cross sections are large compared to those of  $O_2$  and are relatively imprecise and scattered. Also, the  $Bi_2$  results do not appear to exhibit any trend with the branch-independent quantum number  $m$ . Figure 5-10 shows the line broadening cross sections of  $Bi_2$  perturbed by helium

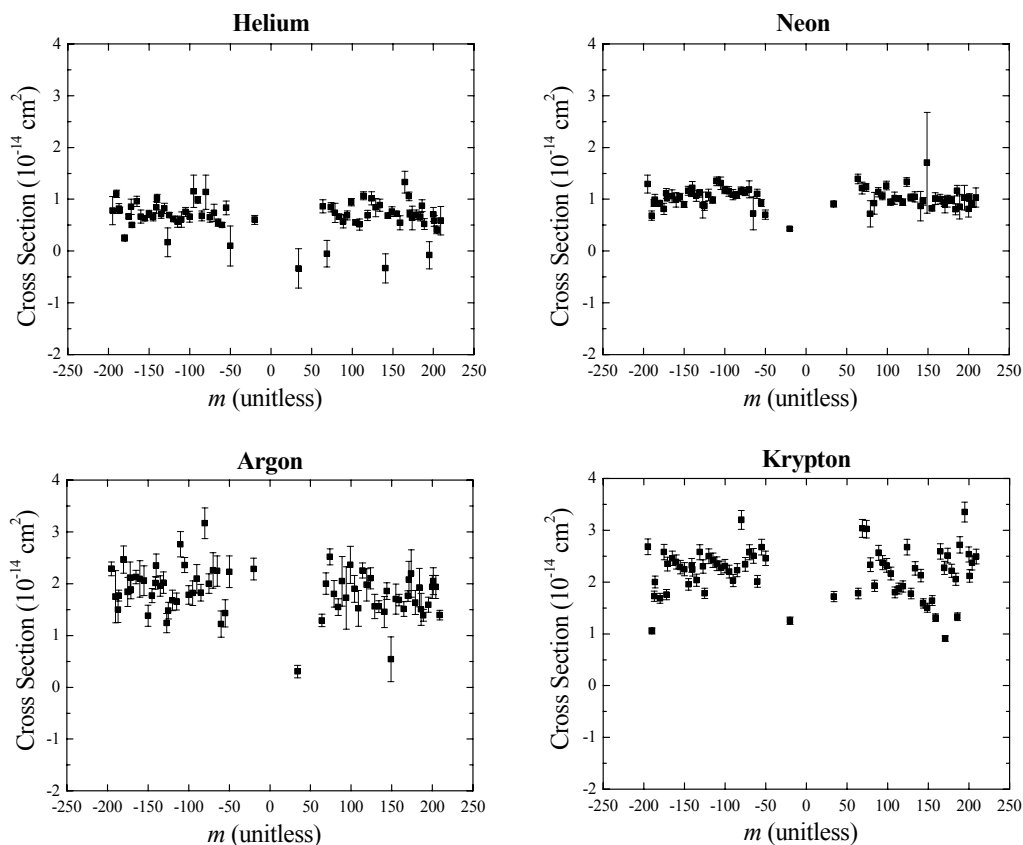


Figure 5-8.  $\text{Bi}_2$  line broadening cross sections of rotational lines in the  $\nu''=3 \rightarrow \nu'=1$  vibrational manifold of the  $X(0_g^+) \rightarrow A(0_u^+)$  electronic transition broadened by helium, neon, argon, and krypton as a function of the branch-independent quantum number  $m$ . These cross sections are computed from the line broadening rates presented in Figure 5-7 using Equation 5-10.

along with the NO results of Pope [41] and the CO results of Luo *et al.* [36]. The assessment of the comparison is the same as for Figure 5-9.

Next, Figures 5-11 and 5-12 plot Pope's  $\text{O}_2$  and NO data respectively [41] along with the line broadening cross sections of  $\text{Bi}_2$  perturbed by neon reported here. The uncertainties in the  $\text{Bi}_2$  cross sections are smaller than in the case of helium, yet there still appears to be a fair amount of scatter in the data points. The orders of magnitude of this

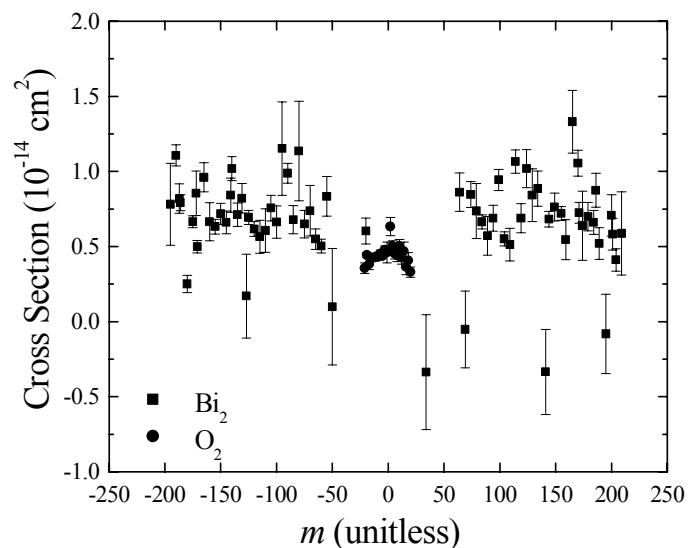


Figure 5-9. Comparison of line broadening cross sections of  $O_2$  rotational lines perturbed by helium (Pope [41]) with the line broadening cross sections of  $Bi_2$  similarly perturbed from this research. Both sets of data are plotted as a function of the branch-independent quantum number  $m$  and all cross sections are computed by Equation 5-10 from the line broadening rates.

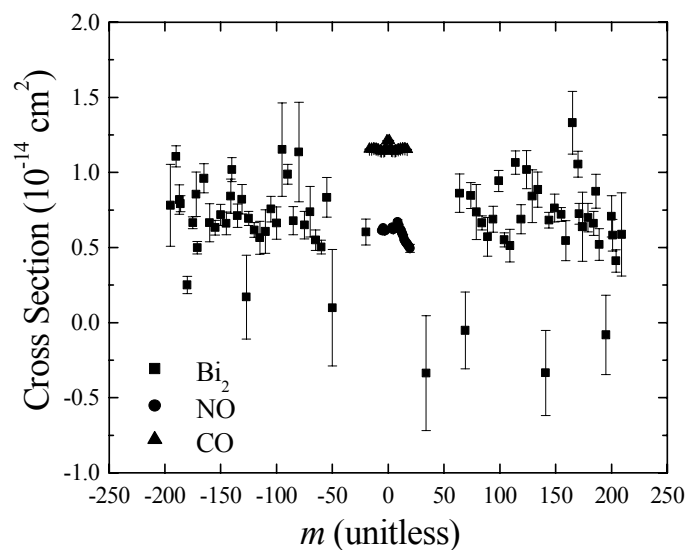


Figure 5-10. Comparison of line broadening cross sections of NO (Pope [41]) and CO (Luo *et al.* [36]) rotational lines perturbed by helium with the line broadening cross sections of  $Bi_2$  similarly perturbed from this research. All sets of data are plotted as a function of the branch-independent quantum number  $m$  and all cross sections are computed by Equation 5-10 from the line broadening rates.

work, however, are certainly on the same order as Pope's. Also again, there is no clear trend of  $\text{Bi}_2$  cross section with  $m$  in contrast to the  $\text{O}_2$  and NO results.

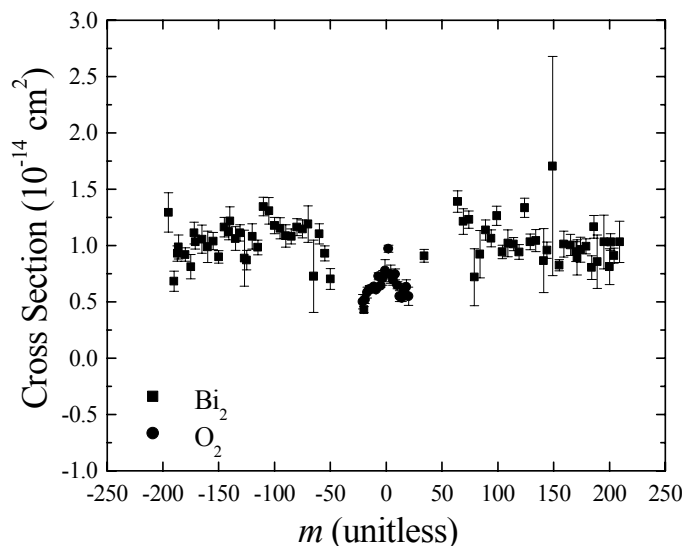


Figure 5-11. Comparison of line broadening cross sections of  $\text{O}_2$  rotational lines perturbed by neon (Pope [41]) with the line broadening cross sections of  $\text{Bi}_2$  similarly perturbed from this research. Both sets of data are plotted as a function of the branch-independent quantum number  $m$  and all cross sections are computed by Equation 5-10 from the line broadening rates.

Figure 5-13 shows a comparison of the line broadening cross sections of  $\text{Bi}_2$  perturbed by argon presented in this work with the line broadening cross sections of  $\text{Br}_2$  and  $\text{O}_2$  published by Innes *et al.* [28] and Pope [41] respectively. Again, the oxygen cross sections show a definite trend with  $m$  while the  $\text{Br}_2$  lines are reported not to. The  $\text{Bi}_2$  cross sections again show no trend with  $m$  and are relatively uncertain and highly erratic by comparison. All three sets of data, however, are on the same order of magnitude. The comparison presented in Figure 5-14, which compares the line

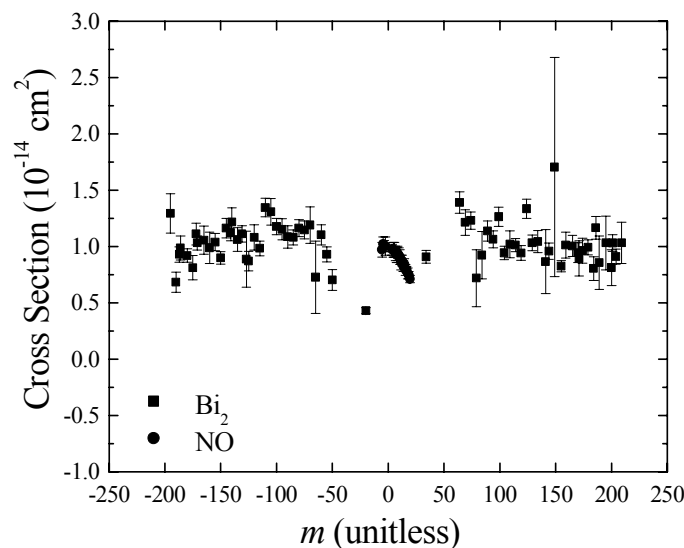


Figure 5-12. Comparison of line broadening cross sections of NO rotational lines perturbed by neon (Pope [41]) with the line broadening cross sections of Bi<sub>2</sub> similarly perturbed from this research. Both sets of data are plotted as a function of the branch-independent quantum number  $m$  and all cross sections are computed by Equation 5-10 from the line broadening rates.

broadening caused by argon of this work with the similar CO work of Luo *et al.* [36] and NO work of Pope [41], shows the same trends.

The final set of comparisons involves line broadening caused by krypton. Figure 5-15 compares the Bi<sub>2</sub> results of this work with the O<sub>2</sub> results and Figure 5-16 with the NO results of Pope [41]. In both comparisons, the O<sub>2</sub> and NO trends with  $m$  are readily visible yet no such trend is observed in Bi<sub>2</sub>. Also, while the Bi<sub>2</sub> cross section uncertainties are rather small, the scatter in the data is every pronounced. All cross sections, however, are on the same order of magnitude.

In summary, the trend of line broadening cross section with  $m$  is evident in the relatively light molecules O<sub>2</sub>, NO, and CO, yet is conspicuously absent in the Bi<sub>2</sub> line broadening cross sections of this research and the Br<sub>2</sub> line broadening cross sections of

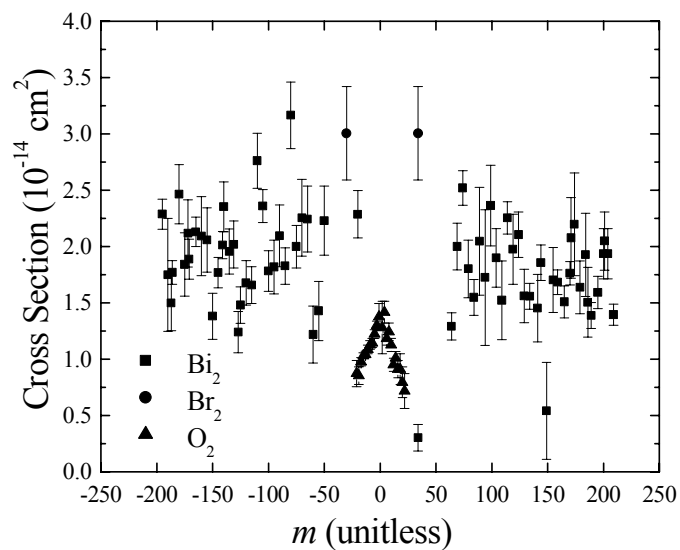


Figure 5-13. Comparison of line broadening cross sections of  $\text{Br}_2$  (Innes *et al.* [28]) and  $\text{O}_2$  (Pope [41]) rotational lines perturbed by argon with the line broadening cross sections of  $\text{Bi}_2$  similarly perturbed from this research. All sets of data are plotted as a function of the branch-independent quantum number  $m$  and all cross sections are computed by Equation 5-10 from the line broadening rates.

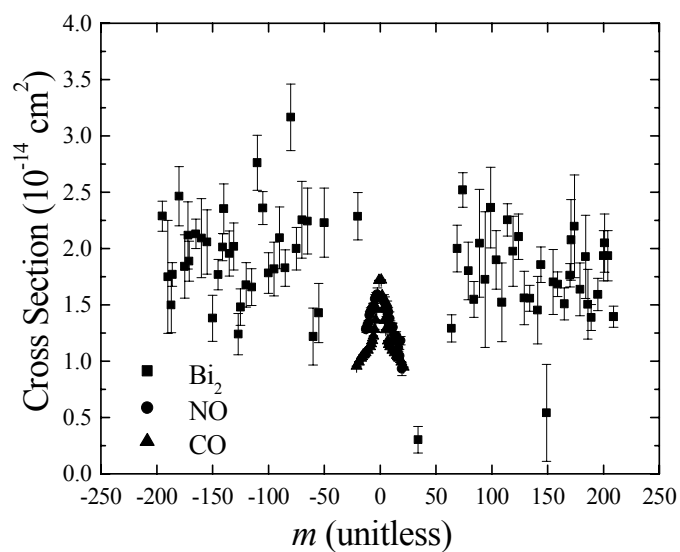


Figure 5-14. Comparison of line broadening cross sections of  $\text{NO}$  (Pope [41]) and  $\text{CO}$  (Luo *et al.* [36]) rotational lines perturbed by argon with the line broadening cross sections of  $\text{Bi}_2$  similarly perturbed from this research. All sets of data are plotted as a function of the branch-independent quantum number  $m$  and all cross sections are computed by Equation 5-10 from the line broadening rates.



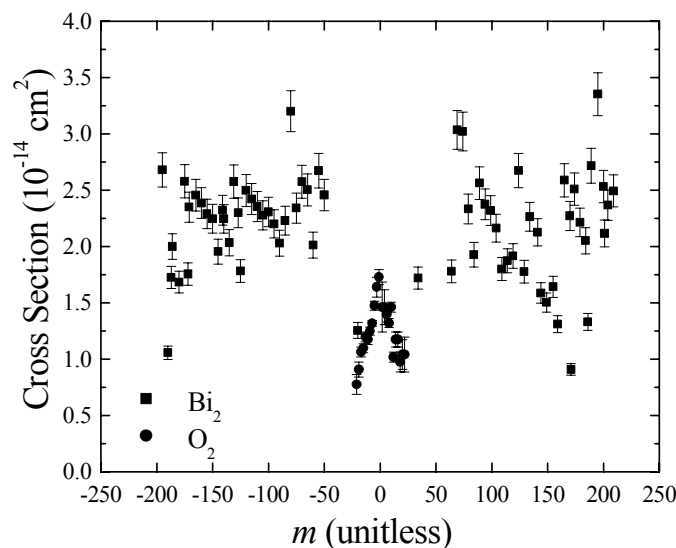


Figure 5-15. Comparison of line broadening cross sections of  $O_2$  rotational lines perturbed by krypton (Pope [41]) with the line broadening cross sections of  $Bi_2$  similarly perturbed from this research. Both sets of data are plotted as a function of the branch-independent quantum number  $m$  and all cross sections are computed by Equation 5-10 from the line broadening rates.

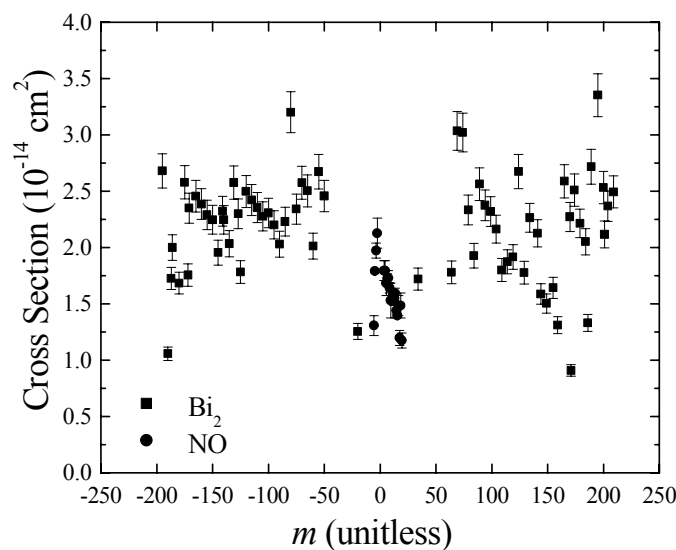


Figure 5-16. Comparison of line broadening cross sections of  $NO$  rotational lines perturbed by krypton (Pope [41]) with the line broadening cross sections of  $Bi_2$  similarly perturbed from this research. Both sets of data are plotted as a function of the branch-independent quantum number  $m$  and all cross sections are computed by Equation 5-10 from the line broadening rates.

Innes *et al.* as well [28]. The reasons for this will be speculated upon in the next subsection.

It is noted that the line broadening cross sections of this work exhibit relatively large uncertainties and are fairly imprecise (*i.e.* there is considerable scatter in the data). This is attributed to the fact that the diatomic bismuth rotational spectrum is extremely dense with lines. As noted in the previous section, the vibrational manifold of interest in this work ( $v''=3 \rightarrow v'=1$ ) is interspersed with rotational lines of the  $v''=4 \rightarrow v'=2$  manifold. These extra lines were included in the lineshape fitting process, which evidently introduced uncertainty into the line broadening measurements of interest. On the whole, however, the line broadening cross sections of this work are on the same order of magnitude as those reported by previous researchers. The cross sections derived from this research are therefore deemed valid.

**5.2.2 Diatomic Bismuth Sum Total Quenching Rate Constants** In this section, several of the diatomic bismuth line broadening rates measured in this research are converted to sum total quenching rate constant and compared with previous total quenching rate constant data. Franklin reported total quenching rate constants from rotational levels in the diatomic bismuth  $v'=1$  vibrational manifold of the  $A(0_u^+)$  electronic state [13]. Since the sum total quenching rate constant is the sum of the lower state and upper state quenching rate constants, Franklin's values represent a lower bound for the sum total quenching rate constants derived from the current research and serves as a comparison.

First, the conversion from line broadening rate to the sum total quenching rate constant is established. This simply involves converting Equation 2-108 to wavenumbers and pressure and solving for the sum total quenching rate constant. This gives

$$k^q = 2\pi k_b Tc \frac{\Delta(\delta x_L)}{\Delta P} \quad (5-12)$$

The conversion is simply a change of variables of the line broadening rate multiplied by a factor of  $2\pi$ .

This conversion is applied to the line broadening rates reported here for the diatomic bismuth P(172) and R(170) rotational lines broadened by helium and the R(200) rotational line broadened by helium, neon, and argon. The P(172) and R(170) rotational lines are chosen because they share the same upper rotational state of  $J'=171$ . Although the P(202) line has the same upper state as the R(200) line, it is obscured in the spectral data by the interloping rotational transitions. Consequently, no data is presented for the P(202) transition. These values are compared in Table 5-3 to the total quenching rate constants of the upper states  $J'=171$  and  $J'=201$  in the  $\nu'=1$  vibrational manifold of the  $A(0_u^+)$  electronic state reported by Franklin [13].

In all cases, the sum total quenching rate constants of this research are larger than the upper state quenching rate constants reported by Franklin. Since Franklin's values represent a lower bound to the sum total quenching rate constants, the present work compares favorably his previous work.

Table 5-3. Comparison of the total quenching rate constants of two diatomic bismuth rotational levels in the  $\nu'=1$  vibrational manifold of the  $A(0_u^+)$  electronic state reported by Franklin [13] with the sum of the total quenching rate constants derived by Equation 5-12 from the appropriate line broadening rates of this work

	$J' = 171$		$J' = 201$	
	Franklin [13]	Holtgrave	Franklin [13]	Holtgrave
	$k_k^q$ ( $10^{-10}$ cm <sup>3</sup> /sec)	$k^q$ ( $10^{-10}$ cm <sup>3</sup> /sec)	$k_k^q$ ( $10^{-10}$ cm <sup>3</sup> /sec)	$k^q$ ( $10^{-10}$ cm <sup>3</sup> /sec)
He	8.91(0.17)	11.6(2.3) <sup>1</sup>	7.65(0.13)	7.9(1.6) <sup>2</sup>
		9.8(1.4) <sup>2</sup>		
Ne	-	-	6.22(0.26)	6.35(0.75) <sup>2</sup>
Ar	-	-	6.41(0.23)	9.2(1.4) <sup>2</sup>
<sup>1</sup> P Branch				
<sup>2</sup> R Branch				

### 5.3 Discussion of the Diatomic Bismuth Line Broadening Experiment

In this final section, some observations are made and conclusions drawn from the diatomic bismuth line broadening rate analysis presented in the previous section. It is split into three subsections; one concerning the diatomic bismuth line broadening cross sections presented in Section 5.2.1, another concerning the diatomic bismuth sum total quenching rate constants presented in Section 5.2.2, and a conclusion and recommendations for future research.

**5.3.1 Discussion of Diatomic Bismuth Line Broadening Cross Sections** The primary observation noted in the analysis of the diatomic bismuth line broadening cross sections is the lack of trend with the branch-independent quantum number  $m$  or, more directly, the total angular momentum quantum number  $J''$  of the initial state. This indicates, but Equation 2-105, that the sum total quenching rate constants of the lower and upper states of the transition do not depend on the total angular momentum of the

initial state. This lack of trend is also noted in the previous work accomplished on Br<sub>2</sub>. The theory which explains line broadening when inelastic collisions dominate is that of inelastic collisions and pressure broadening presented in Chapter II. Therefore, this lack of trend is explained in terms of rotational energy transfer by inelastic collisions.

It is the assertion of this researcher that the lack of line broadening cross section trend with the branch-independent quantum number  $m$  is because the fraction of collisions which have enough energy to raise the molecule to the next higher energy state or beyond remains approximately constant across the range of rotational levels investigated. As derived in Chapter II, the line broadening rate is the sum of the total quenching rate constants from the lower and upper states of the transition when inelastic collisions dominate. The quenching rate constants depend on the fraction of those collisions which inelastically raise or lower the energy of the molecule. Inelastic collisions which lower the energy are always allowed regardless of collision energy. However, collisions which raise the energy are only allowed if there is enough kinetic energy in the collision. Therefore, if this fraction of collisions which may raise the energy of the molecule remains constant for the lower and upper states of all transitions studied, then the line broadening cross section is expected to remain constant as well.

This explanation is supported as follows. According to the Boltzmann distribution, the fraction of bodies  $f(E)dE$  in the vapor phase with translational energy between  $E$  and  $E + dE$  is given by [52]

$$f(E)dE = \frac{2}{\sqrt{\pi}} \left( \frac{1}{k_B T} \right)^{\frac{3}{2}} \sqrt{E} e^{\frac{-E}{k_B T}} dE \quad (5-13)$$

Using this equation and knowing the energy gap to the next higher level of a molecule, it is possible to compute the fraction of collisions with enough translational energy to raise the molecule's energy by integrating Equation 5-13 from this energy to infinity. That is,

$$F = \int_{E_{\min}}^{\infty} f(E)dE \quad (5-14)$$

where  $F$  is the fraction of molecules with energy greater than or equal to  $E_{\min}$ .  $E_{\min}$  is the minimum amount of translational energy needed to inelastically raise the energy state and is the same as the energy difference between a rotational state and the next higher state.

Using Equation 5-8 for  $E_{\min}$  and Equation 5-14, the fraction  $F$  of collisions with enough translational energy to raise a molecule one rotational level and beyond is computed for the diatomic bismuth energy states studied in this research and the energy states of  $\text{Br}_2$ ,  $\text{O}_2$ ,  $\text{NO}$ , and  $\text{CO}$  to which this research is compared. For  $\text{Bi}_2$ , the spectroscopic constants  $B(v)$  are given in Table 2-6 and the temperature was determined to be 343 K as detailed previously. It is clear at this point one must choose which state of the transition for which to compute  $F$ ; the lower state or upper state. Since the relevant rotational constant is nearly the same for both, the choice makes little difference in the final result. For consistency, the state which gives the smaller  $E_{\min}$  is chosen. This is, in all cases, the upper state. Table 5-4 gives the relevant rotational constants for  $\text{Br}_2$ ,  $\text{O}_2$ ,  $\text{NO}$ , and  $\text{CO}$  along with the temperatures at which the respective line broadening rates were measured. All spectroscopic constants in this table are gleaned from Herzberg [24].

The computations of  $F$  described in the previous paragraph are plotted in Figures 5-17 and 5-18. Figure 5-17 plots  $F$  for  $\text{Br}_2$ ,  $\text{O}_2$ ,  $\text{NO}$ , and  $\text{CO}$  while Figure 5-18 plots  $F$

for  $\text{Bi}_2$ . All fractions are plotted as a function of the branch-independent quantum number  $m$  of the transition similar to the way line broadening cross sections are plotted in Figures 5-8 through 5-16.

Table 5-4. Upper state rotational constants of  $\text{Br}_2$ ,  $\text{O}_2$ ,  $\text{NO}$ , and  $\text{CO}$  along with the temperatures at which the line broadening rates of these molecules were measured.

These constants are used in Equations 5-16 and 5-15 to determine the fraction of collisions with enough translational energy to inelastically raise a molecule one rotational level. All constants are quoted from Herzberg [24].

	$B(v')$ ( $\text{cm}^{-1}$ )	$T$ (K)
$\text{Br}_2$	0.0595	300
$\text{O}_2$	1.40041	295
$\text{NO}$	1.7046	295
$\text{CO}$	1.9313	296

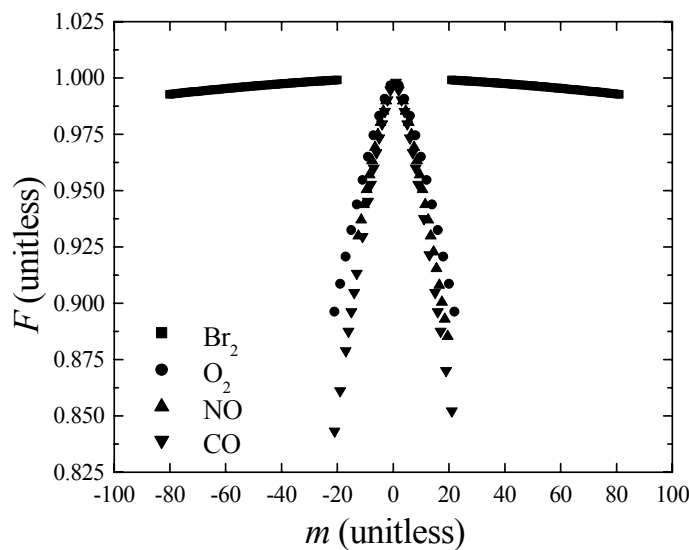


Figure 5-17. Fractions of collisions with enough translational energy for inelastic collisions to raise a molecule one rotational level or more in the upper states of  $\text{Br}_2$ ,  $\text{O}_2$ ,  $\text{NO}$ , and  $\text{CO}$  as a function of the branch-independent quantum number  $m$ . These fractions are computed for the temperatures reported by the researchers.

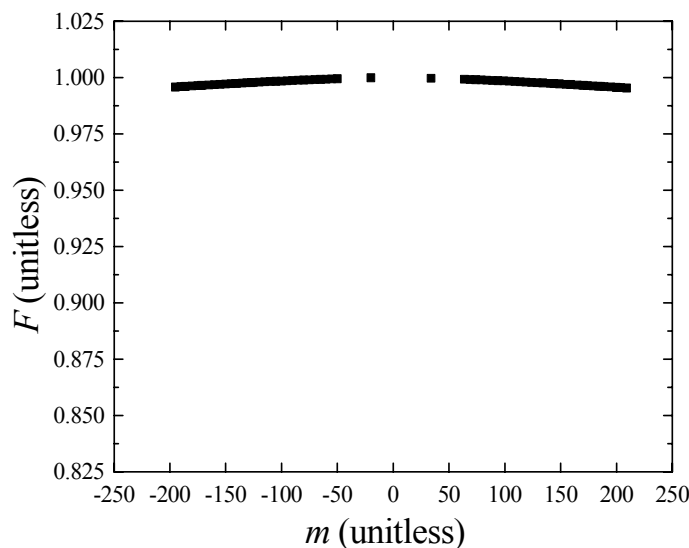


Figure 5-18. Fractions of collisions with enough translational energy for inelastic collisions to raise a molecule one rotational level or more in the upper state of  $\text{Bi}_2$  as a function of the branch-independent quantum number  $m$ . These fractions are computed for 343 K, which is the temperature at which the line broadening rates were measured.

It is clear from Figure 5-17 that the fraction of collisions with enough energy available to inelastically raise a molecule one rotational level and beyond varies significantly for  $\text{O}_2$ ,  $\text{NO}$ , and  $\text{CO}$ , but little for  $\text{Br}_2$ . Also, as shown in Figure 5-18, this fraction varies little for  $\text{Bi}_2$  as well. Therefore, the dependence of the line broadening cross section on  $J''$  (as manifest by the dependence on the branch-independent quantum number  $m$ , which is  $-J''$  in the P branch and  $J''+1$  in the R branch [1]) is due to the dependence of the energy spacing of the rotational states on  $J''$ . In light molecules, like  $\text{O}_2$ ,  $\text{NO}$ , and  $\text{CO}$ , the energy spacings rapidly get large as a function of  $J''$ . This is because their rotational constants are relatively large. In heavy molecules, like  $\text{Br}_2$  and  $\text{Bi}_2$  which have smaller rotational constants, the energy spacings do not change significantly over a large range of  $J''$  values.



### 5.3.2 Discussion of Diatomic Bismuth Sum Total Quenching Rate Constants

As concluded in the analysis, the sum total quenching rate constants derived from the diatomic bismuth line broadening data of this research are larger than the upper state quenching rate constants reported by Franklin. This comparison is favorable since the sum total quenching rate constants represent the sum of the quenching rate constants from the lower and upper states. It is interesting to note in Table 5-3, however, that the sum total quenching rate constants are only slightly larger than the quenching rate constants reported by Franklin [13]. This indicates that the majority of the diatomic bismuth line broadening is caused by quenching collisions from the upper state of the transition rather than the lower state. Currently no theory exists which predicts the magnitudes of the two contributions to the line broadening rate. Therefore, any future theoretical work in this area will have to account for this observation.

**5.3.3 Conclusion and Recommendations for Future Research** In summary, the line broadening cross sections of diatomic bismuth rotational lines in the  $\nu''=3 \rightarrow \nu'=1$  vibrational manifold of the  $X(0_g^+) \rightarrow A(0_u^+)$  electronic transition do not depend on the total angular momentum of the initial state. This observation, and similar observations for  $\text{Br}_2$ , are explained in terms of the energy spacing of their rotational levels. In  $\text{Bi}_2$  and  $\text{Br}_2$ , the rotational energy states are so close together that the fraction of inelastic collisions allowed to raise the energy of the molecule is not significantly different between transitions that start in low-lying rotational states and those that start in high-lying rotational states. Therefore, there is no dependence on  $J''$  or total angular momentum.

Also, when converted to sum total quenching rate constant, the line broadening rates of diatomic bismuth rotational lines agree with previous experimental measurements of the total quenching rate constant of the upper state. That is, the sum total quenching rate constants are consistently larger than the total quenching rate constant as expected. However, the sum total quenching rate constants are only slightly larger indicating that quenching in the upper state causes the majority of line broadening in diatomic bismuth.

For future research, it should be noted that the line broadening measurements of diatomic bismuth performed in this dissertation have never been accomplished before. As with the work on atomic strontium, the results come with large estimates of uncertainty. The problem of acquiring better diatomic bismuth line broadening data is much harder than doing so for atomic strontium because the difficulty in this case was the denseness of the rotational spectra. Fluorescence spectroscopy was used and, as mentioned above, the signal-to-noise ratio was consistently good. The uncertainties in this experiment were caused primarily by the interloping lines which had to be fit along with the lines of interest. The way to avoid this difficulty, then, is to somehow suppress transitions from the vibrational manifold which is not of interest. Accomplishing this, however, is an experimentally daunting task. An idea on how this might be accomplished is presented next.

It may be possible to record the line profiles of selected individual rotational lines with less interference from other lines as follows. Create a bismuth vapor as described in this experiment and allow it to expand rapidly into a vacuum through a pinhole. This should have the effect of cooling the vapor so that fewer molecules are in the  $v''=4$  vibrational manifold as are in the current experiment. This should lead to a reduction in

the signal intensities of the interloping peaks. Also, cooling the vapor has the added benefit of reducing the Gaussian linewidth of each profile thereby reducing the uncertainty in the Lorentzian linewidth.

Another avenue of investigation stemming from this research is the connection between the line broadening rate of a transition broadened by inelastic collisions and the sum total quenching rate constant. This issue was addressed in this research with the comparison of the diatomic bismuth line broadening data with prior total quenching rate constant data from the upper state. The two results, however, are not directly comparable. One is merely expected to be larger than the other. It would be good to further test this connection by actually measuring the total quenching rate constant from the lower state, the total quenching rate constant from the upper state, summing the two, and comparing the result to the line broadening rate.

**Appendix A. Theoretical and Measured Bi<sub>2</sub> Rotational Line Positions**  
**( $\nu''=3 \rightarrow \nu'=1$ ,  $X(0_g^+) \rightarrow A(0_u^+)$ )**

Table A-1. Theoretical and measured diatomic bismuth rotational line positions in the  $\nu''=3 \rightarrow \nu'=1$  vibrational manifold of the  $X(0_g^+) \rightarrow A(0_u^+)$  electronic transition.

Measured line positions are taken from the work of Franklin [13].

$J''$	Theoretical $P(J'')$ (cm <sup>-1</sup> )	Measured $P(J'')$ (cm <sup>-1</sup> )	Theoretical $R(J'')$ (cm <sup>-1</sup> )	Measured $R(J'')$ (cm <sup>-1</sup> )
1	17337.5288	-	17337.6463	-
2	17337.4775	-	17337.6734	-
3	17337.4201	-	17337.6944	-
4	17337.3567	-	17337.7093	-
5	17337.2872	-	17337.7182	-
6	17337.2116	-	17337.7210	-
7	17337.1300	-	17337.7178	-
8	17337.0424	-	17337.7085	-
9	17336.9486	-	17337.6931	-
10	17336.8489	-	17337.6717	-
11	17336.7430	-	17337.6442	-
12	17336.6311	-	17337.6107	-
13	17336.5132	-	17337.5711	-
14	17336.3891	-	17337.5254	-
15	17336.2591	-	17337.4737	-
16	17336.1229	-	17337.4159	-
17	17335.9807	-	17337.3521	-
18	17335.8325	-	17337.2822	-
19	17335.6781	-	17337.2062	-
20	17335.5178	-	17337.1242	-
21	17335.3513	-	17337.0361	-
22	17335.1788	-	17336.9419	-
23	17335.0003	-	17336.8417	-
24	17334.8156	-	17336.7354	-
25	17334.6250	-	17336.6231	-
26	17334.4282	-	17336.5047	-
27	17334.2254	-	17336.3802	-
28	17334.0166	-	17336.2497	-
29	17333.8016	-	17336.1131	-
30	17333.5807	-	17335.9705	-

31	17333.3536	-	17335.8218	-
32	17333.1205	-	17335.6670	-
33	17332.8814	-	17335.5062	-
34	17332.6361	-	17335.3393	-
35	17332.3849	-	17335.1663	-
36	17332.1275	-	17334.9873	-
37	17331.8641	-	17334.8022	-
38	17331.5947	-	17334.6110	-
39	17331.3191	-	17334.4138	-
40	17331.0376	-	17334.2105	-
41	17330.7499	-	17334.0012	-
42	17330.4562	-	17333.7858	-
43	17330.1564	-	17333.5643	-
44	17329.8506	-	17333.3367	-
45	17329.5387	-	17333.1031	-
46	17329.2208	-	17332.8635	-
47	17328.8968	-	17332.6177	-
48	17328.5667	-	17332.3659	-
49	17328.2306	-	17332.1081	-
50	17327.8884	-	17331.8441	-
51	17327.5401	-	17331.5741	-
52	17327.1858	-	17331.2981	-
53	17326.8254	-	17331.0159	-
54	17326.4590	-	17330.7277	-
55	17326.0865	-	17330.4335	-
56	17325.7079	-	17330.1331	-
57	17325.3233	-	17329.8267	-
58	17324.9326	-	17329.5143	-
59	17324.5358	-	17329.1957	-
60	17324.1330	-	17328.8711	-
61	17323.7241	-	17328.5405	-
62	17323.3092	-	17328.2037	-
63	17322.8882	-	17327.8609	-
64	17322.4611	-	17327.5120	-
65	17322.0280	-	17327.1571	-
66	17321.5888	-	17326.7961	-
67	17321.1435	-	17326.4290	-
68	17320.6922	-	17326.0558	-
69	17320.2348	-	17325.6766	-
70	17319.7713	-	17325.2913	-
71	17319.3018	-	17324.9000	-
72	17318.8262	-	17324.5025	-
73	17318.3446	-	17324.0990	-

74	17317.8569	-	17323.6894	-
75	17317.3631	-	17323.2738	-
76	17316.8632	-	17322.8521	-
77	17316.3573	-	17322.4243	-
78	17315.8453	-	17321.9904	-
79	17315.3273	-	17321.5505	-
80	17314.8032	-	17321.1045	-
81	17314.2730	-	17320.6524	-
82	17313.7368	-	17320.1942	-
83	17313.1945	-	17319.7300	-
84	17312.6461	-	17319.2597	-
85	17312.0917	-	17318.7833	-
86	17311.5311	-	17318.3009	-
87	17310.9646	-	17317.8123	-
88	17310.3919	-	17317.3177	-
89	17309.8132	-	17316.8170	-
90	17309.2284	-	17316.3103	-
91	17308.6376	-	17315.7975	-
92	17308.0407	-	17315.2785	-
93	17307.4377	-	17314.7536	-
94	17306.8286	-	17314.2225	-
95	17306.2135	-	17313.6854	-
96	17305.5923	-	17313.1421	-
97	17304.9650	-	17312.5928	-
98	17304.3317	-	17312.0375	-
99	17303.6923	-	17311.4760	-
100	17303.0468	-	17310.9085	-
101	17302.3952	-	17310.3349	-
102	17301.7376	-	17309.7552	-
103	17301.0739	-	17309.1694	-
104	17300.4042	17300.405	17308.5775	-
105	17299.7283	17299.732	17307.9796	-
106	17299.0464	17299.050	17307.3756	-
107	17298.3584	17298.367	17306.7655	-
108	17297.6644	17297.674	17306.1493	-
109	17296.9643	17296.973	17305.5271	-
110	17296.2581	17296.268	17304.8987	-
111	17295.5458	17295.554	17304.2643	-
112	17294.8274	17294.835	17303.6238	-
113	17294.1030	17294.111	17302.9772	-
114	17293.3725	17293.380	17302.3245	-
115	17292.6359	17292.643	17301.6657	-
116	17291.8933	17291.898	17301.0009	-

117	17291.1446	17291.153	17300.3299	17300.332
118	17290.3898	17290.399	17299.6529	17299.659
119	17289.6289	17289.638	17298.9698	17298.976
120	17288.8619	17288.871	17298.2806	17298.291
121	17288.0889	17288.097	17297.5853	17297.597
122	17287.3098	17287.317	17296.8840	-
123	17286.5246	17286.535	17296.1765	17296.188
124	17285.7333	17285.743	17295.4630	17295.472
125	17284.9360	17284.946	17294.7433	17294.753
126	17284.1326	17284.143	17294.0176	-
127	17283.3231	17283.333	17293.2858	17293.295
128	17282.5075	17282.519	17292.5479	17292.557
129	17281.6858	17281.697	17291.8039	17291.813
130	17280.8581	-	17291.0538	17291.065
131	17280.0243	17280.035	17290.2977	17290.308
132	17279.1844	17279.196	17289.5354	-
133	17278.3384	17278.350	17288.7670	17288.784
134	17277.4864	-	17287.9926	17288.003
135	17276.6282	17276.640	17287.2120	-
136	17275.7640	17275.778	17286.4254	-
137	17274.8937	-	17285.6327	-
138	17274.0173	17274.026	17284.8338	-
139	17273.1348	17273.145	17284.0289	-
140	17272.2463	17272.258	17283.2179	17283.231
141	17271.3516	17271.361	17282.4008	17282.414
142	17270.4509	17270.463	17281.5776	17281.591
143	17269.5441	17269.554	17280.7483	17280.761
144	17268.6312	17268.642	17279.9129	-
145	17267.7122	17267.725	17279.0714	17279.084
146	17266.7872	17266.797	17278.2238	17278.238
147	17265.8560	17265.868	17277.3701	17277.383
148	17264.9188	17264.931	17276.5103	17276.526
149	17263.9754	17263.988	17275.6444	17275.662
150	17263.0260	17263.038	17274.7724	17274.784
151	17262.0705	17262.083	17273.8943	17273.906
152	17261.1089	17261.122	17273.0101	17273.022
153	17260.1413	17260.154	17272.1198	-
154	17259.1675	17259.181	17271.2234	17271.237
155	17258.1876	17258.202	17270.3209	-
156	17257.2017	17257.218	17269.4123	17269.427
157	17256.2097	17256.226	17268.4976	17268.510
158	17255.2115	17255.227	17267.5768	17267.590
159	17254.2073	17254.224	17266.6498	17266.663

160	17253.1970	17253.214	17265.7168	17265.733
161	17252.1806	17252.195	17264.7777	-
162	17251.1581	17251.171	17263.8324	17263.852
163	17250.1295	17250.139	17262.8811	17262.897
164	17249.0948	17249.104	17261.9237	17261.940
165	17248.0541	17248.067	17260.9601	17260.978
166	17247.0072	17247.022	17259.9904	17260.004
167	17245.9542	17245.969	17259.0147	17259.029
168	17244.8952	17244.909	17258.0328	-
169	17243.8300	17243.844	17257.0448	17257.059
170	17242.7587	-	17256.0507	17256.066
171	17241.6814	17241.698	17255.0504	17255.065
172	17240.5980	17240.614	17254.0441	17254.059
173	17239.5084	-	17253.0317	17253.047
174	17238.4128	17238.427	17252.0131	17252.029
175	17237.3110	17237.327	17250.9885	17251.006
176	17236.2032	17236.218	17249.9577	17249.970
177	17235.0892	17235.104	17248.9208	17248.933
178	17233.9692	17233.986	17247.8778	17247.894
179	17232.8431	17232.857	17246.8286	17246.844
180	17231.7108	17231.727	17245.7734	17245.789
181	17230.5725	-	17244.7120	17244.730
182	17229.4280	17229.446	17243.6446	17243.661
183	17228.2775	17228.293	17242.5710	17242.588
184	17227.1208	17227.134	17241.4912	17241.508
185	17225.9581	-	17240.4054	17240.419
186	17224.7892	17224.803	17239.3135	17239.329
187	17223.6142	17223.630	17238.2154	17238.231
188	17222.4332	17222.448	17237.1112	17237.126
189	17221.2460	17221.259	17236.0009	17236.017
190	17220.0527	17220.065	17234.8844	17234.901
191	17218.8533	-	17233.7619	17233.778
192	17217.6478	17217.661	17232.6332	17232.648
193	17216.4362	-	17231.4984	-
194	17215.2185	-	17230.3574	17230.374
195	17213.9947	17214.013	17229.2104	17229.226
196	17212.7648	17212.776	17228.0572	17228.074
197	17211.5287	17211.544	17226.8979	-
198	17210.2866	17210.305	17225.7324	17225.747
199	17209.0383	-	17224.5609	17224.576
200	17207.7839	-	17223.3832	17223.399
201	17206.5234	-	17222.1993	17222.215
202	17205.2568	-	17221.0094	17221.023



203	17203.9841	-	17219.8133	17219.826
204	17202.7053	-	17218.6111	17218.629
205	17201.4204	-	17217.4027	-
206	17200.1293	-	17216.1882	17216.205
207	17198.8321	-	17214.9676	17214.985
208	17197.5288	-	17213.7409	17213.758
209	17196.2194	-	17212.5080	17212.521
210	17194.9039	-	17211.2690	-
211	17193.5823	-	17210.0238	17210.037

## Appendix B. Impact Parameter Integrals

This appendix gives the analytical solutions to the impact parameter integrals (Equations 2-92 and 2-93). These solutions were computed by *Mathematica* and are given in standard *Mathematica* notation. “Gamma” refers to the gamma function

$\Gamma(z) = \int_0^\infty t^{z-1} e^{-t} dt$ . “HypergeometricPFQ” refers to the generalized hypergeometric function  ${}_pF_q(a; b; z)$  [58].

$$\begin{aligned}
 B(\alpha) = & \int_0^\infty \sin^2 \left\{ \frac{1}{2} \left( \frac{\alpha}{x^{11}} - \frac{1}{x^5} \right) \right\} x dx = \\
 & \frac{1}{16 \sqrt{11} \pi^2} \left( 5^{5/22} \left( \frac{1}{\alpha^2} \right)^{4/11} \cos \left[ \frac{4\pi}{55} \right] \cos \left[ \frac{3\pi}{11} \right] \cos \left[ \frac{5\pi}{11} \right] \cos \left[ \frac{26\pi}{55} \right] \cos \left[ \frac{37\pi}{55} \right] \cos \left[ \frac{48\pi}{55} \right] \csc \left[ \frac{\pi}{11} \right] \right. \\
 & \csc \left[ \frac{7\pi}{11} \right] \csc \left[ \frac{8\pi}{11} \right] \csc \left[ \frac{9\pi}{11} \right] \csc \left[ \frac{10\pi}{11} \right] \text{Gamma} \left[ \frac{8}{55} \right] \text{Gamma} \left[ \frac{19}{55} \right] \text{Gamma} \left[ \frac{6}{11} \right] \text{Gamma} \left[ \frac{41}{55} \right] \\
 & \text{Gamma} \left[ \frac{52}{55} \right] \text{HypergeometricPFQ} \left[ \left\{ \frac{4}{55}, \frac{19}{110}, \frac{41}{110}, \frac{26}{55}, \frac{63}{110}, \frac{37}{55}, \frac{48}{55}, \frac{107}{110} \right\}, \right. \\
 & \left. \left\{ \frac{3}{22}, \frac{2}{11}, \frac{5}{22}, \frac{7}{22}, \frac{4}{11}, \frac{9}{22}, \frac{5}{11}, \frac{1}{2}, \frac{6}{11}, \frac{13}{22}, \frac{7}{11}, \frac{15}{22}, \right. \right. \\
 & \left. \left. \frac{8}{11}, \frac{9}{11}, \frac{19}{22}, \frac{10}{11}, \frac{21}{22}, \frac{23}{22}, \frac{12}{11} \right\}, \frac{9765625}{333425661488495661520162816 \alpha^{10}} \right] \Bigg) - \\
 & \frac{1}{24 \sqrt{11} \pi^2} \left( 5^{15/22} \left( \frac{1}{\alpha^2} \right)^{13/22} \cos \left[ \frac{12\pi}{55} \right] \cos \left[ \frac{4\pi}{11} \right] \cos \left[ \frac{23\pi}{55} \right] \cos \left[ \frac{5\pi}{11} \right] \cos \left[ \frac{34\pi}{55} \right] \cos \left[ \frac{56\pi}{55} \right] \right. \\
 & \cot \left[ \frac{9\pi}{11} \right] \csc \left[ \frac{\pi}{11} \right] \csc \left[ \frac{8\pi}{11} \right]^2 \csc \left[ \frac{10\pi}{11} \right] \text{Gamma} \left[ \frac{13}{55} \right] \text{Gamma} \left[ \frac{24}{55} \right] \text{Gamma} \left[ \frac{7}{11} \right] \text{Gamma} \left[ \frac{46}{55} \right] \\
 & \text{Gamma} \left[ \frac{57}{55} \right] \text{HypergeometricPFQ} \left[ \left\{ \frac{13}{110}, \frac{12}{55}, \frac{23}{55}, \frac{57}{110}, \frac{34}{55}, \frac{79}{110}, \frac{101}{110}, \frac{56}{55} \right\}, \left\{ \frac{2}{11}, \frac{5}{22}, \right. \right. \\
 & \left. \left. \frac{3}{11}, \frac{4}{11}, \frac{9}{22}, \frac{5}{11}, \frac{1}{2}, \frac{6}{11}, \frac{13}{22}, \frac{7}{11}, \frac{15}{22}, \frac{8}{11}, \frac{17}{22}, \frac{19}{22}, \frac{10}{11}, \frac{21}{22}, \frac{23}{22}, \frac{12}{11}, \frac{25}{22} \right\}, \right. \\
 & \left. \frac{9765625}{333425661488495661520162816 \alpha^{10}} \right] \text{Sign}[\alpha] \Bigg) + \\
 & \left( 16 2^{9/11} \pi^{5/2} \text{Gamma} \left[ \frac{10}{11} \right] \text{HypergeometricPFQ} \left[ \left\{ -\frac{1}{55}, \frac{9}{110}, \frac{31}{110}, \frac{21}{55}, \frac{53}{110}, \frac{32}{55}, \frac{43}{55}, \frac{97}{110} \right\}, \right. \right. \\
 & \left. \left\{ \frac{1}{22}, \frac{1}{11}, \frac{3}{22}, \frac{5}{22}, \frac{3}{11}, \frac{7}{22}, \frac{4}{11}, \frac{9}{22}, \frac{5}{11}, \frac{1}{2}, \frac{6}{11}, \frac{13}{22}, \right. \right. \\
 & \left. \left. \frac{7}{11}, \frac{8}{11}, \frac{17}{22}, \frac{9}{11}, \frac{19}{22}, \frac{10}{11}, \frac{21}{22} \right\}, \frac{9765625}{333425661488495661520162816 \alpha^{10}} \right] \right. \\
 & \left. \sin \left[ \frac{13\pi}{22} \right] \sin \left[ \frac{15\pi}{22} \right] \sin \left[ \frac{17\pi}{22} \right] \sin \left[ \frac{19\pi}{22} \right] \sin \left[ \frac{21\pi}{22} \right] \right) / \\
 & \left( 5^{1/11} \left( \frac{1}{\alpha^2} \right)^{1/11} \text{Gamma} \left[ \frac{13}{110} \right] \text{Gamma} \left[ \frac{7}{22} \right] \text{Gamma} \left[ \frac{57}{110} \right] \text{Gamma} \left[ \frac{79}{110} \right] \text{Gamma} \left[ \frac{101}{110} \right] \right) + \frac{1}{96 \sqrt{11} \pi^2} \\
 & \left( 5 5^{3/22} \left( \frac{1}{\alpha^2} \right)^{9/11} \cos \left[ \frac{9\pi}{55} \right] \cos \left[ \frac{4\pi}{11} \right]^2 \cos \left[ \frac{31\pi}{55} \right] \cos \left[ \frac{42\pi}{55} \right] \cos \left[ \frac{53\pi}{55} \right] \csc \left[ \frac{\pi}{11} \right]^2 \csc \left[ \frac{8\pi}{11} \right]^2 \right.
 \end{aligned}$$

$$\begin{aligned}
& \text{Csc}\left[\frac{9\pi}{11}\right] \text{Gamma}\left[\frac{18}{55}\right] \text{Gamma}\left[\frac{29}{55}\right] \text{Gamma}\left[\frac{8}{11}\right] \text{Gamma}\left[\frac{51}{55}\right] \text{Gamma}\left[\frac{62}{55}\right] \\
& \text{HypergeometricPFQ}\left[\left\{\frac{9}{55}, \frac{29}{110}, \frac{51}{110}, \frac{31}{55}, \frac{73}{110}, \frac{42}{55}, \frac{53}{55}, \frac{117}{110}\right\}, \left\{\frac{5}{22}, \frac{3}{11}, \frac{7}{22}, \frac{9}{22}, \frac{5}{11}, \frac{1}{2}, \frac{6}{11}, \frac{13}{22}, \frac{7}{11}, \frac{15}{22}, \frac{8}{11}, \frac{17}{22}, \frac{9}{11}, \frac{10}{22}, \frac{21}{22}, \frac{23}{22}, \frac{12}{11}, \frac{25}{22}, \frac{13}{11}\right\}, \right. \\
& \left. \frac{9765625}{333425661488495661520162816 \alpha^{10}}\right] \text{Sin}\left[\frac{23\pi}{22}\right] - \\
& \frac{1}{48 \sqrt{11} \pi^2} \left(5^{13/22} \left(\frac{1}{\alpha^2}\right)^{23/22} \text{Cos}\left[\frac{3\pi}{11}\right] \text{Cos}\left[\frac{17\pi}{55}\right] \right. \\
& \text{Cos}\left[\frac{4\pi}{11}\right] \text{Cos}\left[\frac{28\pi}{55}\right] \text{Cos}\left[\frac{39\pi}{55}\right] \text{Cos}\left[\frac{10\pi}{11}\right] \text{Cos}\left[\frac{61\pi}{55}\right] \text{Csc}\left[\frac{\pi}{11}\right]^2 \text{Csc}\left[\frac{6\pi}{11}\right] \\
& \text{Csc}\left[\frac{8\pi}{11}\right] \text{Csc}\left[\frac{9\pi}{11}\right] \text{Gamma}\left[\frac{23}{55}\right] \text{Gamma}\left[\frac{34}{55}\right] \text{Gamma}\left[\frac{9}{11}\right] \text{Gamma}\left[\frac{56}{55}\right] \text{Gamma}\left[\frac{67}{55}\right] \\
& \text{HypergeometricPFQ}\left[\left\{\frac{23}{110}, \frac{17}{55}, \frac{28}{55}, \frac{67}{110}, \frac{39}{55}, \frac{89}{110}, \frac{111}{110}, \frac{61}{55}\right\}, \left\{\frac{3}{11}, \frac{7}{22}, \frac{4}{11}, \frac{5}{11}, \frac{1}{2}, \frac{6}{11}, \frac{13}{22}, \frac{7}{11}, \frac{15}{22}, \frac{8}{11}, \frac{17}{22}, \frac{9}{11}, \frac{19}{22}, \frac{21}{22}, \frac{23}{22}, \frac{12}{11}, \frac{25}{22}, \frac{13}{11}, \frac{27}{22}\right\}, \right. \\
& \left. \frac{9765625}{333425661488495661520162816 \alpha^{10}}\right] \text{Sign}[\alpha] \text{Sin}\left[\frac{23\pi}{22}\right] - \\
& \frac{1}{11 5^{5/22} \pi^2} \left(64 \left(\frac{1}{\alpha^2}\right)^{3/22} \text{Cos}\left[\frac{7\pi}{55}\right] \text{Cos}\left[\frac{18\pi}{55}\right] \right. \\
& \text{Cos}\left[\frac{29\pi}{55}\right] \text{Cos}\left[\frac{8\pi}{11}\right] \text{Cos}\left[\frac{51\pi}{55}\right] \text{Gamma}\left[\frac{3}{55}\right] \text{Gamma}\left[\frac{14}{55}\right] \text{Gamma}\left[\frac{5}{11}\right] \text{Gamma}\left[\frac{36}{55}\right] \\
& \text{Gamma}\left[\frac{47}{55}\right] \text{HypergeometricPFQ}\left[\left\{\frac{3}{110}, \frac{7}{55}, \frac{18}{55}, \frac{47}{110}, \frac{29}{55}, \frac{69}{110}, \frac{91}{110}, \frac{51}{55}\right\}, \left\{\frac{1}{11}, \frac{3}{22}, \frac{2}{11}, \frac{3}{11}, \frac{7}{22}, \frac{4}{11}, \frac{9}{22}, \frac{5}{11}, \frac{1}{2}, \frac{6}{11}, \frac{13}{22}, \frac{7}{11}, \frac{15}{22}, \frac{17}{22}, \frac{9}{11}, \frac{19}{22}, \frac{10}{11}, \frac{21}{22}, \frac{23}{22}\right\}, \right. \\
& \left. \frac{9765625}{333425661488495661520162816 \alpha^{10}}\right] \text{Sign}[\alpha] \text{Sin}\left[\frac{13\pi}{22}\right] \text{Sin}\left[\frac{15\pi}{22}\right] \text{Sin}\left[\frac{17\pi}{22}\right] \text{Sin}\left[\frac{19\pi}{22}\right] \text{Sin}\left[\frac{23\pi}{22}\right] + \\
& \frac{1}{288 \sqrt{11} \pi^2} \left(5^{1/22} \left(\frac{1}{\alpha^2}\right)^{14/11} \text{Cos}\left[\frac{14\pi}{55}\right] \text{Cos}\left[\frac{5\pi}{11}\right] \text{Cos}\left[\frac{36\pi}{55}\right] \text{Cos}\left[\frac{47\pi}{55}\right] \text{Cos}\left[\frac{58\pi}{55}\right] \text{Cot}\left[\frac{3\pi}{11}\right] \right. \\
& \text{Csc}\left[\frac{\pi}{11}\right]^2 \text{Csc}\left[\frac{6\pi}{11}\right] \text{Csc}\left[\frac{9\pi}{11}\right] \text{Gamma}\left[\frac{28}{55}\right] \text{Gamma}\left[\frac{39}{55}\right] \text{Gamma}\left[\frac{10}{11}\right] \text{Gamma}\left[\frac{61}{55}\right] \text{Gamma}\left[\frac{72}{55}\right] \\
& \text{HypergeometricPFQ}\left[\left\{\frac{14}{55}, \frac{39}{110}, \frac{61}{110}, \frac{36}{55}, \frac{83}{110}, \frac{47}{55}, \frac{58}{55}, \frac{127}{110}\right\}, \left\{\frac{7}{22}, \frac{4}{11}, \frac{9}{22}, \frac{1}{2}, \frac{6}{11}, \frac{13}{22}, \frac{7}{11}, \frac{15}{22}, \frac{8}{11}, \frac{17}{22}, \frac{9}{11}, \frac{19}{22}, \frac{10}{11}, \frac{21}{22}, \frac{23}{22}, \frac{12}{11}, \frac{25}{22}, \frac{13}{11}, \frac{27}{22}, \frac{14}{11}\right\}, \right. \\
& \left. \frac{9765625}{333425661488495661520162816 \alpha^{10}}\right] \text{Sin}\left[\frac{23\pi}{22}\right] \text{Sin}\left[\frac{25\pi}{22}\right] - \\
& \frac{1}{8064 \sqrt{11} \pi^2} \left(5^{21/22} \left(\frac{1}{\alpha^2}\right)^{19/11} \text{Cos}\left[\frac{2\pi}{11}\right] \text{Cos}\left[\frac{19\pi}{55}\right] \text{Cos}\left[\frac{41\pi}{55}\right] \text{Cos}\left[\frac{52\pi}{55}\right] \text{Cos}\left[\frac{63\pi}{55}\right] \text{Cot}\left[\frac{3\pi}{11}\right] \right. \\
& \text{Cot}\left[\frac{6\pi}{11}\right] \text{Csc}\left[\frac{\pi}{11}\right]^2 \text{Csc}\left[\frac{4\pi}{11}\right] \text{Gamma}\left[\frac{38}{55}\right] \text{Gamma}\left[\frac{49}{55}\right] \text{Gamma}\left[\frac{12}{11}\right] \text{Gamma}\left[\frac{71}{55}\right] \text{Gamma}\left[\frac{82}{55}\right] \\
& \text{HypergeometricPFQ}\left[\left\{\frac{19}{55}, \frac{49}{110}, \frac{71}{110}, \frac{41}{55}, \frac{93}{110}, \frac{52}{55}, \frac{63}{55}, \frac{137}{110}\right\}, \left\{\frac{9}{22}, \frac{5}{11}, \frac{1}{2}, \frac{13}{22}, \frac{7}{11}, \frac{15}{22}, \frac{8}{11}, \frac{17}{22}, \frac{9}{11}, \frac{19}{22}, \frac{10}{11}, \frac{21}{22}, \frac{12}{11}, \frac{25}{22}, \frac{13}{11}, \frac{27}{22}, \frac{14}{11}, \frac{29}{22}, \frac{15}{11}\right\}, \right. \\
& \left. \frac{9765625}{333425661488495661520162816 \alpha^{10}}\right] \text{Sin}\left[\frac{23\pi}{22}\right] \text{Sin}\left[\frac{25\pi}{22}\right] + \\
& \left((-1 - \sqrt{5})^2 (1 - \sqrt{5}) (-1 + \sqrt{5}) \text{Cos}\left[\frac{2\pi}{11}\right] \text{Cot}\left[\frac{3\pi}{11}\right] \text{Csc}\left[\frac{\pi}{11}\right]^2 \text{Csc}\left[\frac{4\pi}{11}\right] \text{Csc}\left[\frac{6\pi}{11}\right] \right. \\
& \left. \text{HypergeometricPFQ}\left[\left\{\frac{3}{10}, \frac{2}{5}, \frac{3}{5}, \frac{7}{10}, \frac{4}{5}, \frac{9}{10}, 1, \frac{11}{10}, \frac{6}{5}\right\}, \left\{\frac{4}{11}, \frac{9}{22}, \frac{5}{11}\right\}, \right. \right.
\end{aligned}$$

$$\begin{aligned}
& \frac{6}{11} \cdot \frac{13}{22} \cdot \frac{7}{11} \cdot \frac{15}{22} \cdot \frac{8}{11} \cdot \frac{17}{22} \cdot \frac{9}{11} \cdot \frac{19}{22} \cdot \frac{10}{11} \cdot \frac{21}{22} \cdot \frac{23}{22} \cdot \frac{12}{11} \cdot \frac{25}{22} \cdot \frac{13}{11} \cdot \frac{27}{22} \cdot \frac{14}{11} \cdot \frac{29}{22} \Big\}, \\
& \frac{9765625}{333425661488495661520162816 \alpha^{10}} \Big] \sin\left[\frac{23\pi}{22}\right] \sin\left[\frac{25\pi}{22}\right] \Big) / \\
& \left( 16128 \sqrt{55(5-\sqrt{5})(5+\sqrt{5})} \alpha^3 \right) + \frac{1}{36288 \sqrt{11} \pi^2} \\
& \left( 25 5^{9/22} \left( \frac{1}{\alpha^2} \right)^{43/22} \cos\left[\frac{27\pi}{55}\right] \cos\left[\frac{38\pi}{55}\right] \cos\left[\frac{49\pi}{55}\right] \cos\left[\frac{12\pi}{11}\right] \cos\left[\frac{71\pi}{55}\right] \cot\left[\frac{\pi}{11}\right] \cot\left[\frac{2\pi}{11}\right] \right. \\
& \cot\left[\frac{3\pi}{11}\right] \csc\left[\frac{4\pi}{11}\right] \csc\left[\frac{6\pi}{11}\right] \Gamma\left[\frac{43}{55}\right] \Gamma\left[\frac{54}{55}\right] \Gamma\left[\frac{13}{11}\right] \Gamma\left[\frac{76}{55}\right] \Gamma\left[\frac{87}{55}\right] \\
& \text{HypergeometricPFQ}\left[\left\{\frac{43}{110}, \frac{27}{55}, \frac{38}{55}, \frac{87}{110}, \frac{49}{55}, \frac{109}{110}, \frac{131}{110}, \frac{71}{55}\right\}, \left\{\frac{5}{11}, \frac{1}{2}, \frac{6}{11}, \frac{7}{11}, \right. \right. \\
& \left. \left. \frac{15}{22}, \frac{8}{11}, \frac{17}{22}, \frac{9}{11}, \frac{19}{22}, \frac{10}{11}, \frac{21}{22}, \frac{23}{22}, \frac{25}{22}, \frac{13}{11}, \frac{27}{22}, \frac{14}{11}, \frac{29}{22}, \frac{15}{11}, \frac{31}{22}\right\}, \right. \\
& \left. \frac{9765625}{333425661488495661520162816 \alpha^{10}} \right] \text{Sign}[\alpha] \sin\left[\frac{23\pi}{22}\right] \sin\left[\frac{25\pi}{22}\right] \Big) - \\
& \frac{1}{72576 \sqrt{11} \pi^2 \alpha^4} \left( 5 5^{19/22} \left( \frac{1}{\alpha^2} \right)^{2/11} \cos\left[\frac{24\pi}{55}\right] \cos\left[\frac{7\pi}{11}\right] \cos\left[\frac{46\pi}{55}\right] \cos\left[\frac{57\pi}{55}\right] \cos\left[\frac{68\pi}{55}\right] \cot\left[\frac{\pi}{11}\right] \right. \\
& \cot\left[\frac{2\pi}{11}\right] \csc\left[\frac{3\pi}{11}\right] \csc\left[\frac{4\pi}{11}\right] \csc\left[\frac{5\pi}{11}\right] \Gamma\left[\frac{48}{55}\right] \Gamma\left[\frac{59}{55}\right] \Gamma\left[\frac{14}{11}\right] \Gamma\left[\frac{81}{55}\right] \\
& \Gamma\left[\frac{92}{55}\right] \text{HypergeometricPFQ}\left[\left\{\frac{24}{55}, \frac{59}{110}, \frac{81}{110}, \frac{46}{55}, \frac{103}{110}, \frac{57}{55}, \frac{68}{55}, \frac{147}{110}\right\}, \left\{\frac{1}{2}, \frac{6}{11}, \right. \right. \\
& \left. \left. \frac{13}{22}, \frac{15}{22}, \frac{8}{11}, \frac{17}{22}, \frac{9}{11}, \frac{19}{22}, \frac{10}{11}, \frac{21}{22}, \frac{23}{22}, \frac{12}{11}, \frac{13}{11}, \frac{27}{22}, \frac{14}{11}, \frac{29}{22}, \frac{15}{11}, \frac{31}{22}, \frac{16}{11}\right\}, \right. \\
& \left. \frac{9765625}{333425661488495661520162816 \alpha^{10}} \right] \sin\left[\frac{23\pi}{22}\right] \sin\left[\frac{25\pi}{22}\right] \sin\left[\frac{27\pi}{22}\right] \Big) - \\
& \left( 25 5^{7/22} \left( \frac{1}{\alpha^2} \right)^{9/22} \cos\left[\frac{\pi}{55}\right] \cos\left[\frac{32\pi}{55}\right] \cos\left[\frac{43\pi}{55}\right] \cos\left[\frac{13\pi}{11}\right] \cos\left[\frac{76\pi}{55}\right] \cot\left[\frac{\pi}{11}\right] \cot\left[\frac{2\pi}{11}\right] \right. \\
& \csc\left[\frac{3\pi}{11}\right] \csc\left[\frac{4\pi}{11}\right] \csc\left[\frac{5\pi}{11}\right] \Gamma\left[\frac{53}{55}\right] \Gamma\left[\frac{64}{55}\right] \Gamma\left[\frac{15}{11}\right] \Gamma\left[\frac{86}{55}\right] \Gamma\left[\frac{97}{55}\right] \\
& \text{HypergeometricPFQ}\left[\left\{\frac{53}{110}, \frac{32}{55}, \frac{43}{55}, \frac{97}{110}, \frac{54}{55}, \frac{119}{110}, \frac{141}{110}, \frac{76}{55}\right\}, \left\{\frac{6}{11}, \frac{13}{22}, \frac{7}{11}, \frac{8}{11}, \right. \right. \\
& \left. \left. \frac{17}{22}, \frac{9}{11}, \frac{19}{22}, \frac{10}{11}, \frac{21}{22}, \frac{23}{22}, \frac{12}{11}, \frac{25}{22}, \frac{27}{22}, \frac{14}{11}, \frac{29}{22}, \frac{15}{11}, \frac{31}{22}, \frac{16}{11}, \frac{3}{2}\right\}, \right. \\
& \left. \frac{9765625}{333425661488495661520162816 \alpha^{10}} \right] \text{Sign}[\alpha] \sin\left[\frac{23\pi}{22}\right] \sin\left[\frac{25\pi}{22}\right] \sin\left[\frac{27\pi}{22}\right] \Big) / \\
& \left( 798336 \sqrt{11} \pi^2 \alpha^4 \right) + \frac{1}{3293136 \pi^2 \alpha^4} \left( 25 5^{17/22} \left( \frac{1}{\alpha^2} \right)^{7/11} \right. \\
& \cos\left[\frac{29\pi}{55}\right] \cos\left[\frac{8\pi}{11}\right] \cos\left[\frac{51\pi}{55}\right] \cos\left[\frac{62\pi}{55}\right] \cos\left[\frac{73\pi}{55}\right] \Gamma\left[\frac{58}{55}\right] \Gamma\left[\frac{69}{55}\right] \Gamma\left[\frac{16}{11}\right] \\
& \Gamma\left[\frac{91}{55}\right] \Gamma\left[\frac{102}{55}\right] \text{HypergeometricPFQ}\left[\left\{\frac{29}{55}, \frac{69}{110}, \frac{91}{110}, \frac{51}{55}, \frac{113}{110}, \frac{62}{55}, \frac{73}{55}, \frac{157}{110}\right\}, \right. \\
& \left\{ \frac{13}{22}, \frac{7}{11}, \frac{15}{22}, \frac{17}{22}, \frac{9}{11}, \frac{19}{22}, \frac{10}{11}, \frac{21}{22}, \frac{23}{22}, \frac{12}{11}, \frac{25}{22}, \right. \\
& \left. \frac{13}{11}, \frac{14}{11}, \frac{29}{22}, \frac{15}{11}, \frac{31}{22}, \frac{16}{11}, \frac{3}{2}, \frac{17}{11} \right\}, \frac{9765625}{333425661488495661520162816 \alpha^{10}} \Big] \\
& \sin\left[\frac{23\pi}{22}\right] \sin\left[\frac{25\pi}{22}\right] \sin\left[\frac{27\pi}{22}\right] \sin\left[\frac{29\pi}{22}\right] \sin\left[\frac{31\pi}{22}\right] \Big) - \\
& \frac{1}{599350752 \pi^2 \alpha^6} \left( 125 5^{15/22} \left( \frac{1}{\alpha^2} \right)^{1/11} \cos\left[\frac{34\pi}{55}\right] \cos\left[\frac{9\pi}{11}\right] \cos\left[\frac{56\pi}{55}\right] \cos\left[\frac{67\pi}{55}\right] \cos\left[\frac{78\pi}{55}\right] \right. \\
& \Gamma\left[\frac{68}{55}\right] \Gamma\left[\frac{79}{55}\right] \Gamma\left[\frac{18}{11}\right] \Gamma\left[\frac{101}{55}\right] \Gamma\left[\frac{112}{55}\right] \text{HypergeometricPFQ}\left[\left\{\frac{34}{55}, \frac{79}{110}, \right. \right. \\
& \left. \left. \frac{101}{110}, \frac{56}{55}, \frac{123}{110}, \frac{67}{55}, \frac{78}{55}, \frac{167}{110}\right\}, \left\{\frac{15}{22}, \frac{8}{11}, \frac{17}{22}, \frac{19}{22}, \frac{10}{11}, \frac{21}{22}, \frac{23}{22}, \frac{12}{11}, \frac{25}{22}, \right. \right. \\
& \left. \left. \frac{13}{11}, \frac{27}{22}, \frac{14}{11}, \frac{15}{11}, \frac{31}{22}, \frac{16}{11}, \frac{3}{2}, \frac{17}{11}, \frac{35}{22}, \frac{18}{11}\right\}, \frac{9765625}{333425661488495661520162816 \alpha^{10}} \right] \\
& \sin\left[\frac{23\pi}{22}\right] \sin\left[\frac{25\pi}{22}\right] \sin\left[\frac{27\pi}{22}\right] \sin\left[\frac{29\pi}{22}\right] \sin\left[\frac{35\pi}{22}\right] \Big) -
\end{aligned}$$

$$\begin{aligned}
& \frac{1}{42810768 \pi^2 \alpha^4} \left( 125 5^{5/22} \left( \frac{1}{\alpha^2} \right)^{19/22} \cos\left[\frac{37\pi}{55}\right] \cos\left[\frac{48\pi}{55}\right] \right. \\
& \cos\left[\frac{59\pi}{55}\right] \cos\left[\frac{14\pi}{11}\right] \cos\left[\frac{81\pi}{55}\right] \text{Gamma}\left[\frac{63}{55}\right] \text{Gamma}\left[\frac{74}{55}\right] \text{Gamma}\left[\frac{17}{11}\right] \text{Gamma}\left[\frac{96}{55}\right] \\
& \text{Gamma}\left[\frac{107}{55}\right] \text{HypergeometricPFQ}\left[\left\{\frac{63}{110}, \frac{37}{55}, \frac{48}{55}, \frac{107}{110}, \frac{59}{55}, \frac{129}{110}, \frac{151}{110}, \frac{81}{55}\right\}, \right. \\
& \left. \left\{\frac{7}{11}, \frac{15}{22}, \frac{8}{11}, \frac{9}{11}, \frac{19}{22}, \frac{10}{11}, \frac{21}{22}, \frac{23}{22}, \frac{12}{11}, \frac{25}{22}, \frac{13}{11}, \frac{27}{22}, \frac{29}{22}, \frac{15}{11}, \frac{31}{22}, \frac{16}{11}, \frac{3}{2}, \frac{17}{11}, \frac{35}{22}\right\}, \frac{9765625}{333425661488495661520162816 \alpha^{10}} \right] \\
& \left. \text{Sign}[\alpha] \sin\left[\frac{23\pi}{22}\right] \sin\left[\frac{25\pi}{22}\right] \sin\left[\frac{27\pi}{22}\right] \sin\left[\frac{29\pi}{22}\right] \sin\left[\frac{35\pi}{22}\right] \right) + \\
& \left( 125 5^{13/22} \left( \frac{1}{\alpha^2} \right)^{6/11} \cos\left[\frac{39\pi}{55}\right] \cos\left[\frac{10\pi}{11}\right] \right. \\
& \cos\left[\frac{61\pi}{55}\right] \cos\left[\frac{72\pi}{55}\right] \cos\left[\frac{83\pi}{55}\right] \text{Gamma}\left[\frac{78}{55}\right] \text{Gamma}\left[\frac{89}{55}\right] \text{Gamma}\left[\frac{20}{11}\right] \text{Gamma}\left[\frac{111}{55}\right] \\
& \text{Gamma}\left[\frac{122}{55}\right] \text{HypergeometricPFQ}\left[\left\{\frac{39}{55}, \frac{89}{110}, \frac{111}{110}, \frac{61}{55}, \frac{133}{110}, \frac{72}{55}, \frac{83}{55}, \frac{177}{110}\right\}, \right. \\
& \left. \left\{\frac{17}{22}, \frac{9}{11}, \frac{19}{22}, \frac{21}{22}, \frac{23}{22}, \frac{12}{11}, \frac{25}{22}, \frac{13}{11}, \frac{27}{22}, \frac{14}{11}, \frac{29}{22}, \frac{15}{11}, \frac{16}{11}, \frac{3}{2}, \frac{17}{11}, \frac{35}{22}, \frac{18}{11}, \frac{37}{22}, \frac{19}{11}\right\}, \frac{9765625}{333425661488495661520162816 \alpha^{10}} \right] \\
& \left. \sin\left[\frac{23\pi}{22}\right] \sin\left[\frac{25\pi}{22}\right] \sin\left[\frac{27\pi}{22}\right] \sin\left[\frac{35\pi}{22}\right] \sin\left[\frac{37\pi}{22}\right] \right) / (28768836096 \pi^2 \alpha^6) + \\
& \left( 125 5^{3/22} \left( \frac{1}{\alpha^2} \right)^{7/22} \cos\left[\frac{42\pi}{55}\right] \cos\left[\frac{53\pi}{55}\right] \cos\left[\frac{64\pi}{55}\right] \right. \\
& \cos\left[\frac{15\pi}{11}\right] \cos\left[\frac{86\pi}{55}\right] \text{Gamma}\left[\frac{73}{55}\right] \text{Gamma}\left[\frac{84}{55}\right] \text{Gamma}\left[\frac{19}{11}\right] \text{Gamma}\left[\frac{106}{55}\right] \text{Gamma}\left[\frac{117}{55}\right] \\
& \text{HypergeometricPFQ}\left[\left\{\frac{73}{110}, \frac{42}{55}, \frac{53}{55}, \frac{117}{110}, \frac{64}{55}, \frac{139}{110}, \frac{161}{110}, \frac{86}{55}\right\}, \left\{\frac{8}{11}, \frac{17}{22}, \frac{9}{11}, \frac{10}{11}, \frac{21}{22}, \frac{23}{22}, \frac{12}{11}, \frac{25}{22}, \frac{13}{11}, \frac{27}{22}, \frac{14}{11}, \frac{29}{22}, \frac{31}{22}, \frac{16}{11}, \frac{3}{2}, \frac{17}{11}, \frac{35}{22}, \frac{18}{11}, \frac{37}{22}\right\}, \frac{9765625}{333425661488495661520162816 \alpha^{10}} \right] \\
& \left. \text{Sign}[\alpha] \sin\left[\frac{23\pi}{22}\right] \sin\left[\frac{25\pi}{22}\right] \sin\left[\frac{27\pi}{22}\right] \sin\left[\frac{35\pi}{22}\right] \sin\left[\frac{37\pi}{22}\right] \right) / (1798052256 \pi^2 \alpha^6) + \\
& \left( (-1 - \sqrt{5})^2 (1 - \sqrt{5}) (-1 + \sqrt{5}) \text{HypergeometricPFQ}\left[\left\{\frac{4}{5}, \frac{9}{10}, 1, \frac{11}{10}, \frac{6}{5}, \frac{13}{10}, \frac{7}{5}, \frac{8}{5}, \frac{17}{10}\right\}, \right. \right. \\
& \left. \left\{\frac{19}{22}, \frac{10}{11}, \frac{21}{22}, \frac{23}{22}, \frac{12}{11}, \frac{25}{22}, \frac{13}{11}, \frac{27}{22}, \frac{14}{11}, \frac{29}{22}, \frac{15}{11}, \frac{31}{22}, \frac{16}{11}, \frac{17}{11}, \frac{35}{22}, \frac{18}{11}, \frac{37}{22}, \frac{19}{11}, \frac{39}{22}, \frac{20}{11}\right\}, \frac{9765625}{333425661488495661520162816 \alpha^{10}} \right] \right. \\
& \left. \sin\left[\frac{23\pi}{22}\right] \sin\left[\frac{25\pi}{22}\right] \sin\left[\frac{35\pi}{22}\right] \sin\left[\frac{37\pi}{22}\right] \sin\left[\frac{39\pi}{22}\right] \right) / \\
& \left( 1397343467520 \sqrt{5(5 - \sqrt{5})(5 + \sqrt{5})} \alpha^8 \right) - \left( 625 5^{1/22} \left( \frac{1}{\alpha^2} \right)^{17/22} \cos\left[\frac{47\pi}{55}\right] \cos\left[\frac{58\pi}{55}\right] \right. \\
& \cos\left[\frac{69\pi}{55}\right] \cos\left[\frac{16\pi}{11}\right] \cos\left[\frac{91\pi}{55}\right] \text{Gamma}\left[\frac{83}{55}\right] \text{Gamma}\left[\frac{94}{55}\right] \text{Gamma}\left[\frac{21}{11}\right] \text{Gamma}\left[\frac{116}{55}\right] \text{Gamma}\left[\frac{127}{55}\right] \\
& \text{HypergeometricPFQ}\left[\left\{\frac{83}{110}, \frac{47}{55}, \frac{58}{55}, \frac{127}{110}, \frac{69}{55}, \frac{149}{110}, \frac{171}{110}, \frac{91}{55}\right\}, \left\{\frac{9}{11}, \frac{19}{22}, \frac{10}{11}, \frac{23}{22}, \frac{12}{11}, \frac{25}{22}, \frac{13}{11}, \frac{27}{22}, \frac{14}{11}, \frac{29}{22}, \frac{15}{11}, \frac{31}{22}, \frac{3}{2}, \frac{17}{11}, \frac{35}{22}, \frac{18}{11}, \frac{37}{22}, \frac{19}{11}, \frac{39}{22}\right\}, \frac{9765625}{333425661488495661520162816 \alpha^{10}} \right] \right)
\end{aligned}$$

$$\begin{aligned}
& \text{Sign}[\alpha] \sin\left[\frac{23\pi}{22}\right] \sin\left[\frac{25\pi}{22}\right] \sin\left[\frac{35\pi}{22}\right] \sin\left[\frac{37\pi}{22}\right] \sin\left[\frac{39\pi}{22}\right] \Big/ (489070213632 \pi^2 \alpha^6) + \\
& \left( 625 5^{9/22} \left(\frac{1}{\alpha^2}\right)^{5/11} \cos\left[\frac{49\pi}{55}\right] \cos\left[\frac{12\pi}{11}\right] \cos\left[\frac{71\pi}{55}\right] \right. \\
& \quad \cos\left[\frac{82\pi}{55}\right] \cos\left[\frac{93\pi}{55}\right] \text{Gamma}\left[\frac{98}{55}\right] \text{Gamma}\left[\frac{109}{55}\right] \text{Gamma}\left[\frac{24}{11}\right] \text{Gamma}\left[\frac{131}{55}\right] \\
& \quad \text{Gamma}\left[\frac{142}{55}\right] \text{HypergeometricPFQ}\left[\left\{\frac{49}{55}, \frac{109}{110}, \frac{131}{110}, \frac{71}{55}, \frac{153}{110}, \frac{82}{55}, \frac{93}{55}, \frac{197}{110}\right\}, \right. \\
& \quad \left\{\frac{21}{22}, \frac{23}{22}, \frac{25}{22}, \frac{13}{11}, \frac{27}{22}, \frac{14}{11}, \frac{29}{22}, \frac{15}{11}, \frac{31}{22}, \frac{16}{11}, \frac{3}{2}, \frac{17}{11}, \right. \\
& \quad \left. \frac{18}{11}, \frac{37}{22}, \frac{19}{11}, \frac{39}{22}, \frac{20}{11}, \frac{41}{22}, \frac{21}{11}\right\}, \frac{9765625}{333425661488495661520162816 \alpha^{10}} \Big] \\
& \quad \sin\left[\frac{23\pi}{22}\right] \sin\left[\frac{35\pi}{22}\right] \sin\left[\frac{37\pi}{22}\right] \sin\left[\frac{39\pi}{22}\right] \sin\left[\frac{41\pi}{22}\right] \Big/ \\
& (669048052248576 \pi^2 \alpha^8) + \left( 625 5^{21/22} \left(\frac{1}{\alpha^2}\right)^{5/22} \cos\left[\frac{52\pi}{55}\right] \cos\left[\frac{63\pi}{55}\right] \right. \\
& \quad \cos\left[\frac{74\pi}{55}\right] \cos\left[\frac{17\pi}{11}\right] \cos\left[\frac{96\pi}{55}\right] \text{Gamma}\left[\frac{93}{55}\right] \text{Gamma}\left[\frac{104}{55}\right] \text{Gamma}\left[\frac{23}{11}\right] \text{Gamma}\left[\frac{126}{55}\right] \text{Gamma}\left[\frac{137}{55}\right] \\
& \quad \text{HypergeometricPFQ}\left[\left\{\frac{93}{110}, \frac{52}{55}, \frac{63}{55}, \frac{137}{110}, \frac{74}{55}, \frac{159}{110}, \frac{181}{110}, \frac{96}{55}\right\}, \left\{\frac{10}{11}, \frac{21}{22}, \frac{12}{11}, \frac{25}{22}, \right. \right. \\
& \quad \left. \frac{13}{11}, \frac{27}{22}, \frac{14}{11}, \frac{29}{22}, \frac{15}{11}, \frac{31}{22}, \frac{16}{11}, \frac{3}{2}, \frac{35}{22}, \frac{18}{11}, \frac{37}{22}, \frac{19}{11}, \frac{39}{22}, \frac{20}{11}, \frac{41}{22}\right\}, \right. \\
& \quad \left. \frac{9765625}{333425661488495661520162816 \alpha^{10}} \right] \text{Sign}[\alpha] \\
& \quad \sin\left[\frac{23\pi}{22}\right] \sin\left[\frac{35\pi}{22}\right] \sin\left[\frac{37\pi}{22}\right] \sin\left[\frac{39\pi}{22}\right] \sin\left[\frac{41\pi}{22}\right] \Big/ (167262013062144 \pi^2 \alpha^8) - \\
& \left( 625 5^{19/22} \left(\frac{1}{\alpha^2}\right)^{15/22} \cos\left[\frac{57\pi}{55}\right] \cos\left[\frac{68\pi}{55}\right] \right. \\
& \quad \cos\left[\frac{79\pi}{55}\right] \cos\left[\frac{18\pi}{11}\right] \cos\left[\frac{101\pi}{55}\right] \text{Gamma}\left[\frac{103}{55}\right] \text{Gamma}\left[\frac{114}{55}\right] \text{Gamma}\left[\frac{25}{11}\right] \text{Gamma}\left[\frac{136}{55}\right] \\
& \quad \text{Gamma}\left[\frac{147}{55}\right] \text{HypergeometricPFQ}\left[\left\{\frac{103}{110}, \frac{57}{55}, \frac{68}{55}, \frac{147}{110}, \frac{79}{55}, \frac{169}{110}, \frac{191}{110}, \frac{101}{55}\right\}, \right. \\
& \quad \left\{\frac{23}{22}, \frac{12}{11}, \frac{13}{11}, \frac{27}{22}, \frac{14}{11}, \frac{29}{22}, \frac{15}{11}, \frac{31}{22}, \frac{16}{11}, \frac{3}{2}, \frac{17}{11}, \right. \\
& \quad \left. \frac{35}{22}, \frac{37}{22}, \frac{19}{11}, \frac{39}{22}, \frac{20}{11}, \frac{41}{22}, \frac{21}{11}, \frac{43}{22}\right\}, \frac{9765625}{333425661488495661520162816 \alpha^{10}} \Big] \\
& \quad \text{Sign}[\alpha] \sin\left[\frac{35\pi}{22}\right] \sin\left[\frac{37\pi}{22}\right] \sin\left[\frac{39\pi}{22}\right] \sin\left[\frac{41\pi}{22}\right] \sin\left[\frac{43\pi}{22}\right] \Big/ \\
& (14050009097220096 \pi^2 \alpha^8)
\end{aligned}$$

$$\begin{aligned}
S(\alpha) = & \int_0^\infty \sin\left(\frac{\alpha}{x^{11}} - \frac{1}{x^5}\right) x dx = \\
& \frac{1}{12 \sqrt{11} \pi^2} \left( 5^{15/22} \left( \frac{1}{\alpha^2} \right)^{13/22} \cos\left[\frac{13\pi}{110}\right] \cos\left[\frac{7\pi}{22}\right] \cos\left[\frac{4\pi}{11}\right] \cos\left[\frac{5\pi}{11}\right] \cos\left[\frac{57\pi}{110}\right] \cos\left[\frac{79\pi}{110}\right] \right. \\
& \cos\left[\frac{101\pi}{110}\right] \csc\left[\frac{\pi}{11}\right] \csc\left[\frac{8\pi}{11}\right]^2 \csc\left[\frac{9\pi}{11}\right] \csc\left[\frac{10\pi}{11}\right] \Gamma\left[\frac{13}{55}\right] \Gamma\left[\frac{24}{55}\right] \Gamma\left[\frac{7}{11}\right] \\
& \Gamma\left[\frac{46}{55}\right] \Gamma\left[\frac{57}{55}\right] \text{HypergeometricPFQ}\left[\left\{\frac{13}{110}, \frac{12}{55}, \frac{23}{55}, \frac{57}{110}, \frac{34}{55}, \frac{79}{110}, \frac{101}{110}, \frac{56}{55}\right\}, \right. \\
& \left. \left\{\frac{2}{11}, \frac{5}{22}, \frac{3}{11}, \frac{4}{11}, \frac{9}{22}, \frac{5}{11}, \frac{1}{2}, \frac{6}{11}, \frac{13}{22}, \frac{7}{11}, \frac{15}{22}, \frac{8}{11}, \frac{17}{22}, \frac{19}{22}, \frac{10}{11}, \frac{21}{22}, \frac{23}{11}, \frac{25}{22}\right\}, \frac{9765625}{333425661488495661520162816 \alpha^{10}} \right] \Bigg) + \\
& \frac{1}{8 \sqrt{11} \pi^2} \left( 5^{5/22} \left( \frac{1}{\alpha^2} \right)^{4/11} \cos\left[\frac{19\pi}{110}\right] \cos\left[\frac{41\pi}{110}\right] \right. \\
& \cos\left[\frac{5\pi}{11}\right] \cos\left[\frac{63\pi}{110}\right] \cos\left[\frac{17\pi}{22}\right] \cos\left[\frac{107\pi}{110}\right] \csc\left[\frac{\pi}{11}\right] \csc\left[\frac{7\pi}{11}\right] \csc\left[\frac{8\pi}{11}\right] \\
& \csc\left[\frac{9\pi}{11}\right] \csc\left[\frac{10\pi}{11}\right] \Gamma\left[\frac{8}{55}\right] \Gamma\left[\frac{19}{55}\right] \Gamma\left[\frac{6}{11}\right] \Gamma\left[\frac{41}{55}\right] \Gamma\left[\frac{52}{55}\right] \\
& \text{HypergeometricPFQ}\left[\left\{\frac{4}{55}, \frac{19}{110}, \frac{41}{110}, \frac{26}{55}, \frac{63}{110}, \frac{37}{55}, \frac{48}{55}, \frac{107}{110}\right\}, \left\{\frac{3}{22}, \frac{2}{11}, \frac{5}{22}, \frac{7}{22}, \frac{4}{11}, \frac{9}{22}, \frac{5}{11}, \frac{1}{2}, \frac{6}{11}, \frac{13}{22}, \frac{7}{11}, \frac{15}{22}, \frac{8}{11}, \frac{17}{22}, \frac{19}{22}, \frac{10}{11}, \frac{21}{22}, \frac{23}{22}, \frac{12}{11}\right\}, \right. \\
& \left. \frac{9765625}{333425661488495661520162816 \alpha^{10}} \right] \text{Sign}[\alpha] \Bigg) + \\
& \frac{1}{5^{1/11} \pi^{3/2} \left( \frac{1}{\alpha^2} \right)^{1/11} \Gamma\left[\frac{1}{11}\right]} \left( 2^{2^{9/11}} \Gamma\left[\frac{9}{110}\right] \Gamma\left[\frac{31}{110}\right] \Gamma\left[\frac{53}{110}\right] \Gamma\left[\frac{15}{22}\right] \right. \\
& \Gamma\left[\frac{97}{110}\right] \text{HypergeometricPFQ}\left[\left\{-\frac{1}{55}, \frac{9}{110}, \frac{31}{110}, \frac{21}{55}, \frac{53}{110}, \frac{32}{55}, \frac{43}{55}, \frac{97}{110}\right\}, \right. \\
& \left. \left\{\frac{1}{22}, \frac{1}{11}, \frac{3}{22}, \frac{5}{22}, \frac{3}{11}, \frac{7}{22}, \frac{4}{11}, \frac{9}{22}, \frac{5}{11}, \frac{1}{2}, \frac{6}{11}, \frac{13}{22}, \frac{7}{11}, \frac{8}{11}, \frac{17}{22}, \frac{9}{11}, \frac{19}{22}, \frac{10}{11}, \frac{21}{22}\right\}, \frac{9765625}{333425661488495661520162816 \alpha^{10}} \right] \\
& \text{Sign}[\alpha] \sin\left[\frac{13\pi}{22}\right] \sin\left[\frac{15\pi}{22}\right] \sin\left[\frac{17\pi}{22}\right] \sin\left[\frac{19\pi}{22}\right] \sin\left[\frac{21\pi}{22}\right] \Bigg) + \frac{1}{24 \sqrt{11} \pi^2} \\
& \left( 5^{13/22} \left( \frac{1}{\alpha^2} \right)^{23/22} \cos\left[\frac{23\pi}{110}\right] \cos\left[\frac{3\pi}{11}\right] \cos\left[\frac{4\pi}{11}\right] \cos\left[\frac{9\pi}{22}\right] \cos\left[\frac{67\pi}{110}\right] \cos\left[\frac{89\pi}{110}\right] \cos\left[\frac{111\pi}{110}\right] \right. \\
& \csc\left[\frac{\pi}{11}\right]^2 \csc\left[\frac{6\pi}{11}\right] \csc\left[\frac{8\pi}{11}\right] \csc\left[\frac{9\pi}{11}\right] \Gamma\left[\frac{23}{55}\right] \Gamma\left[\frac{34}{55}\right] \Gamma\left[\frac{9}{11}\right] \Gamma\left[\frac{56}{55}\right] \\
& \Gamma\left[\frac{67}{55}\right] \text{HypergeometricPFQ}\left[\left\{\frac{23}{110}, \frac{17}{55}, \frac{28}{55}, \frac{67}{110}, \frac{39}{55}, \frac{89}{110}, \frac{111}{110}, \frac{61}{55}\right\}, \left\{\frac{3}{11}, \frac{7}{22}, \frac{4}{11}, \frac{5}{11}, \frac{1}{2}, \frac{6}{11}, \frac{13}{22}, \frac{7}{11}, \frac{15}{22}, \frac{8}{11}, \frac{17}{22}, \frac{9}{11}, \frac{19}{22}, \frac{21}{22}, \frac{23}{22}, \frac{12}{11}, \frac{25}{22}, \frac{13}{11}, \frac{27}{22}\right\}, \right. \\
& \left. \frac{9765625}{333425661488495661520162816 \alpha^{10}} \right] \sin\left[\frac{23\pi}{22}\right] \Bigg) + \\
& \frac{1}{48 \sqrt{11} \pi^2} \left( 5^{5^{3/22}} \left( \frac{1}{\alpha^2} \right)^{9/11} \cos\left[\frac{29\pi}{110}\right] \cos\left[\frac{4\pi}{11}\right] \cos\left[\frac{51\pi}{110}\right] \cos\left[\frac{73\pi}{110}\right] \cos\left[\frac{19\pi}{22}\right] \cos\left[\frac{117\pi}{110}\right] \right. \\
& \csc\left[\frac{\pi}{11}\right]^2 \csc\left[\frac{8\pi}{11}\right]^2 \csc\left[\frac{9\pi}{11}\right] \Gamma\left[\frac{18}{55}\right] \Gamma\left[\frac{29}{55}\right] \Gamma\left[\frac{8}{11}\right] \Gamma\left[\frac{51}{55}\right] \Gamma\left[\frac{62}{55}\right] \\
& \text{HypergeometricPFQ}\left[\left\{\frac{9}{55}, \frac{29}{110}, \frac{51}{110}, \frac{31}{55}, \frac{73}{110}, \frac{42}{55}, \frac{53}{55}, \frac{117}{110}\right\}, \left\{\frac{5}{22}, \frac{3}{11}, \frac{7}{22}, \frac{9}{22}, \frac{5}{11}, \frac{1}{2}, \frac{6}{11}, \frac{13}{22}, \frac{7}{11}, \frac{15}{22}, \frac{8}{11}, \frac{17}{22}, \frac{9}{11}, \frac{10}{11}, \frac{21}{22}, \frac{23}{22}, \frac{12}{11}, \frac{25}{22}, \frac{13}{11}\right\}, \right. \\
& \left. \frac{9765625}{333425661488495661520162816 \alpha^{10}} \right] \Bigg) +
\end{aligned}$$

$$\begin{aligned}
& \frac{9765625}{333425661488495661520162816 \alpha^{10}} \left[ \text{Sign}[\alpha] \sin\left[\frac{23\pi}{22}\right] \right] + \frac{1}{11 \cdot 5^{5/22} \pi^2} \left( 128 \left(\frac{1}{\alpha^2}\right)^{3/22} \cos\left[\frac{3\pi}{110}\right] \right. \\
& \cos\left[\frac{5\pi}{22}\right] \cos\left[\frac{47\pi}{110}\right] \cos\left[\frac{69\pi}{110}\right] \cos\left[\frac{91\pi}{110}\right] \text{Gamma}\left[\frac{3}{55}\right] \text{Gamma}\left[\frac{14}{55}\right] \text{Gamma}\left[\frac{5}{11}\right] \text{Gamma}\left[\frac{36}{55}\right] \\
& \text{Gamma}\left[\frac{47}{55}\right] \text{HypergeometricPFQ}\left[\left\{\frac{3}{110}, \frac{7}{55}, \frac{18}{55}, \frac{47}{110}, \frac{29}{55}, \frac{69}{110}, \frac{91}{110}, \frac{51}{55}\right\}, \right. \\
& \left. \left\{\frac{1}{11}, \frac{3}{22}, \frac{2}{11}, \frac{3}{11}, \frac{7}{22}, \frac{4}{11}, \frac{9}{22}, \frac{5}{11}, \frac{1}{2}, \frac{6}{11}, \frac{13}{22}, \frac{7}{11}, \frac{15}{22}, \frac{17}{22}, \frac{9}{11}, \frac{19}{22}, \frac{10}{11}, \frac{21}{22}, \frac{23}{22}\right\}\right] \cdot \frac{9765625}{333425661488495661520162816 \alpha^{10}} \left. \right] \\
& \sin\left[\frac{13\pi}{22}\right] \sin\left[\frac{15\pi}{22}\right] \sin\left[\frac{17\pi}{22}\right] \sin\left[\frac{19\pi}{22}\right] \sin\left[\frac{23\pi}{22}\right] \Big) - \\
& \frac{1}{18144 \sqrt{11} \pi^2} \left( 25 \cdot 5^{9/22} \left(\frac{1}{\alpha^2}\right)^{43/22} \cos\left[\frac{43\pi}{110}\right] \cos\left[\frac{13\pi}{22}\right] \cos\left[\frac{87\pi}{110}\right] \cos\left[\frac{109\pi}{110}\right] \cos\left[\frac{131\pi}{110}\right] \right. \\
& \cot\left[\frac{\pi}{11}\right] \cot\left[\frac{2\pi}{11}\right] \cot\left[\frac{3\pi}{11}\right] \csc\left[\frac{4\pi}{11}\right] \csc\left[\frac{6\pi}{11}\right] \text{Gamma}\left[\frac{43}{55}\right] \text{Gamma}\left[\frac{54}{55}\right] \text{Gamma}\left[\frac{13}{11}\right] \text{Gamma}\left[\frac{76}{55}\right] \\
& \text{Gamma}\left[\frac{87}{55}\right] \text{HypergeometricPFQ}\left[\left\{\frac{43}{110}, \frac{27}{55}, \frac{38}{55}, \frac{87}{110}, \frac{49}{55}, \frac{109}{110}, \frac{131}{110}, \frac{71}{55}\right\}, \left\{\frac{5}{11}, \frac{1}{2}, \frac{6}{11}, \frac{7}{11}, \frac{15}{22}, \frac{8}{11}, \frac{17}{22}, \frac{9}{11}, \frac{19}{22}, \frac{10}{11}, \frac{21}{22}, \frac{23}{22}, \frac{25}{22}, \frac{13}{11}, \frac{27}{11}, \frac{14}{22}, \frac{29}{22}, \frac{15}{11}, \frac{31}{22}\right\}\right] \cdot \frac{9765625}{333425661488495661520162816 \alpha^{10}} \left. \right] \sin\left[\frac{23\pi}{22}\right] \sin\left[\frac{25\pi}{22}\right] \Big) + \\
& \frac{1}{144 \sqrt{11} \pi^2} \left( 5 \cdot 5^{1/22} \left(\frac{1}{\alpha^2}\right)^{14/11} \cos\left[\frac{39\pi}{110}\right] \cos\left[\frac{61\pi}{110}\right] \cos\left[\frac{83\pi}{110}\right] \cos\left[\frac{21\pi}{22}\right] \cos\left[\frac{127\pi}{110}\right] \cot\left[\frac{3\pi}{11}\right] \right. \\
& \csc\left[\frac{\pi}{11}\right]^2 \csc\left[\frac{6\pi}{11}\right] \csc\left[\frac{9\pi}{11}\right] \text{Gamma}\left[\frac{28}{55}\right] \text{Gamma}\left[\frac{39}{55}\right] \text{Gamma}\left[\frac{10}{11}\right] \text{Gamma}\left[\frac{61}{55}\right] \text{Gamma}\left[\frac{72}{55}\right] \\
& \text{HypergeometricPFQ}\left[\left\{\frac{14}{55}, \frac{39}{110}, \frac{61}{110}, \frac{36}{55}, \frac{83}{110}, \frac{47}{55}, \frac{58}{55}, \frac{127}{110}\right\}, \left\{\frac{7}{22}, \frac{4}{11}, \frac{9}{22}, \frac{1}{2}, \frac{6}{11}, \frac{13}{22}, \frac{7}{11}, \frac{15}{22}, \frac{8}{11}, \frac{17}{22}, \frac{9}{11}, \frac{19}{22}, \frac{10}{11}, \frac{23}{22}, \frac{12}{11}, \frac{25}{22}, \frac{13}{11}, \frac{27}{11}, \frac{14}{22}, \frac{29}{22}, \frac{15}{11}\right\}\right] \cdot \frac{9765625}{333425661488495661520162816 \alpha^{10}} \left. \right] \sin\left[\frac{23\pi}{22}\right] \sin\left[\frac{25\pi}{22}\right] \Big) - \\
& \frac{1}{4032 \sqrt{11} \pi^2} \left( 5 \cdot 5^{21/22} \left(\frac{1}{\alpha^2}\right)^{19/11} \cos\left[\frac{2\pi}{11}\right] \cos\left[\frac{49\pi}{110}\right] \cos\left[\frac{71\pi}{110}\right] \cos\left[\frac{93\pi}{110}\right] \cos\left[\frac{23\pi}{22}\right] \cos\left[\frac{137\pi}{110}\right] \right. \\
& \cot\left[\frac{3\pi}{11}\right] \csc\left[\frac{\pi}{11}\right]^2 \csc\left[\frac{4\pi}{11}\right] \csc\left[\frac{6\pi}{11}\right] \text{Gamma}\left[\frac{38}{55}\right] \text{Gamma}\left[\frac{49}{55}\right] \text{Gamma}\left[\frac{12}{11}\right] \text{Gamma}\left[\frac{71}{55}\right] \\
& \text{Gamma}\left[\frac{82}{55}\right] \text{HypergeometricPFQ}\left[\left\{\frac{19}{55}, \frac{49}{110}, \frac{71}{110}, \frac{41}{55}, \frac{93}{110}, \frac{52}{55}, \frac{63}{55}, \frac{137}{110}\right\}, \left\{\frac{9}{22}, \frac{5}{11}, \frac{1}{2}, \frac{13}{22}, \frac{7}{11}, \frac{15}{22}, \frac{8}{11}, \frac{17}{22}, \frac{9}{11}, \frac{19}{22}, \frac{10}{11}, \frac{21}{22}, \frac{12}{11}, \frac{25}{22}, \frac{13}{11}, \frac{27}{11}, \frac{14}{22}, \frac{29}{22}, \frac{15}{11}\right\}\right] \cdot \frac{9765625}{333425661488495661520162816 \alpha^{10}} \left. \right] \sin\left[\frac{23\pi}{22}\right] \sin\left[\frac{25\pi}{22}\right] \Big) - \\
& \frac{1}{36288 \sqrt{11} \pi^2 \alpha^4} \left( 5 \cdot 5^{19/22} \left(\frac{1}{\alpha^2}\right)^{2/11} \cos\left[\frac{59\pi}{110}\right] \cos\left[\frac{81\pi}{110}\right] \cos\left[\frac{103\pi}{110}\right] \cos\left[\frac{25\pi}{22}\right] \cos\left[\frac{147\pi}{110}\right] \right. \\
& \cot\left[\frac{\pi}{11}\right] \cot\left[\frac{2\pi}{11}\right] \csc\left[\frac{3\pi}{11}\right] \csc\left[\frac{4\pi}{11}\right] \csc\left[\frac{5\pi}{11}\right] \text{Gamma}\left[\frac{48}{55}\right] \text{Gamma}\left[\frac{59}{55}\right] \text{Gamma}\left[\frac{14}{11}\right] \text{Gamma}\left[\frac{81}{55}\right] \\
& \text{Gamma}\left[\frac{92}{55}\right] \text{HypergeometricPFQ}\left[\left\{\frac{24}{55}, \frac{59}{110}, \frac{81}{110}, \frac{46}{55}, \frac{103}{110}, \frac{57}{55}, \frac{68}{55}, \frac{147}{110}\right\}, \left\{\frac{1}{2}, \frac{6}{11}, \frac{13}{22}, \frac{15}{22}, \frac{8}{11}, \frac{17}{22}, \frac{9}{11}, \frac{19}{22}, \frac{10}{11}, \frac{21}{22}, \frac{23}{22}, \frac{12}{11}, \frac{13}{11}, \frac{27}{22}, \frac{14}{11}, \frac{29}{22}, \frac{15}{11}, \frac{31}{22}, \frac{16}{11}\right\}\right] \cdot \frac{9765625}{333425661488495661520162816 \alpha^{10}} \left. \right] \sin\left[\frac{23\pi}{22}\right] \sin\left[\frac{25\pi}{22}\right] \sin\left[\frac{27\pi}{22}\right] \Big) - \\
& \frac{1}{399168 \sqrt{11} \pi^2 \alpha^4} \left( 25 \cdot 5^{7/22} \left(\frac{1}{\alpha^2}\right)^{9/22} \cos\left[\frac{15\pi}{22}\right] \cos\left[\frac{97\pi}{110}\right] \cos\left[\frac{119\pi}{110}\right] \cos\left[\frac{141\pi}{110}\right] \right. \\
& \cot\left[\frac{\pi}{11}\right] \cot\left[\frac{2\pi}{11}\right] \csc\left[\frac{3\pi}{11}\right] \csc\left[\frac{4\pi}{11}\right] \csc\left[\frac{5\pi}{11}\right] \text{Gamma}\left[\frac{53}{55}\right] \text{Gamma}\left[\frac{64}{55}\right] \text{Gamma}\left[\frac{15}{11}\right] \\
& \text{Gamma}\left[\frac{86}{55}\right] \text{Gamma}\left[\frac{97}{55}\right] \text{HypergeometricPFQ}\left[\left\{\frac{53}{110}, \frac{32}{55}, \frac{43}{55}, \frac{97}{110}, \frac{54}{55}, \frac{119}{110}, \frac{141}{110}, \frac{76}{55}\right\}, \right.
\end{aligned}$$



$$\begin{aligned}
& \left\{ \frac{6}{11}, \frac{13}{22}, \frac{7}{11}, \frac{8}{11}, \frac{17}{22}, \frac{9}{11}, \frac{19}{22}, \frac{10}{11}, \frac{21}{22}, \frac{23}{22}, \frac{12}{11}, \right. \\
& \quad \left. \frac{25}{22}, \frac{27}{22}, \frac{14}{11}, \frac{29}{22}, \frac{15}{11}, \frac{31}{22}, \frac{16}{11}, \frac{3}{2} \right\}, \frac{9765625}{333425661488495661520162816 \alpha^{10}} \Big] \\
& \sin\left[\frac{\pi}{55}\right] \sin\left[\frac{23\pi}{22}\right] \sin\left[\frac{25\pi}{22}\right] \sin\left[\frac{27\pi}{22}\right] + \\
& \frac{1}{1646568 \pi^2 \alpha^4} \left( 25 5^{17/22} \left(\frac{1}{\alpha^2}\right)^{7/11} \cos\left[\frac{69\pi}{110}\right] \cos\left[\frac{91\pi}{110}\right] \right. \\
& \quad \cos\left[\frac{113\pi}{110}\right] \cos\left[\frac{27\pi}{22}\right] \cos\left[\frac{157\pi}{110}\right] \Gamma\left[\frac{58}{55}\right] \Gamma\left[\frac{69}{55}\right] \Gamma\left[\frac{16}{11}\right] \Gamma\left[\frac{91}{55}\right] \\
& \quad \Gamma\left[\frac{102}{55}\right] \text{HypergeometricPFQ}\left[\left\{\frac{29}{55}, \frac{69}{110}, \frac{91}{110}, \frac{51}{55}, \frac{113}{110}, \frac{62}{55}, \frac{73}{55}, \frac{157}{110}\right\}, \right. \\
& \quad \left. \left\{\frac{13}{22}, \frac{7}{11}, \frac{15}{22}, \frac{17}{22}, \frac{9}{11}, \frac{19}{22}, \frac{10}{11}, \frac{21}{22}, \frac{23}{22}, \frac{12}{11}, \frac{25}{22}, \right. \right. \\
& \quad \left. \left. \frac{13}{11}, \frac{14}{11}, \frac{29}{22}, \frac{15}{11}, \frac{31}{22}, \frac{16}{11}, \frac{3}{2}, \frac{17}{11}\right\} \right], \frac{9765625}{333425661488495661520162816 \alpha^{10}} \Big] \\
& \text{Sign}[\alpha] \sin\left[\frac{23\pi}{22}\right] \sin\left[\frac{25\pi}{22}\right] \sin\left[\frac{27\pi}{22}\right] \sin\left[\frac{29\pi}{22}\right] \sin\left[\frac{31\pi}{22}\right] + \\
& \frac{1}{21405384 \pi^2 \alpha^4} \left( 125 5^{5/22} \left(\frac{1}{\alpha^2}\right)^{19/22} \cos\left[\frac{63\pi}{110}\right] \cos\left[\frac{17\pi}{22}\right] \right. \\
& \quad \cos\left[\frac{107\pi}{110}\right] \cos\left[\frac{129\pi}{110}\right] \cos\left[\frac{151\pi}{110}\right] \Gamma\left[\frac{63}{55}\right] \Gamma\left[\frac{74}{55}\right] \Gamma\left[\frac{17}{11}\right] \Gamma\left[\frac{96}{55}\right] \\
& \quad \Gamma\left[\frac{107}{55}\right] \text{HypergeometricPFQ}\left[\left\{\frac{63}{110}, \frac{37}{55}, \frac{48}{55}, \frac{107}{110}, \frac{59}{55}, \frac{129}{110}, \frac{151}{110}, \frac{81}{55}\right\}, \right. \\
& \quad \left. \left\{\frac{7}{11}, \frac{15}{22}, \frac{8}{11}, \frac{9}{11}, \frac{19}{22}, \frac{10}{11}, \frac{21}{22}, \frac{23}{22}, \frac{12}{11}, \frac{25}{22}, \frac{13}{11}, \right. \right. \\
& \quad \left. \left. \frac{27}{22}, \frac{29}{22}, \frac{15}{11}, \frac{31}{22}, \frac{16}{11}, \frac{3}{2}, \frac{17}{11}, \frac{35}{22}\right\} \right], \frac{9765625}{333425661488495661520162816 \alpha^{10}} \Big] \\
& \sin\left[\frac{23\pi}{22}\right] \sin\left[\frac{25\pi}{22}\right] \sin\left[\frac{27\pi}{22}\right] \sin\left[\frac{29\pi}{22}\right] \sin\left[\frac{35\pi}{22}\right] - \\
& \frac{1}{299675376 \pi^2 \alpha^6} \left( 125 5^{15/22} \left(\frac{1}{\alpha^2}\right)^{1/11} \cos\left[\frac{79\pi}{110}\right] \cos\left[\frac{101\pi}{110}\right] \right. \\
& \quad \cos\left[\frac{123\pi}{110}\right] \cos\left[\frac{29\pi}{22}\right] \cos\left[\frac{167\pi}{110}\right] \Gamma\left[\frac{68}{55}\right] \Gamma\left[\frac{79}{55}\right] \Gamma\left[\frac{18}{11}\right] \Gamma\left[\frac{101}{55}\right] \\
& \quad \Gamma\left[\frac{112}{55}\right] \text{HypergeometricPFQ}\left[\left\{\frac{34}{55}, \frac{79}{110}, \frac{101}{110}, \frac{56}{55}, \frac{123}{110}, \frac{67}{55}, \frac{78}{55}, \frac{167}{110}\right\}, \right. \\
& \quad \left. \left\{\frac{15}{22}, \frac{8}{11}, \frac{17}{22}, \frac{19}{22}, \frac{10}{11}, \frac{21}{22}, \frac{23}{22}, \frac{12}{11}, \frac{25}{22}, \frac{13}{11}, \frac{27}{22}, \right. \right. \\
& \quad \left. \left. \frac{14}{11}, \frac{15}{11}, \frac{31}{22}, \frac{16}{11}, \frac{3}{2}, \frac{17}{11}, \frac{35}{22}, \frac{18}{11}\right\} \right], \frac{9765625}{333425661488495661520162816 \alpha^{10}} \Big] \\
& \text{Sign}[\alpha] \sin\left[\frac{23\pi}{22}\right] \sin\left[\frac{25\pi}{22}\right] \sin\left[\frac{27\pi}{22}\right] \sin\left[\frac{29\pi}{22}\right] \sin\left[\frac{35\pi}{22}\right] - \\
& \frac{1}{899026128 \pi^2 \alpha^6} \left( 125 5^{3/22} \left(\frac{1}{\alpha^2}\right)^{7/22} \cos\left[\frac{73\pi}{110}\right] \cos\left[\frac{19\pi}{22}\right] \right. \\
& \quad \cos\left[\frac{117\pi}{110}\right] \cos\left[\frac{139\pi}{110}\right] \cos\left[\frac{161\pi}{110}\right] \Gamma\left[\frac{73}{55}\right] \Gamma\left[\frac{84}{55}\right] \Gamma\left[\frac{19}{11}\right] \Gamma\left[\frac{106}{55}\right] \\
& \quad \Gamma\left[\frac{117}{55}\right] \text{HypergeometricPFQ}\left[\left\{\frac{73}{110}, \frac{42}{55}, \frac{53}{55}, \frac{117}{110}, \frac{64}{55}, \frac{139}{110}, \frac{161}{110}, \frac{86}{55}\right\}, \right. \\
& \quad \left. \left\{\frac{8}{11}, \frac{17}{22}, \frac{9}{11}, \frac{10}{11}, \frac{21}{22}, \frac{23}{22}, \frac{12}{11}, \frac{25}{22}, \frac{13}{11}, \frac{27}{22}, \frac{14}{11}, \right. \right. \\
& \quad \left. \left. \frac{29}{22}, \frac{31}{22}, \frac{16}{11}, \frac{3}{2}, \frac{17}{11}, \frac{35}{22}, \frac{18}{11}, \frac{37}{22}\right\} \right], \frac{9765625}{333425661488495661520162816 \alpha^{10}} \Big] \\
& \sin\left[\frac{23\pi}{22}\right] \sin\left[\frac{25\pi}{22}\right] \sin\left[\frac{27\pi}{22}\right] \sin\left[\frac{35\pi}{22}\right] \sin\left[\frac{37\pi}{22}\right] + \\
& \frac{1}{14384418048 \pi^2 \alpha^6} \left( 125 5^{13/22} \left(\frac{1}{\alpha^2}\right)^{6/11} \cos\left[\frac{89\pi}{110}\right] \cos\left[\frac{111\pi}{110}\right] \cos\left[\frac{133\pi}{110}\right] \cos\left[\frac{31\pi}{22}\right] \right. \\
& \quad \cos\left[\frac{177\pi}{110}\right] \Gamma\left[\frac{78}{55}\right] \Gamma\left[\frac{89}{55}\right] \Gamma\left[\frac{20}{11}\right] \Gamma\left[\frac{111}{55}\right] \Gamma\left[\frac{122}{55}\right] \text{HypergeometricPFQ}\left[ \right.
\end{aligned}$$

$$\begin{aligned}
& \left\{ \frac{39}{55}, \frac{89}{110}, \frac{111}{110}, \frac{61}{55}, \frac{133}{110}, \frac{72}{55}, \frac{83}{55}, \frac{177}{110} \right\}, \left\{ \frac{17}{22}, \frac{9}{11}, \frac{19}{22}, \frac{21}{22}, \frac{23}{22}, \frac{12}{11}, \frac{25}{22}, \frac{13}{11}, \frac{27}{22}, \right. \\
& \quad \left. \frac{14}{11}, \frac{29}{22}, \frac{15}{11}, \frac{16}{11}, \frac{3}{2}, \frac{17}{11}, \frac{35}{22}, \frac{18}{11}, \frac{37}{22}, \frac{19}{11} \right\}, \frac{9765625}{333425661488495661520162816 \alpha^{10}} \Big] \\
& \quad \text{Sign}[\alpha] \sin\left[\frac{23\pi}{22}\right] \sin\left[\frac{25\pi}{22}\right] \sin\left[\frac{27\pi}{22}\right] \sin\left[\frac{35\pi}{22}\right] \sin\left[\frac{37\pi}{22}\right] \Big) + \\
& \quad \frac{1}{244535106816 \pi^2 \alpha^6} \left( 625 5^{1/22} \left( \frac{1}{\alpha^2} \right)^{17/22} \cos\left[\frac{83\pi}{110}\right] \cos\left[\frac{21\pi}{22}\right] \right. \\
& \quad \cos\left[\frac{127\pi}{110}\right] \cos\left[\frac{149\pi}{110}\right] \cos\left[\frac{171\pi}{110}\right] \text{Gamma}\left[\frac{83}{55}\right] \text{Gamma}\left[\frac{94}{55}\right] \text{Gamma}\left[\frac{21}{11}\right] \text{Gamma}\left[\frac{116}{55}\right] \\
& \quad \text{Gamma}\left[\frac{127}{55}\right] \text{HypergeometricPFQ}\left[\left\{ \frac{83}{110}, \frac{47}{55}, \frac{58}{55}, \frac{127}{110}, \frac{69}{55}, \frac{149}{110}, \frac{171}{110}, \frac{91}{55} \right\}, \right. \\
& \quad \left\{ \frac{9}{11}, \frac{19}{22}, \frac{10}{11}, \frac{23}{22}, \frac{12}{11}, \frac{25}{22}, \frac{13}{11}, \frac{27}{22}, \frac{14}{11}, \frac{29}{22}, \frac{15}{11}, \right. \\
& \quad \left. \frac{31}{22}, \frac{3}{2}, \frac{17}{11}, \frac{35}{22}, \frac{18}{11}, \frac{37}{22}, \frac{19}{11}, \frac{39}{22} \right\}, \frac{9765625}{333425661488495661520162816 \alpha^{10}} \Big] \\
& \quad \sin\left[\frac{23\pi}{22}\right] \sin\left[\frac{25\pi}{22}\right] \sin\left[\frac{35\pi}{22}\right] \sin\left[\frac{37\pi}{22}\right] \sin\left[\frac{39\pi}{22}\right] \Big) - \\
& \quad \frac{1}{83631006531072 \pi^2 \alpha^8} \left( 625 5^{21/22} \left( \frac{1}{\alpha^2} \right)^{5/22} \cos\left[\frac{93\pi}{110}\right] \cos\left[\frac{23\pi}{22}\right] \right. \\
& \quad \cos\left[\frac{137\pi}{110}\right] \cos\left[\frac{159\pi}{110}\right] \cos\left[\frac{181\pi}{110}\right] \text{Gamma}\left[\frac{93}{55}\right] \text{Gamma}\left[\frac{104}{55}\right] \text{Gamma}\left[\frac{23}{11}\right] \text{Gamma}\left[\frac{126}{55}\right] \\
& \quad \text{Gamma}\left[\frac{137}{55}\right] \text{HypergeometricPFQ}\left[\left\{ \frac{93}{110}, \frac{52}{55}, \frac{63}{55}, \frac{137}{110}, \frac{74}{55}, \frac{159}{110}, \frac{181}{110}, \frac{96}{55} \right\}, \right. \\
& \quad \left\{ \frac{10}{11}, \frac{21}{22}, \frac{12}{11}, \frac{25}{22}, \frac{13}{11}, \frac{27}{22}, \frac{14}{11}, \frac{29}{22}, \frac{15}{11}, \frac{31}{22}, \frac{16}{11}, \right. \\
& \quad \left. \frac{3}{2}, \frac{35}{22}, \frac{18}{11}, \frac{37}{22}, \frac{19}{11}, \frac{39}{22}, \frac{20}{11}, \frac{41}{22} \right\}, \frac{9765625}{333425661488495661520162816 \alpha^{10}} \Big] \\
& \quad \sin\left[\frac{23\pi}{22}\right] \sin\left[\frac{35\pi}{22}\right] \sin\left[\frac{37\pi}{22}\right] \sin\left[\frac{39\pi}{22}\right] \sin\left[\frac{41\pi}{22}\right] \Big) + \\
& \quad \frac{1}{334524026124288 \pi^2 \alpha^8} \left( 625 5^{9/22} \left( \frac{1}{\alpha^2} \right)^{5/11} \cos\left[\frac{109\pi}{110}\right] \cos\left[\frac{131\pi}{110}\right] \right. \\
& \quad \cos\left[\frac{153\pi}{110}\right] \cos\left[\frac{35\pi}{22}\right] \cos\left[\frac{197\pi}{110}\right] \text{Gamma}\left[\frac{98}{55}\right] \text{Gamma}\left[\frac{109}{55}\right] \text{Gamma}\left[\frac{24}{11}\right] \text{Gamma}\left[\frac{131}{55}\right] \\
& \quad \text{Gamma}\left[\frac{142}{55}\right] \text{HypergeometricPFQ}\left[\left\{ \frac{49}{55}, \frac{109}{110}, \frac{131}{110}, \frac{71}{55}, \frac{153}{110}, \frac{82}{55}, \frac{93}{55}, \frac{197}{110} \right\}, \right. \\
& \quad \left\{ \frac{21}{22}, \frac{23}{22}, \frac{25}{22}, \frac{13}{11}, \frac{27}{22}, \frac{14}{11}, \frac{29}{22}, \frac{15}{11}, \frac{31}{22}, \frac{16}{11}, \frac{3}{2}, \right. \\
& \quad \left. \frac{17}{11}, \frac{18}{11}, \frac{37}{22}, \frac{19}{11}, \frac{39}{22}, \frac{20}{11}, \frac{41}{22}, \frac{21}{11} \right\}, \frac{9765625}{333425661488495661520162816 \alpha^{10}} \Big] \\
& \quad \text{Sign}[\alpha] \sin\left[\frac{23\pi}{22}\right] \sin\left[\frac{35\pi}{22}\right] \sin\left[\frac{37\pi}{22}\right] \sin\left[\frac{39\pi}{22}\right] \sin\left[\frac{41\pi}{22}\right] \Big) + \\
& \quad \frac{1}{7025004548610048 \pi^2 \alpha^8} \left( 625 5^{19/22} \left( \frac{1}{\alpha^2} \right)^{15/22} \cos\left[\frac{103\pi}{110}\right] \cos\left[\frac{25\pi}{22}\right] \cos\left[\frac{147\pi}{110}\right] \right. \\
& \quad \cos\left[\frac{169\pi}{110}\right] \cos\left[\frac{191\pi}{110}\right] \text{Gamma}\left[\frac{103}{55}\right] \text{Gamma}\left[\frac{114}{55}\right] \text{Gamma}\left[\frac{25}{11}\right] \text{Gamma}\left[\frac{136}{55}\right] \text{Gamma}\left[\frac{147}{55}\right] \\
& \quad \text{HypergeometricPFQ}\left[\left\{ \frac{103}{110}, \frac{57}{55}, \frac{68}{55}, \frac{147}{110}, \frac{79}{55}, \frac{169}{110}, \frac{191}{110}, \frac{101}{55} \right\}, \left\{ \frac{23}{22}, \frac{12}{11}, \frac{13}{11}, \frac{27}{22}, \right. \right. \\
& \quad \left. \frac{14}{11}, \frac{29}{22}, \frac{15}{11}, \frac{31}{22}, \frac{16}{11}, \frac{3}{2}, \frac{17}{11}, \frac{35}{22}, \frac{37}{22}, \frac{19}{11}, \frac{39}{22}, \frac{20}{11}, \frac{41}{22}, \frac{21}{11}, \frac{43}{22} \right\}, \right. \\
& \quad \left. \frac{9765625}{333425661488495661520162816 \alpha^{10}} \right] \sin\left[\frac{35\pi}{22}\right] \sin\left[\frac{37\pi}{22}\right] \sin\left[\frac{39\pi}{22}\right] \sin\left[\frac{41\pi}{22}\right] \\
& \quad \sin\left[\frac{43\pi}{22}\right] \Big)
\end{aligned}$$

## Appendix C. Line Broadening and Shifting Rates and Cross Sections

Table C-1. Line broadening and shifting rates and cross sections of atomic strontium for all transitions and noble gases studied in this research

	Broadening Rate ( $10^{-4} \text{ cm}^{-1}/\text{Torr}$ )	Shifting Rate ( $10^{-5} \text{ cm}^{-1}/\text{Torr}$ )	Broadening Cross Section ( $10^{-14} \text{ cm}^2$ )	Shifting Cross Section ( $10^{-14} \text{ cm}^2$ )
$5s^2 \ ^1S_0 \rightarrow 5s5p \ ^3P_1$ ( $14504.351 \text{ cm}^{-1}$ )				
He	2.53(0.11)	4.09(0.21)	0.894(0.040)	0.290(0.015)
Ne	1.733(0.085)	-2.12(0.14)	1.269(0.062)	-0.310(0.021)
Ar	1.636(0.024)	-4.84(0.13)	1.571(0.023)	-0.929(0.026)
Kr	2.06(0.10)	-5.09(0.16)	2.43(0.12)	-1.206(0.037)
Xe	2.29(0.15)	-5.035(0.097)	3.01(0.20)	-1.320(0.025)
$5s5p \ ^3P_0 \rightarrow 5s6s \ ^3S_1$ ( $14721.275 \text{ cm}^{-1}$ )				
He	3.94(0.50)	6.41(0.65)	1.98(0.25)	0.646(0.066)
Ne	1.56(0.30)	-2.49(0.23)	1.63(0.32)	-0.520(0.047)
Ar	3.70(0.36)	-12.0(1.0)	4.99(0.48)	-3.24(0.27)
Kr	3.48(0.46)	-10.39(0.39)	5.86(0.78)	-3.50(0.13)
Xe	3.65(0.11)	-12.334(0.085)	6.80(0.20)	-4.600(0.032)
$5s5p \ ^3P_1 \rightarrow 5s6s \ ^3S_1$ ( $14534.444 \text{ cm}^{-1}$ )				
He	4.86(0.28)	5.63(0.54)	2.45(0.14)	0.567(0.054)
Ne	1.63(0.23)	-1.45(0.29)	1.69(0.24)	-0.302(0.061)
Ar	3.44(0.50)	-11.135(0.082)	4.64(0.67)	-3.001(0.022)
Kr	3.17(0.32)	-9.69(0.64)	5.34(0.54)	-3.26(0.22)
Xe	3.90(0.88)	-9.7(1.4)	7.3(1.6)	-3.61(0.52)
$5s5p \ ^3P_2 \rightarrow 5s6s \ ^3S_1$ ( $14140.232 \text{ cm}^{-1}$ )				
He	3.64(0.48)	6.88(0.41)	1.83(0.24)	0.692(0.042)
Ne	1.57(0.12)	-1.51(0.10)	1.64(0.12)	-0.315(0.022)
Ar	3.13(0.23)	-13.17(0.45)	4.22(0.31)	-3.55(0.12)
Kr	3.46(0.23)	-9.33(0.32)	5.83(0.38)	-3.14(0.11)
Xe	3.70(0.15)	-12.12(0.38)	6.90(0.29)	-4.52(0.14)

Table C-2. Line broadening rates and cross sections of diatomic bismuth P branch rotational lines in the  $\nu''=3 \rightarrow \nu'=1$  vibrational manifold of the  $X(0_g^+) \rightarrow A(0_u^+)$  electronic transition perturbed by helium

P( $J''$ )	Broadening Rate ( $10^{-4} \text{ cm}^{-1}/\text{Torr}$ )	Broadening Cross Section ( $10^{-14} \text{ cm}^2$ )
20	1.22(0.16)	0.604(0.086)
50	0.20(0.78)	0.10(0.39)
55	1.69(0.25)	0.83(0.13)
60	1.018(0.072)	0.503(0.046)
65	1.11(0.12)	0.549(0.068)
70	1.49(0.33)	0.74(0.17)
75	1.31(0.17)	0.650(0.091)
80	2.30(0.66)	1.14(0.33)
85	1.37(0.17)	0.679(0.094)
90	1.999(0.072)	0.988(0.067)
95	2.33(0.62)	1.15(0.31)
100	1.34(0.20)	0.66(0.11)
105	1.53(0.15)	0.756(0.085)
110	1.23(0.29)	0.61(0.15)
115	1.15(0.21)	0.57(0.11)
120	1.248(0.067)	0.617(0.048)
125	1.404(0.053)	0.694(0.047)
127	0.34(0.56)	0.17(0.28)
131	1.66(0.17)	0.822(0.098)
135	1.44(0.13)	0.713(0.078)
140	2.06(0.11)	1.019(0.079)
141	1.70(0.21)	0.84(0.11)
145	1.34(0.13)	0.661(0.076)
150	1.45(0.11)	0.718(0.070)
155	1.280(0.067)	0.633(0.049)
160	1.34(0.24)	0.66(0.13)
165	1.94(0.16)	0.960(0.097)
171	1.009(0.064)	0.499(0.042)
172	1.73(0.28)	0.85(0.15)
175	1.345(0.024)	0.665(0.040)
180	0.51(0.11)	0.251(0.058)
186	1.602(0.059)	0.792(0.054)
187	1.66(0.17)	0.819(0.098)
190	2.239(0.062)	1.107(0.070)
195	1.58(0.54)	0.78(0.27)

Table C-3. Line broadening rates and cross sections of diatomic bismuth R branch rotational lines in the  $\nu''=3 \rightarrow \nu'=1$  vibrational manifold of the  $X(0_g^+) \rightarrow A(0_u^+)$  electronic transition perturbed by helium

R( $J''$ )	Broadening Rate ( $10^{-4}$ cm $^{-1}$ /Torr)	Broadening Cross Section ( $10^{-14}$ cm $^2$ )
33	-0.68(0.77)	-0.34(0.38)
63	1.74(0.24)	0.86(0.13)
68	-0.10(0.52)	-0.05(0.26)
73	1.71(0.15)	0.846(0.086)
78	1.49(0.36)	0.74(0.18)
83	1.344(0.055)	0.664(0.047)
88	1.16(0.25)	0.57(0.13)
93	1.39(0.16)	0.689(0.086)
98	1.909(0.093)	0.944(0.071)
103	1.115(0.073)	0.551(0.048)
108	1.04(0.21)	0.51(0.11)
113	2.157(0.099)	1.066(0.078)
118	1.39(0.18)	0.688(0.097)
123	2.06(0.23)	1.02(0.13)
128	1.70(0.34)	0.84(0.18)
133	1.79(0.21)	0.89(0.12)
140	-0.68(0.57)	-0.33(0.28)
143	1.380(0.073)	0.682(0.053)
148	1.54(0.17)	0.763(0.092)
154	1.458(0.038)	0.721(0.045)
158	1.10(0.26)	0.55(0.13)
164	2.69(0.39)	1.33(0.21)
169	2.14(0.12)	1.056(0.086)
170	1.47(0.11)	0.725(0.070)
173	1.29(0.46)	0.64(0.23)
178	1.42(0.17)	0.700(0.094)
183	1.34(0.14)	0.661(0.080)
185	1.77(0.20)	0.87(0.11)
188	1.05(0.20)	0.52(0.11)
194	-0.17(0.54)	-0.08(0.26)
199	1.43(0.26)	0.71(0.14)
200	1.18(0.20)	0.58(0.11)
203	0.83(0.14)	0.411(0.075)
208	1.19(0.55)	0.59(0.28)

Table C-4. Line broadening rates and cross sections of diatomic bismuth P branch rotational lines in the  $\nu''=3 \rightarrow \nu'=1$  vibrational manifold of the  $X(0_g^+) \rightarrow A(0_u^+)$  electronic transition perturbed by neon

P( $J''$ )	Broadening Rate ( $10^{-4} \text{ cm}^{-1}/\text{Torr}$ )	Broadening Cross Section ( $10^{-14} \text{ cm}^2$ )
20	0.395(0.011)	0.430(0.027)
50	0.646(0.076)	0.703(0.092)
55	0.854(0.037)	0.931(0.067)
60	1.013(0.059)	1.104(0.090)
65	0.67(0.29)	0.73(0.32)
70	1.09(0.14)	1.19(0.16)
75	1.053(0.042)	1.147(0.080)
80	1.068(0.033)	1.163(0.075)
85	0.993(0.024)	1.082(0.067)
90	0.997(0.071)	1.086(0.099)
95	1.058(0.062)	1.152(0.094)
100	1.082(0.024)	1.178(0.072)
105	1.202(0.085)	1.31(0.12)
110	1.236(0.028)	1.346(0.082)
115	0.903(0.030)	0.984(0.065)
120	0.993(0.085)	1.08(0.11)
125	0.799(0.064)	0.871(0.086)
127	0.82(0.22)	0.89(0.25)
131	1.021(0.033)	1.113(0.073)
135	0.975(0.078)	1.06(0.10)
140	1.117(0.097)	1.22(0.13)
141	1.031(0.029)	1.123(0.071)
145	1.068(0.051)	1.164(0.086)
150	0.825(0.021)	0.898(0.056)
155	0.954(0.045)	1.039(0.077)
160	0.91(0.12)	0.99(0.14)
165	0.97(0.10)	1.06(0.13)
171	0.947(0.021)	1.032(0.063)
172	1.020(0.068)	1.111(0.097)
175	0.746(0.089)	0.81(0.11)
180	0.844(0.025)	0.920(0.059)
186	0.906(0.084)	0.99(0.11)
187	0.854(0.040)	0.930(0.068)
190	0.628(0.075)	0.684(0.090)
195	1.19(0.15)	1.29(0.18)

Table C-5. Line broadening rates and cross sections of diatomic bismuth R branch rotational lines in the  $\nu''=3 \rightarrow \nu'=1$  vibrational manifold of the  $X(0_g^+) \rightarrow A(0_u^+)$  electronic transition perturbed by neon

R( $J''$ )	Broadening Rate ( $10^{-4} \text{ cm}^{-1}/\text{Torr}$ )	Broadening Cross Section ( $10^{-14} \text{ cm}^2$ )
33	0.834(0.022)	0.909(0.057)
63	1.277(0.048)	1.392(0.095)
68	1.114(0.084)	1.21(0.11)
73	1.130(0.028)	1.231(0.077)
78	0.66(0.23)	0.72(0.25)
83	0.85(0.19)	0.92(0.21)
88	1.044(0.056)	1.138(0.089)
93	0.977(0.043)	1.064(0.076)
98	1.161(0.040)	1.265(0.084)
103	0.866(0.025)	0.944(0.060)
108	0.936(0.095)	1.02(0.12)
113	0.9303(0.0032)	1.013(0.058)
118	0.866(0.033)	0.943(0.064)
123	1.226(0.034)	1.336(0.084)
128	0.948(0.033)	1.033(0.069)
133	0.959(0.071)	1.045(0.098)
140	0.795(0.26)	0.87(0.28)
143	0.881(0.043)	0.960(0.072)
148	1.57(0.89)	1.71(0.97)
154	0.757(0.015)	0.825(0.049)
158	0.930(0.090)	1.01(0.11)
164	0.923(0.068)	1.005(0.093)
169	0.868(0.064)	0.945(0.088)
170	0.82(0.14)	0.89(0.16)
173	0.884(0.089)	0.96(0.11)
178	0.911(0.033)	0.992(0.067)
183	0.739(0.087)	0.80(0.11)
185	1.071(0.069)	1.17(0.10)
188	0.78(0.21)	0.86(0.24)
194	0.95(0.21)	1.03(0.24)
199	0.75(0.14)	0.81(0.16)
200	0.947(0.040)	1.032(0.073)
203	0.835(0.039)	0.910(0.067)
208	0.95(0.16)	1.03(0.18)

Table C-6. Line broadening rates and cross sections of diatomic bismuth P branch rotational lines in the  $\nu''=3 \rightarrow \nu'=1$  vibrational manifold of the  $X(0_g^+) \rightarrow A(0_u^+)$  electronic transition perturbed by argon

P( $J''$ )	Broadening Rate ( $10^{-4} \text{ cm}^{-1}/\text{Torr}$ )	Broadening Cross Section ( $10^{-14} \text{ cm}^2$ )
20	1.53(0.11)	2.29(0.21)
50	1.49(0.19)	2.23(0.31)
55	0.95(0.17)	1.43(0.26)
60	0.81(0.16)	1.22(0.25)
65	1.50(0.18)	2.24(0.29)
70	1.50(0.21)	2.26(0.34)
75	1.33(0.10)	2.00(0.19)
80	2.11(0.16)	3.17(0.30)
85	1.219(0.082)	1.83(0.16)
90	1.40(0.16)	2.09(0.27)
95	1.21(0.14)	1.82(0.24)
100	1.189(0.099)	1.78(0.18)
105	1.574(0.038)	2.36(0.15)
110	1.84(0.13)	2.76(0.25)
115	1.105(0.089)	1.66(0.16)
120	1.12(0.12)	1.68(0.20)
125	0.987(0.092)	1.48(0.16)
127	0.83(0.11)	1.24(0.18)
131	1.35(0.12)	2.02(0.21)
135	1.31(0.11)	1.96(0.20)
140	1.57(0.12)	2.35(0.22)
141	1.343(0.025)	2.01(0.12)
145	1.179(0.061)	1.77(0.14)
150	0.92(0.13)	1.38(0.20)
155	1.37(0.17)	2.06(0.29)
160	1.40(0.22)	2.09(0.35)
165	1.421(0.031)	2.13(0.13)
171	1.259(0.095)	1.89(0.18)
172	1.41(0.18)	2.12(0.30)
175	1.23(0.17)	1.84(0.28)
180	1.64(0.15)	2.47(0.26)
186	1.181(0.022)	1.77(0.11)
187	1.00(0.15)	1.50(0.25)
190	1.17(0.33)	1.75(0.50)
195	1.526(0.019)	2.29(0.13)



Table C-7. Line broadening rates and cross sections of diatomic bismuth R branch rotational lines in the  $\nu''=3 \rightarrow \nu'=1$  vibrational manifold of the  $X(0_g^+) \rightarrow A(0_u^+)$  electronic transition perturbed by argon

R( $J''$ )	Broadening Rate ( $10^{-4} \text{ cm}^{-1}/\text{Torr}$ )	Broadening Cross Section ( $10^{-14} \text{ cm}^2$ )
33	0.202(0.078)	0.30(0.12)
63	0.861(0.064)	1.29(0.12)
68	1.33(0.12)	2.00(0.21)
73	1.681(0.038)	2.52(0.15)
78	1.20(0.16)	1.80(0.26)
83	1.033(0.087)	1.55(0.16)
88	1.37(0.31)	2.05(0.48)
93	1.15(0.40)	1.73(0.60)
98	1.58(0.22)	2.36(0.36)
103	1.27(0.16)	1.90(0.26)
108	1.02(0.22)	1.52(0.35)
113	1.504(0.043)	2.25(0.14)
118	1.32(0.19)	1.98(0.31)
123	1.40(0.11)	2.11(0.20)
128	1.04(0.15)	1.56(0.24)
133	1.040(0.049)	1.56(0.11)
140	0.97(0.19)	1.45(0.30)
143	1.238(0.079)	1.86(0.16)
148	0.36(0.29)	0.54(0.43)
154	1.14(0.18)	1.70(0.29)
158	1.123(0.034)	1.68(0.11)
164	1.007(0.076)	1.51(0.14)
169	1.176(0.019)	1.76(0.10)
170	1.39(0.23)	2.08(0.36)
173	1.47(0.29)	2.20(0.46)
178	1.09(0.14)	1.64(0.23)
183	1.29(0.24)	1.93(0.37)
185	1.00(0.20)	1.51(0.31)
188	0.926(0.056)	1.39(0.12)
194	1.062(0.074)	1.59(0.14)
199	1.29(0.13)	1.94(0.22)
200	1.37(0.15)	2.05(0.26)
203	1.29(0.13)	1.94(0.22)
208	0.930(0.032)	1.395(0.093)

Table C-8. Line broadening rates and cross sections of diatomic bismuth P branch rotational lines in the  $\nu''=3 \rightarrow \nu'=1$  vibrational manifold of the  $X(0_g^+) \rightarrow A(0_u^+)$  electronic transition perturbed by krypton

P( $J''$ )	Broadening Rate ( $10^{-4} \text{ cm}^{-1}/\text{Torr}$ )	Broadening Cross Section ( $10^{-14} \text{ cm}^2$ )
20	0.605	1.255(0.071)
50	1.18	2.46(0.14)
55	1.29	2.67(0.15)
60	0.970	2.01(0.11)
65	1.21	2.50(0.14)
70	1.24	2.58(0.15)
75	1.13	2.34(0.13)
80	1.54	3.20(0.18)
85	1.08	2.23(0.13)
90	0.979	2.03(0.12)
95	1.06	2.20(0.13)
100	1.11	2.31(0.13)
105	1.10	2.28(0.13)
110	1.14	2.36(0.13)
115	1.17	2.42(0.14)
120	1.20	2.50(0.14)
125	0.859	1.78(0.10)
127	1.11	2.30(0.13)
131	1.24	2.58(0.15)
135	0.981	2.03(0.12)
140	1.08	2.25(0.13)
141	1.12	2.32(0.13)
145	0.943	1.96(0.11)
150	1.08	2.25(0.13)
155	1.10	2.29(0.13)
160	1.15	2.39(0.14)
165	1.18	2.46(0.14)
171	1.13	2.35(0.13)
172	0.846	1.76(0.10)
175	1.24	2.58(0.15)
180	0.812	1.684(0.096)
186	0.964	2.00(0.11)
187	0.832	1.725(0.098)
190	0.510	1.058(0.060)
195	1.29	2.68(0.15)

Table C-9. Line broadening rates and cross sections of diatomic bismuth R branch rotational lines in the  $\nu''=3 \rightarrow \nu'=1$  vibrational manifold of the  $X(0_g^+) \rightarrow A(0_u^+)$  electronic transition perturbed by krypton

R( $J''$ )	Broadening Rate ( $10^{-4} \text{ cm}^{-1}/\text{Torr}$ )	Broadening Cross Section ( $10^{-14} \text{ cm}^2$ )
33	0.829	1.720(0.098)
63	0.858	1.78(0.10)
68	1.46	3.03(0.17)
73	1.46	3.02(0.17)
78	1.13	2.33(0.13)
83	0.929	1.93(0.11)
88	1.24	2.56(0.15)
93	1.15	2.38(0.14)
98	1.12	2.32(0.13)
103	1.04	2.16(0.12)
108	0.868	1.80(0.10)
113	0.903	1.87(0.11)
118	0.924	1.92(0.11)
123	1.29	2.67(0.15)
128	0.857	1.78(0.10)
133	1.09	2.26(0.13)
140	1.02	2.13(0.12)
143	0.766	1.588(0.090)
148	0.725	1.504(0.085)
154	0.792	1.643(0.093)
158	0.632	1.311(0.075)
164	1.25	2.59(0.15)
169	1.10	2.27(0.13)
170	0.438	0.909(0.052)
173	1.21	2.51(0.14)
178	1.07	2.22(0.13)
183	0.989	2.05(0.12)
185	0.641	1.330(0.076)
188	1.31	2.72(0.15)
194	1.62	3.35(0.19)
199	1.22	2.53(0.14)
200	1.02	2.12(0.12)
203	1.14	2.37(0.13)
208	1.20	2.49(0.14)

## Bibliography

1. Banwell, C. N. *Fundamentals of Molecular Spectroscopy* (2nd Edition). London: McGraw-Hill Publishing Company Limited, 1972.
2. Barsanti, M., L. Gianfrani, F. Pavone, A. Sasso, C. Silvestrini, and G. M. Tino. "Isotope Shifts and Hyperfine Structures Investigation of Doubly Excited Levels in SrI," *Zeitschrift für Physik D – Atoms, Molecules and Clusters*, 23: 145-49 (1992).
3. Bevington, Philip R. and D. Keith Robinson. *Data Reduction and Error Analysis for the Physical Sciences* (2nd Edition). New York: McGraw-Hill, Incorporated, 1992.
4. Brown, Theodore L., H. Eugene LeMay, Jr. and Bruce E. Bursten. *Chemistry: the Central Science* (7th Edition). Upper Saddle River NJ: Prentice-Hall, Incorporated, 1997.
5. Ch'en, Shang Y. and Arvid T. Lonseth. "Pressure Effects of Rare Gases on the Absorption Line Ca 4227. I. The Effects of Argon and Helium," *Physical Review A*, 3: 946-50 (1971).
6. Crane, John K., Michael J. Shaw, and R. W. Presta. "Measurement of the Cross Sections for Collisional Broadening of the Intercombination Transitions in Calcium and Strontium," *Physical Review A*, 49: 1666-74 (1994).
7. Demtröder, Wolfgang. *Laser Spectroscopy* (2nd Edition). Berlin: Springer-Verlag, 1996.
8. Devdariani, A. Z., Y. I. Ponomarev, and Y. N. Sebyakin. "Broadening and Shift of Resonance Lines of Second-Group Atoms by Light Inert Gases: Interaction Potentials," *Optical Spectroscopy (USSR)*, 59: 26-8 (1985).
9. Dolezal, Michael W. *Spectroscopic Constants, Lifetimes and Predissociation Rates for Bi<sub>2</sub> A(0<sub>u</sub><sup>+</sup>)*. Air Force Institute of Technology (AU), Wright-Patterson AFB OH, March 2001 (AD-A390968)(3003813).
10. Ehrlacher, E. and J. Huennekens. "Noble-gas Broadening Rates for Barium Transitions Involving the Metastable 6s 5d <sup>3</sup>D<sub>J</sub> Levels," *Physical Review A*, 46: 2642-8 (1992).

11. Ehrlacher, E. and J. Huennekens. "Noble-gas Broadening Rates for the  $6s^2\ ^1S_0 \rightarrow 6s\ 6p\ ^{1,3}P_1$  Resonance and Intercombination Lines of Barium," *Physical Review A*, 47: 3097-104 (1993).
12. Farr, J. M. and W. R. Hindmarsh. "Collision Broadening in the Strontium Resonance Line,  $\lambda\ 4607\ \text{\AA}$ ," *Journal of Physics B: Atomic and Molecular Physics*, 4: 568-73 (1971).
13. Franklin, Robert E. *Spectroscopic and Kinetic Studies of Bismuth Dimers*. Air Force Institute of Technology (AU), Wright-Patterson AFB OH, February 1997 (AD-A323253)(9721815).
14. Franklin, Robert E. and Glen P. Perram. "Laser Excitation Spectra and Franck-Condon Factors for  $\text{Bi}_2\ X^1\Sigma_g^+ \rightarrow A(0_u^+)$ ," *Journal of Molecular Spectroscopy*, 194: 1-7 (1999).
15. García, Gustavo and José Campos. "Transition Probabilities for Triplet Levels of Sr(I)," *Journal of Quantitative Spectroscopy and Radiative Transfer*, 39: 477-83 (1988).
16. Gaskill, Jack D. *Linear Systems, Fourier Transforms, and Optics*. New York: John Wiley & Sons, Incorporated, 1978.
17. Gerstenkorn, S. and P. Luc. *Atlas du Spectre D'Absorption de la Molécule D'Iode*. Publications Scientifiques et Littéraire, 1979.
18. Giles, R. G. and E. L. Lewis. "Collision Broadening and Shifts in the Spectra of Neutral and Singly Ionised Magnesium, Calcium and Strontium," *Journal of Physics B: Atomic and Molecular Physics*, 15: 2871-80 (1982).
19. Harima, H., Y. Fukuzo, K. Tachibana, and Y. Urano. "Absorption Coefficients for the Wing of the Sr Resonance Line at  $4607\ \text{\AA}$  Broadened by Ar and Xe," *Journal of Physics B: Atomic and Molecular Physics*, 14: 3069-77 (1981).
20. Harima, H., T. Yanagisawa, K. Tachibana, and Y. Urano. "Absorption Coefficients for the Wings of the Sr Resonance Line at  $4607\ \text{\AA}$  Broadened by He, Ne and Kr," *Journal of Physics A: Mathematical and General Physics*, 16: 4365-74 (1983).
21. Harris, M., E. L. Lewis, D. McHugh, and I. Shannon. "Measurement of the Broadening and Asymmetry of the Calcium Resonance Line ( $422.7\ \text{nm}$ )," *Journal of Physics B: Atomic and Molecular Physics*, 19: 3207-15 (1986).
22. Havey, M. D., L. C. Balling, and J. J. Wright. "Measurement of the  $^3P_1$  Lifetime in Sr," *Physical Review A*, 13: 1269-70 (1976).

23. Herzberg, Gerhard. *Atomic Spectra and Atomic Structure*. New York: Dover Publications, Incorporated, 1944.
24. Herzberg, Gerhard. *Molecular Spectra and Molecular Structure, Volume I: Spectra of Diatomic Molecules* (2nd Edition). Malabar FL: Krieger Publishing Company, 1950.
25. Hindmarsh, W. R. and Judith M. Farr. "Collision Broadening of Spectral Lines by Neutral Atoms," in *Progress in Quantum Electronics* (Volume 2). Oxford: Pergamon Press, 1972.
26. Hirschfelder, Joseph O., Charles F. Curtiss, and R. Byron Bird. *Molecular Theory of Gases and Liquids*. New York: John Wiley & Sons, Incorporated, 1954.
27. Hühn, R. and H. J. Kusch. "Broadening and Shift of Calcium Lines by van der Waals Interaction with Argon Atoms and by Electron Impact," *Astronomy and Astrophysics*, 28: 159-64 (1973).
28. Innes, K. K., S. J. Jackling III, and T. W. Tolbert. "Pressure Shift and/or Broadening of Lines in the Electronic Spectra of Cl<sub>2</sub>, Br<sub>2</sub>, I<sub>2</sub>, O<sub>2</sub>, HD, AlH and H<sub>2</sub>CO," *Journal of Quantitative Spectroscopy and Radiative Transfer*, 16: 443-50 (1976).
29. Jandel Scientific Software. *PeakFit User's Manual*. San Rafael CA: AISN Software Incorporated, 1995.
30. Jansson, Peter A. *Deconvolution with Applications in Spectroscopy*. San Diego: Academic Press, Incorporated, 1984.
31. Kelly, J. F., M. Harris, and A. Gallagher. "Collisional Transfer Within the Sr( $5^3P_J^0$ ) Multiplet Due to Nearly Adiabatic Collisions with Noble Gases," *Physical Review A*, 37: 2354-60 (1988).
32. Kliner, Dahv A. V. and Roger L. Farrow. "Measurements of Ground-State OH Rotational Energy-Transfer Rates," *Journal of Chemical Physics*, 110: 412-22 (1999).
33. Krane, Kenneth S. *Introductory Nuclear Physics*. New York: John Wiley & Sons, Incorporated, 1988.
34. Kuchta, E., R. J. Alvarez II, Y. H. Li, D. A. Krueger, and C. Y. She. "Collisional Broadening of Ba I Line (553.5 nm) by He or Ar," *Applied Physics B: Photophysics and Laser Chemistry*, 50: 129-32 (1990).

35. Lide, David R. (Editor-in-Chief) *CRC Handbook of Chemistry and Physics* (76th Edition). Boca Raton FL: CRC Press, 1996.
36. Luo, Caiyan, R. Wehr, J. R. Drummond, A. D. May, F. Thibault, J. Boisssoles, J. M. Launay, C. Boulet, J. -P. Bouanich, and J. -M. Hartmann. "Shifting and Broadening in the Fundamental Band of CO Highly Diluted in He and Ar: A Comparison with Theory," *Journal of Chemical Physics*, 115: 2198-206 (2001).
37. Malvern, A. R. "The Pressure Broadening of Calcium Perturbed by Inert Gases," *Journal of Physics B: Atomic and Molecular Physics*, 10: L593-7 (1977).
38. Moore, Charlotte E. *Atomic Energy Levels Volume II*. Washington: Government Printing Office, 1952.
39. O'Neill, J. A. and G. Smith. "Collisional Broadening of Spectral Lines in Laboratory and Solar Spectra I. The 6162, 6122, 6102 Å Multiplet of Neutral Calcium," *Astronomy and Astrophysics*, 81: 100-7 (1980).
40. Park, K., L. R. Zink, K. M. Evenson, K. V. Chance, and I. G. Nolt. "Pressure Broadening of the 83.869 cm<sup>-1</sup> Rotational Lines of OH by N<sub>2</sub>, O<sub>2</sub>, H<sub>2</sub>, and He," *Journal of Quantitative Spectroscopy and Radiative Transfer*, 55: 285-7 (1996).
41. Pope, Robert S. *Collisional Effects in the Absorption Spectra of the Oxygen A Band and Nitric Oxide Fundamental Band*. Air Force Institute of Technology (AU), Wright-Patterson AFB OH, December 1998 (AD-A361408)(9921302).
42. Predoi-Cross, Adriana, J. P. Bouanich, D. C. Benner, A. D. May, and J. R. Drummond. "Broadening, Shifting, and Line Asymmetries in the 2 ← 0 Band of CO and CO-N<sub>2</sub>: Experimental Results and Theoretical Calculations." *Journal of Chemical Physics*, 113: 158-68 (2000).
43. Röhe-Hansen, J. and V. Helbig. "Pressure Broadening of the Calcium 657.3 nm Line by Helium, Neon and Argon," *Journal of Physics B: Atomic, Molecular and Optical Physics*, 25: 71-82 (1992).
44. Rotondaro, Matthew D. and Glen P. Perram. "Collisional Broadening and Shift of the Rubidium D<sub>1</sub> and D<sub>2</sub> Lines (5<sup>2</sup>S<sub>1/2</sub> → 5<sup>2</sup>P<sub>1/2</sub>, 5<sup>2</sup>P<sub>3/2</sub>) by Rare Gases, H<sub>2</sub>, D<sub>2</sub>, N<sub>2</sub>, CH<sub>4</sub> and CF<sub>4</sub>," *Journal of Quantitative Spectroscopy and Radiative Transfer*, 57: 497-507 (1997).
45. Shabanova, L. N. "Potentials for the Interaction Between Certain Metal Atoms and Inert Gas Atoms," *Optical Spectroscopy*, 36: 13-5 (1974).
46. Smith, G. "Collision Broadening and Shift in the Resonance Line of Calcium," *Journal of Physics B: Atomic and Molecular Physics*, 5: 2310-9 (1972).

47. Smith, G. and D. St J. Raggett. "Oscillator Strengths and Collisional Damping Parameters for Lines of Neutral Calcium," *Journal of Physics B: Atomic and Molecular Physics*, 14: 4015-24 (1981).
48. Spielfiedel, A., N. Feautrier, G. Chambaud, and B. Lévy. "Collision Broadening of the  $4s4p(^3P^0)$ - $4s5s(^3S)$  Line of Calcium Perturbed by Hydrogen and Collision Induced Transitions Among the  $4s4p(^3P^0)$  States," *Journal of Physics B: Atomic, Molecular and Optical Physics*, 24: 4711-21 (1991).
49. Steinfeld, Jeffrey I., Joseph S. Francisco, and William L. Hase. *Chemical Kinetics and Dynamics*. Englewood Cliffs NJ: Prentice Hall, Incorporated, 1989.
50. Svanberg, Sune. *Atomic and Molecular Spectroscopy: Basic Aspects and Practical Applications*. Berlin: Springer-Verlag, 1991.
51. Szudy, J. and W. E. Baylis. "Unified Franck-Condon Treatment of Pressure Broadening of Spectral Lines," *Journal of Quantitative Spectroscopy and Radiative Transfer*, 15: 641-68 (1975).
52. Tolman, Richard C. *The Principles of Statistical Mechanics*. New York: Dover Publications, Incorporated, 1979.
53. Townes, Charles H. and Arthur L. Schawlow. *Microwave Spectroscopy*. New York: Dover Publications, Incorporated, 1975.
54. Varga, T. K. and C. Bello. *Periodic Table of Elements*. Concord Ontario: Papertech Marketing Group, Incorporated, 1994.
55. Verdeyen, Joseph T. *Laser Electronics* (2nd Edition). Englewood Cliffs NJ: Prentice-Hall, Incorporated, 1981.
56. Walker, F. William, Josef R. Parrington, and Frank Feiner. *Chart of the Nuclides* (14th Edition). San Jose: General Electric Company, 1989.
57. Wang, Shih Y. and Shang Y. Ch'en. "Pressure Effects of He and Xe on the Resonance Line of Strontium," *Journal of Quantitative Spectroscopy and Radiative Transfer*, 22: 87-91 (1979).
58. Wolfram, Stephen. *The Mathematica Book* (3rd Edition). Champaign IL: Wolfram Media, Incorporated, 1996.



## **Vita**

Major Jeremy C. Holtgrave graduated from Central Community High School in Breese, Illinois. He attended the University of Illinois at Urbana-Champaign, graduating with a Bachelor of Science in Physics in May 1990. While at the University of Illinois, he enrolled in the Air Force ROTC program and received a commission as a second lieutenant in the United States Air Force upon graduation. His first assignment was to the Air Force Institute of Technology, Wright-Patterson AFB, Ohio where he was promoted to first lieutenant and graduated with a Master of Science in Engineering Physics in December 1992. Lieutenant Holtgrave's next assignment was to the Arnold Engineering Development Center, Arnold AFB, Tennessee where he served as a project manager for space systems testing and as manager of rocket facilities planning and requirements. He was also promoted to captain during this tour. His third assignment brought him back to the Air Force Institute of Technology where he began the Doctor of Philosophy program in Physics in 1996. In 1999, Captain Holtgrave was assigned to the Air Force Technical Applications Center, Patrick AFB, Florida, where he served in the Nuclear Treaty Monitoring Directorate as chief of the Space Research, Development, and Analysis Branch. In December 2001 he was promoted to major and the following year was assigned to the Air Force Studies and Analyses Agency, Pentagon, Washington D.C.

<b>REPORT DOCUMENTATION PAGE</b>				<i>Form Approved OMB No. 0704-0188</i>	
<small>The public reporting burden for this collection of information is estimated to average 1 hour per response, including the time for reviewing instructions, searching existing data sources, gathering and maintaining the data needed, and completing and reviewing the collection of information. Send comments regarding this burden estimate or any other aspect of this collection of information, including suggestions for reducing the burden, to Department of Defense, Washington Headquarters Services, Directorate for Information Operations and Reports (0704-0188), 1215 Jefferson Davis Highway, Suite 1204, Arlington, VA 22202-4302. Respondents should be aware that notwithstanding any other provision of law, no person shall be subject to any penalty for failing to comply with a collection of information if it does not display a currently valid OMB control number.</small>					
<b>PLEASE DO NOT RETURN YOUR FORM TO THE ABOVE ADDRESS.</b>					
<b>1. REPORT DATE (DD-MM-YYYY)</b>		<b>2. REPORT TYPE</b>		<b>3. DATES COVERED (From - To)</b>	
<b>4. TITLE AND SUBTITLE</b>				<b>5a. CONTRACT NUMBER</b>	
				<b>5b. GRANT NUMBER</b>	
				<b>5c. PROGRAM ELEMENT NUMBER</b>	
<b>6. AUTHOR(S)</b>				<b>5d. PROJECT NUMBER</b>	
				<b>5e. TASK NUMBER</b>	
				<b>5f. WORK UNIT NUMBER</b>	
<b>7. PERFORMING ORGANIZATION NAME(S) AND ADDRESS(ES)</b>				<b>8. PERFORMING ORGANIZATION REPORT NUMBER</b>	
<b>9. SPONSORING/MONITORING AGENCY NAME(S) AND ADDRESS(ES)</b>				<b>10. SPONSOR/MONITOR'S ACRONYM(S)</b>	
				<b>11. SPONSOR/MONITOR'S REPORT NUMBER(S)</b>	
<b>12. DISTRIBUTION/AVAILABILITY STATEMENT</b>					
<b>13. SUPPLEMENTARY NOTES</b>					
<b>14. ABSTRACT</b>					
<b>15. SUBJECT TERMS</b>					
<b>16. SECURITY CLASSIFICATION OF:</b>			<b>17. LIMITATION OF ABSTRACT</b>	<b>18. NUMBER OF PAGES</b>	<b>19a. NAME OF RESPONSIBLE PERSON</b>
<b>a. REPORT</b>	<b>b. ABSTRACT</b>	<b>c. THIS PAGE</b>			<b>19b. TELEPHONE NUMBER (Include area code)</b>